DEVELOPMENT AND APPLICATIONS OF SENSOR INTEGRATED HYBRID RFID SYSTEM

By

Saikat Mondal

A DISSERTATION

Submitted to
Michigan State University
in partial fulfillment of the requirements
for the degree of

Electrical and Computer Engineering — Doctor of Philosophy

ABSTRACT

DEVELOPMENT AND APPLICATIONS OF SENSOR INTEGRATED HYBRID RFID SYSTEM

By

Saikat Mondal

Today, Radio Frequency Identification (RFID) has become a multibillion-dollar industry. RFID is primarily used for numerous object tagging and tracking applications such as road toll collection service, facility access control, asset tracking in a supply chain to name a few. Batteryless tag architecture and modern fabrication technology has enabled the miniaturization and cost reduction of ultra-high frequency (UHF) passive RFIDs. There is growing interest in the use of RFIDs for supply chain sensors (e.g., agricultural products and pharmaceuticals), underground object tagging (e.g., plastic pipes), low-power wearable devices, etc. However, the RFID designs in their current form cannot meet the stringent requirements of these new applications. Four key challenges that hinders the direct adoption of existing RFIDs for these applications are: (a) clutter effect, (b) integration of sensors, (c) response time, and (d) prolonged RF transmission from RFID reader for continuous sensor monitoring. In this work, the fundamental limitations of conventional RFID system are described in detail first, followed by proposed solutions leading to new RFID designs.

First, a dual frequency harmonic RFID system is proposed and demonstrated to mitigate the clutter effect. Second, a low power digital interface sensing platform is demonstrated for electrochemical pH sensor, targeted towards biochemical applications as an example. Third, detailed analysis is performed at the component level to understand the efficiency and response time dependence of the energy harvester within the RFID designs. Based on

the analysis, a model was proposed to estimate the response time of a conventional RFID tag. Fourth, a dual mode RFID is proposed and demonstrated to reduce the transmit time of RFID reader, hence reducing the effective RF transmission. Furthermore, the compatibility of integrating these solutions together in a single platform are presented. This is important as more than one challenge can be present in a single application. Finally, a hybrid RFID configuration is proposed and demonstrated that is capable of simultaneously mitigating all these four challenges.

This dissertation is dedicated to my beloved family. . .

ACKNOWLEDGMENTS

I am grateful to a number of people who has contributed to help me complete my PhD study at Michigan State University. First and foremost, I would like to thank one of the essential contributors to this thesis, my advisor Dr. Premjeet Chahal for providing me the privilege to be his student and then for his constant guidance and support throughout my Ph.D. journey, for which I am forever indebted. I also thank him for introducing me to a broad spectrum of research ideas and providing me the flexibility to pursue them over the years. Next, I am thankful to the rest of my committee members Dr. Yiming Deng, Dr. Jeffrey A. Nanzer, and Dr. Arun Ross for their valuable suggestions and feedback through my PhD work. I would also like to thank Dr. Edward J. Rothwell, Dr. Shanker Balasubramaniam, and Dr. Tim Hogan for providing me valuable insights in the various courses and encouraging me professionally.

I would like to thank the Department of Transportation (DoT), The AXIA Institute, Michigan Translational Research and Commercialization (MTRAC) Innovation Hub, and Ford Motor Company for sponsoring my research and making all this work possible. Special mention for Dr. Mahmoud Ghannam, Mark Cuddihy, Dr. Chris Oakley, and Dr. Ali Attaran from Ford, for their suggestions, which shaped many parts of this thesis. I would also like to thank MSU College of Engineering for providing me multiple fellowships and travel awards throughout my PhD program.

I appreciate all ECE department administrators and staff members for their help, specially Mr. Brain Wright, Mr. Gregg Mulder, Mr. Cameron Crump from MSU ECE shop, and Mr. Karl Dersch from ECE cleanroom, without whose support most of the work presented in this thesis would not be possible.

I would like to thank my fellow colleagues and alumni from the Electromagnetics Research Group (EMRG). I am thankful to our previous members Dr. Amanpreet Kaur and Dr. Mohd Ifwat Mohd Ghazali, Dr. Jennifer Byford for all their wisdom and advices. Further, I would like to mention about my special friends and co-workers, who made my PhD journey a memorable one: Dr. Saranraj Karuppuswami, Dr. Suhas Vidhate, and Deepak Kumar. I would like to mention my other colleagues and friends Yihang Chu, Yamini Kotriwar, Kanishka Wijewardena, Pratik Chatterjee, Dr. Yuxiao He, Dr. Michael Craton, Dr. Vinny Gjokaj, Stavros Vakalis, Serge Mghabghab, Anton Schlegel, Omkar Ramachandran, Abdel Alsnayyan, Zane Crawford, Dr. Scott OConnor, Dr. Sean Ellison, Eric Klinefelter, Elliot Lu and everyone else in EMRG. I would like to thank my friends Dhrubajit, Atri, Anmol, Rahul, Ritesh, Kunal, and my old kgp buddies Debashis, Shobhit, Sourin, and Subhosit.

Finally, I would like to thank my parents specially my mother for all their endless love, support and motivation not only through my PhD but also throughout my life. I am also thankful to Oindrilla Dutta for all her continuous support during my PhD journey.

TABLE OF CONTENTS

LIST (OF TABLES
LIST (OF FIGURES
Chapte	er 1 Introduction
1.1	Applications
	1.1.1 Electronic toll system
	1.1.2 Supply chain application
	1.1.3 Financial banking
	1.1.4 Sensing with identification
1.2	RFID System and Components
1.3	Backscatter Modulation
	1.3.1 Coupled antenna impedance
1.4	Thesis Organization
C 1 4	O Challes we with Consenting I DEID
Chapte	9
2.1	Clutter and Multipath Effect
	2.1.1 Clutter formulation
2.2	2.1.2 Clutter measurement
2.2	Sensor Integration
2.3	Low Power Operation and response Time
2.4	Prolonged RF transmission from reader
2.5	Summary
Chapte	er 3 Harmonic RFID
3.1	Background
3.2	Nonlinear Transmission Line: NLTL
	3.2.1 Design principle
	3.2.2 Simulation and measurement
3.3	Harmonic RFID: Gen I
	3.3.1 Antennas
	3.3.1.1 Meandered dipole antenna
	3.3.1.2 Yagi-Uda antenna
	3.3.2 Harmonic tag design
	3.3.2.1 HD using NLTL
	3.3.2.2 Energy Harvesting Unit (EHU) 50
	3.3.2.3 Digital Modulation Unit (DMU)
	3.3.2.4 Power Splitter (PS)
	3.3.3 Reader design
	3.3.4 Wireless measurement
3.4	Harmonic RFID: Gen II

3.4.2 Tag circuit 66 3.4.3 Wireless measurement 68 3.5 Harmonic RFID Tag Efficiency 70 3.6 Harmonic RFID Performance Under Clutter 71 3.7 Summary 73 Chapter 4 RFID With Integrated Sensor 77 4.1 Background 78 4.2 Design and Fabrication 81 4.2.1 RF interrogator 81 4.2.2 Readout circuit 82 4.2.3 pH sensor fabrication 86 4.3.1 Electrode performance 86 4.3.2 Elemental analysis of sensor electrodes 88 4.3.3 Multiple sensor electrode response 91 4.3.4 Readout circuit 91 4.3.5 Wireless measurement 92 4.4.1 Antenna design 96 4.4.2 Mouthguard design 97 4.5 Summary 96 Chapter 5 Energy Harvester Modeling 101 5.1 Background 102 5.2 Modified Dickson Charge Pump 103 5.3 Effect of Matching Network 105 5.3 Unities stage formulation 107 5.5 Measurement Results 111 6.1 Background 116		3.4.1 Antenna
3.5 Harmonic RFID Tag Efficiency 76 3.6 Harmonic RFID Performance Under Clutter 71 3.7 Summary 74 Chapter 4 RFID With Integrated Sensor 77 4.1 Background 78 4.2 Design and Fabrication 81 4.2.1 RF interrogator 81 4.2.2 Readout circuit 82 4.2.3 pH sensor fabrication 85 4.3.1 Electrode performance 86 4.3.2 Elemental analysis of sensor electrodes 88 4.3.3 Multiple sensor electrode response 91 4.3.4 Readout circuit 91 4.3.5 Wireless measurement 98 4.4.1 Antenna design 96 4.4.2 Mouthguard design 97 4.5 Summary 96 Chapter 5 Energy Harvester Modeling 101 5.1 Background 102 5.2 Modified Dickson Charge Pump 103 5.3 Effect of Matching Network 105 5.3 In Singl		3.4.2 Tag circuit
3.5 Harmonic RFID Tag Efficiency 76 3.6 Harmonic RFID Performance Under Clutter 71 3.7 Summary 74 Chapter 4 RFID With Integrated Sensor 77 4.1 Background 78 4.2 Design and Fabrication 81 4.2.1 RF interrogator 81 4.2.2 Readout circuit 82 4.2.3 pH sensor fabrication 85 4.3.1 Electrode performance 86 4.3.2 Elemental analysis of sensor electrodes 86 4.3.3 Multiple sensor electrode response 91 4.3.4 Readout circuit 91 4.3.5 Wireless measurement 92 4.4.1 Antenna design 94 4.4.2 Mouthguard design 96 4.4.2 Mouthguard design 97 4.5 Summary 96 5.1 Background 102 5.2 Modified Dickson Charge Pump 103 5.3 Effect of Matching Network 105 5.3.1 Single-stage formul		3.4.3 Wireless measurement
3.6 Harmonic RFID Performance Under Clutter 71 3.7 Summary 74 Chapter 4 RFID With Integrated Sensor 77 4.1 Background 78 4.2 Design and Fabrication 81 4.2.1 RF interrogator 81 4.2.2 Readout circuit 82 4.2.3 pH sensor fabrication 86 4.3.1 Electrode performance 86 4.3.2 Elemental analysis of sensor electrodes 85 4.3.3 Multiple sensor electrode response 91 4.3.4 Readout circuit 91 4.3.5 Wireless measurement 93 4.4 Application: Wearable Mouthguard 94 4.4.1 Antenna design 96 4.4.2 Mouthguard design 96 4.5 Summary 96 Chapter 5 Energy Harvester Modeling 101 5.1 Background 102 5.2 Modified Dickson Charge Pump 103 5.3 Effect of Matching Network 105 5.3 I Si	3.5	Harmonic RFID Tag Efficiency
3.7 Summary 74 Chapter 4 RFID With Integrated Sensor 77 4.1 Background 78 4.2 Design and Fabrication 81 4.2.1 RF interrogator 81 4.2.2 Readout circuit 82 4.2.3 pH sensor fabrication 83 4.3 Results 86 4.3.1 Electrode performance 86 4.3.2 Elemental analysis of sensor electrodes 88 4.3.3 Multiple sensor electrode response 91 4.3.4 Readout circuit 91 4.3.5 Wireless measurement 93 4.4 Application: Wearable Mouthguard 94 4.4.1 Antenna design 96 4.4.2 Mouthguard design 96 4.5 Summary 98 Chapter 5 Energy Harvester Modeling 101 5.1 Background 102 5.2 Modified Dickson Charge Pump 103 5.3 Effect of Matching Network 105 5.3.1 Single-stage formulation 107 5.3.2 Multi-stage formulation 107 5.3.5 Measurement Results 111 5.6 Summary 114 Chapter 6 Effective Transmit Time Reduction of RFID Reader<	3.6	
Chapter 4 RFID With Integrated Sensor 77 4.1 Background 78 4.2 Design and Fabrication 81 4.2.1 RF interrogator 81 4.2.2 Readout circuit 82 4.2.3 pH sensor fabrication 86 4.3.1 Electrode performance 86 4.3.2 Elemental analysis of sensor electrodes 88 4.3.3 Multiple sensor electrode response 91 4.3.4 Readout circuit 91 4.3.5 Wireless measurement 93 4.4 Application: Wearable Mouthguard 94 4.4.1 Antenna design 96 4.4.2 Mouthguard design 97 4.5 Summary 98 Chapter 5 Energy Harvester Modeling 10 5.1 Background 102 5.3 Effect of Matching Network 105 5.3.1 Single-stage formulation 107 5.3 Multi-stage formulation 107 5.5	3.7	
4.1 Background 78 4.2 Design and Fabrication 81 4.2.1 RF interrogator 81 4.2.2 Readout circuit 82 4.2.3 pH sensor fabrication 83 4.3 Results 86 4.3.1 Electrode performance 86 4.3.2 Elemental analysis of sensor electrodes 85 4.3.3 Multiple sensor electrode response 99 4.3.4 Readout circuit 91 4.3.5 Wireless measurement 96 4.3.4 Readout circuit 91 4.3.5 Wireless measurement 92 4.4 Application: Wearable Mouthguard 94 4.4.1 Antenna design 96 4.4.2 Mouthguard design 97 4.5 Summary 96 Chapter 5 Energy Harvester Modeling 101 5.1 Background 102 5.2 Modified Dickson Charge Pump 103 5.3 Effect of Matching Network 105 5.3.1 Single-stage formulation		
4.1 Background 78 4.2 Design and Fabrication 81 4.2.1 RF interrogator 81 4.2.2 Readout circuit 82 4.2.3 pH sensor fabrication 83 4.3 Results 86 4.3.1 Electrode performance 86 4.3.2 Elemental analysis of sensor electrodes 85 4.3.3 Multiple sensor electrode response 99 4.3.4 Readout circuit 91 4.3.5 Wireless measurement 96 4.3.4 Readout circuit 91 4.3.5 Wireless measurement 92 4.4 Application: Wearable Mouthguard 94 4.4.1 Antenna design 96 4.4.2 Mouthguard design 97 4.5 Summary 96 Chapter 5 Energy Harvester Modeling 101 5.1 Background 102 5.2 Modified Dickson Charge Pump 103 5.3 Effect of Matching Network 105 5.3.1 Single-stage formulation	Chapte	er 4 RFID With Integrated Sensor
4.2.1 RF interrogator 81 4.2.1 RF interrogator 81 4.2.2 Readout circuit 82 4.2.3 pH sensor fabrication 85 4.3 Results 86 4.3.1 Electrode performance 86 4.3.2 Elemental analysis of sensor electrodes 88 4.3.3 Multiple sensor electrode response 91 4.3.4 Readout circuit 91 4.3.5 Wireless measurement 95 4.4 Application: Wearable Mouthguard 94 4.4.1 Antenna design 96 4.4.2 Mouthguard design 97 4.5 Summary 98 Chapter 5 Energy Harvester Modeling 101 5.1 Background 102 5.2 Modified Dickson Charge Pump 103 5.3 Effect of Matching Network 105 5.3.1 Single-stage formulation 107 5.3.2 Multi-stage formulation 106 5.4 Transient Model for Arbitrary Load 108 5.5 Measurement Results 111 5.6 Summary 114 Chapter 6 Effective Transmit Time Reduction of RFID Reader 115 6.1 Background 116 6.2.1 M ₀ stat	-	
4.2.1 RF interrogator 81 4.2.2 Readout circuit 82 4.2.3 pH sensor fabrication 83 4.3 Results 86 4.3.1 Electrode performance 86 4.3.2 Elemental analysis of sensor electrodes 85 4.3.3 Multiple sensor electrode response 91 4.3.4 Readout circuit 91 4.3.5 Wireless measurement 93 4.4 Application: Wearable Mouthguard 94 4.4.1 Antenna design 96 4.4.2 Mouthguard design 97 4.5 Summary 96 Chapter 5 Energy Harvester Modeling 101 5.1 Background 102 5.2 Modified Dickson Charge Pump 103 5.3 Effect of Matching Network 105 5.3.1 Single-stage formulation 107 5.3.2 Multi-stage formulation 106 5.5 Measurement Results 111 5.6 Summary 114 Chapter 6 Effective Transmit Time Reduction of RFID Reader 115 6.1 Background 115 6.2 Finite State Machine and Event Driven Modes 118 6.2.1 M ₀ state: Tag backscatter communication 118 <td>4.2</td> <td>G .</td>	4.2	G .
4.2.2 Readout circuit 82 4.2.3 pH sensor fabrication 83 4.3 Results 86 4.3.1 Electrode performance 86 4.3.2 Elemental analysis of sensor electrodes 85 4.3.3 Multiple sensor electrode response 91 4.3.4 Readout circuit 91 4.3.5 Wireless measurement 93 4.4 Application: Wearable Mouthguard 94 4.4.1 Antenna design 96 4.4.2 Mouthguard design 97 4.5 Summary 98 Chapter 5 Energy Harvester Modeling 101 5.1 Background 102 5.2 Modified Dickson Charge Pump 103 5.3 Effect of Matching Network 105 5.3.1 Single-stage formulation 107 5.3.2 Multi-stage formulation 106 5.4 Transient Model for Arbitrary Load 108 5.5 Measurement Results 111 5.6 Summary 114 Chapter 6 Effective Transmit Time Reduction of RFID Reader 115 6.1 Background 115 6.2 Finite State Machine and Event Driven Modes 115 6.2.1 M ₀ state: Tag backscatter communication <td< td=""><td></td><td></td></td<>		
4.2.3 pH sensor fabrication 85 4.3.1 Results 86 4.3.1 Electrode performance 86 4.3.2 Elemental analysis of sensor electrodes 85 4.3.3 Multiple sensor electrode response 91 4.3.4 Readout circuit 91 4.3.5 Wireless measurement 96 4.4 Application: Wearable Mouthguard 94 4.4.1 Antenna design 96 4.4.2 Mouthguard design 97 4.5 Summary 98 Chapter 5 Energy Harvester Modeling 101 5.1 Background 102 5.3 Effect of Matching Network 105 5.3.1 Single-stage formulation 106 5.4 Transient Model for Arbitrary Load 106 5.5 Measurement Results 111 5.6 Summary 114 Chapter 6 Effective Transmit Time Reduction of RFID Reader 115 6.1 Background 115 6.2 Finite State Machine and Event Driven Modes 118 6.2.1 M ₀ state: Tag backscatter communication 118 6.2.2 M ₁ state: Tag active transmit 119 6.2.3 Events and driven modes 119 6.3		9
4.3 Results 86 4.3.1 Electrode performance 86 4.3.2 Elemental analysis of sensor electrodes 88 4.3.3 Multiple sensor electrode response 91 4.3.4 Readout circuit 91 4.3.5 Wireless measurement 93 4.4 Application: Wearable Mouthguard 94 4.4.1 Antenna design 96 4.4.2 Mouthguard design 97 4.5 Summary 98 Chapter 5 Energy Harvester Modeling 101 5.1 Background 102 5.2 Modified Dickson Charge Pump 103 5.3 Effect of Matching Network 105 5.3.1 Single-stage formulation 107 5.3.2 Multi-stage formulation 106 5.4 Transient Model for Arbitrary Load 106 5.5 Measurement Results 111 5.6 Summary 114 Chapter 6 Effective Transmit Time Reduction of RFID Reader 115 6.1 Background 115 6.2 Finite State Machine and Event Driven Modes 118 6.2.1 M_0 state: Tag backscatter communication 118 6.2.2 M_1 state: Tag active transmit 115 6.3 System Architectu		
$4.3.1$ Electrode performance 86 $4.3.2$ Elemental analysis of sensor electrodes 85 $4.3.3$ Multiple sensor electrode response 91 $4.3.4$ Readout circuit 91 $4.3.5$ Wireless measurement 93 4.4 Application: Wearable Mouthguard 94 $4.4.1$ Antenna design 96 $4.4.2$ Mouthguard design 97 4.5 Summary 92 Chapter 5 Energy Harvester Modeling 101 5.1 Background 102 5.2 Modified Dickson Charge Pump 103 5.3 Effect of Matching Network 105 $5.3.1$ Single-stage formulation 107 $5.3.2$ Multi-stage formulation 105 5.4 Transient Model for Arbitrary Load 105 5.5 Measurement Results 111 5.6 Summary 114 Chapter 6 Effective Transmit Time Reduction of RFID Reader 115 6.1 Background 116 6.2 M_1 st	43	•
$\begin{array}{cccccccccccccccccccccccccccccccccccc$	1.0	
4.3.3 Multiple sensor electrode response 91 4.3.4 Readout circuit 91 4.3.5 Wireless measurement 93 4.4 Application: Wearable Mouthguard 94 4.4.1 Antenna design 96 4.4.2 Mouthguard design 97 4.5 Summary 98 Chapter 5 Energy Harvester Modeling 101 5.1 Background 102 5.2 Modified Dickson Charge Pump 103 5.3 Effect of Matching Network 105 5.3.1 Single-stage formulation 107 5.3.2 Multi-stage formulation 106 5.4 Transient Model for Arbitrary Load 108 5.5 Measurement Results 111 5.6 Summary 114 Chapter 6 Effective Transmit Time Reduction of RFID Reader 115 6.1 Background 115 6.2 Finite State Machine and Event Driven Modes 118 6.2.1 M_0 state: Tag active transmit 118 6.2.2 M_1 state: Tag active transmit		1
4.3.4 Readout circuit 91 4.3.5 Wireless measurement 93 4.4 Application: Wearable Mouthguard 94 4.4.1 Antenna design 96 4.4.2 Mouthguard design 97 4.5 Summary 98 Chapter 5 Energy Harvester Modeling 101 5.1 Background 102 5.2 Modified Dickson Charge Pump 103 5.3 Effect of Matching Network 105 5.3.1 Single-stage formulation 107 5.3.2 Multi-stage formulation 109 5.4 Transient Model for Arbitrary Load 108 5.5 Measurement Results 111 5.6 Summary 114 Chapter 6 Effective Transmit Time Reduction of RFID Reader 115 6.1 Background 115 6.2 Finite State Machine and Event Driven Modes 115 6.2 Finite State Tag backscatter communication 118 6.2.1 M ₀ state: Tag backscatter communication 118 6.2.2 M ₁ state: Tag active transmit 119 6.3 Events and driven modes 115 6.3 System Architecture 121 6.3.1.1 Energy harvester 122 6.3.1.2 Reader code dem		V
$4.3.5$ Wireless measurement 93 4.4 Application: Wearable Mouthguard 94 $4.4.1$ Antenna design 96 $4.4.2$ Mouthguard design 97 4.5 Summary 98 Chapter 5 Energy Harvester Modeling 101 5.1 Background 102 5.2 Modified Dickson Charge Pump 103 5.3 Effect of Matching Network 105 $5.3.1$ Single-stage formulation 107 $5.3.2$ Multi-stage formulation 106 5.4 Transient Model for Arbitrary Load 108 5.5 Measurement Results 111 5.6 Summary 114 Chapter 6 Effective Transmit Time Reduction of RFID Reader 115 6.1 Background 115 6.2 $Finite State Machine and Event Driven Modes 116 6.2.1 M_0 state: Tag backscatter communication 118 6.2.2 M_1 state: Tag active transmit 119 6.3.3 Events and driven modes 111 6.3$		
4.4 Application: Wearable Mouthguard 94 4.4.1 Antenna design 96 4.4.2 Mouthguard design 97 4.5 Summary 96 Chapter 5 Energy Harvester Modeling 101 5.1 Background 102 5.2 Modified Dickson Charge Pump 103 5.3 Effect of Matching Network 103 5.3 Single-stage formulation 107 5.3.1 Single-stage formulation 109 5.4 Transient Model for Arbitrary Load 109 5.5 Measurement Results 111 5.6 Summary 114 Chapter 6 Effective Transmit Time Reduction of RFID Reader 115 6.1 Background 115 6.2 Finite State Machine and Event Driven Modes 118 6.2.1 M ₀ state: Tag backscatter communication 118 6.2.2 M ₁ state: Tag active transmit 118 6.2.3 Events and driven modes 119 6.3 1.7 Energy harvester 122 6.3.1.1 Energy harvest		
$4.4.1$ Antenna design 96 $4.4.2$ Mouthguard design 97 4.5 Summary 98 Chapter 5 Energy Harvester Modeling 101 5.1 Background 102 5.2 Modified Dickson Charge Pump 103 5.3 Effect of Matching Network 105 $5.3.1$ Single-stage formulation 107 $5.3.2$ Multi-stage formulation 109 5.4 Transient Model for Arbitrary Load 109 5.5 Measurement Results 111 5.6 Summary 114 Chapter 6 Effective Transmit Time Reduction of RFID Reader 115 6.1 Background 115 6.2 Finite State Machine and Event Driven Modes 118 $6.2.1$ M_0 state: Tag backscatter communication 118 $6.2.2$ M_1 state: Tag active transmit 119 $6.3.3$ Events and driven modes 119 6.3 System Architecture 121 $6.3.1.1$ Energy harvester 122 $6.3.1.2$ Reader code demodulator 123	1.1	
$4.4.2$ Mouthguard design97 4.5 Summary98Chapter 5Energy Harvester Modeling101 5.1 Background102 5.2 Modified Dickson Charge Pump103 5.3 Effect of Matching Network105 $5.3.1$ Single-stage formulation107 $5.3.2$ Multi-stage formulation109 5.4 Transient Model for Arbitrary Load109 5.5 Measurement Results111 5.6 Summary114Chapter 6Effective Transmit Time Reduction of RFID Reader115 6.1 Background115 6.2 Finite State Machine and Event Driven Modes118 $6.2.1$ M_0 state: Tag backscatter communication118 $6.2.2$ M_1 state: Tag active transmit119 $6.2.3$ Events and driven modes119 6.3 System Architecture121 $6.3.1$ Tag design121 $6.3.1.1$ Energy harvester122 $6.3.1.2$ Reader code demodulator123	4.4	
Chapter 5Energy Harvester Modeling101 5.1 Background102 5.2 Modified Dickson Charge Pump103 5.3 Effect of Matching Network105 $5.3.1$ Single-stage formulation107 $5.3.2$ Multi-stage formulation109 5.4 Transient Model for Arbitrary Load109 5.5 Measurement Results111 5.6 Summary114Chapter 6Effective Transmit Time Reduction of RFID Reader115 6.1 Background118 6.2 Finite State Machine and Event Driven Modes118 $6.2.1$ M_0 state: Tag backscatter communication118 $6.2.2$ M_1 state: Tag active transmit119 $6.3.1$ Events and driven modes119 $6.3.3$ Events and driven modes120 $6.3.1$ Tag design121 $6.3.1.1$ Energy harvester122 $6.3.1.2$ Reader code demodulator123		
Chapter 5 Energy Harvester Modeling101 5.1 Background102 5.2 Modified Dickson Charge Pump103 5.3 Effect of Matching Network105 $5.3.1$ Single-stage formulation107 $5.3.2$ Multi-stage formulation109 5.4 Transient Model for Arbitrary Load109 5.5 Measurement Results111 5.6 Summary114Chapter 6 Effective Transmit Time Reduction of RFID Reader115 6.1 Background116 6.2 Finite State Machine and Event Driven Modes118 $6.2.1$ M_0 state: Tag backscatter communication118 $6.2.2$ M_1 state: Tag active transmit119 $6.3.3$ Events and driven modes119 $6.3.1$ Tag design121 $6.3.1.1$ Energy harvester122 $6.3.1.2$ Reader code demodulator123	15	
5.1Background1025.2Modified Dickson Charge Pump1035.3Effect of Matching Network1055.3.1Single-stage formulation1075.3.2Multi-stage formulation1095.4Transient Model for Arbitrary Load1095.5Measurement Results1115.6Summary114Chapter 6 Effective Transmit Time Reduction of RFID Reader1156.1Background1156.2Finite State Machine and Event Driven Modes1186.2.1 M_0 state: Tag backscatter communication1186.2.2 M_1 state: Tag active transmit1196.2.3Events and driven modes1196.3System Architecture1216.3.1Tag design1216.3.1.1Energy harvester1226.3.1.2Reader code demodulator123	4.0	Summary
5.1Background1025.2Modified Dickson Charge Pump1035.3Effect of Matching Network1055.3.1Single-stage formulation1075.3.2Multi-stage formulation1095.4Transient Model for Arbitrary Load1095.5Measurement Results1115.6Summary114Chapter 6 Effective Transmit Time Reduction of RFID Reader1156.1Background1156.2Finite State Machine and Event Driven Modes1186.2.1 M_0 state: Tag backscatter communication1186.2.2 M_1 state: Tag active transmit1196.2.3Events and driven modes1196.3System Architecture1216.3.1Tag design1216.3.1.1Energy harvester1226.3.1.2Reader code demodulator123	Chapte	er 5 Energy Harvester Modeling
5.2Modified Dickson Charge Pump1035.3Effect of Matching Network105 $5.3.1$ Single-stage formulation107 $5.3.2$ Multi-stage formulation1085.4Transient Model for Arbitrary Load1095.5Measurement Results1115.6Summary114Chapter 6 Effective Transmit Time Reduction of RFID Reader1156.1Background1156.2Finite State Machine and Event Driven Modes1186.2.1 M_0 state: Tag backscatter communication1186.2.2 M_1 state: Tag active transmit1196.3Events and driven modes1196.3System Architecture1216.3.1Tag design1216.3.1.1Energy harvester1226.3.1.2Reader code demodulator123	-	3.
$ 5.3 \text{Effect of Matching Network} \qquad 105 \\ 5.3.1 \text{Single-stage formulation} \qquad 107 \\ 5.3.2 \text{Multi-stage formulation} \qquad 109 \\ 5.4 \text{Transient Model for Arbitrary Load} \qquad 109 \\ 5.5 \text{Measurement Results} \qquad 111 \\ 5.6 \text{Summary} \qquad 114 \\ \hline $		0
$5.3.1$ Single-stage formulation 107 $5.3.2$ Multi-stage formulation 109 5.4 Transient Model for Arbitrary Load 109 5.5 Measurement Results 111 5.6 Summary 114 5.6 Summary 114 5.6 Effective Transmit Time Reduction of RFID Reader 115 6.1 Background 115 6.2 Finite State Machine and Event Driven Modes 118 $6.2.1$ M_0 state: Tag backscatter communication 118 $6.2.2$ M_1 state: Tag active transmit 119 $6.2.3$ Events and driven modes 119 6.3 System Architecture 121 $6.3.1$ Tag design 121 $6.3.1.1$ Energy harvester 122 $6.3.1.2$ Reader code demodulator 123		-
5.3.2 Multi-stage formulation	0.0	
5.4Transient Model for Arbitrary Load1095.5Measurement Results1115.6Summary114Chapter 6 Effective Transmit Time Reduction of RFID Reader6.1Background1156.2Finite State Machine and Event Driven Modes1186.2.1 M_0 state: Tag backscatter communication1186.2.2 M_1 state: Tag active transmit1196.2.3Events and driven modes1196.3System Architecture1216.3.1Tag design1216.3.1.1Energy harvester1226.3.1.2Reader code demodulator123		
5.5Measurement Results1115.6Summary114Chapter 6 Effective Transmit Time Reduction of RFID Reader1156.1Background1156.2Finite State Machine and Event Driven Modes1186.2.1 M_0 state: Tag backscatter communication1186.2.2 M_1 state: Tag active transmit1196.2.3Events and driven modes1196.3System Architecture1216.3.1Tag design1216.3.1.1Energy harvester1226.3.1.2Reader code demodulator123	5.4	Θ
5.6Summary114Chapter 6Effective Transmit Time Reduction of RFID Reader1156.1Background1156.2Finite State Machine and Event Driven Modes1186.2.1 M_0 state: Tag backscatter communication1186.2.2 M_1 state: Tag active transmit1196.2.3Events and driven modes1196.3System Architecture1216.3.1Tag design1216.3.1.1Energy harvester1226.3.1.2Reader code demodulator123		
Chapter 6Effective Transmit Time Reduction of RFID Reader115 6.1 Background115 6.2 Finite State Machine and Event Driven Modes118 $6.2.1$ M_0 state: Tag backscatter communication118 $6.2.2$ M_1 state: Tag active transmit119 $6.2.3$ Events and driven modes119 6.3 System Architecture121 $6.3.1$ Tag design121 $6.3.1.1$ Energy harvester122 $6.3.1.2$ Reader code demodulator123		
6.1 Background1156.2 Finite State Machine and Event Driven Modes118 $6.2.1 M_0$ state: Tag backscatter communication118 $6.2.2 M_1$ state: Tag active transmit119 $6.2.3$ Events and driven modes119 6.3 System Architecture121 $6.3.1$ Tag design121 $6.3.1.1$ Energy harvester122 $6.3.1.2$ Reader code demodulator123	5.0	Summary
6.1 Background1156.2 Finite State Machine and Event Driven Modes118 $6.2.1 M_0$ state: Tag backscatter communication118 $6.2.2 M_1$ state: Tag active transmit119 $6.2.3$ Events and driven modes119 6.3 System Architecture121 $6.3.1$ Tag design121 $6.3.1.1$ Energy harvester122 $6.3.1.2$ Reader code demodulator123	Chapte	er 6 Effective Transmit Time Reduction of RFID Reader 11:
6.2 Finite State Machine and Event Driven Modes118 $6.2.1 M_0$ state: Tag backscatter communication118 $6.2.2 M_1$ state: Tag active transmit119 $6.2.3$ Events and driven modes119 6.3 System Architecture121 $6.3.1$ Tag design121 $6.3.1.1$ Energy harvester122 $6.3.1.2$ Reader code demodulator123	-	
$6.2.1 M_0 \text{ state: Tag backscatter communication} \qquad \qquad 118$ $6.2.2 M_1 \text{ state: Tag active transmit} \qquad \qquad 119$ $6.2.3 \text{Events and driven modes} \qquad \qquad 119$ $6.3 \text{System Architecture} \qquad \qquad 121$ $6.3.1 \text{Tag design} \qquad \qquad 121$ $6.3.1.1 \text{Energy harvester} \qquad \qquad 122$ $6.3.1.2 \text{Reader code demodulator} \qquad \qquad 123$		
$6.2.2$ M_1 state: Tag active transmit 119 $6.2.3$ Events and driven modes 119 6.3 System Architecture 121 $6.3.1$ Tag design 121 $6.3.1.1$ Energy harvester 122 $6.3.1.2$ Reader code demodulator 123	0.2	
6.2.3 Events and driven modes 119 6.3 System Architecture 121 6.3.1 Tag design 121 6.3.1.1 Energy harvester 122 6.3.1.2 Reader code demodulator 123		· · · · · · · · · · · · · · · · · · ·
6.3 System Architecture 121 6.3.1 Tag design 121 6.3.1.1 Energy harvester 122 6.3.1.2 Reader code demodulator 123		1 0
6.3.1 Tag design	63	
6.3.1.1 Energy harvester 122 6.3.1.2 Reader code demodulator 123	0.5	v
6.3.1.2 Reader code demodulator		
		0,

		6.3.1.4	Charge contr	rol module					 				 124
		6.3.1.5	Micro contro	oller					 				 126
		6.3.1.6	Antenna and	d front end					 				 126
	6.3.2	Reader d	lesign										
6.4	Charg	ging and D	ischarging O _l	peration .					 				 129
	6.4.1	Charging	g time						 				 129
		6.4.1.1	Controlled c	urrent chai	rging				 				 129
		6.4.1.2	Bi-directiona	al charging					 				 131
	6.4.2	Discharg	ing time						 				 133
6.5	Meası	rement R	esults						 				 134
6.6	Summ	nary				•			 			•	 137
													139
${ m Chapt}\epsilon$	$\mathbf{er} \; 7$	Conclusi	on \dots						 			•	
Chapt∈ 7.1			on										
-		e Work							 				 140
-	Future	e Work Miniatur	ization						 				 140 140
-	Future	e Work Miniatur 7.1.1.1		small anter	 nna .		•		 		· ·		 140 140 141
-	Future 7.1.1	e Work Miniatur 7.1.1.1 Security	ization Electrically s	small anter	··· ··· nna ·	•	•		 	 			 140 140 141 142
7.1	Future 7.1.1 7.1.2 7.1.3	e Work Miniatur 7.1.1.1 Security Packagin	ization Electrically s	small anter	 		•		 	 			 140 140 141 142 143
7.1 APPE I	Future 7.1.1 7.1.2 7.1.3 NDIC:	e Work Miniatur 7.1.1.1 Security Packagin	ization Electrically s	small anter	 nna . 				 	 			 140 140 141 142 143 144
7.1 Appe i App	Future 7.1.1 7.1.2 7.1.3 NDICE PENDICE	e Work Miniatur 7.1.1.1 Security Packagin ES X A Modu	ization Electrically s	small anter		RF		 Tag	 	 			 140 140 141 142 143 144 145

LIST OF TABLES

Table 1.1:	Advancement of RFID technology through decades	2
Table 3.1:	The dimension of different antenna designs	43
Table 3.2:	Comparison with other work reported in literature	58
Table 4.1:	Performance comparison with other works	99
Table 5.1:	Comparison with relevant literature	113
Table 6.1:	Current consumption branches	134

LIST OF FIGURES

Figure 1.1:	Widely used RFID for toll system (a) an EZ-Pass tag, (b) inside of an EZ-Pass, and (c) the inside circuit of an EZ-Pass	3
Figure 1.2:	Low cost example UHF RFID tags for supply chain applications	5
Figure 1.3:	Contactless credit card with NFC reader	6
Figure 1.4:	A commercial moisture sensor with interdigited capacitance for sensing	8
Figure 1.5:	A typical RFID system with reader and tag	8
Figure 1.6:	RFID tag antenna and IC at the center	9
Figure 1.7:	Block diagram of RFID internal circuit	9
Figure 1.8:	Two cylindrical dipole antennas with different dimensions	12
Figure 1.9:	Normalized scattered impedance change at the reader antenna for different cases according to Equation (A.23). Normalization was performed with respect to case I	13
Figure 1.10:	Normalized percentage change in impedance at the reader antenna for the same six different cases as shown in Fig. 1.9. Normalization was performed with respect to case I	14
Figure 2.1:	Different sources of clutter (a) self-jamming [1], (b) multi-reader jamming [1], (c) reflection from human body in a BAN sensor [2]	17
Figure 2.2:	Single frequency RFID tag and background reflector	19
Figure 2.3:	(a) Tag modulated signal, (b) Received tag signal at the reader in absence of any reflector and (c) Received tag signal at the reader in presence of a reflector	20

Figure 2.4:	Front-end of a standard single frequency RFID reader	23
Figure 2.5:	Phase noise after FFT analysis for cases when the reader antenna is (a) 25 cm, (b) 40 cm away from the clutter source, and (c) 40 cm away from an absorber	23
Figure 2.6:	Wireless and batteryless sensing system: (a) a pH sensor with sensor output embedded in phase information [3]; (b) a food volatile sensor with sensor output embedded in the resonance frequency shift [4]	24
Figure 2.7:	Example of sensor integrated with conventional RFID IC: (a) the sensing element is integrated on top of the antenna [5]; (b) the sensor tag antenna and in the inset sensing element integrated in between antenna and RFID IC [6]	25
Figure 2.8:	Schematic block diagram of the RFID tag during energy harvest	27
Figure 2.9:	Analysis on energy harvest at the tag vs. distance with varying consumption.	28
Figure 2.10:	(a) RF radiation on human body, and (b) Desired effective RF radiation time reduction from the reader	30
Figure 3.1:	(a) Harmonic phase based localization in presence of a scatterer [7] (b) Harmonic phase based sensing with better immunity to background clutter [3]	32
Figure 3.2:	Fundamental and harmonic antenna setup in between the tag and reader.	34
Figure 3.3:	(a) Example of NLTL: (a) Discrete diode with CPW line [8] (b) Discrete inductors and diodes shown at the top [9]	35
Figure 3.4:	Lumped element representation of the NLTL with a single cell NLTL at the bottom	37
Figure 3.5:	(a) S_{11} and (b) S_{21} for different number of NLTL stages	40
Figure 3.6:	(a) S_{11} and (b) S_{21} for three number of NLTL stages at different DC bias.	41

Figure 3.7:	(a) S_{11} and (b) S_{21} for four number of NLTL stages at different DC bias.	41
Figure 3.8:	Antenna structures for (a) Meandered dipole (434 MHz) for tag side, (b) Meandered dipole (868 MHz) for tag and interrogator sides and (c) Yagi-Uda (434 MHz) for interrogator side	43
Figure 3.9:	Effect of T-match on input impedance shown on Smith chart from 100 MHz to 600 MHz	44
Figure 3.10:	Radiation pattern of the Yagi-Uda with and without the back reflector	44
Figure 3.11:	Simulation and measurement results for (a) 434 MHz meandered dipole, (b) 434 MHz Yagi-Uda and, (c) 868 MHz meandered dipole antenna	45
Figure 3.12:	Harmonic tag architecture with different components	47
Figure 3.13:	A three stage nonlinear transmission line (NLTL) with matched termination at 434 MHz	48
Figure 3.14:	Measured second harmonic output power of a three stage NLTL as function of DC bias for input power of -10 dBm at 434 MHz	49
Figure 3.15:	Measured reflection coefficient of the matched termination with and without $2f_0$ antenna	50
Figure 3.16:	4-stage charge pump circuit with matching network and DC voltage regulator	51
Figure 3.17:	The unregulated and regulated DC voltage generated by the EHU	52
Figure 3.18:	Input impedance of the EHU with marker at 434 MHz	52
Figure 3.19:	The different stages of signal generated by the DMU. Description from top to bottom: 1) Serial output of the shift register, which is the ID, 2) LD signal, and 3) Clock signal	54
Figure 3.20:	The D flip-flop setup to generate the LD signal from the Clock signal	54

Figure 3.21:	DC power consumption and harvest by HD, DMU, and EHU independently.	55
Figure 3.22:	Total power consumption and harvest for equal and unequal power splitting.	56
Figure 3.23:	Power splitter design with unequal power division	56
Figure 3.24:	The tag circuit photograph with different components as compared to a penny	57
Figure 3.25:	Integrated interrogator system	59
Figure 3.26:	Demodulated received signal (a) after digitization, (b) after averaging, and (c) after pulse shaping and bit recovery	60
Figure 3.27:	(a) The block diagram and (b) fabricated part of the single antenna harmonic tag	62
Figure 3.28:	Dual frequency designed antenna. All the dimensions are in mm	63
Figure 3.29:	The reflection co-efficient of the dual frequency antenna	63
Figure 3.30:	The step by step procedure for dual frequency single antenna design	64
Figure 3.31:	Measured results for (a) S_{11} and (b) S_{21} for different number of NLTL stages at no bias condition; (c) S_{11} and (d) S_{21} for two stage NLTL at different bias	66
Figure 3.32:	Measured results for (a) conversion loss and (b) DC power consumption for different number of NLTL stages	67
Figure 3.33:	Measured reflection co-efficient of the energy harvester with and without NLTL	68
Figure 3.34:	Measured harmonic voltage at different distance and modulation frequency.	69
Figure 3.35:	Efficiency calculation block diagram of harmonic RFID for (a) harmonic efficiency and (b) energy harvester of charge pump	70

Figure 3.36:	Measurement setup for performance comparison	72
Figure 3.37:	Measurement setup with commercial RFID tag at the center	72
Figure 3.38:	Correlation in between transmitted power and tag detection count	72
Figure 3.39:	Power profile for 10 dBm transmitted power at 926 MHz with (a) no tag or reflector, (b) only tag is present, and (c) tag in presence of reflector	73
Figure 4.1:	High level picture of analog sensor integration with ADC and microconroller.	78
Figure 4.2:	Interaction of a handheld reader with identical pH sensors with different IDs	80
Figure 4.3:	The block diagram of the measurement setup with an interrogator and the RFID sensor	82
Figure 4.4:	The sensor voltage readout digital circuit with ID generation	83
Figure 4.5:	Fabrication procedure of pH combination electrodes a) Cu plated RT/duroid 5880 substrate; b) patterning of Cu layer to create 'T' shaped Cu backbone interconnect; c) sputtering followed by lift-off of Sb metal; d) oxidation of Sb layer; e) sputtering followed by lift-off of Ag metal; f) chlorination of Ag layer	85
Figure 4.6:	Voltage response of the fabricated electrode in different pH solutions	86
Figure 4.7:	Stability of the voltage response of the electrode in different pH solutions.	87
Figure 4.8:	Repeatability test of the electrode in different pH solutions	87
Figure 4.9:	Locations for EDX elemental characterization: (a) reference electrode with highlighted black box for Ag/AgCl layer and red box for Nafion layer, (b) pH sensitive electrode with highlighted black box for Sb/Sb_2O_3 layer	89
Figure 4 10.	Elemental characterization for Ag/AgCl laver.	90

Figure 4.11:	Elemental characterization for Nafion layer	90
Figure 4.12:	Elemental characterization for $\mathrm{Sb/Sb_2O_3}$ layer	90
Figure 4.13:	Voltage response of the three different fabricated electrode in different pH solutions	92
Figure 4.14:	From top to bottom: a) The ID bit '101101001' b) 8 bits ADC output '10010000' of analog bias 1 V, and c) combined ID and ADC output bits. The 'idle time' in between the bit streams is also highlighted	93
Figure 4.15:	The complete sensor tag with zoomed in view of the electrode pair in the inset. The scale is shown in inches. In the inset, the left electrode is Nafion coated Ag/AgCl and the right one is Sb/Sb_2O_3 electrode	94
Figure 4.16:	Digital bit response of the tag at different pH solutions in wireless setup. From top to bottom: a) bit response of '111010' at pH 4.3, b) bit response of '1001100' at pH 7, and c) bit response of '1010110' at pH 8.6	95
Figure 4.17:	Antenna dimensions for (a) inside human mouth, and (b) in air medium.	96
Figure 4.18:	Simulated reflection co-efficient for in-air and in-mouth antenna designs.	97
Figure 4.19:	The sensor tag integrated on mouthguard (a) bare mouthguard, (b) digital part of the transponder at the right side and (c) RF circuit of the transponder at the left side of the mouthguard	98
Figure 4.20:	Detected signal in Oscilloscope in buffer pH solution of 5.3	98
Figure 4.21:	Detected signal in Oscilloscope in buffer pH solution of 9.5	98
Figure 5.1:	(a) The block diagram of a wireless batteryless system with a multi-stage modified Dickson charge pump; (b) Measurement setup with a fabricated 5-stage charge pump	103
Figure 5.2:	(a) A single stage CP, and it's equivalent circuit for (b) negative half cycle, and (c) positive half cycle	103

Figure 5.3:	Effect of pump capacitor C_P on steady state voltage	105
Figure 5.4:	(a) A Schottky diode model with pad parasitics. (b) 'L-match' as two- element matching network for <i>n</i> -stage CP	105
Figure 5.5:	A typical matching trajectory (dotted line) of single stage CP. For case (a), the matching network uses series inductor and shunt inductor $(X_1 > 0, X_2 > 0)$. For case (b), the matching network uses series inductor and shunt capacitor $(X_1 > 0, X_2 < 0)$	107
Figure 5.6:	(a) n stage charge pump, and (b) it's simplified impedance model	108
Figure 5.7:	Equivalent transient model for (a) single stage CP, and (b) n stage CP	110
Figure 5.8:	(a) Extracted pump resistance (R_P) of a single stage CP at different input power. (b) Model vs. discrete circuit based single stage CP simulation time comparison	11(
Figure 5.9:	Measurement results of reflection co-efficient (S_{11}) (a) single stage CP at different input power, and (b) multiple stages CP at -10 dBm input power.	112
Figure 5.10:	Voltage normalized transient response of CPs with different stages with $C_{load} = 100$ nF and no external R_{load}	112
Figure 5.11:	(a) Voltage normalized transient response of a 2-stage CP at different load conditions. (b) Measured efficiency of CPs with different stages. (c) Scaling factor of T_{rn} and V_{ssn} compared to a single stage CP	113
Figure 6.1:	Dual mode RFID tags for patients' sleep monitoring system	116
Figure 6.2:	Different modes of communication in between the reader and tag	117
Figure 6.3:	Different sub-modules of the tag circuit	121
Figure 6.4:	Energy harvester with 3-stage Dickson charge pump configuration	122
Figure 6.5:	Reader code demodulator to decode reader instruction at the tag	123

Figure 6.6:	Oscillator circuit to generate 900 MHz RF carrier	124
Figure 6.7:	Charge control module with (a) switches and a 2.2 mF storage capacitor, and (b) voltage comparator	125
Figure 6.8:	(a) Input and output ports connections of micro controller, and (b) sensor circuit configuration	126
Figure 6.9:	Antenna dimensions with front and side views	127
Figure 6.10:	Simulated and measured PIFA antenna reflection co-efficient comparison.	127
Figure 6.11:	The reader to interrogate the tags in two modes	128
Figure 6.12:	Charging of the capacitor using controlled current	129
Figure 6.13:	V_{MC} and V_{cap} voltage level for 3 cases: input power is -1 dBm and $\alpha=1$, input power is -3 dBm and $\alpha=1$, input power is -3 dBm and $\alpha=0.86$ for initial 9.2 s and later $\alpha=1$	132
Figure 6.14:	(a) Dual mode RFID tag circuit with SMA, and (b) front and back side of the PIFA antenna with SMA outlet, compatible to be embedded within seat	135
Figure 6.15:	Storage capacitor and micro-controller voltage level at different switching signals	136
Figure 6.16:	Activation of a dual mode tag due to specific code sent from the reader.	136
Figure 6.17:	The information received at the reader sent by a dual mode RFID tag. $$.	137
Figure A.1:	Two cylindrical dipole antennas with different dimensions	146
Figure A.2:	Four-terminal impedance network for two antenna system	146
Figure A.3:	A single center-fed dipole antenna	147

Chapter 1

Introduction

Radio Frequency Identification (RFID) has become an integral part of numerous applications such as road toll collection service, access control, tracking assets in supply chain, credit cards, batteryless sensors to name a few [10–12]. RFID system works on a wide range of RF spectrum starting from 100 kHz to few GHz. Among available RFID bands, the most popular bands are 125 kHz at low frequency (LF), 13.5 MHz at high frequency (HF), 433 MHz, 868 MHz, 915 MHz at ultra-high frequency (UHF), and lastly 2.4 GHz at super high frequency (SHF). RFIDs operating at 125 kHz, 13.5 MHz, 868 MHz, 915 MHz are generally batteryless or passive in nature. Whereas, RFIDs operating at 433 MHz and 2.4 GHz are usually battery powered or active in nature. Passive tags have limited range of operation as they can be only powered by the reader, hence distance from the reader will greatly impact the operation range. On the other hand, active tags can have long range more than 100 m as the available power at the tag is not a major issue. The UHF RFIDs working in 868 MHz or 915 MHz band has become the most commercially popular due to long range operation in passive mode, miniaturized antenna with acceptable radiation efficiency, available band with high power transmission capability, structured and defined regulatory protocols, low cost manufacturing capability, and finally longer period of research and development. The most recent UHF RFID protocol is EPC Gen 2, which primarily outlines the frequency of operation, effective transmit power limit, two-way modulation specification, data encoding

Table 1.1: Advancement of RFID technology through decades.

Decade	Event
1940-1950	Radar refined and used, a major World War II development effort.
	Concept of RFID proposed in 1945~48.
1950-1960	Development of RFID technology, primarily in laboratory.
1960-1970	Development of RFID theory with field trials.
1970-1980	Large companies such as Raytheon, RCA started development of
	RFID technology.
1980-1990	Early implementation of RFID started.
1990-2000	RFID started being widely deployed. E-Z pass was formed.
2000-2010	Introduction of EPC Gen 2 protocol, a unified protocol for RFIDs.
	Started being implemented for supply chain, animal tracking.
2010-	RFID industry worth around \$8.5 billion in 2016.

scheme, timing and memory requirement, instruction set architectures (ISAs), anti-collision protocols among many others [13]. The development history of RFID technology, as summarized in Table 1.1, is quite fascinating and can be traced back around World War II era [14].

An important development of RFID tag with practical demonstration was reported from Los Alamos Scientific Laboratory [15]. A subcarrier was introduced at the tag side to perform the backscatter modulation of the tag antenna. The subcarrier was introduced to remove the clutter, which are caused from background reflection. Other notable development of RFID tags from early days are Raytheon's Raytag, Richard Klensch's electronic identification system from RCA. Apart from the system level design, there was also requirement of CMOS fabrication technology miniaturization for small circuitry, development of EM theory for efficient backscatter modulation, development of required software for adoption in large scale business, development of printing techniques for manufacturing the RFID tags at very low cost. All of the factors played a major role in creating a multi-billion dollar RFID industry. Today's RFID industry has become successful in numerous supply chain, electronic

toll system, financial banking, e-passport, library book tracking, building access, inventory management as well as anti-counterfeiting for different parts in car industry. Each of the major applications are discussed very briefly in the following section.

1.1 Applications

1.1.1 Electronic toll system

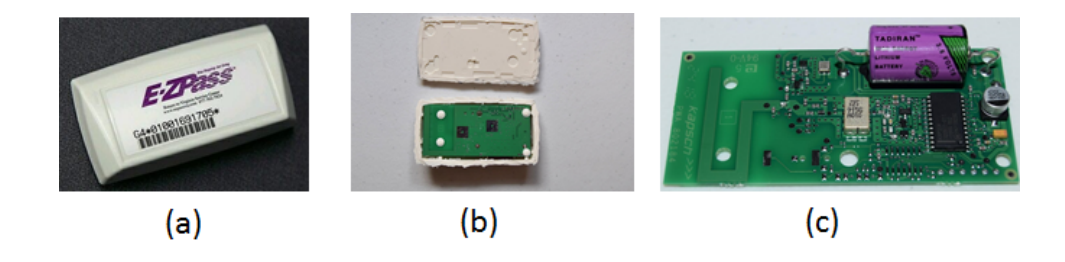


Figure 1.1: Widely used RFID for toll system (a) an EZ-Pass tag, (b) inside of an EZ-Pass, and (c) the inside circuit of an EZ-Pass.

RFID technology has shaped public transportation largely by making the transportation system seamless. Among all RFID applications, electronic toll system was the first application to be commercially implemented. As an RFID tag embedded car reaches at a toll booth, the overhead RFID reader scans the specific unique information from the tag. In the US, electronic toll collection as efficient and effective method that eliminates long lines of traffic. EZ-Pass is widely used in US and the inside circuit is shown in Fig. 1.1 (c). The RFID tag works at 900 MHz but requires an external power supply for example an on-board battery. Hence, the RFID tag in EZ-Pass is an active type.

1.1.2 Supply chain application

The major problem in supply chain management today is to locate a weak node in the chain for proper functioning of the complete network. The problems can be leaving a package or product behind during loading, misplaced during transportation, or proper storage in warehouse. There can be multiple reasons for those problems, primarily of them is related to human error due to manual interaction. Although major advancements in technology have happened over the past decade, still partially manual driven supply chain is a part of any modern supply chain.

Using RFID technology, an end to end monitoring and accounting is possible. The added benefits of using RFID in supply chain are increased product visibility and transparency with added location accuracy. Hence, RFID technology is proposed for multiple supply chain sectors such as healthcare, food industry, agriculture etc. [16–18]. Among those supply chain sectors, in food industry RFID was proposed earlier due to its low cost and small size to ensure food safety by increasing the traceability of the food products in the food supply chain [17, 19]. The importance of RFID-based temperature sensor tags for cold food supply chain has been described in [19]. The sensor enabled tags can record the temperature of individual food packages and track the real time shelf life in case of any deviations in environmental conditions during storage or transportation. According to [19], if food products with reduced shelf lives arrive unexpectedly at a retailer, priority should be given to sell those items to reduce the amount of food wastage. In [17], a detailed review has been performed to discuss the potential of RFID technology in logistic development of different sectors for the food supply chain. However, the visibility of the food products is limited by the amount of information shared by each supply chain stage to its next stage. Implementing RFID technology along with cloud based services would provide a digital trace of the food products during their lifetime and thus making the food supply chain visible to everyone.

Auto-ID Labs network was initiated in 1999 in the field of networked RFID and emerging integrated sensing technologies. Auto-ID was responsible to design the architecture for the Internet of Things (IoT) and Electronic Product Code (EPCglobal) for identification of the items in the supply chain [20, 21]. The primary objective was to develop hardware, software, protocol, communication interface, specification, and business research related to RFID [22, 23]. The business case was very important for the supply chain to succeed as a huge cost scaling down was necessary, which was demonstrated in [23] making a tag cost around 5 cents.



Figure 1.2: Low cost example UHF RFID tags for supply chain applications.

In recent days, RFID has huge application in modern days supply chain industry. To compete with existing barcode or QR code based optical system for object identification, RFID tag price required to be significantly cheaper. By late 2000, with screen printing and availability of low cost miniaturized RFID IC, bulk manufacturing of cheap RFID tags was possible. Re-usability, long read range, and electronic surveillance made possible to monitor products in a supply chain seamlessly. Embedding the RFID tags within products will also help to fight counterfeiting as well as maintain inventory in numerous industries [24,25]. The tags primarily used in supply chain are usually passive and work at UHF band. An example screen printed RFID tag is shown in Fig. 1.2.

1.1.3 Financial banking

Another major application of RFID technology is in financial banking for contactless transaction. Multiple contactless transaction systems such as Google pay, Android pay, wireless credit card has been introduced [26, 27]. The technology although based on RFID, is a little variant due to requirement of enhanced security [28]. More precisely, the technology is Near Field Communication (NFC) which uses a near field antenna and NFC chip. The communication range is limited to very short distance to avoid confusion in transactions and protect the cards from stealing sensitive information from long distance. The NFC chip along with antenna is embedded within the wireless credit cards, and the smartphones during manufacturing of the devices. Since, a separate and completely independent chip is embedded, the communication is independent of SIM card or other wireless connection of the smartphone. In Fig. 1.3, a NFC credit card with a NFC reader is shown. There can be few security issues with the NFC based communication [28]. The primary security issues are 1) eavesdropping, 2) data corruption and modification, 3) data insertion, 4) middle-manattack. Multiple schemes have been proposed to counter the attacks such as encryption, token system etc.



Figure 1.3: Contactless credit card with NFC reader.

Usually, the NFC card uses a token system to restrict the use of sensitive data. In the

token system, the NFC card sends a token to the NFC reader and the NFC reader sends the token to Token Service Provider (TSP). The TSP maps the token to find where the card information is stored and the stored information is fetched from Card Data Vault (CDV). Once the card transaction is verified, a confirmation is sent back to the NFC reader, which confirms the transaction. For the contactless cards, no additional pin or identification is used from the user side, which makes the transaction fast compared to other traditional magnetic strip or chip based cards.

1.1.4 Sensing with identification

Recently, another interesting topic of research has been the integration of sensors along with identification. As the RFID ICs already have harvested energy, the power can be used for additional sensing operation. In literature, multiple cases of sensor integrated RFID is demonstrated [29–31]. The conventional RFID architecture primarily relied on system concepts which exclusively serve one-way and low data rate traffic, and was designed for sending short message consisting only ID and was never intended for streaming sensor data. Proposed RFID sensor network design required extra functionality and processing power at the tag. Also, as the harvested power is limited at the passive tags, the read range would be limited for higher data-rate sensor data transmission.

The architecture of the sensor integrated RFID is more or less similar with the following components: 1) the RF front end including the antenna and the circuity for rectification and voltage regulation, and 3) a (low power) digital back end. when a carrier is sent from the reader, the induced RF voltage at the tag antenna is rectified and regulated for a fixed DC voltage. Usually all the functionality are performed using a single IC in commercial RFID chip. However, for sensor coupled RFID, there are not any additional pins for the

sensor integration. Hence, in literature the proposed RFID based sensors are based on microcontroller and discrete circuit components.



Figure 1.4: A commercial moisture sensor with interdigited capacitance for sensing.

Recently, few commercial RFID based sensor tags are active in market for different sensing applications such as temperature, moisture, positioning etc. [32]. However, majority of the sensor tags are non-customizable, which means the sensor based RFIDs will work only for a specific application. An example moisture sensor is shown in Fig. 1.4 with interdigited capacitance for sensing at the center. A RFID platform (SLA) for different type of sensors is commercially available. However, the SLA architecture consumes lot of power, which limits the read range of the sensor in passive mode of operation.

1.2 RFID System and Components



Figure 1.5: A typical RFID system with reader and tag.

A RFID system primarily consists of a reader and multiple tags, where the reader obtains information from the tags wirelessly. A typical RFID system with a reader and a tag is shown in Fig. 1.5. In RFID communication, the reader provides the RF carrier signal,

which is backscatter modulated by a tag according to a specific bit stream. The bit stream is called digital address or ID of the RFID tag and the address is saved in a non-volatile memory inside RFID tag. The digital address is either programmed as factory set condition or reprogrammable during later operation. This address is non-programmable in a read-only tag and rewritable in a read-write tag. Like any other wireless communication, the backscatter modulation technique requires an antenna for transmission and reception of RF energy. Hence, A RFID tag contains two building block components: an antenna and an IC for providing the digital address as shown in Fig. 1.7.



Figure 1.6: RFID tag antenna and IC at the center.

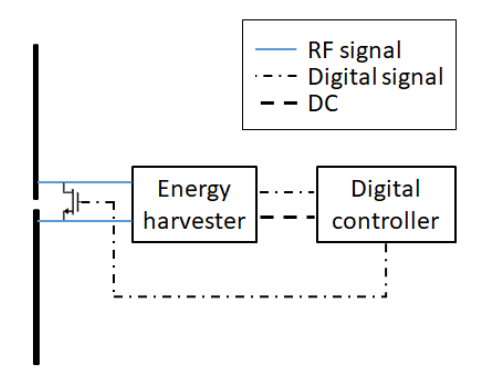


Figure 1.7: Block diagram of RFID internal circuit.

A generic basic block diagram of the internal circuitry of a RFID chip is given in Fig. 1.7. As mentioned earlier, the RFID tag contains an antenna and an IC. Within the IC, there are primarily two major components: 1) energy harvester, and b) digital microcontroller. Once a RFID tag is illuminated with RF power, the energy harvester converts the RF power into DC, which drives the digital microcontroller. The efficiency of the energy harvester is very

important as it will primarily dictate the read range of the tag from the reader. When the DC power is available, the detector circuitry is activated within the microcontroller. The detector circuitry detects the specific code sequence, sent by the RFID reader. Based on the code, the microcontroller decides what task to perform. A programmable tag can perform multiple actions based on the reader query: 1) write specific digital address or ID at the tag, 2) send the ID data to the reader, 3) perform a specific action such as writing at specific registers, etc. The digital controller contains non-volatile EEPROM register, where the ID is stored. Some advanced microcontroller includes a password protection scheme to access the registers and hence to change the ID address. The microcontroller can be more complicated based on the intended applications. Among other important analog sub-circuit parts, two noteworthy components are a) voltage regulator, and b) random number generator. The voltage regulator maintains the rectified DC voltage at a defined level to protect from over voltage. When multiple tags are present in the environment, tag collision happens if more than one tag reply simultaneously. To avoid this scenario, the microcontroller activates the random number generator to decide when to transmit back to reader. The tag performs backscatter modulation by switching on and off the high frequency switch, which is connected parallel to the antenna as shown in Fig. 1.7. The mathematical formulation and physical interpretation of backscatter modulation is provided in next section.

1.3 Backscatter Modulation

The conventional single frequency RFID operates on back-scattering principle. The early development of back-scattering principle started around in early 1950's after Yagi-Uda antenna was reported. In back-scattering, impedance change in one antenna can be measured

by another antenna coupled to it. A few notable works on coupling of multiple antennas were reported in [33–35]. In those works, as a general approach, a simultaneous integral equation using Hallen's method and variational expression is formulated. Then the expressions are further simplified and solved for different purposes for example a) determining broadside back-scattering cross section for a center loaded cylindrical dipole with arbitrary load impedance [33], b) analyzing impedance parameters of coupled antennas [34], and c) a generalized scattering formulation applicable for back-scattering and bi-static scattering with active or passive loads extendable to N loads [35].

In back-scattering, a single antenna is used as transmitter and receiver for measuring the impedance change of the target antenna. And in bi-static scattering two separate antennas are used as transmitter and receiver for impedance change of target antenna. Although back-scattering RFID is predominantly used, bi-static RFID is not very uncommon [36]. Bi-static RFID is usually helpful for localizing a RFID tag in 3D space. If there is only a reader antenna and a tag antenna, then the formulation is a two port network. However, the network changes to N port based on number of reader antennas or tags present. To keep the formulation simple, single reader and tag antenna is considered with the medium in between them reciprocal. Also, only passive load is considered for the RFID tag loading.

The detailed mathematical formulation of backscatter modulation working principle is provided in Appendix A with two antenna system as shown in Fig. 1.8. The objective of the analysis was to find the analytical expression of modulation depth due to two different load impedance at the RFID tag antenna during modulation. Maximum modulation depth is always desired as that would ensure the detectable signal level over the inherent noise level. Now, with the help of modulation depth expression (1.1), it would be easy to find the realistic load impedance combination during modulation that would provide maximum modulation

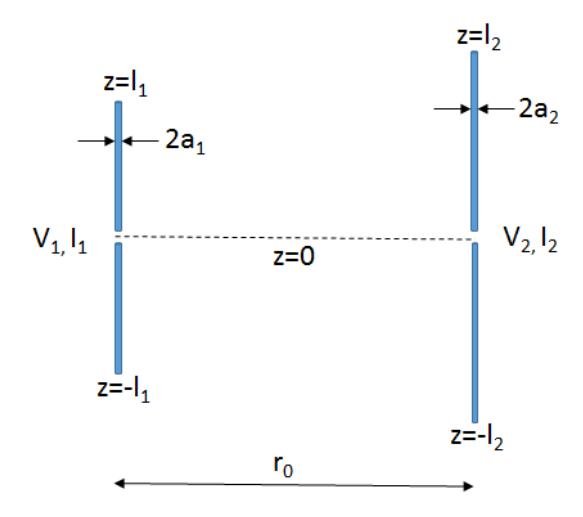


Figure 1.8: Two cylindrical dipole antennas with different dimensions.

depth. In the analysis, the tag antenna was considered a dipole antenna with infinitesimally small width and the reader antenna was considered infinitesimally small dipole for simplified expression.

$$V_r^s(2) - V_r^s(1) = Z_{12}^2 \left[\frac{1}{Z_{22} + Z_{L2}} - \frac{1}{Z_{22} + Z_{L1}} \right] I_1(0)$$
 (1.1)

1.3.1 Coupled antenna impedance

Computation and simulation are performed to verify the antenna coupling effect with different load impedance at one of the coupling antennas. Using small reader antenna approximation described above, computation is performed for different combination of load impedance for maximum modulation depth. For computation, six different combinations are considered. The combination pairs for load impedance considered are [0, 73], [0, 30], [30, 73], [30, 200], [73, 200], and [0, 200]. Each of the cases are termed as case I, II, III, IV, V, and VI and the modulation depth is computed for those six cases according to Equation (A.23). The simulation was performed in Ansys HFSS. In the simulation, the percentage

change in impedance at the reader antenna was measured for load impedance change at the tag antenna for the previously mentioned six test cases. In the simulation, both the reader and tag antennas were considered as quarter-wavelength antennas. For both computation and simulation, l/a is considered as 560 to make sufficiently thin-wire approximation while maintaining smooth meshing during simulation. The operating frequency considered is 900 MHz, and the separation distance between two antennas is 1.2λ . For computation, the small reader antenna length is considered as dl/l = .025.

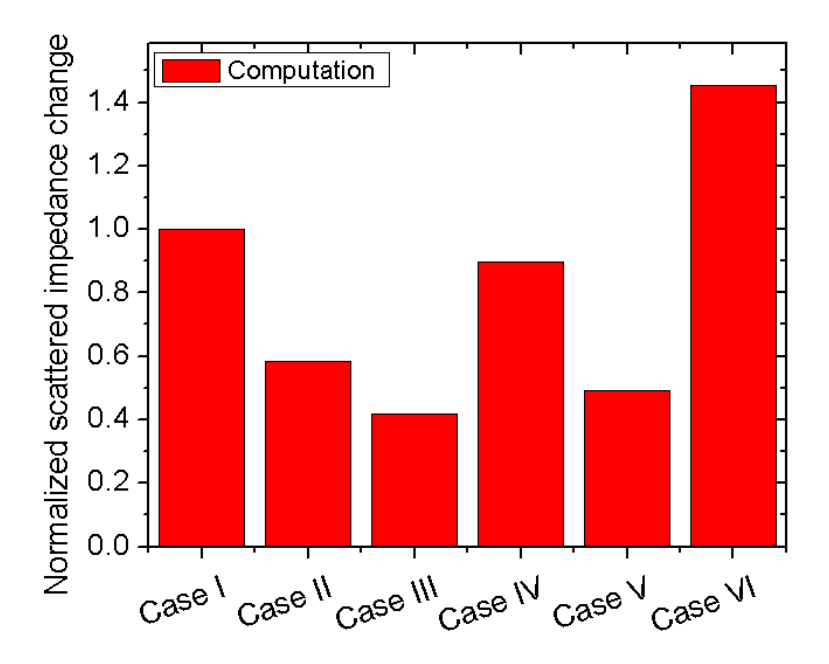


Figure 1.9: Normalized scattered impedance change at the reader antenna for different cases according to Equation (A.23). Normalization was performed with respect to case I.

In Fig. 1.9, the normalized scattered impedance is plotted due to two different load conditions. In Fig. 1.10, the percentage change of reader antenna input impedance for different cases of load impedance pair across the tag antenna is tabulated. From Fig.s 1.9 and 1.10, it is evident that the simulation result closely follows the pattern of computed result. The best modulation depth is found for the load impedance pair of 0 Ω and 200 Ω . As the load impedance increases further from 200 Ω towards infinity, the modulation

depth becomes more stronger. In the test case analysis, 73 Ω was chosen because of the real impedance of a standard dipole antenna at resonance is 73 Ω . However, as the RFID tag is supposed to do energy harvesting, one of the antenna impedance choice should be the conjugate of energy harvester input impedance, which is standard impedance as 50 Ω . The another impedance choice can be either a short or open circuit. Circuit-wise performing short operation at the antenna input is easier compared to open operation. Hence, the best suited load impedance pair for the coupled antenna based modulation architecture are 0 Ω and 50 Ω . In chapter 4, a standard RFID with sensor is demonstrated with two load impedance pair as 0 Ω and 50 Ω for two different modulation states.

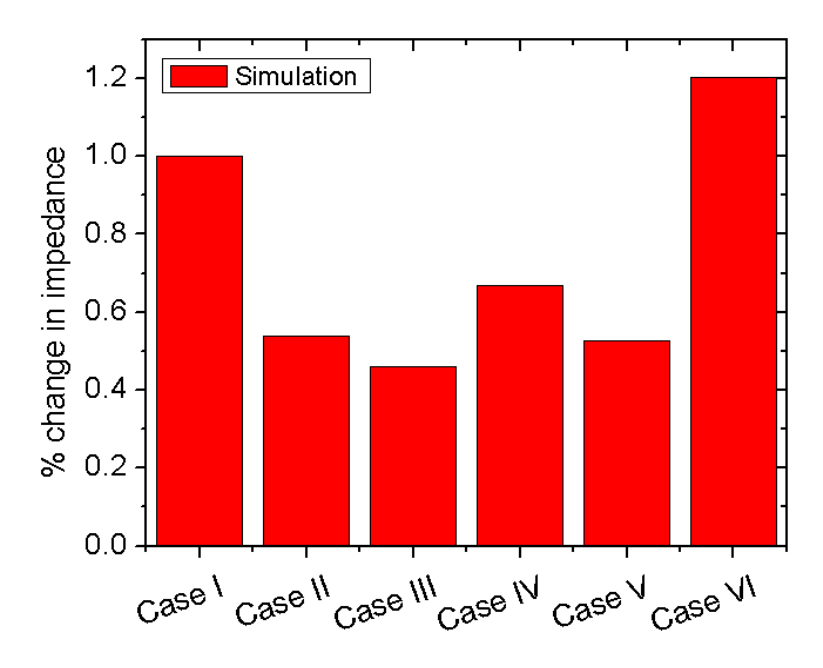


Figure 1.10: Normalized percentage change in impedance at the reader antenna for the same six different cases as shown in Fig. 1.9. Normalization was performed with respect to case I.

1.4 Thesis Organization

The dissertation thesis is organized as followed:

• Chapter 2 presents the four primary challenges in conventional RFID. Solution to each

of the problems is presented from Chapter 3 to Chapter 6.

- Chapter 3 presents the harmonic RFID, capable of mitigating the clutter effects.
- Chapter 4 presents a low power generalized digital RFID platform, which can be used to integrate analog sensors with digital RFID interface.
- Chapter 5 presents component level study on energy harvester for efficiency and response time analysis.
- Chapter 6 presents a dual mode RFID, capable of reducing RF transmission time significantly from RF reader.
- Chapter 7 finally concludes the thesis and proposes the possible future works.

Chapter 2

Challenges with Conventional RFIDs

In the previous chapter, the applications and simple working principle of conventional RFID is demonstrated. Undoubtedly, RFID has become a multi-billion dollar industry today, and applicability of conventional RFIDs in new areas is being researched. One of the primary success reasons for passive RFID is the batteryless and small footprint architecture. This specific feature enabled RFID desirable for applications such as: 1) underground or buried object tagging and sensing, 2) RFID as a sensing platform (RaaSP) for a broad range of sensors, 3) Low power operation for longer range or operating in a lossy medium, 4) Sensing and monitoring in an environment where prolonged RF power transmission is not desired. In spite of having many advantages, conventional RFID in its current form is not capable of working for those applications due to fundamental working principle. The primary challenges outlined are as followed:

- Clutter and multipath effect
- Sensor integration
- Low power operation and response time
- RF transmission from the reader

Each of the challenges are analyzed in detail and the best possible solutions are proposed in the upcoming chapters. This chapter is primarily dedicated towards understanding the physical limitations of conventional RFID. One chapter is dedicated for each of the four challenges to propose a solution or understand the fundamental limits. All those solutions are combined into a single new type of hybrid RFID, which is proposed in the last chapter, mitigating all these four primary challenges.

2.1 Clutter and Multipath Effect

Clutter is described as an unwanted signal, which can obscure the desired signal and hence diminish the system performance. Clutter source in conventional RFID can be several: 1) self-jamming due to mismatch at the antenna port, 2) multi-reader jamming when multiple RFID readers are transmitting simultaneously and one can jam the another, 3) reflection from nearby objects [1,2,37]. The primary clutter objects are usually different in different applications. For example, primary clutter object is biological body for a body area network (BAN) sensor or sensor monitoring body vitals [38]. In underground object tagging, the ground is the primary source of clutter [39,40]. Similarly, in industrial environment, metal objects are source of clutter [41]. The different clutter sources are shown pictorially for multiple scenarios in Fig. 2.1.

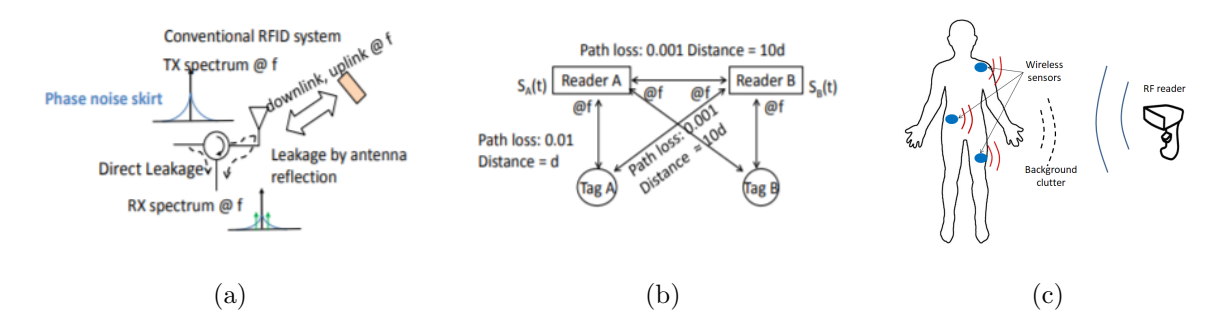


Figure 2.1: Different sources of clutter (a) self-jamming [1], (b) multi-reader jamming [1], (c) reflection from human body in a BAN sensor [2].

In [41], mathematical formulation is provided to show how the clutter phase noise can

shadow the low power tag return modulation signal. Also, experimentally it was demonstrated that the read rate of a conventional RFID reduces in presence of a clutter source. The read rate is directly correlated to signal to clutter ratio (SCR), and hence, read rate can be monitored to quantify the clutter effect. The reflection clutter was measured in [2] using the conventional RFID front end. In the reader front end, the baseband amplifier should be of very low noise in order to measure the system phase noise [42]. If the tag returned signal is of very low power and low frequency, it can get buried under the strong clutter phase noise.

RFID has become widely accepted in enterprise supply chain management system as it improves the efficiency of inventory tracking. In the supply chain, RFID tagged object localization using RF signal is a desired feature. The RF localization is primarily done using received signal strength (RSS), or phase based, or combination of both [43, 44]. However, precise localization in conventional RFID system is a challenge due to a) multipath effect, b) undesired interference, c) presence of multiple tagged objects [45]. In RSS based localization, the signal attenuation level is monitored and the distance is estimated from Friis transmission equation. Multipath effect is stronger in this method due to received signal power level measurement. In phase based measurement, the phase of arrival of the backscattered signal is measured. However, accurate phase based localization is possible when the bandwidth is wider, which is difficult for conventional RFID system with only 30 MHz bandwidth. Interference among multiple readers is possible and can contribute for distance uncertainty. Also, when the RFID tags are densely populated, it becomes difficult to remove localization ambiguity among the tags. The inherent problem lies at the frequency of operation and the ambiguity reduces with increase in the operating frequency of operation.

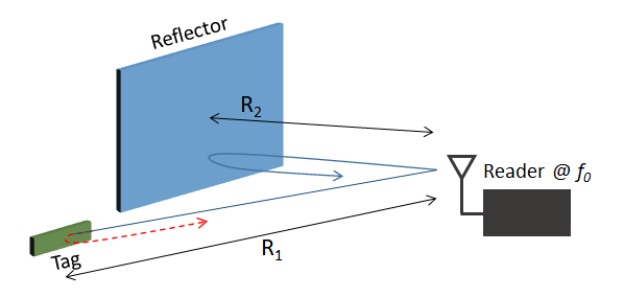


Figure 2.2: Single frequency RFID tag and background reflector.

2.1.1 Clutter formulation

RFID systems operating at single frequency are susceptible to clutter noise or self-jamming in multiple readers setup and an analysis on signal to interference ratio (SIR) was shown in [1] in case of self-jamming when multiple readers would be transmitting together. Additionally, single frequency RFID tags can be disadvantageous while operating in a cluttered environment. In Fig. 2.2, a single frequency RFID tag is shown in presence of a background reflector. If the tag and the reflector are at a distance R_1 and R_2 respectively, the received power at the reader due to tag and the reflector represented as P_{rt} and P_{rr} can be shown as in (2.1) and (2.2) respectively.

$$P_{rt} = \frac{P_t G_t^2 G_r^2 \lambda^4 \Gamma}{(4\pi R_1)^4} \tag{2.1}$$

$$P_{rr} = \frac{P_t G_t^2 \lambda^2 \sigma}{(4\pi)^3 R_2^4} \tag{2.2}$$

In (2.1), P_t and G_t represent the transmitted power and antenna gain of the reader, G_r represents the tag antenna gain and Γ depends on the on-off switching of the tag. When Γ is 1, the tag behaves like an ideal reflector and when Γ is 0, the tag is an ideal absorber. From the presence and absence of reflected power, the ID sequence is decoded at the reader.

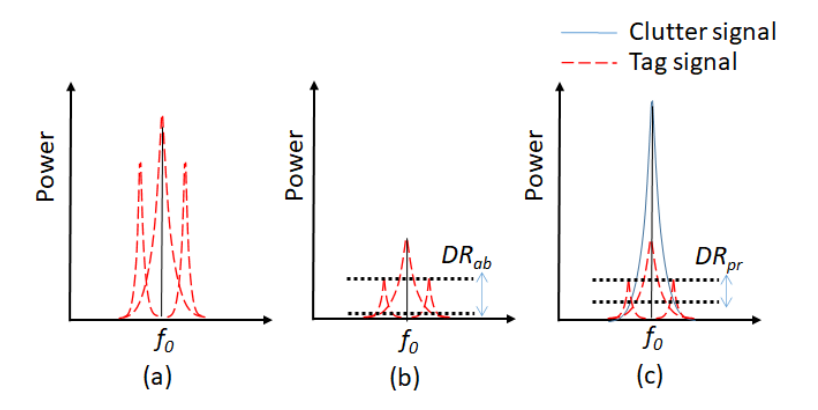


Figure 2.3: (a) Tag modulated signal, (b) Received tag signal at the reader in absence of any reflector and (c) Received tag signal at the reader in presence of a reflector.

In (2.2), σ represents the radar cross section (RCS) of the reflector.

When a RFID tag receives a single frequency signal f_0 , it modulates the signal at $f_0 + \Delta f$ and $f_0 - \Delta f$, which appears as the sideband of f_0 as shown in Fig. 2.3(a). Once the tag modulated signal reaches to the reader, the reader extracts the tag encoded ID at Δf by heterodyne mixing. In absence of any reflector, the dynamic range (DR) of the tag DR_{ab} would be determined by (2.3), where Γ_{fund} represents the conversion efficiency for a practical tag at fundamental frequency and RS represents the reader's sensitivity level at $f_0 + \Delta f$ or $f_0 - \Delta f$. However, the scenario would be different in presence of any reflector within the field of view of reader antenna. As the reader oscillator is not an ideal one, the oscillator would have phase noise (PN) at $f_0 + \Delta f$ or $f_0 - \Delta f$, which would be backscattered by a reflector. As a result, there would be reduction in DR as shown in Fig. 2.3(c) leading to poor tag detection rate when PN dominates over RS. The clutter signal effects more strongly when the received tag signal is close to RS level. The DR in presence of reflector DR_{pr} as given in (2.4) would depend on the distance, dimension and shape of the reflector. In this scenario, even though the RS level is improved, it would not improve the tag read range in presence of strong reflectors.

$$DR_{ab} = \frac{P_t G_t^2 G_r^2 \lambda^4 \Gamma_{fund}}{(4\pi R_1)^4} - RS(f_0 + \Delta f)$$
 (2.3)

$$DR_{pr} = \frac{P_t G_t^2 G_r^2 \lambda^4 \Gamma_{fund}}{(4\pi R_1)^4} - PN(f_0 + \Delta f)$$
where,
$$PN(f_0) = \frac{P_t G_t^2 \lambda^2 \sigma}{(4\pi)^3 R_2^4}$$
(2.4)

2.1.2 Clutter measurement

It is important to quantify the clutter effect after mathematical formulation. A standard single frequency RFID reader system is shown in Fig. 2.4. In general, any oscillator has its standard phase noise around the carrier center frequency. In the presence of a strong clutter object, the background clutter will appear along with the tag modulation signal. In absence of clutter, the noise level will be primarily determined by the reader's minimum sensitivity. In presence of strong clutter signal, the noise level will be primarily determined by the reflected clutter signal, which may dominate under strong reflections.

Based on the conventional RFID reader front-end, a RFID reader was constructed as shown in Fig. 2.4 to measure the effect of clutter. In the reader, first the single frequency signal is amplified and transmitted through a transmitter antenna. Now the back-scattered tag signal or clutter will be received at the same antenna. The return signal is downconverted using the carrier signal to obtain the baseband signal. To ensure the reader noise figure minimization, an ultra-low noise amplifier with input voltage noise density of $2.4 \text{ nV}/\sqrt{\text{Hz}}$ was used to amplify the baseband signal before sampling and performing FFT analysis. In the baseband signal, there are two parts: 1) tag modulation, and 2) return clutter signal. The phase noise of the transmitted signal will dominate under strong cluttered environment. The

experimental setup to demonstrate the clutter effect is shown in Fig. 2.4. In the experiment, a metallic cabinet was used for the clutter source. Three set of measurements were taken at different distance from clutter source to show how clutter can effect the low frequency tag-modulated signal.

At first, the RFID reader was kept at a distance of 25 cm from the clutter object and the downconverted baseband signal is shown in Fig. 2.5(a). Due to specific phase noise characteristics of the oscillator, when transmitted signal from the reader gets reflected from the clutter object and after downconversion the phase noise was captured as shown in Fig. 2.5. When the distance was increased from 25 cm to 40 cm, the pattern of the phase noise remains same with decreased amplitude, as expected, as shown in Fig. 2.5(b). The response without any clutter source was measured using a broadband microwave absorber. In absence of strong reflected signal, the background noise dominates over the phase noise as shown in Fig. 2.5(c). The spikes in all the three graphs consist of even and odd harmonics of 60 Hz noise, which can be eliminated using better DC source. It is clearly visible that in the presence of a clutter object, the phase noise level impacts significantly at lower frequency. Hence, single frequency conventional RFID system can have disadvantage specifically in biological systems under strong clutter for low frequency tag modulation (lower or equivalent to 200 Hz).

2.2 Sensor Integration

RFID technology has become a good choice for sensing and monitoring at remote location, where it is difficult to probe or wired future maintenance access such as battery change is not possible. Many applications are in the field of structural health monitoring (SHM)

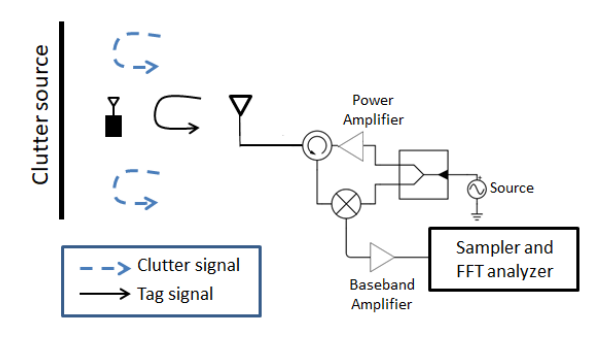


Figure 2.4: Front-end of a standard single frequency RFID reader.

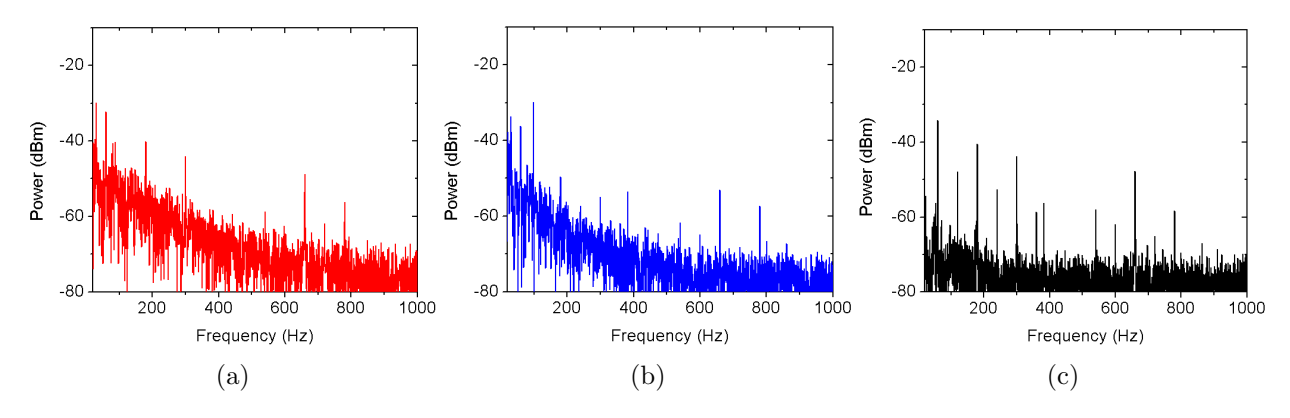


Figure 2.5: Phase noise after FFT analysis for cases when the reader antenna is (a) 25 cm, (b) 40 cm away from the clutter source, and (c) 40 cm away from an absorber.

[46, 47], intra-vehicular sensing network [48], utility such as gas pipeline sensing [40, 49], remote monitoring of hazardous environment [3,50], low-cost sensing for end to end supply chain [4,51–53], non-invasive human vitals sensing for health monitoring [54]. The primary objective of those reported sensors is to integrate them with RFID system and operate them wirelessly and without battery. The earlier reported sensors can work nicely wirelessly and without battery. However, the sensing elements are fundamentally analog in nature. The sensors convert physical parameters to electrically realizable signal such as voltage, current or impedance. As the output voltage, current, and impedance from the sensors are analog in nature, interfacing those sensors with conventional RFID system becomes requires use of digital interface, which is a challenge in nature due to requirement of low power ADCs.

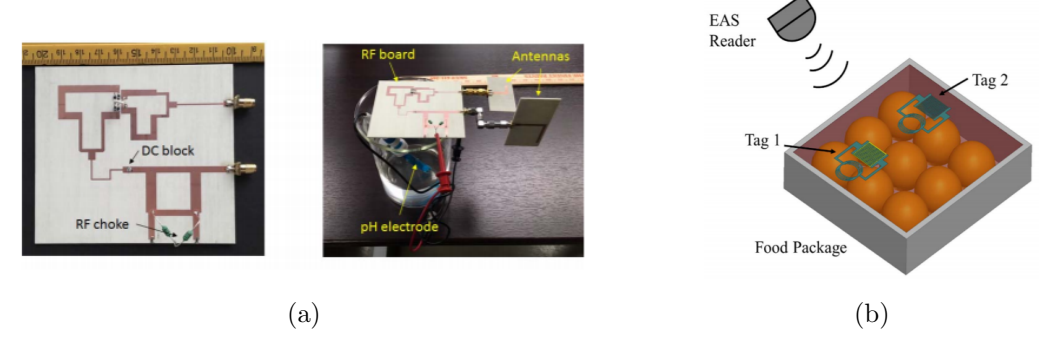


Figure 2.6: Wireless and batteryless sensing system: (a) a pH sensor with sensor output embedded in phase information [3]; (b) a food volatile sensor with sensor output embedded in the resonance frequency shift [4].

In earlier reported wireless and batteryless sensing systems, the analog sensors are usually integrated to directly impact the phase or coupling power level of the interrogating signal. For example, in [3, 50] the sensor output is converted into phase and integrated with the interrogating signal. The sensor signal is extracted at the interrogator from the relative phase change. However, the system needs initial calibration for the phase change due to distance traversed by interrogating signal, which propagates through the medium between sensor tag and interrogator. The scenario becomes specially challenging when the sensor tag is not static and the relative distance of the tag from the interrogator is continuously changing. Among other analog sensing methods, the resonance frequency shift method is also very popular [4,51]. In resonance frequency method, coupling of two coils are used, where one coil is with the sensing element and the other with the interrogator. The sensing element is usually capacitively coupled with the inductive sensor coil, forming a LC tank. The capacitive loading of the sensor is detected from the shift in resonance frequency. Coupled coil based sensing has become very popular as they require minimum components. However, there are two major challenges with this kind of sensing: 1) a comparatively wide frequency sweep is required to ascertain the resonance frequency peak, requiring a wider system bandwidth; and 2) the coupling co-efficient starts reducing drastically when the relative distance between the sensor and interrogator increases, hence the minimum detection limit is a function of relative distance. Also, the relative orientation of the coupled coils greatly affects the coupling co-efficient. Examples for both type of wireless and batteryless sensor system is shown in Fig. 2.6.

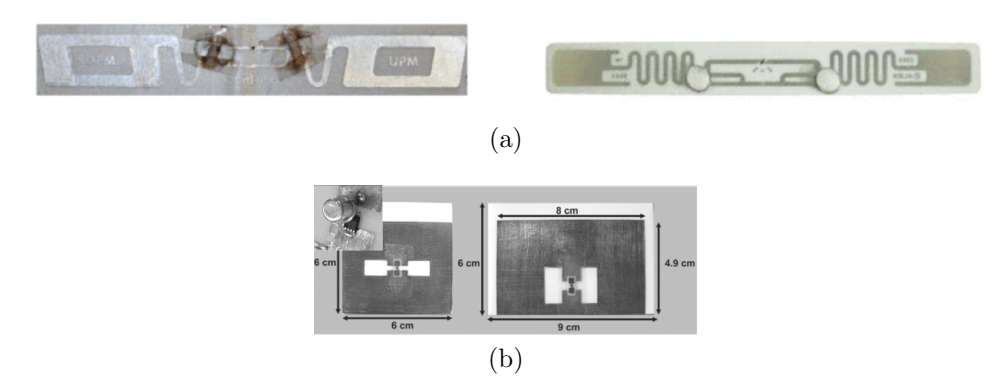


Figure 2.7: Example of sensor integrated with conventional RFID IC: (a) the sensing element is integrated on top of the antenna [5]; (b) the sensor tag antenna and in the inset sensing element integrated in between antenna and RFID IC [6].

In order to integrate the wireless and batteryless sensors with RFID, another alternative approach became popular, where the sensing element is directly embedded on the antenna of conventional RFID tag or in between the antenna and RFID IC [5,6]. In [5], two example sensors are demonstrated, where the sensing element is placed on the antenna and the sensing element changes impedance based on external stimulus. As the antenna impedance changes, the power received at the interrogator changes and from the change, the sensor output is extracted. Similarly, in [6], the sensor is placed in between the tag and antenna. Based on the impedance change, the reflected power level from the tag is changed, which would provide the sensor state. Those kind of RFID integrated sensors are simple in architecture, but the tag reflected power level will also be effected by the environment. To mitigate that effect, a redundant tag can be used to provide the reference sensor level. However, other

complexities such as coupling between multiple tags, area requirement, special packaging will arise. Examples for both type of conventional RFID IC integrated sensor system are shown in Fig. 2.7.

A more practical approach is demonstrated in [55], where the analog output of the sensor is converted into digital bits and integrated with the RFID tag ID bits before sending the ID sequence back to the reader. In this method, the sensor output is not susceptible to environment factors. However, an extra analog to digital converter (ADC) is required to convert analog signal into digital bits, which usually consumes extra energy unless selectively chosen. However, this kind of sensing introduces quantization error, which reduces the tag sensor sensitivity.

2.3 Low Power Operation and response Time

Passive RFIDs predominately operate on harvested energy and RF to DC conversion is used due to ubiquitous operation requirement independent of light, temperature, or wind. Hence, the power consumption at the tag is limited by the energy harvesting. Naturally, the range of the tag is limited by the power consumption, which increases with addition of functionality such as digital sensing, security, and so on. Hence, a popular idea is to charge a comparatively large storage capacitor for longer time and use the stored energy within a short interval of time. This technique helps in reduction of average power consumption but at the cost of longer start-up time due to charging of larger capacitance. Hence, a tradeoff should be maintained between the following two factors while designing an energy harvesting unit: (a) maximum discharge energy, and (b) start-up time.

The power consumption at the tag for digital operation are primarily (a) static, and (b)

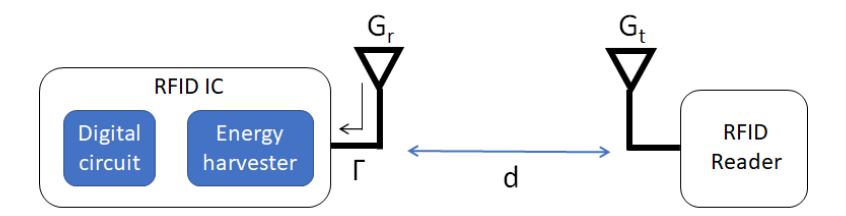


Figure 2.8: Schematic block diagram of the RFID tag during energy harvest.

dynamic consumption. The static power consumption remains constant at a fixed voltage but the dynamic power consumption strongly depends upon the switching frequency. In digital circuits, the dynamic power consumption usually contains the larger share of total consumption and is denoted as in (2.5).

$$P_{dynamic} \propto \alpha f V_{DD}^2 \tag{2.5}$$

From (2.5), it is evident that the power consumption increases in proportionate to the frequency of operation f and in square law to the voltage of operation V_{DD} . In (2.5), α is termed as the switching probability between the '0' and '1' state. For low power operation, the operating frequency and V_{DD} level should be kept as small as possible. V_{DD} level is determined by the process technology using which the monolithic IC is fabricated. With introduction of smaller process nodes such as 10nm, 7nm, or 5nm, the power consumption can be substantially reduced. On the other hand, the frequency of operation is primarily a design parameter and can be reduced by efficient design architecture.

Apart from power consumption, the energy harvesting should be efficient enough to supply the necessary power for consumption. The harvested energy at the tag $P_{harvest}$ is expressed as in (2.5), where the reader transmitted power is P_t , antenna gain is G_t , distance between tag and antenna is d, tag antenna gain is G_r , reflection co-efficient between tag IC and tag antenna is Γ , energy harvester efficiency is η assuming $d > (2D^2/\lambda)$, where D is the

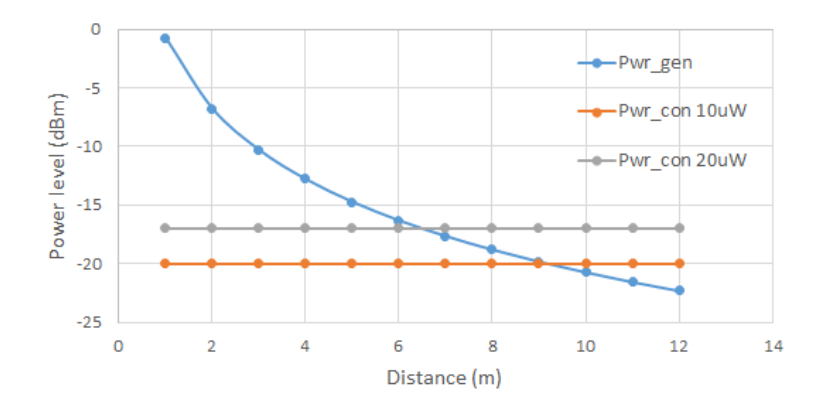


Figure 2.9: Analysis on energy harvest at the tag vs. distance with varying consumption.

largest aperture of the reader antenna, and $G_t >> G_r$. The scenario is shown in Fig. 2.8 and expressed in (2.6).

$$P_{harvest} = \frac{P_t G_t G_r \lambda^2}{(4\pi d)^2} (1 - \Gamma^2) \eta \tag{2.6}$$

The maximum range of the tag d_{max} is defined as the distance between the tag and reader, for which the following condition is fulfilled as expressed in (2.7), where $P_{dynamic}$ is the dynamic power consumption at the tag and P_{static} is the static power consumption.

$$P_{harvest} \ge P_{dynamic} + P_{static} \tag{2.7}$$

A simple analysis with $P_t = 30$ dBm, $G_t = 6$ dBi, $G_r = 0$ dBi, $\Gamma = 0$, and $\eta = 30\%$, is shown in Fig. 2.9 about the read range of the tag, considering different power consumption at the tag. The maximum read range decreases from 9 m to 6 m, when the power consumption at the tag increases from 10 uW to 20 uW. Hence, the average power consumption at the tag should be as low as possible for maximum read range. A detailed analysis on the energy harvesting will be performed to show the efficiency and response time dependency on the circuit components.

2.4 Prolonged RF transmission from reader

Continuous RF radiation from the reader is another challenge in conventional RFID. To keep the RFID tag functional, the reader should be always illuminating and continuous RF radiation may not be always desired. Recently, there has been multiple studies on the adverse effects of prolonged RF radiation on human body [56–58], with few studies reporting significant chromosomal DNA damage. Most of the studies included cellular, bluetooth, wearable device frequency bands, starting from 700 MHz upto 5 GHz. Among different applications of UHF RFID, few desired ones are sensor integrated RFID within human body, or integrated sensors as wearable devices or in vicinity of human body. Continuous RF radiation can be detrimental in those cases if the radiation time is long and of high power. As the conventional RFID tags can backscatter only when RF carrier is present, continuous RF power should always reach at the tag for desired modulation. Hence, it is fundamentally impossible to extract sensor information from conventional sensor integrated RFID without radiating RF power from the reader. The scenario is described pictorially in Fig. 2.10, where the desired scenario with reduced RF radiation transmit time from the reader is shown in Fig. 2.10(b).

As a preventive measure, alternate ways of reduced RF transmit time was explored in this work. The proposed dual mode RFID will be capable of backscattering as well as synthesizing its own carrier to communicate with the reader. The dual mode RFID has significant advantage in reduction of effective transmit time while monitoring the tag integrated seamlessly.

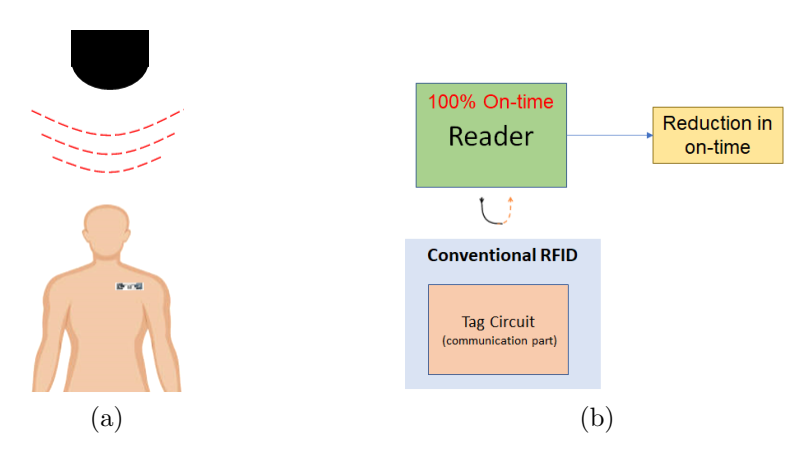


Figure 2.10: (a) RF radiation on human body, and (b) Desired effective RF radiation time reduction from the reader.

2.5 Summary

Different challenges in conventional RFID are outlined in this chapter. The solutions for the four major problems as outlined at the beginning of the chapter, are proposed individually in the subsequent chapters from Chapter 3 to Chapter 6. In Chapter 7, the possibility of a single integrated hybrid RFID is proposed, capable of mitigating all the four major problems.

Chapter 3

Harmonic RFID

In chapter 2, the challenge due to clutter issue in conventional RFID was discussed in detail. To overcome clutter issue, different digital encoding schemes were explored in the literature. In [59], an optimum maximum-likelihood sequence detector (MLSD) scheme was implemented which showed a 3 dB improved system performance compared to the conventional ML sequence detector. However, there is a fundamental limit to the system performance of passive tags under the same frequency operation [60,61]. The SCR can be increased dramatically by implementing the RFID communication channel in two different frequency bands, one for uplink and the other for downlink. In this dual frequency operation, the weak signal from the RFID tag can easily be filtered and amplified at the interrogator to obtain a clutter-free signal. Harmonic RFID tags operate in two frequency bands by transmitting ID data at the harmonic of the received signal frequency and thus it has emerged as a potential solution for long-range RFID tags in a cluttered environment [1].

3.1 Background

Clutter and localization issues can be substantially mitigated by employing harmonic RFID solution. In harmonic RFID, the tag and reader operates at two different frequencies:
a) reader to tag downlink at fundamental frequency, and b) tag to reader uplink at harmonic frequency. In harmonic RFID, the tag generates harmonic of the reader transmitted signal

and uses the harmonic as carrier for modulation. Harmonic RFID has advantage over clutter as the clutter appears at fundamental frequency, whereas the tag return signal is at harmonic frequency. Hence, the clutter cannot obscure the desired signal unlike the conventional RFID system.

Similarly, the localization is also improved using harmonic RFID. In [7], it was experimentally shown that as the phase information is contained within the second harmonic, interferences and phase errors caused by direct reflections of the interrogating signal are greatly reduced. Also, the phase information is better preserved in harmonic operation and immune to background interference, as demonstrated in [3]. Simultaneously, as the readers transmit only fundamental frequency, reader to reader interference will be greatly reduced. Additionally, as the harmonic frequency reduces the operating wavelength, the localization accuracy is significantly enhanced [62].

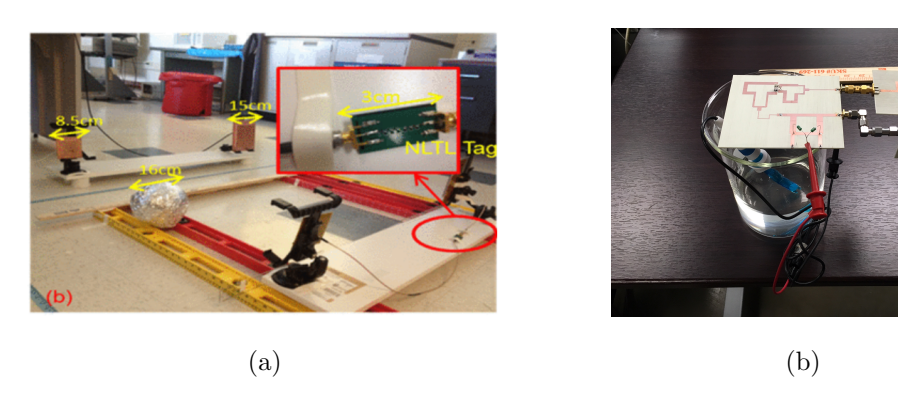


Figure 3.1: (a) Harmonic phase based localization in presence of a scatterer [7] (b) Harmonic phase based sensing with better immunity to background clutter [3].

CMOS based frequency multipliers are quite popular as they can readily be integrated with other digital processing CMOS circuits, albeit their high power consumption [63]. Other choices are the use of zero bias Schottky diodes [39] or varactor diodes, largely used in the design of nonlinear transmission line (NLTL) [64]. However, Schottky diode based harmonic

generators are not suitable for ID modulation because of self-biasing and large current requirements during the on stage. On the other hand, the potential of NLTL as a harmonic RFID was shown in [65] and a developed tag circuit was reported in [1]. However, the harmonic RFID tag in [1] used a microcontroller based architecture, which required relatively high power during operation ($\sim 100~\mu W$) and was not a cost-effective solution. Due to high power consumption, the range of a microcontroller based RFID tag would be limited. In some architectures, the power is harvested over a long period of time and the tag sends the ID within a very short time period after activation [66]. In this case, a complex system architecture and signal latency would be an issue. To overcome these problems, an ultra-low power harmonic RFID tag is proposed in this work that operates in a continuous mode.

The wireless communication link of RFID tags can be categorized broadly into two groups:

1) mutual coupling of the magnetic field through coupled coils [67] and, 2) using antennas for far-field communications [39]. For the first type, the tag is mutually coupled to an interrogator within one wavelength distance usually in LF and HF bands. Whereas, far field antenna based tags mostly operate in UHF band as high as 2.5 GHz [39]. In the spectrum of license-free RF bands, there are very few bands available, which meet the criteria of fundamental and harmonic bands. Among the license-free bands, available bands are ISM 6.78 MHz and ISM 13.56 MHz duplex, ISM 13.56 MHz and ISM 27.12 MHz duplex or ISM 434 MHz and SRD 868 MHz duplex [68]. At low frequency, RF communication is performed using magnetically coupled coils, which are inefficient in power transfer [69]. Hence, relatively high-frequency band 434 MHz and 868 MHz duplex were chosen for harmonic tag design in this work. The proposed harmonic RFID system consists of an interrogator and an harmonic RFID tag. The interrogator transmits a signal at fundamental frequency (f₀). When the signal is received by the harmonic tag, it generates and transmits back the second harmonic

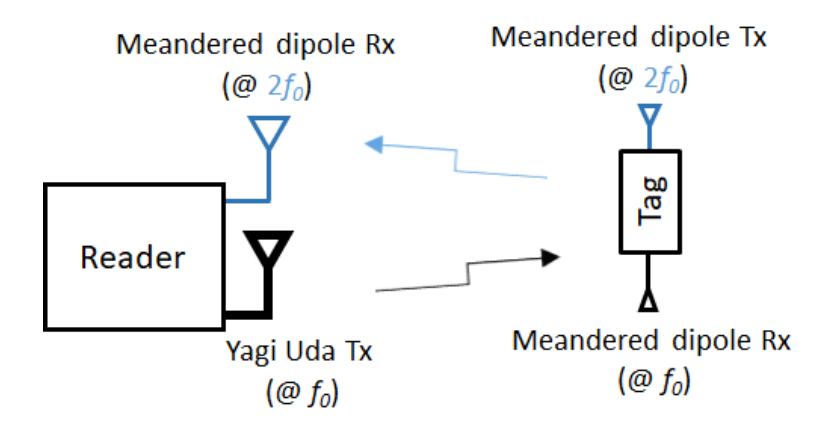


Figure 3.2: Fundamental and harmonic antenna setup in between the tag and reader.

 $(2f_0)$ of the fundamental frequency at a specific sequence, which is decided by the ID or IP address of the tag. Upon receiving the transmitted signal from the tag, the interrogator demodulates the sequence at $2f_0$ and the specific ID of the tag is obtained.

This chapter is organized as followed:

- Design of NLTL, a low power harmonic generator is discussed.
- A first generation harmonic RFID tag with two antennas is shown.
- A second generation single antenna based miniaturized harmonic RFID is shown.
- Lastly, efficacy of harmonic RFID in presence of clutter is illustrated.

3.2 Nonlinear Transmission Line: NLTL

In this section, it will be shown how the harmonic generation efficiency can be enhanced by using specific operating condition and multiple number of varactor diode as harmonic generator elements. The generated harmonic signals from multiple sections are added in-phase to generate very low conversion loss harmonic output. One such structure is called nonlinear transmission line (NLTL). The NLTL can be a continuous co-planar waveguide (CPW) line

on a semiconductor substrate with discrete metal semiconductor junction diodes [8, 70], or distributed configuration using metal-semiconductor junction on GaAs substrate [71], or discrete inductor and varactor diode structure fabricated monolithically [9], or discrete inductor and varactor diode structure fabricated on a PCB using discrete packaged components [72]. As the maximum bandwidth is dictated by the NLTL cut-off frequency, a monolithic fabrication would provide the most operational bandwidth as high as 20-30 GHz [8]. Examples of differently fabricated NLTLs are shown in Fig. 3.3, for (a) discrete diodes on CPW line, and (b) discrete diodes and inductors.

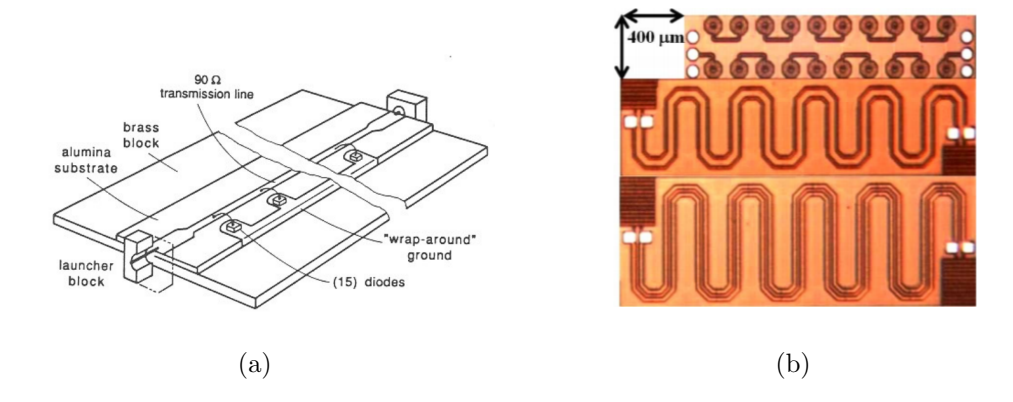


Figure 3.3: (a) Example of NLTL: (a) Discrete diode with CPW line [8] (b) Discrete inductors and diodes shown at the top [9].

3.2.1 Design principle

The design principle of NLTL is described in detail in [2,8,72] with periodic structure of multiple sections of NLTL. There are different methods of designing NLTL circuits, among which the prevalent one is to approximate an equivalent LC network similar to a transmission line but with nonlinear capacitance due to diode instead of constant capacitance.

Any diode operating in nonlinear region acts as a harmonic generator. The voltage dependent capacitance of a diode is expressed as followed in Equation (3.1). In (3.1), C_{j0} ,

 V_j and m are diode characteristics parameters, where V_j is the forward junction voltage and m depends on the doping profile of the semiconductor. The voltage V denotes the applied voltage across the diode, which consists of a DC term V_{dc} and an AC term V_{ac} . The DC term denotes the fixed voltage, at which the diode is biased constantly. The time varying charge q(t) across the diode can be represented by time varying AC voltage and the DC bias as shown in Equation (3.2).

$$C = \frac{C_{j0}}{\left(1 + \frac{V}{V_j}\right)^m} \quad \text{where, } V = V_{dc} + V_{ac}$$
(3.1)

$$q(t) = C_{j0} \left[1 + \frac{V_{dc} + V_{ac}(t)}{V_j} \right]^{-m} (V_{dc} + V_{ac}(t))$$
(3.2)

If Equation (3.2) is expanded, q(t) is expressed as a combination of different higher order AC voltage terms. In (3.3), a_0 , a_1 , and a_2 are the co-efficients of corresponding DC, first order AC, and second order AC (or harmonic) terms of the time varying voltage. The other higher order modes are neglected, as primary focus is generation of second order harmonic.

$$q(t) = a_0 + a_1 V_{ac}(t) + a_2 V_{ac}^2(t) + a_3 V_{ac}^3(t) + \dots$$
(3.3)

If the diode is terminated across a load R, the output voltage can be obtained in terms of all harmonics or higher order modes of applied time varying input voltage. If the input voltage is a single sinusoid term, all the harmonics will appear at the output, as shown below.

$$V_{out}(t) = i(t) * R$$

$$= V'_{ac}(t) * \left[a_1 + 2a_2 V_{ac}(t) + 3a_3 V_{ac}^2(t) + \dots \right]$$
(3.4)

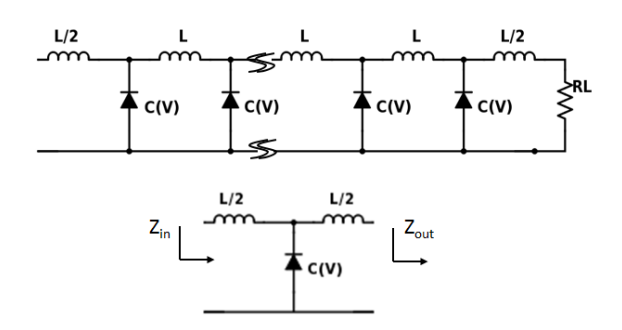


Figure 3.4: Lumped element representation of the NLTL with a single cell NLTL at the bottom.

The amplitude of the output harmonic power will primarily depend on the diode parameters such as m, and V_j . Additionally, the constant DC bias V_{dc} will also effect the harmonic generation. Physically, any diode or nonlinear device generates strong harmonics at its maximum non-linear region. The maximum non-linearity region can be obtained of a varactor diode by measuring capacitance with change in bias voltage. Curvature co-efficient γ , which is a pre-factor of non-linearity can be extracted from the C-V curve of a varactor diode.

Once, conditions for maximum harmonic generation from a single varactor diode is obtained, the efficiency can be further enhanced by combining multiple varactor diodes, and the design topology is termed as nonlinear transmission line (NLTL). Due to periodicity, one popular way to model the lumped element based NLTL sections is use of ABCD matrix. The lumped element based NLTL is shown in Fig. 3.4 with a single cell. The ABCD matrix of a single cell NLTL is first formulated. Based on the single cell model, the multi-cell NLTL can be extended with cascaded multiple single cell. For a single cell NLTL as shown in Fig. 3.4, the ABCD matrix is expressed as given in Equation (3.5). After simplification, the form of the ABCD matrix becomes as given in Equation (3.6).

$$\begin{bmatrix} A & B \\ C & D \end{bmatrix}_{single}^{lossless} = \begin{bmatrix} 1 & j\omega L/2 \\ 0 & 1 \end{bmatrix} \cdot \begin{bmatrix} 1 & 0 \\ j\omega C & 1 \end{bmatrix} \cdot \begin{bmatrix} 1 & j\omega L/2 \\ 0 & 1 \end{bmatrix}$$
(3.5)

$$\begin{bmatrix} A & B \\ C & D \end{bmatrix}_{single}^{lossless} = \begin{bmatrix} 1 - \frac{\omega^2 LC}{2} & L(1 - \frac{\omega^2 LC}{4}) \\ j\omega C & 1 - \frac{\omega^2 LC}{2} \end{bmatrix}$$
(3.6)

$$\begin{bmatrix} A & B \\ C & D \end{bmatrix}_{single}^{tossy} = \begin{bmatrix} k & j\omega(R + \frac{j\omega L}{2})k \\ G + j\omega C & k \end{bmatrix}$$
where, $k = 1 + RG - \frac{\omega^2 LC}{2} + j\omega\left(\frac{LG}{2} + RC\right)$ (3.7)

Now, as the NLTL system should be symmetric at a fixed C, the ABCD matrix given in (3.6) should be symmetric in nature. However, the expression in (3.6) is in simplified form ignoring the loss in series inductors and shunt capacitors. By incorporating the series resistance R and parallel conductance G, the expression in (3.6) can be modified as in (3.7). With the simplified symmetric condition of ABCD matrix being imposed, the characteristics impedance of the NLTL as Z_{NLTL} can be expressed in terms of design parameters as in (3.8). The solution for L can be readily derived by solving (3.8) with the known capacitance of the diode.

$$\frac{L}{C} - \frac{\omega^2 L^2}{4} = Z_{NLTL}^2 \tag{3.8}$$

For a long network of NLTL with multi-stage elements of m, the total composed ABCD matrix of the m-stage network becomes as given in Equation (3.9). Now, with any order of NLTL, the final composed network will be symmetric in nature too, as each of the elemental matrix is symmetric in nature. The loss effect increases exponentially With more number

of stages from the derived ABCD matrix for lossy case. Hence, an optimum stage number exist, beyond which the harmonic generation does not improve with addition of more stage number. A theoretical analysis was performed in [73] to describe the harmonic generation by a NLTL.

$$\begin{bmatrix} A & B \\ C & D \end{bmatrix}_{mstage} = \begin{bmatrix} A & B \\ C & D \end{bmatrix}_{single}^{m}$$
(3.9)

The Telegrapher's equations for NLTL was solved in [73] to express the output at harmonic frequency in terms of nonlinearity factor and fundamental frequency input. As mentioned earlier, number of NLTL stages is important as it decides the maximum harmonic output power availability. Primarily two major events happen in NLTL: (a) the output harmonic power is added in-phase as the input propagates through the NLTL, and (b) attenuation of both harmonic and input power as the physical NLTL is lossy in nature. The in-phase output power addition is used extensively in optical regime as parametric mixing [74,75]. In parametric mixing, a high power pump signal and a low power idler signal is provided as input and the difference term is obtained as mixing output. When the idler is exactly at twice frequency of pump frequency, a harmonic generator is obtained. However, in microwave harmonic generators, the idler is not required to be provided separately as there is always small amount of harmonic will be present with the pump signal. The optimum number of stages or the NLTL length would be based on this two contrasting factors, until the harmonic generation is more than attenuation. As a good practice, the NLTL attenuation should be kept as low as possible for maximum harmonic output power.

3.2.2 Simulation and measurement

Prior to the design, all the required circuit simulations were performed using ADS from Keysight. For the simulation, varactor diode model recommended by Skyworks was used. As lumped components were used for the design, lumped passive components were used in simulation. After modeling, the simulation result was later verified with the measurement result. The measurements were performed using a Vector Network Analyzer (VNA) for reflection and transmission co-efficients of the NLTL circuit. The results are shown below for different number of stages.

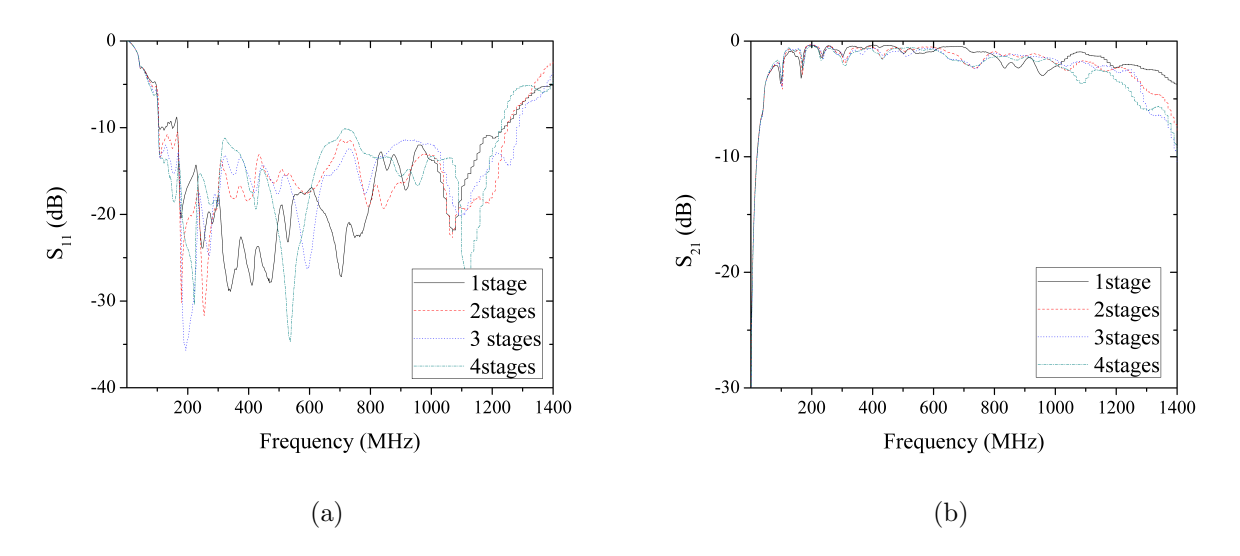


Figure 3.5: (a) S_{11} and (b) S_{21} for different number of NLTL stages.

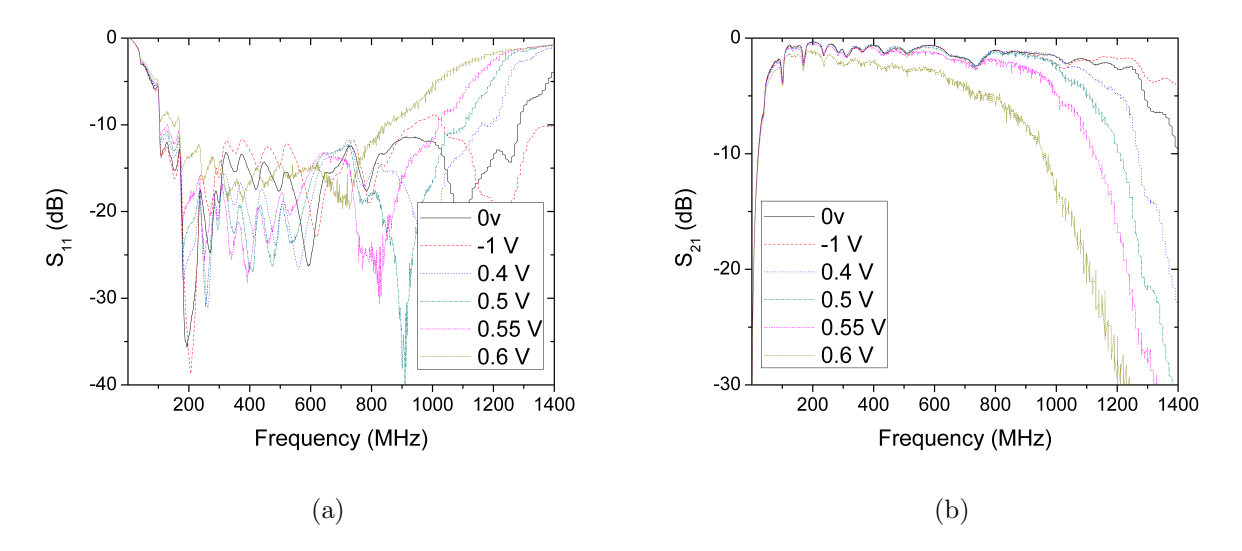


Figure 3.6: (a) S_{11} and (b) S_{21} for three number of NLTL stages at different DC bias.

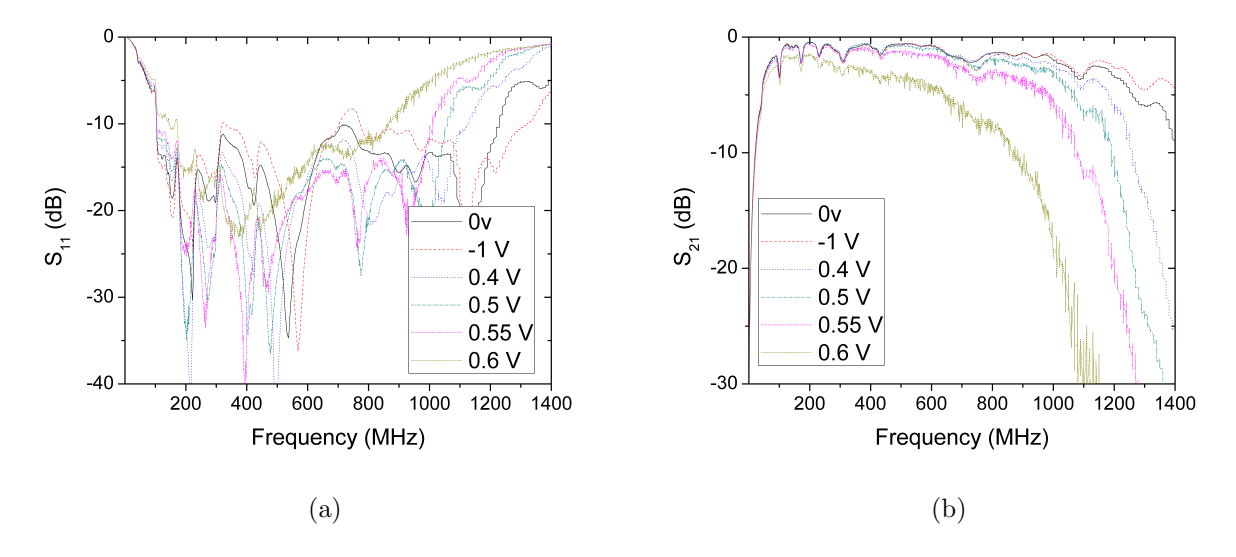


Figure 3.7: (a) S_{11} and (b) S_{21} for four number of NLTL stages at different DC bias.

The measurement results show the transmission line behavior of the NLTL. As the number of stages are increased, the roll-off of the S_{21} increases as shown Fig. 3.7(b) and 3.6(b). The S_{11} behavior of different NLTL stages shows that most of the power is passed through the NLTL upto 1 GHz. When the bias voltage is changed, the effective capacitance of the

varactor diode changes, and it will change the transmission characteristics of the NLTL.

3.3 Harmonic RFID: Gen I

The first generation harmonic RFID developed at MSU is presented in this section. The harmonic RFID system in general includes RFID reader and tag. The primary features of this harmonic RFID system are:

- Gen I harmonic RFID tag has 8-bit ID integrated with it.
- It has two antennas, one for transmission and other for reception at the tag and reader.
- The tag has a RF power splitter to provide RF energy for harmonic generation and energy harvesting.

Different parts of the Gen I harmonic RFID system are discussed in detail subsequently. The three parts discussed here are: (a) antennas used for both reader and tag, (b) harmonic tag circuit, and (c) harmonic reader circuit.

3.3.1 Antennas

The antenna provides the wireless link for power and data transfer in between the harmonic RFID tag and interrogator. Three different antennas designs are needed for the complete system design as illustrated in Fig. 3.2. The antennas associated with the tag should be small for a miniaturized tag design. On the other hand, the reader antenna should have a high realized gain for efficient long range tag interrogation. Additionally, the size constraint is not stringent on the reader antenna as compared to the tag. Hence, two different type of antennas were designed at the fundamental frequency (f_0) for the reader and

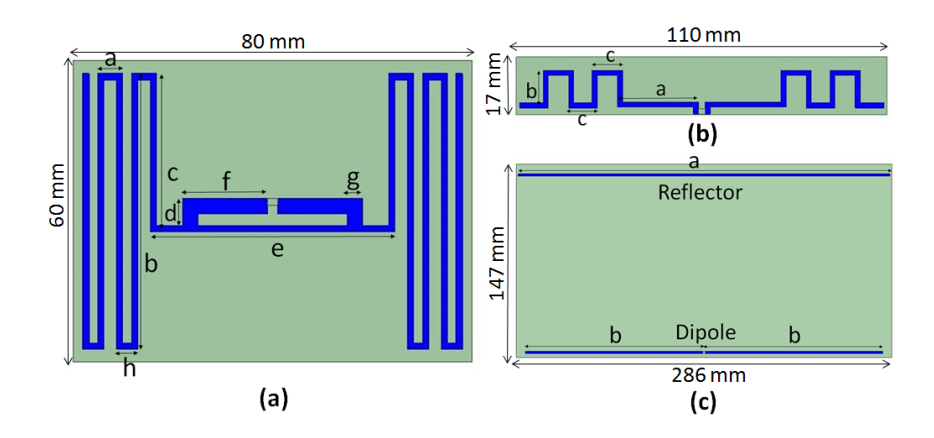


Figure 3.8: Antenna structures for (a) Meandered dipole (434 MHz) for tag side, (b) Meandered dipole (868 MHz) for tag and interrogator sides and (c) Yagi-Uda (434 MHz) for interrogator side.

Table 3.1: The dimension of different antenna designs

$\mathbf{Yagi\text{-}Uda}(f_0)$			
Reflector		Director	
Parameter	Dimension(mm)	Parameter	Dimension(mm)
a	282	b	134
Meandered Dipole (f_0)			
Parameter	Dimension(mm)	Parameter	Dimension(mm)
a	6.25	e	48
b	55	f	17
С	31	g	3
d	6.75	h	5
Meandered Dipole $(2f_0)$			
Parameter	Dimension(mm)	Parameter	Dimension(mm)
a	23	С	8
b	10		

tag. The transmitting antenna of the reader is a high gain two elements Yagi-Uda antenna and the receiving tag antenna is a small meandered dipole antenna operating at (f_0) . Apart from f_0 , the harmonic system also operates at $2f_0$ as shown in Fig. 3.2. Hence, a common meandered dipole at harmonic $(2f_0)$ frequency was designed and implemented for the tag transmitter and the interrogator receiving end.

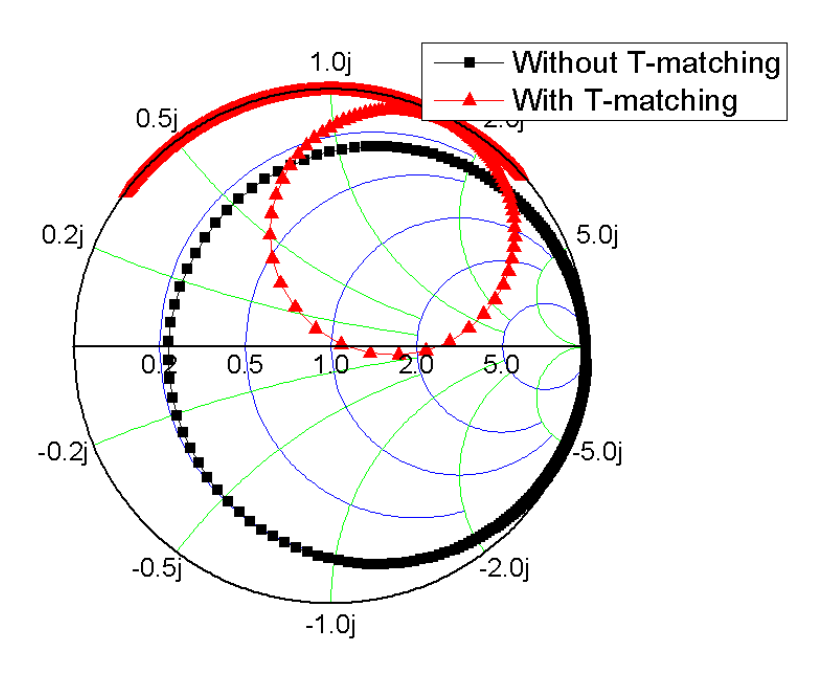


Figure 3.9: Effect of T-match on input impedance shown on Smith chart from $100~\mathrm{MHz}$ to $600~\mathrm{MHz}$.

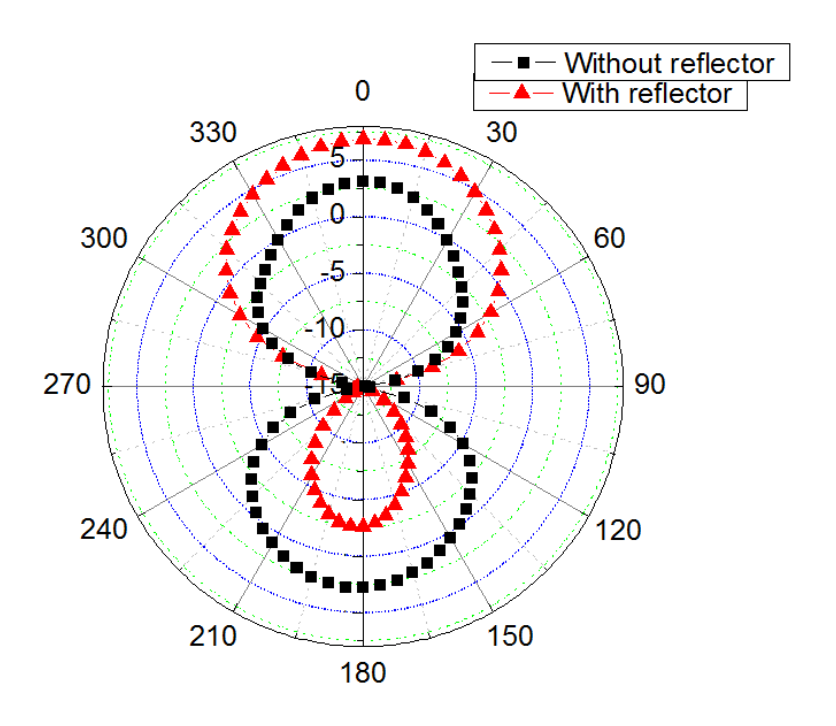


Figure 3.10: Radiation pattern of the Yagi-Uda with and without the back reflector.

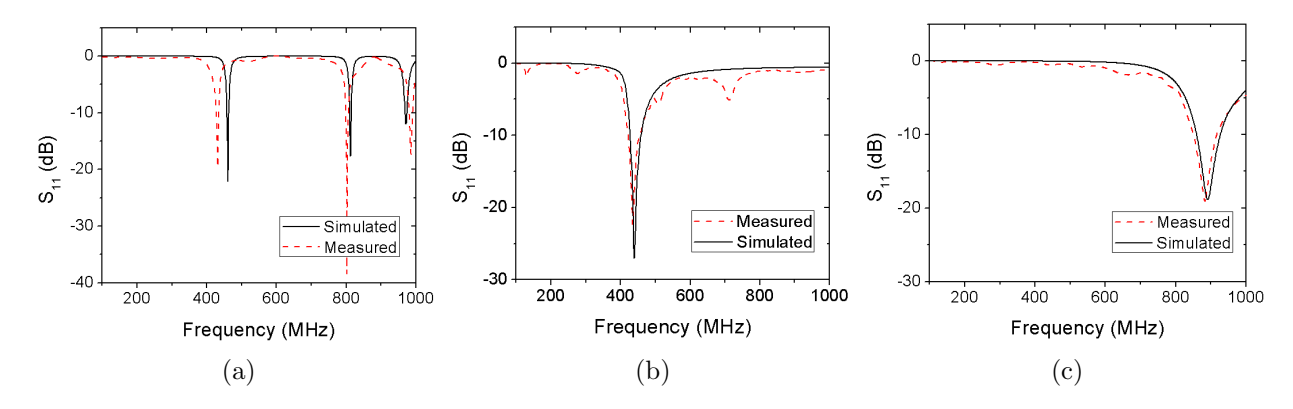


Figure 3.11: Simulation and measurement results for (a) 434 MHz meandered dipole, (b) 434 MHz Yagi-Uda and, (c) 868 MHz meandered dipole antenna.

3.3.1.1 Meandered dipole antenna

Different meandered dipole or loop antenna designs have been proposed to achieve compact size in the UHF frequency band [76,77]. Meandered dipole antennas have become popular for RFID applications due to their compact size and easier to impedance match to high impedance RFID ICs [76]. Here, a $\lambda_g/2$ meandered dipole antenna was designed and fabricated on RO4350B board from Rogers Corporation. It has a dielectric constant (ϵ_r) of 3.6, where λ_g corresponds to the effective wavelength at (f_0). By meandering, the effective dipole length of the antenna is maintained while reducing the board size. However, there is a tradeoff between antenna effective size and gain. In [78], genetic algorithm was used to optimize in between gain and area occupied by the meandered dipole. In this work, an optimized design topology from [78,79] was adopted for the meandered dipole with reasonable gain while maintaining small size. The meandered dipole antenna as shown in Fig. 3.8(a) has a gain of 0.98 dBi with an effective board area of 48 cm² at (f_0) after simulation. Additionally, the input radiation resistance of a meandered dipole reduces from the standard dipole as described in [80]. Conventionally, a T-match is used to match the low impedance antenna to a high impedance system [76]. The antenna design parameters are shown in

Table 1.1. The effect of T-match on input impedance matching of the meandered dipole is shown in Fig. 3.9 with respect to a 50 Ω measurement system.

Another meandered dipole at $(2f_0)$ was designed following the same design principles. This antenna showed a gain of 2.1 dBi with an effective board area of 18.7 cm^2 at $(2f_0)$ from the simulation. The design parameters of the antennas are provided in Table 3.1 as shown in Fig. 3.8(b). This way two meandered dipole antennas were designed at fundamental (f_0) 434 MHz frequency and harmonic $(2f_0)$ 868 MHz frequency.

3.3.1.2 Yagi-Uda antenna

A two element Yagi-Uda antenna was designed for the interrogator to achieve high gain during transmission. As the fundamental operating frequency is at 434 MHz, a planar multi-element Yagi-Uda implementation would occupy large space on the board. Hence, the design was restricted only to two elements having one driving element and one reflector element. The design parameters of the antenna elements is shown in Fig. 3.8(c) are provided in Table 3.1. Simulated antenna gain patterns in the E-plane are shown in Fig. 3.10 with and without the back reflector. From the simulation result, it can be verified that the forward gain improves by 4 dB and an improved front to back ratio (FBR) of 10 dB compared to a simple dipole design.

The antennas were fabricated on a 1.52 mm thick RO4350B board using a milling machine. The reflection coefficients (S_{11}) were measured using a network analyzer. Fig. 3.11 shows the simulation and measured results of the antennas. The conductor line width is 1.5 mm for all the antennas unless it is mentioned otherwise.

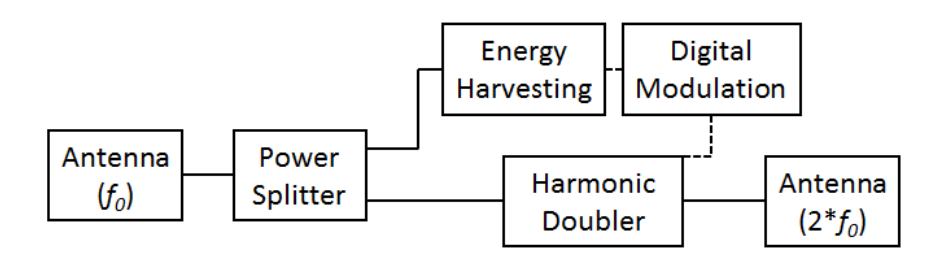


Figure 3.12: Harmonic tag architecture with different components.

3.3.2 Harmonic tag design

The architecture of the harmonic tag circuit along with antennas is shown in Fig. 3.12. It consists of the following components: 1) Power splitter (PS), 2) Harmonic doubler (HD), 3) Energy harvesting unit (EHU) and 4) Digital modulation unit (DMU). The PS, at the input, divides the received RF signal into two parts: (a) for energy harvesting in the EHU and (b) for harmonic generation from the fundamental carrier signal (f_0) in HD. One advantage of the designed harmonic tag is that it can operate in continuous mode, which means that it harvests energy and transmits ID information simultaneously. This is in contrast to a conventional tag, which first harvests and then transmits the ID. Here, once the EHU harvests the required energy, it activates the DMU, which triggers the HD 'off' and 'on' sequentially. A simple amplitude shift keying (ASK) based modulation was adopted for triggering. Based on the 'off' and 'on' sequence, the HD subsequently generates the harmonic signal. The interrogator identifies the ID by reading only the harmonic signal.

3.3.2.1 HD using NLTL

Use of NLTL as an efficient HD has been reported previously [64]. The equivalent discrete component realization of a NLTL is shown in Fig. 3.13. It consists of a periodic series inductance and shunt varactor diode combination. The capacitance of a varactor diode shows non-linear behavior as a function of DC bias. The harmonics of the input f_0 signal

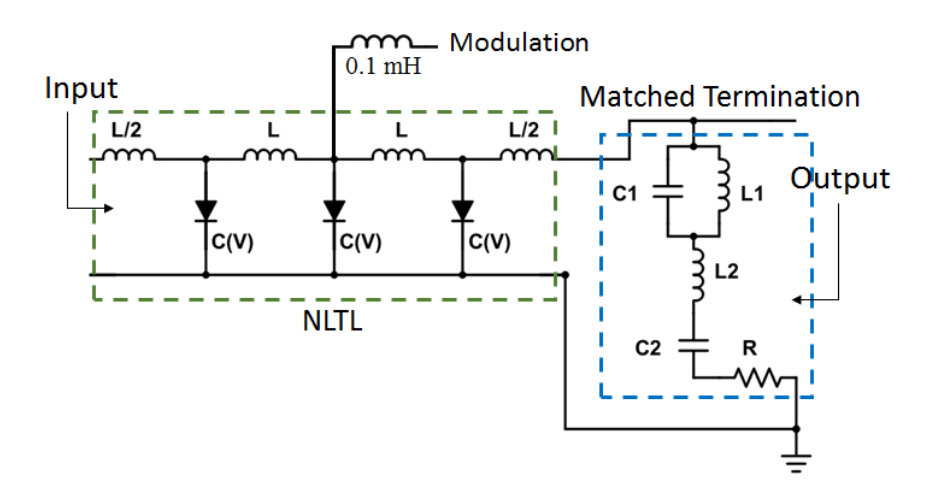


Figure 3.13: A three stage nonlinear transmission line (NLTL) with matched termination at 434 MHz.

are generated at the varactor due to its inherent non-linearity. The varactor should be biased at the strongest nonlinear region of its C-V characteristics for maximum harmonic power generation as described in [65]. Once this bias condition was determined, the inductance value was calculated for impedance matching to a 50 Ω load at 434 MHz (f_0). A three-stage NLTL was designed using L=10 nH and Skyworks SMV1405 varactor diodes. The varactor diode shows maximum non-linearity close to its threshold voltage, where the depletion width is minimum. The DC sweep of the three-stage NLTL shows a maximum harmonic generation at 0.6 V forward bias as shown in Fig. 3.14. However, increasing the bias voltage further did not help as the varactor started operating in the conduction mode. As shown in Fig. 3.14, the NLTL produces a maximum harmonic power of -25 dBm at a 0.6 V bias. In comparison, at 0 V it produces -51 dBm at an input power of -10 dBm. Hence, an analog DC voltage 0.6 V was used for digital state '1' and 0 V for the digital state '0' to achieve an RF isolation of 26 dB between the 'on' and 'off' states. The modulation signal from DMU was fed through an high impedance inductor, 0.1 mH, to isolate the RF path from the low-frequency digital signal as shown in Fig. 3.13.

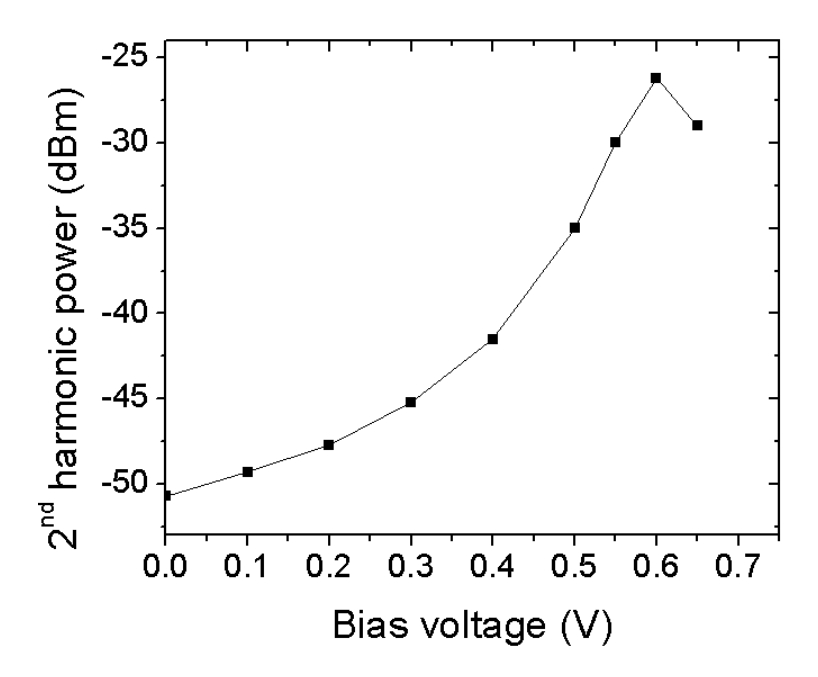


Figure 3.14: Measured second harmonic output power of a three stage NLTL as function of DC bias for input power of -10 dBm at 434 MHz.

During wireless operation, one end of the NLTL was terminated with an antenna operating at f_0 for RF reception and another end with an antenna operating at $2f_0$ for harmonic transmission. However, the $2f_0$ operating antenna does not show 50 Ω input impedance at f_0 as shown in Fig. 3.8(b). Hence, the NLTL was terminated with the $2f_0$ antenna through a matched termination circuit as shown in Fig. 3.13. The other choice was to choose the inductors of the NLTL for impedance matching with the $2f_0$ antenna. However, this would complicate the performance evaluation of the NLTL, which would be easier when matched to the standard instrument impedance of 50Ω . The matched termination uses a high frequency 50Ω resistor for impedance matching at f_0 . Additionally, the matched circuit includes a series resonator at $2f_0$ to prevent the drainage of harmonic power into the resistor. The reflection coefficient (S_{11}) of the matched termination is shown in Fig. 3.15 with and without the $2f_0$ operating antenna. A good matching was observed at f_0 irrespective of the presence of the ($2f_0$) operating antenna. Whereas at $2f_0$, all the input power was reflected back in

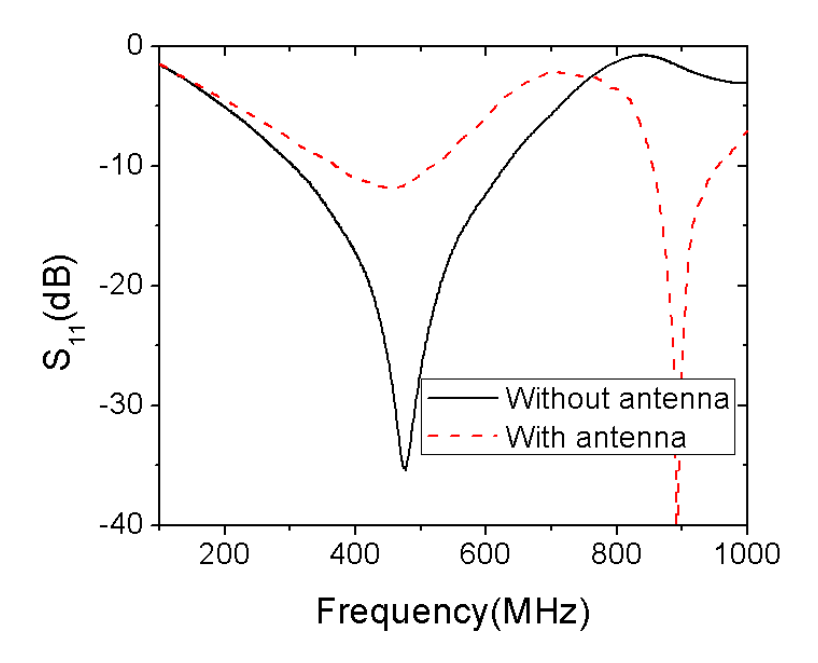


Figure 3.15: Measured reflection coefficient of the matched termination with and without $2f_0$ antenna.

the absence of antenna and radiated in the presence of antenna. Hence, the harmonic power was transmitted instead of being absorbed by the resistor. The design parameters for the matched termination are provided as C1=6.8 pF, L1=5 nH, C2=8.2 pF, L2=9 nH and R=50 Ω .

3.3.2.2 Energy Harvesting Unit (EHU)

The EHU provides the required DC power to drive the DMU and HD. Among the many energy harvesting methods that can be used, here an RF energy harvesting circuit (RF rectifier) was adopted. Diode-based RF rectifiers are usually used due to good conversion efficiency from RF to DC power. Schottky diode HSMS-2850 was chosen due to its higher conversion efficiency at low RF power [81]. As the RFID tag was intended to use at very low received power (< -5 dBm), the DC voltage level generated by a single rectifier was not sufficient to drive other modules. Hence, a voltage multiplier topology was adopted to boost

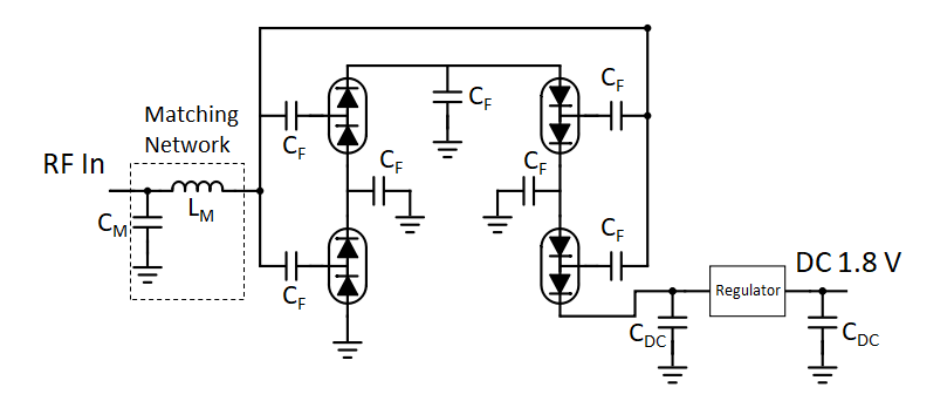


Figure 3.16: 4-stage charge pump circuit with matching network and DC voltage regulator.

up the rectified voltage. A conventional Dickson charge pump configuration was adopted as shown in Fig. 3.16 [82]. The 8 diodes were connected along a long chain of 4-stage in this configuration. A matching network was designed using $C_M = 10$ pF and $L_M = 26$ nH to maximize power conversion at f_0 . However, the DC voltage at the charge pump output was not regulated. Hence, a 1.8 V Linear Drop Output (LDO) voltage regulator (TPS79718Q) by Texas Instruments was used to supply regulated DC voltage within the circuit. Two capacitors $C_{DC} = 10$ μ F were used at the input and output of the voltage regulator to maintain a stable DC supply and remove high-frequency noises. The measurement results of regulated and unregulated DC voltage are shown in Fig. 3.17. The EHU was capable of generating regulated 1.8 V at the minimum input power of -12 dBm.

The input impedance of the EHU is shown in Fig. 3.18, which shows good matching at 434 MHz. The designed EHU had a measured quality factor of 8 with the matching network.

3.3.2.3 Digital Modulation Unit (DMU)

The DMU provides the 'on' or 'off' ASK modulation signal to the HD according to the ID. A simple design from [83] was adopted in this work for the modulation scheme. The design uses a parallel to serial 8-bit shift register to load up the stored digital data and

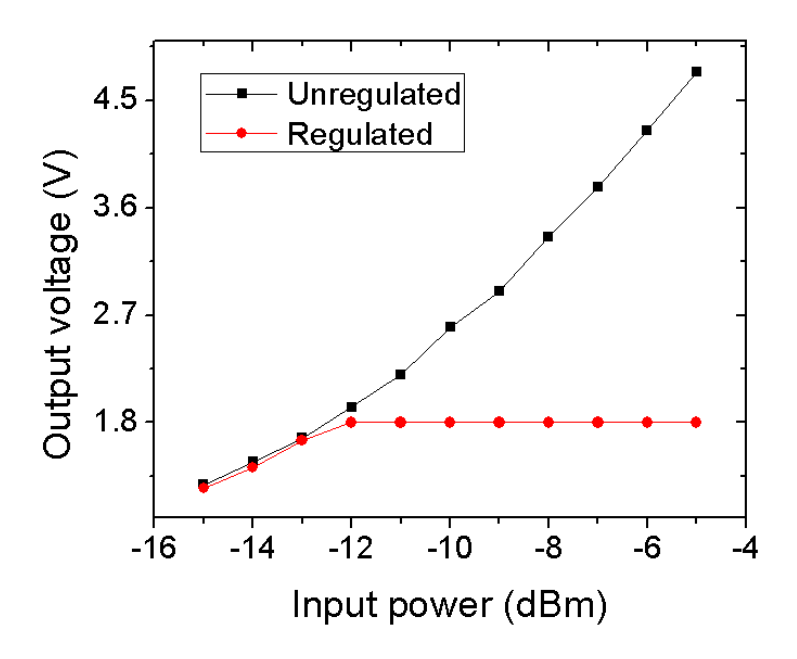


Figure 3.17: The unregulated and regulated DC voltage generated by the EHU.

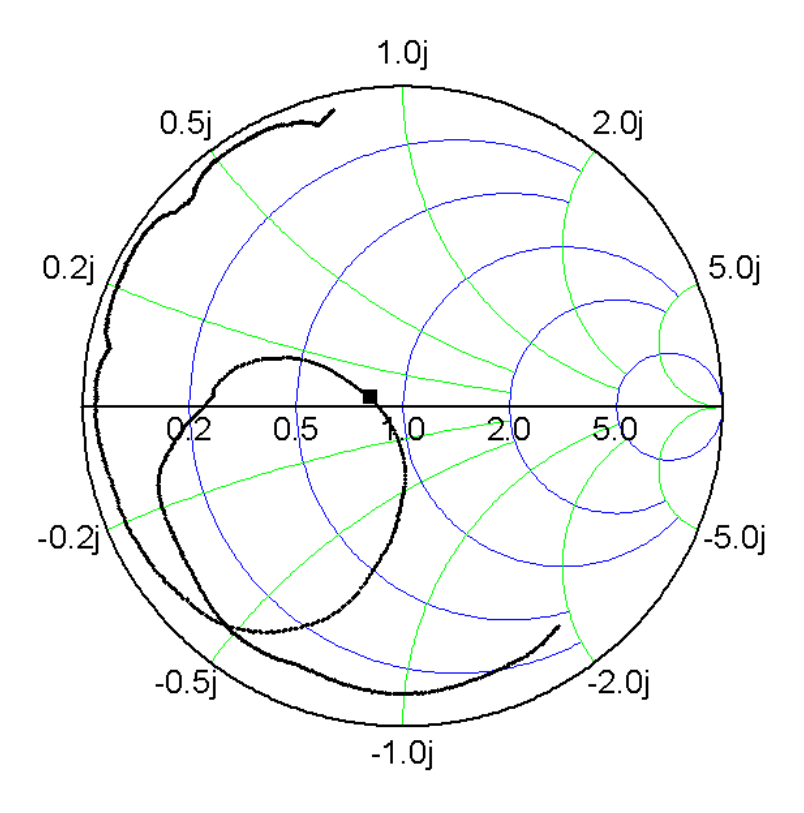


Figure 3.18: Input impedance of the EHU with marker at 434 MHz.

transmit it. When the LD pin of the shift register (SN74HC165PWRG3) was activated, it loaded the 8-bit ID in parallel and then transmitted serially upon deactivation of the LD pin. The timing diagram of the serial output pin due to clock and LD input signal is shown in Fig. 3.19. The LD signal should be deactivated for 8 clock periods as the shift register sends 8 bit of data signal serially during that period. The in-phase LD signal was derived from the clock signal using four D flip-flops. The block diagram of the LD signal generation from the clock along with the serial ID is shown in Fig. 3.20. The low power D flip-flops (SN74AUP1G80DCKR) generated the LD signal at frequency $f_{clk}/8$, where f_{clk} was the frequency of the clock signal. An ultra-low power oscillator by Micro Crystal was used to generate the clock signal at 32.768 kHz. Each component of the DMU was designed to work at least at 1.8 V. However, the complete DMU can work properly without bit loss at comparably lower DC voltage of 1.5 V. Implementation of the DMU using this architecture would be cost and power effective and easy to implement compared to a microcontroller, where programming is required. The number of ID bits is scalable by using multiple shift registers and synchronizing the clock timing. Serial output from the shift register was fed to a voltage divider to convert the CMOS voltage levels into NLTL realizable voltage levels, which was 0.6 V for high state and 0 V for low state.

3.3.2.4 Power Splitter (PS)

In contrast to conventional RFIDs, the tag was designed to operate in a continuous mode, which means the tag would send the ID data continuously during interrogation. In this mode, the EHU and HD need to operate simultaneously. Hence, a PS was implemented to divide the received power into two parts: 1) The first part would be harvested in EHU and power up the DMU 2) the second part would provide the fundamental input signal

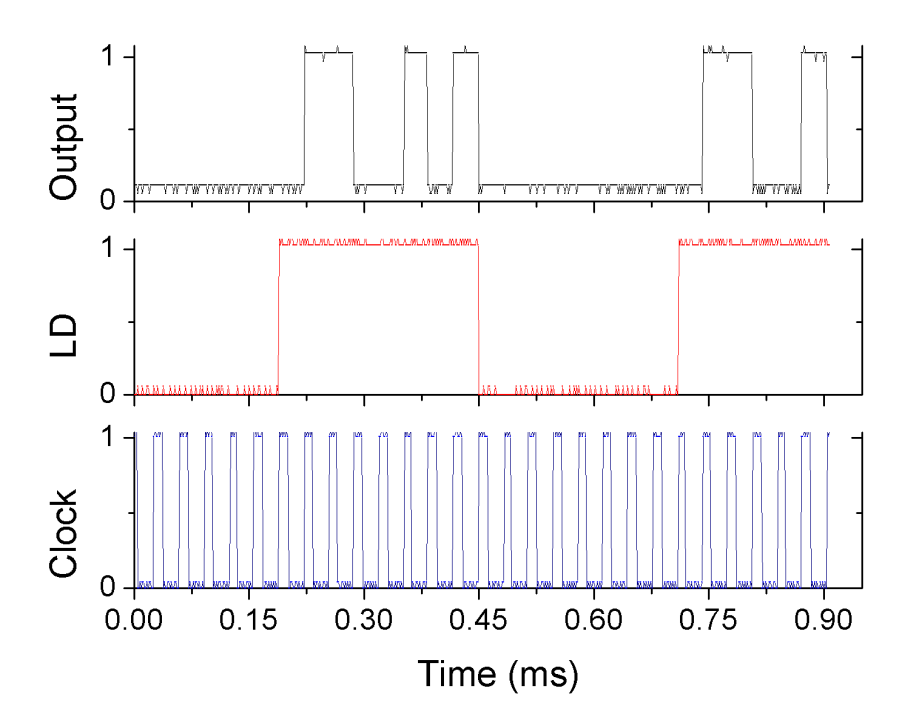


Figure 3.19: The different stages of signal generated by the DMU. Description from top to bottom: 1) Serial output of the shift register, which is the ID, 2) LD signal, and 3) Clock signal.

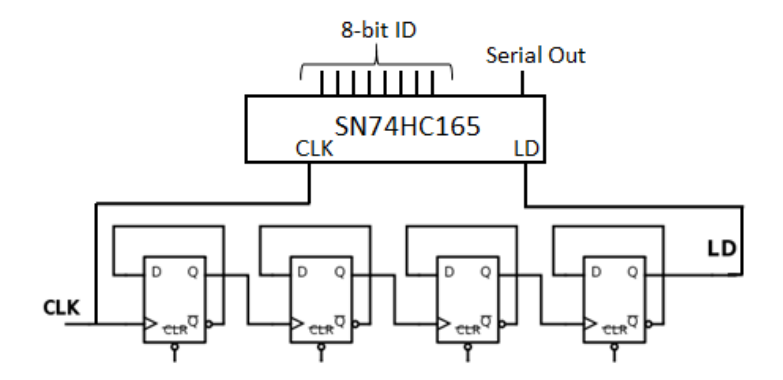


Figure 3.20: The D flip-flop setup to generate the LD signal from the Clock signal.

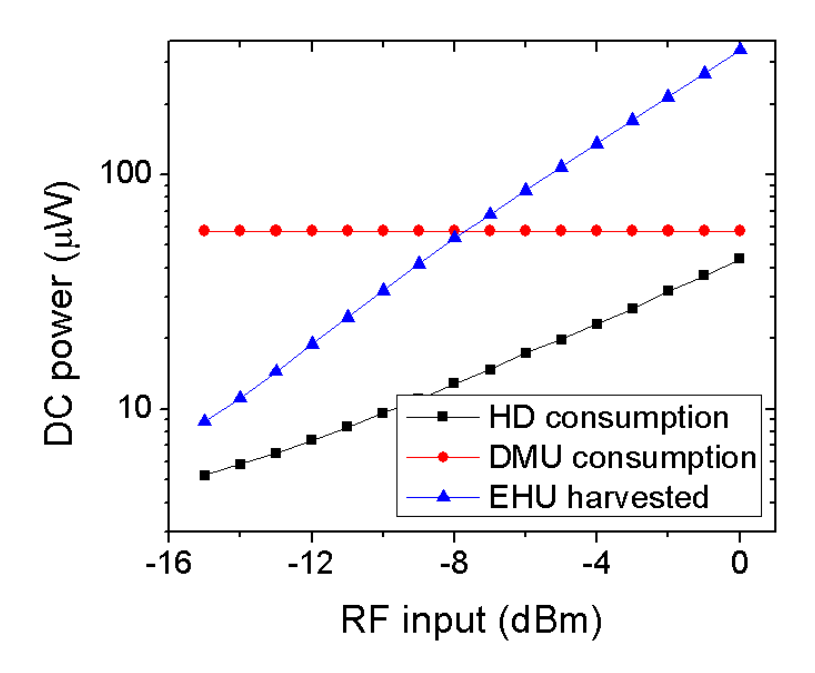


Figure 3.21: DC power consumption and harvest by HD, DMU, and EHU independently.

to the HD. Apart from the DMU, the HD also consumed DC power at logic 'high' state. However, the power requirement by the DMU and the HD unit was different. To determine the DC power needed by these units, the DC power consumption of each unit was measured independently at varying RF input power, as shown in Fig. 3.21. The generated DC power in EHU was calculated from the efficiency of the Schottky diode as described in [84]. The DMU consumed a constant DC power of 32.5 µW irrespective of the input RF power. However, the DC power consumption by the HD was dependent on the input RF power. The total DC power consumption was the addition of HD and DMU power consumption. The tag can only operate properly when the harvested DC power is more than the total DC power consumed. From Fig. 3.21, it is evident that the majority of the DC power was consumed by the DMU compared to the HD at low RF power. Hence, more RF power should be channeled into the EHU compared to the HD to minimize the RF activation power of the tag.

For comparison, two studies were performed, one with equal and the other with unequal

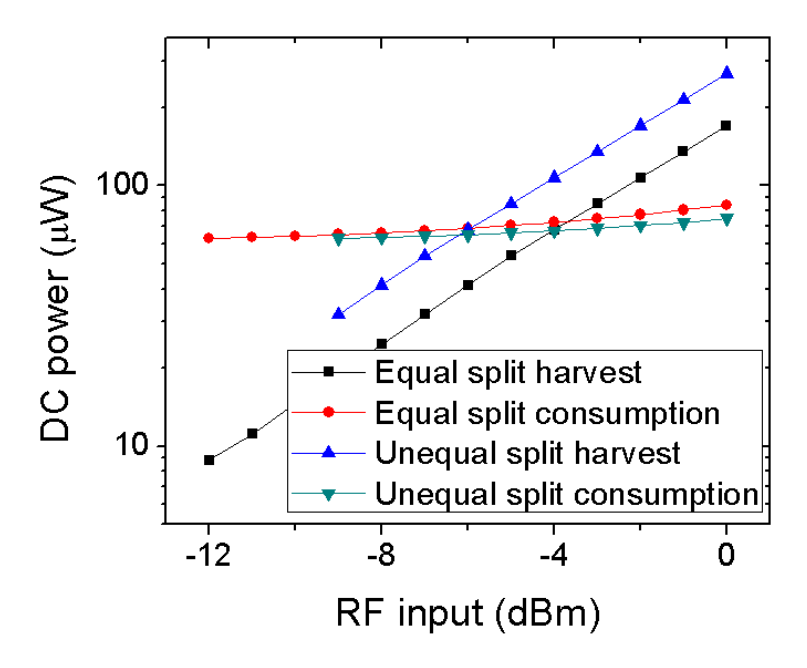


Figure 3.22: Total power consumption and harvest for equal and unequal power splitting.

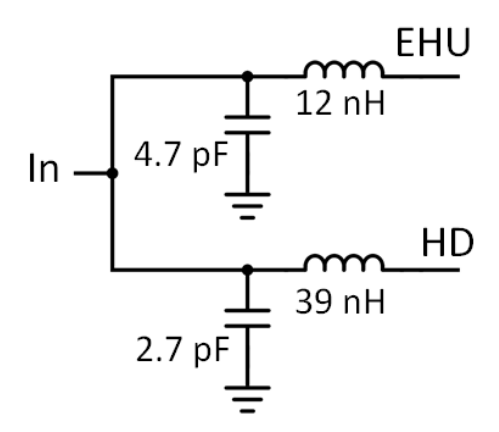


Figure 3.23: Power splitter design with unequal power division.

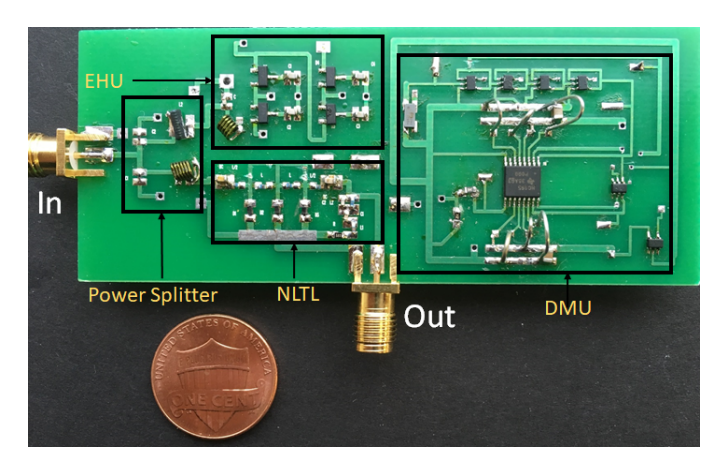


Figure 3.24: The tag circuit photograph with different components as compared to a penny.

power splitting. In the first case, the PS divided RF signal equally to the EHU and HD. Whereas in the second case, the EHU received 6 dB more power compared to the HD. Both the cases were plotted in Fig. 3.22 and it can be noted that the unequal power splitting activated the tag at 3 dB less power compared to equal power splitting. However, due to unequal splitting, the HD received 4 dB less RF input signal compared to equal splitting, which means the generated output harmonic power would be lower for unequal splitting, which was compensated by increasing the LNA gain in the interrogator.

The PS was designed as shown in Fig. 3.23 for unequal division. Load impedance of 50Ω at (f_0) was considered at all input and output ports of the PS design. After the design and measurement validation of each component, the complete tag was assembled on a printed circuit board (PCB) using surface mount discrete components. A photograph of the completed tag circuit is shown in Fig. 3.24. Antennas were attached with the tag circuit using SMA connectors to form a complete harmonic RFID tag.

Table 3.2: Comparison with other work reported in literature.

Ref	Technology	Architecture	ID	Frequency	Min. Input	Read Range
				Band	Power	
[1]	Microcontroller	Harmonic RFID	Yes	915 MHz-	0 dBm	NA
				1.8 GHz		
[85]	Microcontroller	Single frequency RFID	Yes	915 MHz	0 dBm	4.5 m @ 30 dBm
						transmitted
[86]	0.13 μm CMOS	Single frequency RFID	EPC Gen2	915 MHz	-14 dBm	7 m
[87]	Schottky diode	Harmonic RFID	No	1.2 GHz-	NA	40 cm @ 8 dBm
				2.4 GHz		transmitted
[88]	0.35 μm CMOS	Single frequency RFID	Yes	900 MHz	-18.5 dBm	4.5 m @ 4 W EIRP
					$Q I_{load} = 1.5 \mu A$	transmitted
[89]	NA	Single frequency RFID	Yes	900 MHz	-22 dBm	NA
This work	Discrete component	Harmonic RFID	Yes	434 MHz-	-6 dBm	1.8 m @ 18 dBm
				868 MHz		transmitted and 7.2 m
						@ 30 dBm projected

3.3.3 Reader design

An interrogator was developed as shown in Fig. 3.25 to read out the ID from the harmonic RFID tag. A stable frequency synthesizer was used to generate the 434 MHz (f_0) signal. The (f_0) signal was amplified at 18 dBm using a power amplifier (PA). As the receiver works at the second harmonic $(2f_0)$ frequency, it was important to mitigate the transmission of harmonics, which were generated from the PA. Hence, a low-pass filter with a cut-off frequency of 500 MHz was used at the output of the PA and before antenna element. When a harmonic tag is activated within the illuminated area it sends back the modulated $(2f_0)$ signal to the interrogator. Once the interrogator receives the harmonic $(2f_0)$ signal from a tag, the signal is passed through a high-pass filter to eliminate the clutter at (f_0) . It should be noted that the reduction of coupling between the receiving and the transmitting antenna at both (f_0) and $(2f_0)$ enhances the SCR, antenna performance, and the maximum detectable range. Hence, in addition to the filters and narrowband antennas, the transmitting and receiving antennas were aligned in a cross-polarization position in both tag and interrogator to further minimize coupling. The received RF signal at $(2f_0)$ was then amplified using an LNA with 34 dB gain before feeding it to an envelope detector. As the returned harmonic power has a weak signal, a sensitive detector diode was used for the envelope detection. In the subsequent stage, an RC low pass filter was used to obtain only the low-frequency ID signal to remove the high-frequency RF signal. Once the time domain demodulated sampled data is acquired from a digitizer, sample averaging is performed followed by pulse shaping to obtain the digital ID bits.

3.3.4 Wireless measurement

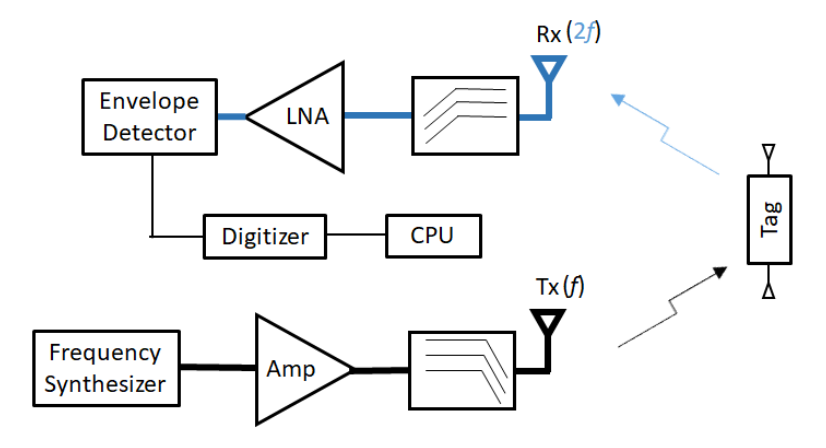


Figure 3.25: Integrated interrogator system.

After assembly of the board, the harmonic tag was programmed with an ID sequence of '01100101' and kept at a distance of 1.8 meters from the interrogator for the measurements. Different processing stages of the demodulated received signal are shown in Fig. 3.26. The SNR of the signal improved once it was averaged over 100 points. The pulses were shaped to logic levels after comparing them to the zero crossing voltage value, which was dynamically assigned from the average of 'high' and 'low' level of voltage magnitudes.

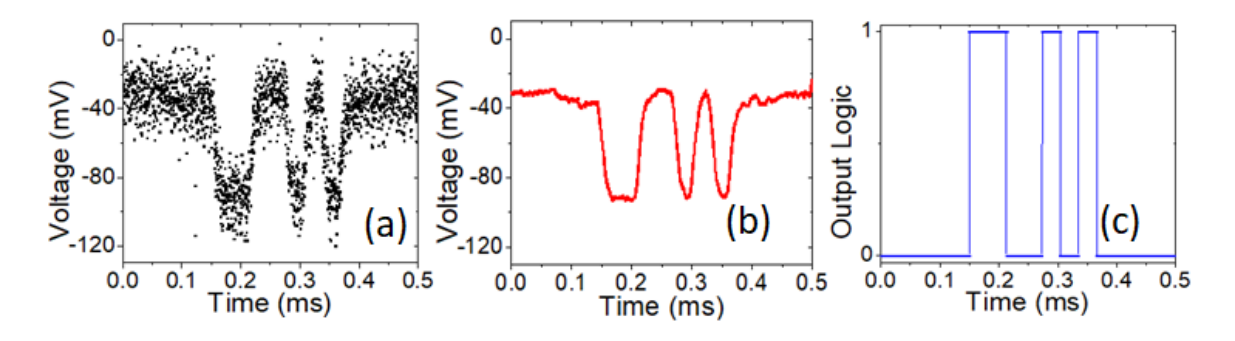


Figure 3.26: Demodulated received signal (a) after digitization, (b) after averaging, and (c) after pulse shaping and bit recovery.

3.4 Harmonic RFID: Gen II

Although the Gen I tag satisfied all the functional conditions, it had few disadvantages, which are prevalent in contemporary harmonic RFID tags. The reported harmonic tags have a major disadvantage of using multiple antennas or inefficient energy harvesting mechanism. Due to operation at two separate carrier frequencies for uplink and downlink communication, miniaturized compact antenna design is a challenge for harmonic RFID. The total antenna occupied area increases dramatically for multiple antennas [38,41]. The harmonic RFID tag was improved in Gen II version. The primary features of Gen II harmonic RFID system are:

- Gen II harmonic RFID tag has programmable and expandable memory for ID generation.
- Number of antenna at the tag was reduced to one. The reader still uses two antennas like in Gen I.
- This tag does not require extra RF power splitter. Hence, the number of functional components is reduced.

Apart from antenna design, harmonic RFID tag circuit configuration also needs to be improved for enhanced harvested power. In RFID operation, the modulation is performed by periodically changing the antenna impedance, shorting for one state and matched termination for the other state. When the antenna is shorted, no RF energy enters in the tag and hence the tag requires a latency time for sufficient energy harvesting before starting modulation. In other harmonic RFID tag configuration, reflection mode harmonic back-scattering was used similar to conventional RFID, where the entire RF energy is directed towards the harmonic generator at one of the modulation states [1]. In both cases, the energy harvester does not harvest for one of the modulation states. The clock speed for modulation can be increased or additional energy hungry operation such as sensing or computation can be included within the tag circuit by harvesting energy during both the modulation states.

In this work, a compact single antenna based harmonic tag is proposed, which can harvest RF energy during entire modulation period. As the development was primarily done for tag circuit, development of Gen II tag is only discussed here. The harmonic tag has two components 1) antenna and 2) tag circuit. The block diagram and the fabricated tag design is shown in Fig. 3.27. First, the dual frequency compact antenna design procedure and response is shown. In following, detailed design of NLTL integrated energy harvester as a harmonic RFID tag is discussed.

3.4.1 Antenna

The design procedure of the dual frequency antenna is described step by step in this section. One primary objective of the antenna design is miniaturization. Among different techniques, meandering is a popular choice for miniaturized antenna from design perspective [78]. However, a dipole antenna usually starts to show as a narrow-band behavior with increase

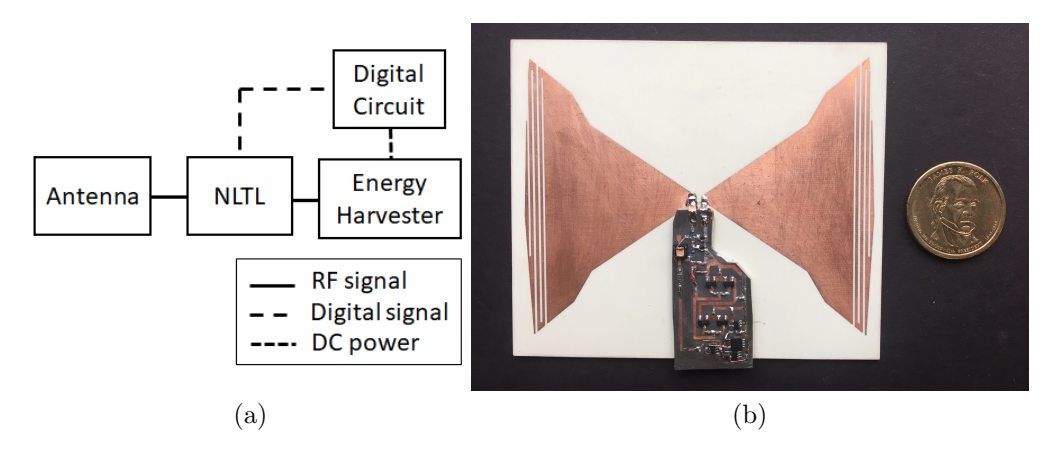


Figure 3.27: (a) The block diagram and (b) fabricated part of the single antenna harmonic tag.

in meandering [79]. Now, if the responses at both fundamental and harmonic frequency are narrow-band, with a frequency shift due to fabrication tolerance, the new narrow-band harmonic resonance may not be exactly twice of the new narrow-band fundamental resonance. Hence, making one of the two resonance frequency wide-band will minimize the issues from fabrication tolerance. The harmonic frequency was chosen for the wider band resonance for a compact tag size. First, a simple bow-tie was designed at the harmonic resonance frequency. In the next step, meandering was performed at the side edges of the bow tie until a second resonance is observed at the fundamental frequency. Finally, the design was fine tuned to obtain good matching at both fundamental and harmonic resonances. However, it should be noted that although the meandering will create a second resonance, the radiation will not be efficient at that frequency. As meandering is performed to miniaturize the antenna at low frequency, the bandwidth at low frequency is very narrow.

The antenna design starts with a simple bow-tie as shown in Fig. 3.30(a). A planar feed is added to connect the circuit with the antenna. First the bow-tie is optimized for a broad-band response at the harmonic frequency of 900 MHz. At this stage, the antenna has bandwidth of 110 MHz with center frequency at 900 MHz from the simulation result.

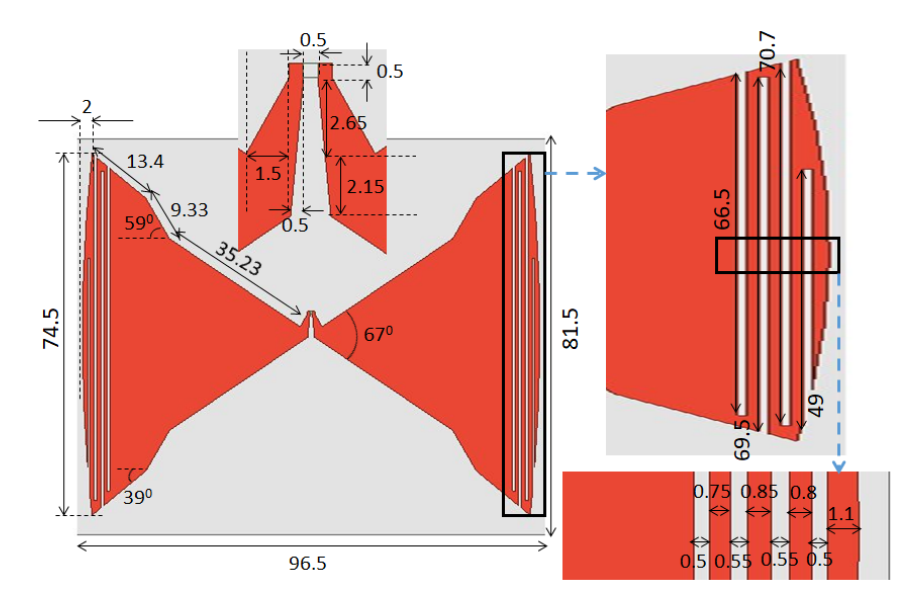


Figure 3.28: Dual frequency designed antenna. All the dimensions are in mm .

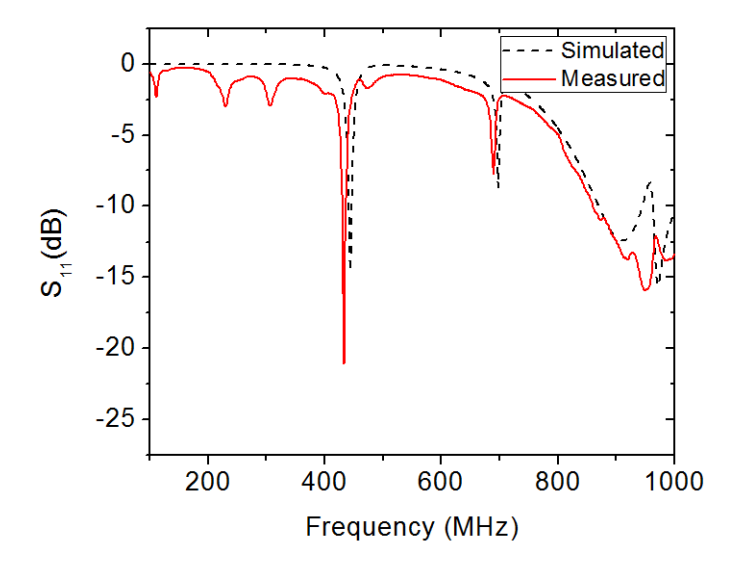


Figure 3.29: The reflection co-efficient of the dual frequency antenna.

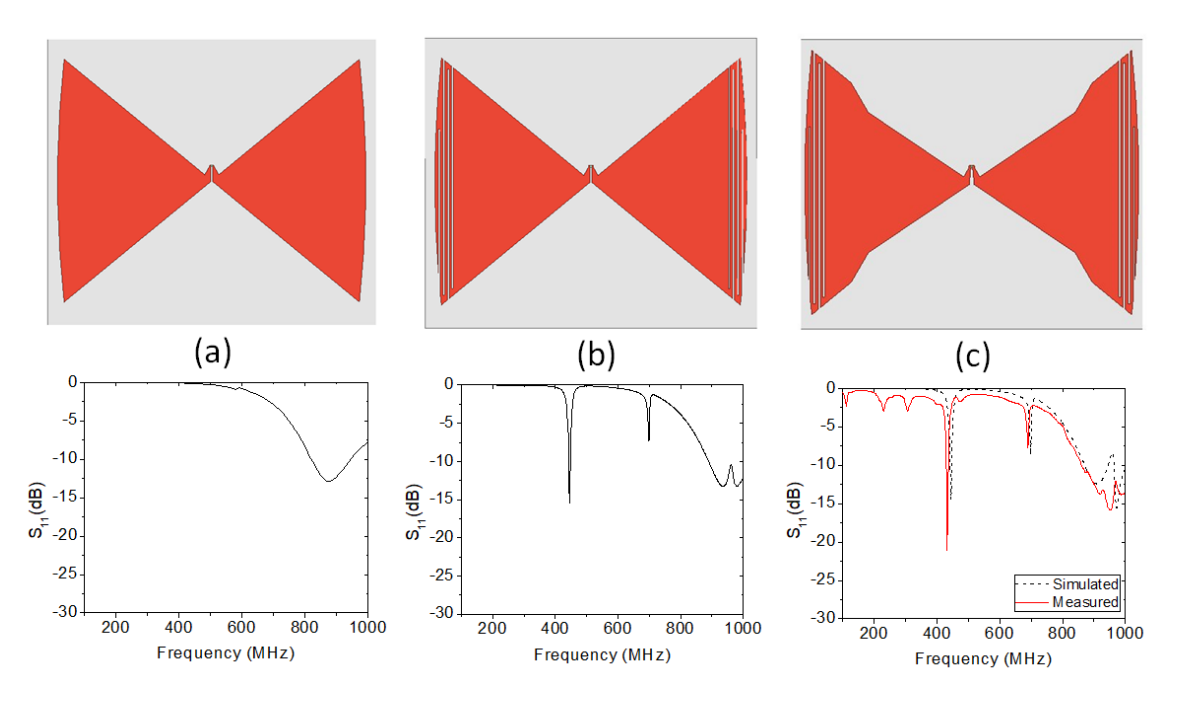


Figure 3.30: The step by step procedure for dual frequency single antenna design.

In the consecutive step, slits are cut at the ends of the bow tie to provide effective line length for the fundamental resonance frequency as shown in Fig. 3.30(b). As shown in reflection co-efficient response, the harmonic resonance frequency remains almost unaltered for structure in Fig. 3.30(b) due to negligible edge current at harmonic frequency. At fundamental frequency, the new resonance frequency is obtained at 445 MHz. At this stage, the antenna has bandwidth of 5 MHz with center frequency at 445 MHz and bandwidth of 70 MHz with center at 935 MHz. The shift of harmonic resonance frequency center is due to the slits. At the final stage, the antenna was fine-tuned as shown in Fig. 3.30(c) to obtain desired fundamental and harmonic frequency response with center at 445 MHz and 890 MHz respectively. The simulation was performed using HFSS by ANSYS to validate the final design before fabrication.

In Fig. 3.29, the simulation and measured results are shown for the designed antenna as in Fig. 3.28. Simulation was performed using Ansys HFSS and the antenna was fabricated on

top of Rogers RO4350 board using standard lithography process as outlined in APPENDIX B. Due to fabrication tolerance, the fundamental resonance frequency has shifted by 11 MHz. As 70 MHz bandwidth was considered at the designed harmonic resonance, with the fundamental resonance frequency shift, the antenna still resonates at the harmonic of the new fundamental resonance. the post-fabrication final working pair of fundamental and harmonic frequency pair are at 434 MHz and 868 MHz respectively.

3.4.2 Tag circuit

The tag circuit primarily has three components: 1) Energy harvester, 2) Nonlinear Transmission Line (NLTL), and digital circuit. NLTL can be realized by periodically arranged inductor and varactor diodes with detailed design procedure as demonstrated in [41]. The NLTL generates multiple harmonics when interrogated by a single frequency RF signal under activation due to the nonlinear varactor diodes. In Fig. 3.31 the NLTL response with multiple stages and different bias conditions is shown.

When measured using a VNA, the NLTL with different number of stages show a broadband response from 100 MHz to 1 GHz. The broadband response remains unaltered ($S_{11} \le$ -10 dB) upto 900 MHz for a two stage NLTL under forward bias condition from 0 V to 0.6 V as shown in Figs. 3.31(a) and 3.31(c). At 0 V bias, the transmission loss in 2-stage NLTL is primarily due to lossy inductors. When the NLTL is driven at forward bias condition, due to sub-threshold conduction of the varactor diodes, the NLTL starts behaving as a lossy line and the transmission loss increases with increase in bias as shown in Fig. 3.31(d). Additionally, the loss also increases with higher number of NLTL stages at higher applied bias. The purpose of applying DC bias is to generate strong harmonics from the NLTL. In Fig. 3.32(a), the conversion loss for different number of NLTL stages is shown. The maximum harmonic

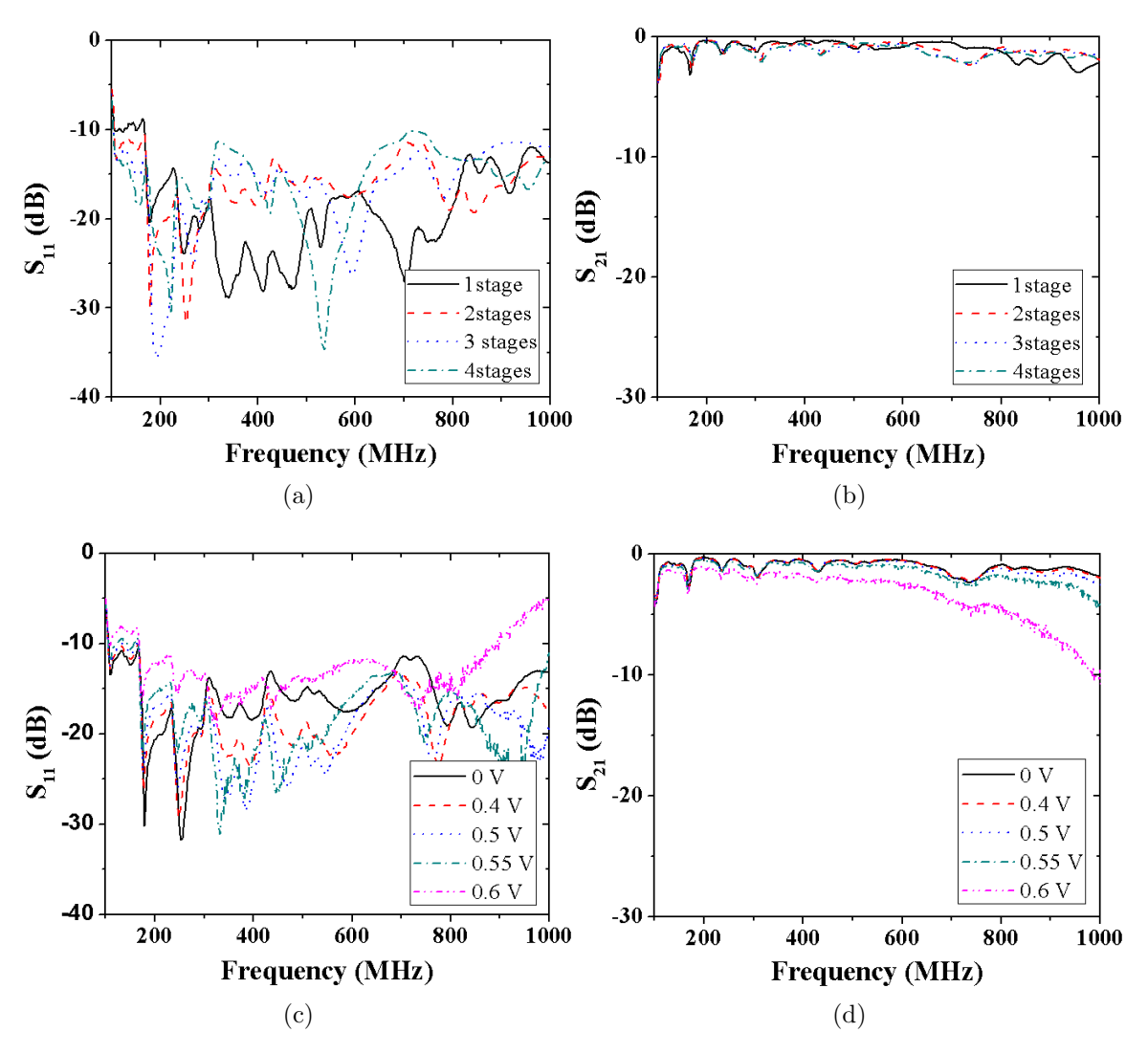


Figure 3.31: Measured results for (a) S_{11} and (b) S_{21} for different number of NLTL stages at no bias condition; (c) S_{11} and (d) S_{21} for two stage NLTL at different bias.

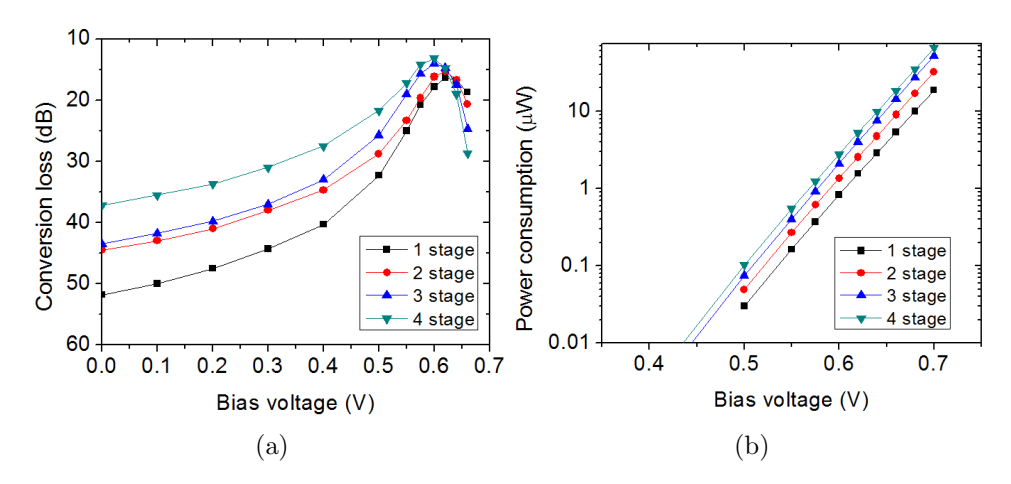


Figure 3.32: Measured results for (a) conversion loss and (b) DC power consumption for different number of NLTL stages.

is generated close to 0.6 V and the the conversion loss increases with reduction or further increase in bias voltage. Due to forward biasing, the NLTL consumes very small amount of DC power and the power consumption for different number of NLTL stages is shown in Fig. 3.32(b). Based on the power consumption, conversion loss, component requirement, and transmission characteristics, 2-stage NLTL was chosen for the tag circuit.

However, the broadband behavior of the NLTL changes when it is terminated with the energy harvester in place of a 50 Ω load. Impedance matching is required for the energy harvester at the fundamental and harmonic frequency regions for the desired matching of the NLTL at both operating frequencies. This deign approach helps in realizing two objectives: 1) replacement of the 50 Ω load, and 2) energy harvest while modulation. When the 2-stage NLTL is at 'off' state or under 0 V bias condition, the measured S_{21} is -1.2 dB and at 'on' state or 0.55 V bias the S_{21} is -1.21 dB at 434 MHz. Hence, the energy harvester is receiving almost same amount of input power at both the modulation states. A 10 stage Schottky diode based charge pump configuration was used for energy harvesting as described in detail in [41]. The reflection co-efficient of the energy harvester only and energy harvester

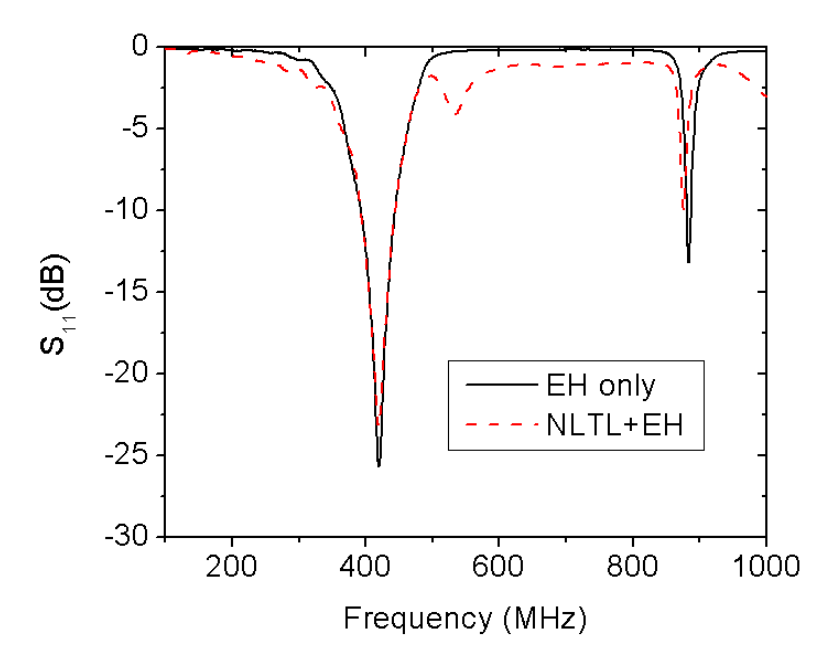


Figure 3.33: Measured reflection co-efficient of the energy harvester with and without NLTL.

coupled with NLTL is shown in Fig. 3.33. In both cases, good matching is observed at 434 MHz, at which the energy harvesting is performed. The DC power harvested by energy harvesting unit is consumed by the digital circuit for generating the ID. A low power voltage regulator was used in between the energy harvesting unit and digital circuit. The major part of the digital circuit is microcontroller (MC), which was programmed for the bit sequence to generate the modulation. The voltage level from the MC output was level shifted by series diodes to the NLTL realizable voltage level.

3.4.3 Wireless measurement

Once the tag was designed and fabricated, wireless measurement was performed to find the maximum operable range of the harmonic RFID tag. Reader circuit as described in [41] was used to retrieve the information or ID from the harmonic tag. The reader transmitted 30 dBm of power at 434 MHz in continuous mode. A separate antenna was used to receive the harmonic power at 864 MHz at the reader. The output power is visualized directly in an

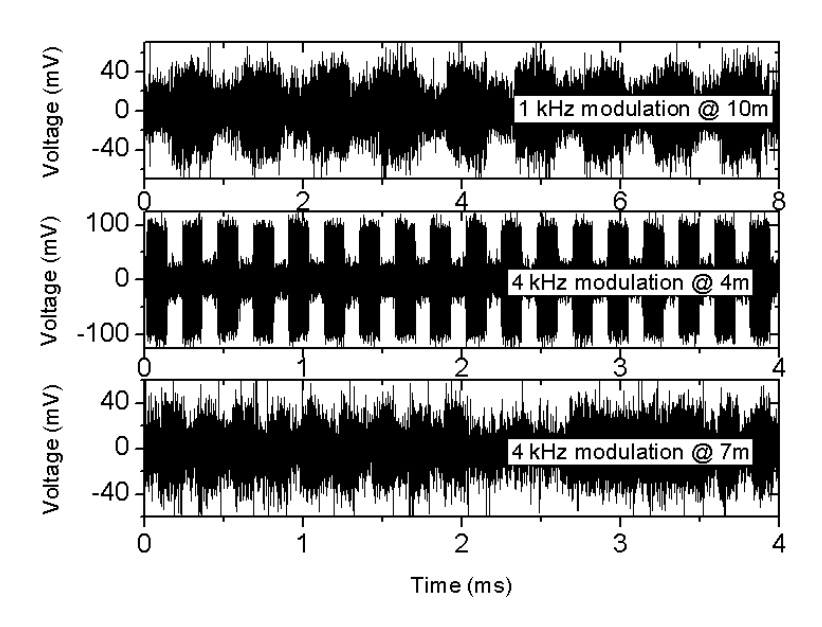
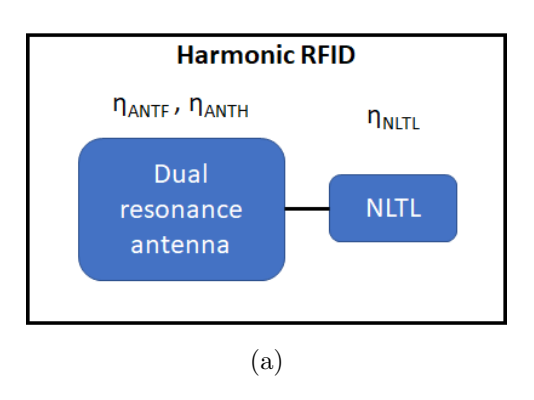


Figure 3.34: Measured harmonic voltage at different distance and modulation frequency.

Oscilloscope after the amplification of the harmonic power received from the tag. The power consumption in the MC is directly related to the frequency of the operating internal clock. To show that the tag is capable of harvesting during both the modulation cycles, the MC was programmed for periodic bit stream of '1' and '0' continuously. In the first experiment, the internal clock was set at 32 kHz, which corresponds to 1 kHz of data modulation frequency. At this clock, the current consumption of the MC was 17 μ A at 3 V bias. With this setup, the tag could operate at 10 m from the reader. The demodulated harmonic periodic signal is shown in Fig. 3.34. In the next part of experiment, the MC was programmed at 125 kHz internal clock, which corresponds to 4 kHz of data modulation. The sequence of bit-stream '1' and '0' was kept same as earlier. At this clock rate, the power consumption went up significantly higher at 109 μ A at 3 V bias. Due to increased power consumption, the tag could perform the modulation as expected upto 4 m from the reader. When the distance was increased to 7 m, the bit error rate increased significantly within MC due to significant increase in power consumption. The demodulated harmonic signal is shown in Fig. 3.34 at



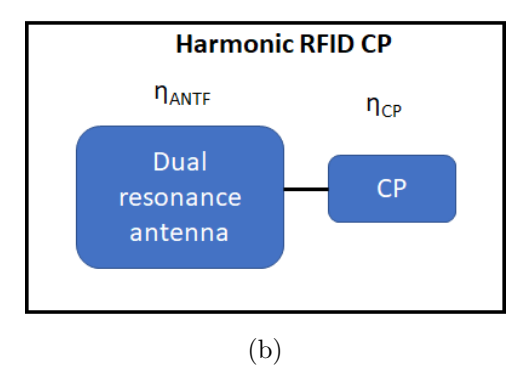


Figure 3.35: Efficiency calculation block diagram of harmonic RFID for (a) harmonic efficiency and (b) energy harvester of charge pump.

4 kHz data modulation for both at 4 m and 7 m. The tag is deactivated completely once the distance in increased further at 4 kHz of data modulation. As expected, the read range decreases with higher clock rate operation as the power consumption dominates over the power harvest.

3.5 Harmonic RFID Tag Efficiency

The harmonic RFID tag has multiple components and the overall efficiency analysis of harmonic generation is also required. The efficiency of NLTL and different antennas has been shown earlier separately. The cumulative efficiency of the harmonic RFID tag is shown in Fig. 3.35 with individual efficiency of antenna, energy harvester charge pump (CP), and harmonic generator. The individual efficiency of antenna at fundamental frequency is given as η_{ANTF} , at harmonic frequency as η_{ANTH} , CP efficiency as η_{CP} , and NLTL efficiency as η_{NLTL} . The cumulative efficiency of the harmonic generation system will be $\eta_{ANTF} \times \eta_{NLTL} \times \eta_{ANTH}$. Also, the harvesting efficiency should be enough in parallel, so that the computation part of the tag can generate the modulation signal. The cumulative efficiency of the antenna and CP system will be $\eta_{ANTF} \times \eta_{CP}$. A harmonic RFID tag has

a minimum sensitivity of P_{sen} , below which the tag is not activated. If the received power of harmonic RFID is P_{in} , then the cumulative efficiency of the harmonic RFID tag will be $\eta_{ANTF} \times \eta_{NLTL} \times \eta_{ANTH}$, provided that $(\eta_{ANTF} \times \eta_{CP} \times P_{in} > P_{sen})$.

3.6 Harmonic RFID Performance Under Clutter

After development and testing of the harmonic tag, efficacy of Gen I harmonic tag performance over single frequency commercial tag was tested. First, performance of commercial tag under clutter is measured. M6E Nano UHF RFID reader (-80 dbm RS) with circularly polarized antenna (8 dBi gain) was used to monitor the single frequency tag backscattered signal at 926 MHz. The reader internally generates 10 dBm of RF power, which was fed to the antenna through two circulators as shown in Fig. 3.36. Transmit power of 10 dBm was chosen for small area anechoic chamber requirement. To emulate the scenario of 30 dBm RFID transmit power, extra 20 dB attenuation was added to the tag emitted return signal. The 20 dB attenuation represents the extra 20 dB path loss. The complete setup as shown in Fig. 3.37 enables test experiment of 30 dBm transmit power within a small chamber. First, the dynamic range (DR) was quantized in terms of correct tag ID detection counts per second. With reduction in transmit power, the DR would decrease with fixed reader sensitivity and hence the detection rate would drop. Impinj Monza R6 UHF RFID tag was selected as commercial single frequency RFID tag for its high sensitivity (-22 dBm). The detection rate was measured with a=52 cm without any presence of reflectors as shown in Fig. 3.38. As the transmit power was decreased from 10 dBm to 5 dBm, the detection rate dropped from 15.67 counts/s to 2 counts/s. Once the DR was quantized, the effect of a reflector was measured in terms of detection rate.

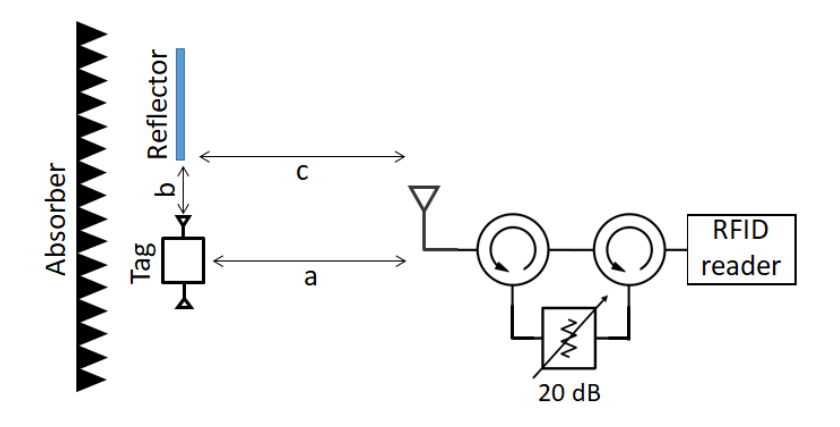


Figure 3.36: Measurement setup for performance comparison.



Figure 3.37: Measurement setup with commercial RFID tag at the center.

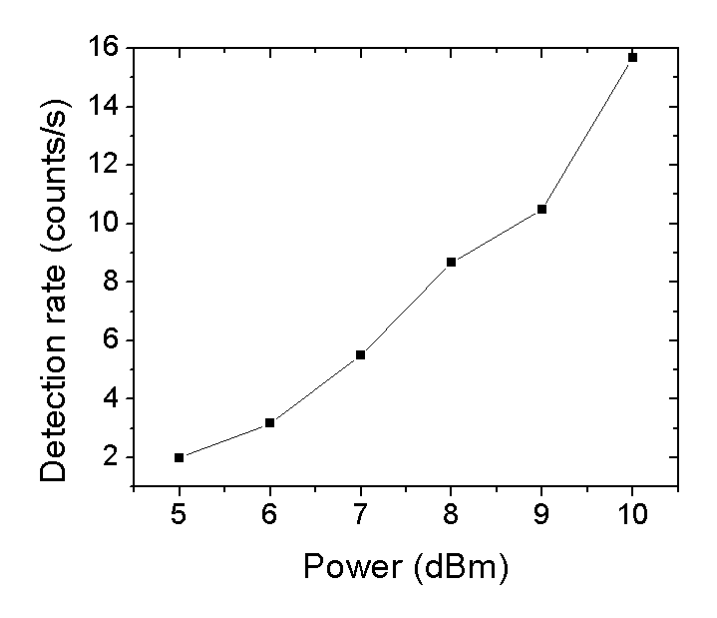


Figure 3.38: Correlation in between transmitted power and tag detection count.

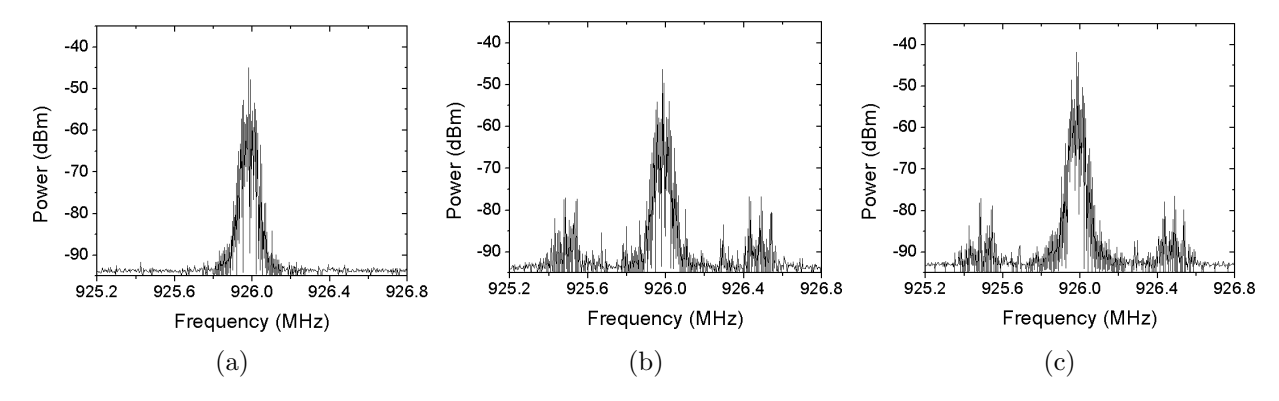


Figure 3.39: Power profile for 10 dBm transmitted power at 926 MHz with (a) no tag or reflector, (b) only tag is present, and (c) tag in presence of reflector.

The transmitted carrier signal was fixed at 10 dBm and 926 MHz for the measurements as shown in Fig. 3.39 and the return signal was measured using a spectrum analyzer at bandwidth of 1 KHz. When the tag is not present within the reader antenna's field of view, only the reader query modulation signal is visible as shown in Fig. 3.39(a). When the tag was kept at a=52 cm, the perturbation in power spectrum was clearly visible as shown in Fig. 3.39(b). The detection rate was found to be 15.5 count/s without any reflector. When a reflector of size (15 cm X 25 cm) was kept at b=10 cm and c=44 cm, the tag was still activated as shown in Fig. 3.39(c) but the detection rate dropped to no detection due to increased clutter level. The clutter from the reflector obstructed the RFID tag signal by dropping the DR level. However, it should be noted that the actual tag response signal is buried under the reader query signal as both of them operate within 500 kHz channel using time multiplexing. With the query and tag modulation signal superimposed on top of 926 MHz single tone, It is not possible to experimentally demonstrate only the single tone phase noise behavior as explained in Fig. 2.3 with the commercial RFID system. However, it can be noticed that the peak amplitude of the return signal is 4 dB higher in Fig. 3.39(c) compared to Fig. 3.39(b). The increase in peak power is due to the reflected signal from reflector analogous to Fig. 2.3.

Next, the clutter effect was measured on the designed harmonic tag. The tag and a square reflector (30 cm X 50 cm metal foil) was placed at a=104 cm, b=20 cm and c=88 cm using similar setup as shown in Fig. 3.36. The distances a, b and c were scaled according to the wavelength of operation. The RFID reader was replaced by a 434 MHz source and the reflected power from tag was monitored using an antenna resonating at 868 MHz at the source side. During the measurement, the transmitter power was set at 18 dBm at 434 MHz after power amplification. When no reflector was present, the read count was measured to be 2 count/ms. In presence of the reflector, the read count barely changed to 1.98 count/ms. The read counts were averaged with 10 measurements. When only the harmonic power was measured, it barely changed (<0.5 dB, within measurement error) in presence or absence of any reflector. This experiment clearly shows that an RFID operating at single frequency will suffer a decrease in DR due to increase in background clutter as compared to a harmonic RFID.

3.7 Summary

The design and implementation of a complete ultra-low power Gen I harmonic RFID tag with integrated antennas is demonstrated. The harmonic tag can operate at a minimum received signal strength of -6 dBm. A simple interrogator is also designed to demodulate the ID from the harmonic tag. A read range of 1.8 m was achieved with the transmitted power of 18 dBm. The read range can be extrapolated to 7.2 m based on one-way path loss with 30 dBm power transmitted while achieving good SCR of the return signal. As long as the tag can receive the minimum activation power (-6 dBm), it can generate the harmonic and the

weak harmonic signal can be amplified at the interrogator to compensate the return path loss. In comparison to tag designs reported in open literature, this tag provides superior performance with respect to read range while working in a cluttered environment. The read range can be further increased by using high gain antennas, high transmitted power, low power tag circuitry and a sensitive detector. The harmonic RFID tag system demonstrated here holds significant potential for a range of tagging applications.

A miniaturized Gen II single antenna based harmonic RFID tag is demonstrated next. With the use of a simplified design architecture, minimum number of components was used for the harmonic RFID. The design can be easily adopted by replacing the antenna modulation switch in conventional RFID with the harmonic generator NLTL. Another advantage of the proposed harmonic tag is continuous harvesting, which is not possible for existing single frequency RFID antennas. At 1 kHz data modulation by the harmonic tag, a read range of 10 m was achieved. However, the read range decreased when the data modulation rate was increased due to more power consumption. The circuit can be miniaturized by fabricating the complete circuit using a monolithic process. Harmonic RFID tags are useful for underground or biological applications, where the background clutter phase noise can dominate over tag return signal.

Gen I harmonic RFID tag was also demonstrated for its improved performance and was compared with a single frequency commercial state-of-the-art RFID tag in presence of strong clutter source. From the results, it was clear that even the conventional tag was activated in presence of reflector, the detection rate can drop due to poor SCR. On the other hand, the clutter signal had almost no effect on the harmonic tag. Hence, conventional single frequency tags would not be suitable for long range applications in presence of strong background clutter. The harmonic RFID tag would be useful for RFID applications in case

of self-jamming and also in cluttered environment such as underground object tagging, long range tag detection in an industrial set up with strong reflectors such a metal in the vicinity of the tag.

Chapter 4

RFID With Integrated Sensor

The various drawbacks of sensor integration with conventional RFID system are provided in Chapter 2. The most accepted platform for RFID integrated sensor system is wireless identification and sensing platform (WISP) [55]. Diverse range of sensors were integrated with the proposed RFID platform, light, temperature, camera, human activity, and neural signal to name a few [90–93]. In the proposed works, the analog output from the sensors is digitized and integrated with the ID bits of the RFID. A high level schematic of analog sensor integration with digital interface of ADC and microcontroller is shown in Fig. 4.1. In those architectures, primarily there are two major concerns: 1) power consumption at the tag, and 2) impact of quantization error on sensitivity. As the passive RFID tags are operated on harvested energy, it is very important to minimize the power consumption at the tag to maximize the read range of the sensor integrated RFID tags. Hence, the read range of sensor integrated RFID will be lower than the conventional RFID due to addition of ADC functionality. The power consumption of the ADC should be carefully monitored to keep the read range at a desired distance. Also, many times an impedance buffer is required between the sensor output and ADC input. This scenario particularly arises when an ADC within a microcontroller is used. The substantial internal microcontroller leakage path in between sensor output and ADC input leads to requirement of impedance buffer, which consumes further DC power. Another important scenario is quantization error, which arises due to

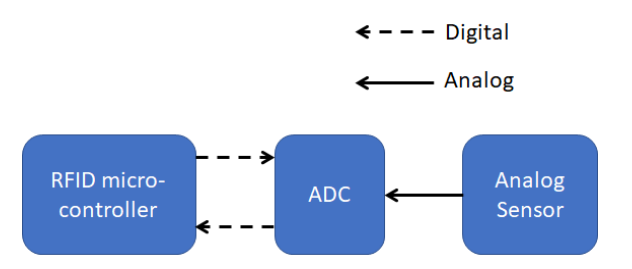


Figure 4.1: High level picture of analog sensor integration with ADC and microconroller.

analog to digital conversion. The quantization error leads to reduction of sensitivity of the sensor. To address this, either more conversion bits are to be used or the analog reference voltage level difference used for conversion should be reduced.

Among many applications of sensor integrated passive RFIDs, one major field is biosensing. With recent advancements in healthcare, now it has become possible to monitor many physical and chemical vitals of human body such as blood pressure, heart rate, glucose, pH, uric acid, specific cations such as sodium and potassium in sweat [94–97]. Wireless configuration of the proposed sensors are using either low energy bluetooth [97], or near field coupling based communication methods [95]. In this work, batteryless and wireless communication method of electrochemical pH sensor is proposed for biological applications.

4.1 Background

Batteryless wireless pH sensors received significant attention recently due to their longer shelf life, reduced cost, wireless measurement, and less hazardous as a body implant. Over the years, the need for wireless pH sensing has increased in healthcare due to ease of diagnosis of different potential medical conditions such as gingivitis, periodontitis or gastroesophageal reflux disease (GERD) by wirelessly monitoring pH of salivary or gastroesophageal fluid [98–101]. Additionally, continuous wireless pH monitoring has a huge potential to track

the quality of meat and fish based perishable products in cold food supply chain [102, 103]. In literature, multiple wireless methods have been proposed to track the pH [96, 101–105]. Coupled coil based resonance frequency shift method is quite popular among the wireless methods due to simple setup and least number of circuit components required. However, as the resonance frequency strongly depends on the mutual coupling in between the sensor and reader coils, the measurement accuracy depends on the orientation of the coils and hence requires an initial calibration [105]. The measurement setup also requires experienced personnel to interpret the sensor data accurately using instruments such as Vector Network Analyzer (VNA) or Impedance Analyzer (IA). As an alternative, digital modulation method is proposed in this work for pH measurement, which is less dependent on antenna coupling and is compatible with commercial UHF RFID technology. In digital modulation technique, the pH electrode voltage is converted into digital bits, which are transmitted wirelessly [96, 101]. In digital systems, identification (ID) can be integrated easily along with the sensors, which is an integral component to distinguish among similar objects. In Fig. 4.2, a scenario is shown where more than one identical pH sensor tags are present. The handheld interrogator sends a RF signal, and the sensor tags reply with different IDs. Without the physical ID, it will be very difficult for a machine to separate the data from identical sensors. However, digital modulation requires a DC power supply module to drive the modulation circuit, which makes the sensor design and reader setup complicated. In this batteryless pH sensor, the battery is replaced with an energy harvesting circuit to make the pH sensor compatible as a body implant, because the hazardous chemicals can be harmful in case of battery leakage [106].

Apart from different sensing methods, different types of pH electrodes are also well researched. pH is quantified as the H⁺ ion concentration within a fluid environment and is

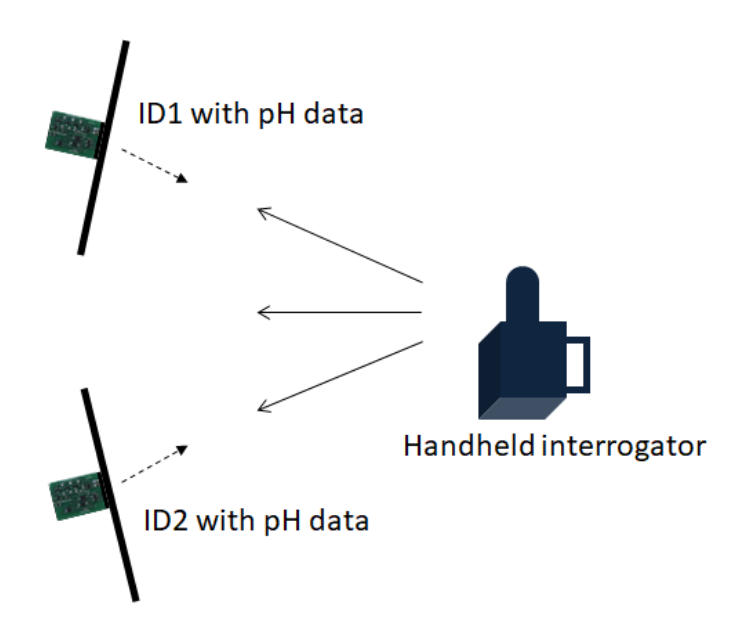


Figure 4.2: Interaction of a handheld reader with identical pH sensors with different IDs.

electrically measured using a combination of reference electrode and a pH sensitive electrode. Double junction glass electrodes are commonly used due to high linearity and stability over a wide pH range (0-14). However, the glass electrode fabrication is not compatible with standard photolithography, making it difficult to integrate the sensor with standard CMOS process. Hence, a combination of different type of metal oxide electrode with silver/silver chloride (Ag/AgCl) reference electrode was developed to fabricate pH microelectrodes along with solid state readout circuit. In literature, different type of pH sensitive electrodes such as iridium oxide, antimony oxide, mixed metal oxide, carbon nanotube are reported [104, 105, 107]. Among these, iridium is a costly transition metal and carbon nanotube electrode requires complicated fabrication process. Hence, a cost effective antimony/antimony oxide (Sb/Sb₂O₃) electrode was chosen for the pH sensor design.

In this work, we first present the design, fabrication and characterization of Ag/AgCl and Sb/Sb₂O₃ based combination pH electrodes along with the sensor readout electronic circuit. In next section, the design and fabrication of pH electrodes and sensor tag circuit is

discussed. Next, the measurement results are shown to demonstrate a fully working wireless ID integrated pH sensor and finally a potential application of this work is demonstrated.

4.2 Design and Fabrication

The measurement system consists of two main parts: 1) a pH sensor electrode pair with an electronic readout circuit, and 2) an RF interrogator to wake up the digital sensor and extract the ID and sensor information wirelessly. First, the working principle of the complete system is presented. Then, the pH electrode fabrication process is described followed by the design of the readout circuit.

4.2.1 RF interrogator

The RF interrogator is required to activate the sensor wirelessly and extract the sensor data. The RF source generates a continuous RF signal at 900 MHz, which is split equally in two branches using a power splitter. One signal branch is power amplified and transmitted through an antenna resonating at 900 MHz. A meandered dipole antenna from [41] is used for this purpose, which has reported gain of 2.1 dBi in simulation using Ansys HFSS. Once the sensor replies back with the modulated RF signal, the reply signal is mixed with the other signal branch in a RF mixer to demodulate the sensor signal. The RF circulator enables the transmission of continuous RF signal and reception of the modulated signal using a single antenna. A baseband amplifier with 26 dB gain and a cut-off frequency of 150 kHz was used to further amplify the low power demodulated signal with high frequency spurious signal rejection before feeding it to the scope. The block diagram of the complete setup is shown in Fig. 4.3.

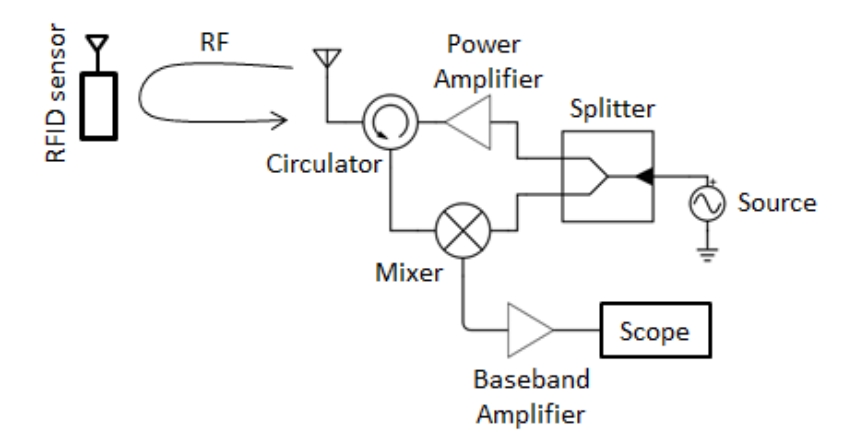


Figure 4.3: The block diagram of the measurement setup with an interrogator and the RFID sensor.

4.2.2 Readout circuit

The electronic readout circuit at the sensor consists of two major parts: 1) an RF front end with antenna for energy harvesting, and 2) a digital back end to process the analog sensor signal into digital bit sequence and to generate the ID. The RF communication works at 900 MHz UHF RFID frequency. When the sensor tag receives RF power, it first harvests the RF energy and converts it into DC for biasing in order to drive the sensor and the digital circuit. HSMS 2852 low barrier Schottky diode is used to harvest energy from the incoming RF signal. Six diodes are used in a Dickson charge pump configuration to boost up the DC voltage at desired level. The details of the charge pump rectifier circuit design is provided in our earlier work [41]. The generated DC voltage is rectified using a low power voltage regulator (TPS79730) at 3 V to drive the digital circuit. The schematic of the electronic readout circuit is shown in Fig. 4.4. A low power compact microcontroller (PIC12LF1822) is used to generate the digital ID sequence. An ADC is required to convert the analog voltage generated by the electrode pair into a digital bit stream. The use of internal ADC within the microcontroller was avoided as the DC current consumption increases by 335 μA upon

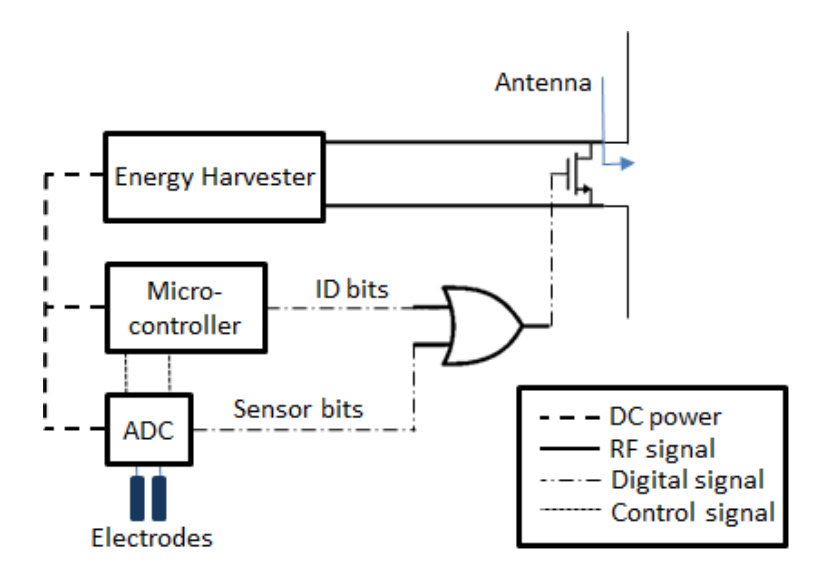


Figure 4.4: The sensor voltage readout digital circuit with ID generation.

the ADC activation. Hence, an external ultra-low power 8 bit SAR ADC (ADS7040) is used. Apart from ID, the microcontroller also generates the control signals for the ADC. Finally, a low power 'OR' gate (SN74AUP1G32) is used to combine the ID and the ADC bits into a single channel. Once the digital circuit generates the single channel digital bit sequence, a high frequency switch (BF1105R) is used to modulate the antenna impedance according to the digital bit sequence [108]. A detailed analysis is shown in Chapter 1 about the choice of two impedance states for good modulation depth at the reader. Based on the analysis, 50 Ω and 0 Ω were chosen across the tag antenna load for digital '0' and '1' modulation depth. The modulation is captured at the interrogator and the digital bit is demodulated for pH measurement.

4.2.3 pH sensor fabrication

The pH electrode pair consists of one Ag/AgCl electrode and another Sb/Sb₂O₃ electrode, fabricated on top of a 0.38 mm thick flexible PTFE Rogers RT/duroid 5880 board. PTFE

based substrate is chosen as it has a very low moisture absorption (0.02%) capacity. Hence, the effect of potential change due to the solution in contact from the backside of the electrode is negligible. At the initial step, the copper metal on top of the substrate was patterned and etched to create a 'T' shaped backbone interconnect for the electrodes. Between the two electrodes, Sb/Sb₂O₃ electrode was fabricated first since it requires a high temperature oxidation process. S1813 negative photoresist from Shipley was patterned to create an inverse mask for a subsequent lift-off process. A 6 nm thick titanium (Ti) layer followed by a 2.5 μm thick Sb layer was sputter deposited on top of the substrate. The thin Ti layer helps in better adhesion of Sb layer to the substrate. After deposition, lift-off process was followed to remove the unwanted Sb layer. The selectively deposited Sb metal was oxidized using a Nordon March RIE 1701 at 99% oxygen concentration followed by annealing. The annealing process was performed by ramping the temperature from 100 °C to 300 °C in 3 equal steps with 10 minutes time duration at each step. Rapid and high temperature heating was avoided to prevent forming of cracks in the thin continuous Sb film due to thermal stress. The process of oxidation followed by annealing was performed twice for obtaining a thicker oxide layer. As shown in Fig. 4.9(b), the antimony electrode surface becomes uneven during heat treatment. Hence, a thicker oxide will reduce the possibility of leaving an oxide layer defect.

The Ag/AgCl electrode was fabricated next on the other half of exposed copper backbone. Ag was deposited in similar way by sputter depositing a 2.5 μ m thick Ag layer on the inverse photoresist mask followed by a lift-off process. A thin layer of AgCl was formed on top of the Ag electrode using an electrochemical chlorination. In the chlorination process, 2 V was applied at the Ag electrode with respect to a Pt cathode of 0.5 mm diameter for 50 s in a 0.1 M potassium chloride (KCl) solution. The Ag/AgCl electrode was then heated at 90 °C

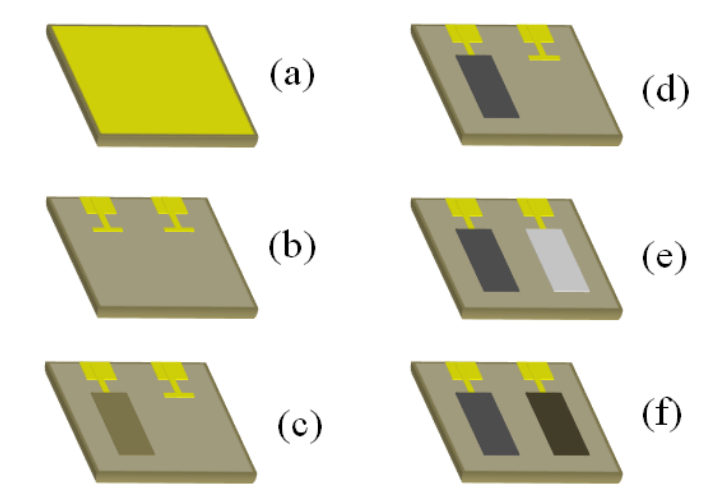


Figure 4.5: Fabrication procedure of pH combination electrodes a) Cu plated RT/duroid 5880 substrate; b) patterning of Cu layer to create 'T' shaped Cu backbone interconnect; c) sputtering followed by lift-off of Sb metal; d) oxidation of Sb layer; e) sputtering followed by lift-off of Ag metal; f) chlorination of Ag layer.

for 20 minutes to allow a uniform diffusion of chloride ions. Following the AgCl deposition, the electrode was dip-coated with a protective Nafion layer by dipping in 5% Nafion solution of Methanol (Liquion-1105-MeOH) from Ion Power for three times to create a thick layer. After dip coating, the electrode pair was dried at 110 °C for 1 hour in a vacuum chamber to evaporate away methanol [109]. Nafion was chosen for its ion exchange selectivity as it allows the H⁺ cations to pass through but prevents Cl⁻ anions to migrate from the electrode. The complete fabrication process of the electrodes is described in Fig. 4.5.

The contamination of thin Ag or Sb layer can happen by interdiffusion of Cu atoms from the underlying layer [110]. Additionally, as the Ag layer or Sb layer is very thin, irregularity in the deposition can create small pockets, through which the electrolyte can directly interact with Cu layer, and thus can change the desired potential. Hence, a continuous Cu backbone layer was avoided beneath the electrodes. Detailed elemental analysis of the pH electrodes is demonstrated later.

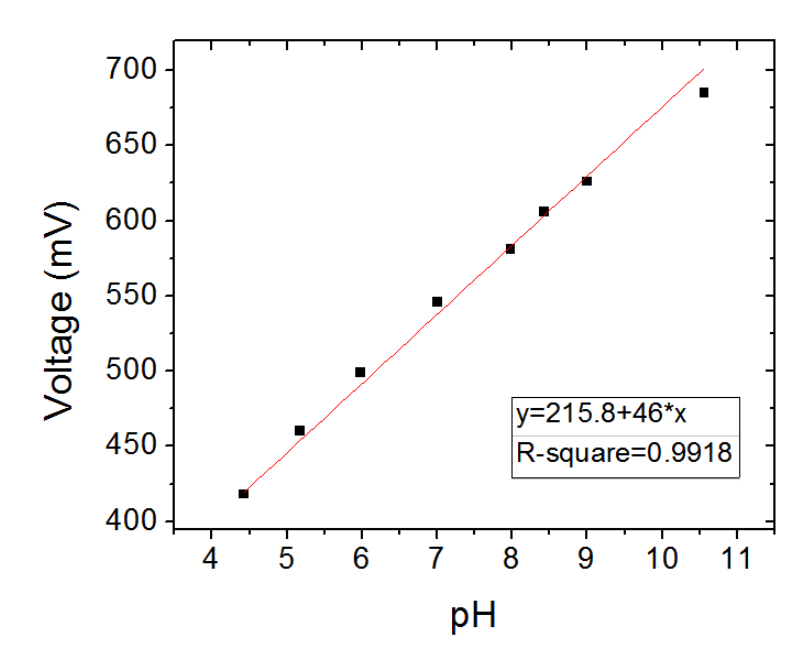


Figure 4.6: Voltage response of the fabricated electrode in different pH solutions.

4.3 Results

4.3.1 Electrode performance

The pH electrode pair performance was characterized in terms of 1) stability, 2) repeatability, 3) sensitivity, and 4) response time. The output voltage was measured from the electrode pair using a digital multimeter with an input impedance of 2 M Ω . The voltage reading from the multimeter was acquired using LabView. All the buffer solutions used for pH measurement were prepared using proper mixture of Potassium diHydrogen Phosphate (KH₂PO₄) in water with 0.1 M Sodium Hydroxide (NaOH) solution. The pH of all the buffer solutions were measured using a commercial pH meter (Checker plus HI98100) from Hannah Instruments.

First, the linearity and sensitivity of the electrode pair were measured. The pH of the buffer solution was varied from 4.3 to 10.7 and the output voltage was measured as shown

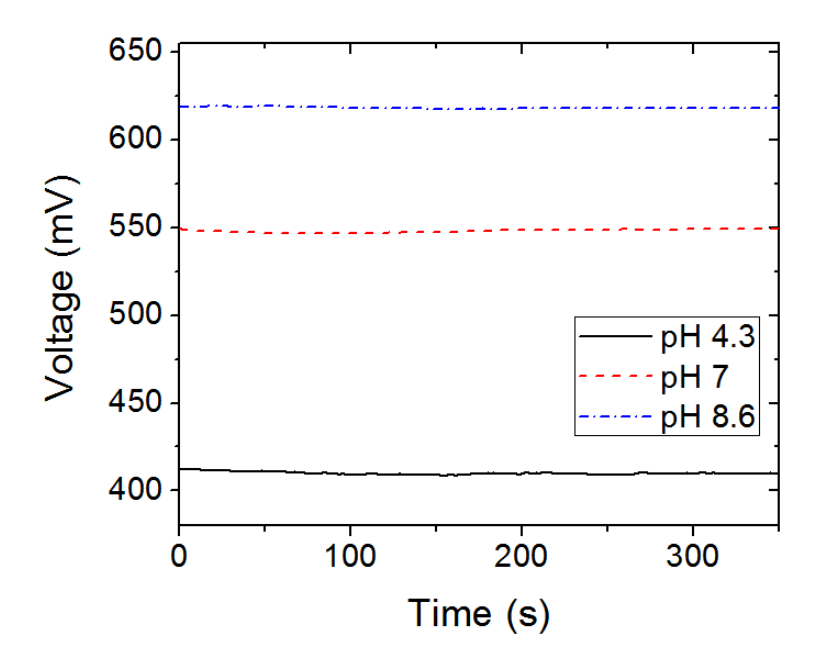


Figure 4.7: Stability of the voltage response of the electrode in different pH solutions.

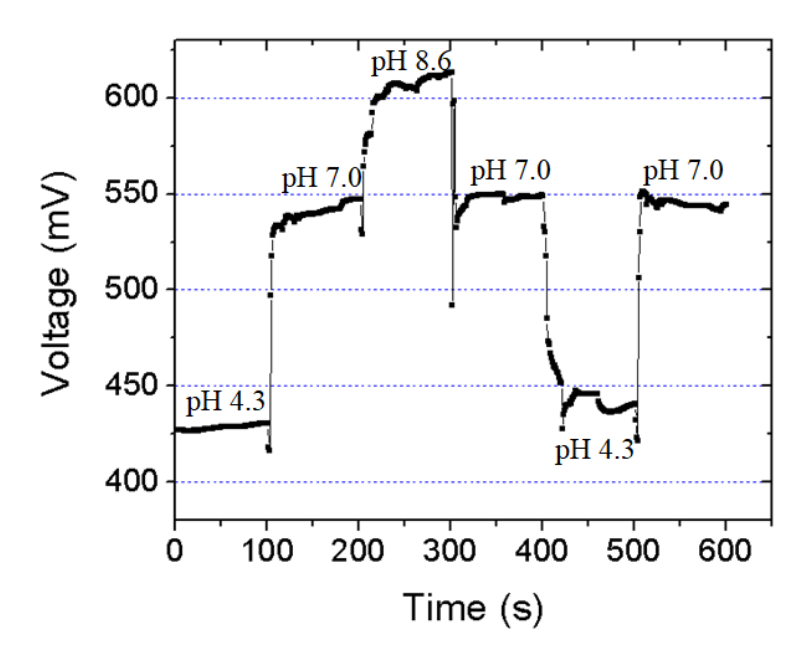


Figure 4.8: Repeatability test of the electrode in different pH solutions.

in Fig. 4.6. During measurement, the Ag/AgCl and Sb/Sb₂O₃ electrodes were connected respectively to the positive and negative terminals of the multimeter. The R-square value shows that the voltage response as a function of pH is fairly linear. Also, the electrode pair shows good sensitivity of 46 mV/pH, which is consistent to earlier reported result on a similar thick electrode [104]. The electrode pair was washed in DI water in between measurements to avoid contamination from different buffer solution mixing. The measurement was taken five minutes after dipping the electrode pair in the target solutions to provide enough time for voltage stabilization.

Once the sensitivity of the electrode pair was measured, next the voltage stability was monitored. The sensor electrode is dipped into different buffer solutions of pH 4.3, 7, and 8.6 and the voltage stability was measured for more than 5 minutes as shown in Fig. 4.7. The maximum voltage deviation is noticed to be 3.8 mV among all the three pH buffer solutions over time.

Next, the repeatability of the sensor electrode was measured in three different pH solutions. The sensor electrode was dipped into each pH solution and output voltage was recorded for 100 seconds at an interval of 1 second. As shown in Fig. 4.8, the electrode was first dipped into pH 4.3 solution, then it was transferred to pH 7 solution and finally to pH 8.6 solution. The same procedure was repeated in reverse order to observe the repeatability. The maximum voltage response time is 10 s including the electrode transfer time from one solution to another. The presented thin film electrode helps in reducing the response time by 20 s compared to a thick film based electrode presented in [104]. As observed in Fig. 4.8, the settling time in pH 7 solution is smaller compared to other two pH solutions as the pH 7 solution is more stable compared to the others. However, it should be noted that while performing the repeatability test, the sensor electrode was not washed in DI water before

transferring from one pH solution to another. As the test pH solution volume was low (\sim 10 mL) contamination of pH solution can happen during electrode transfer. Among the three test solutions, pH 4.3 was the weakest and hence the drift in voltage is more noticeable for pH 4.3.

4.3.2 Elemental analysis of sensor electrodes

Elemental analysis of the electrodes was performed to verify the material composition of the electrodes. The samples were examined in a JEOL-JSM-7500F Scanning Electron Microscope (SEM) and Energy Dispersive X-ray Spectroscopy (EDX) was performed using an Oxford Instruments AZtec system, using a 20 mm² Silicon Drift Detector crystal (6610LV) and an ultrathin window. The samples were coated with 10 nm thick osmium for SEM imaging and examined across cross-sectional cut.

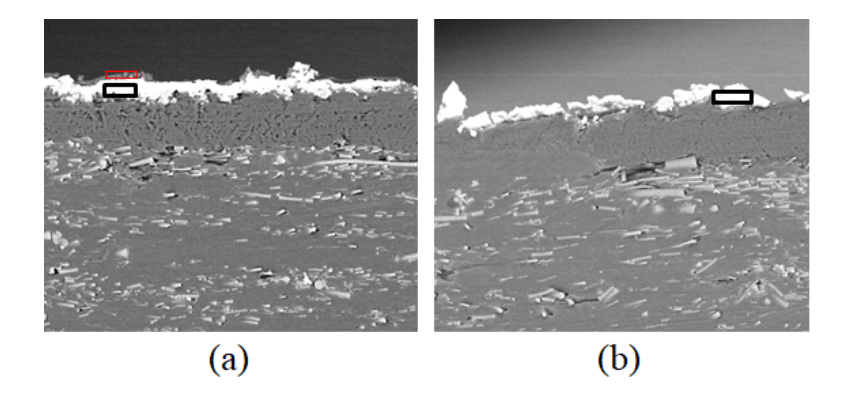


Figure 4.9: Locations for EDX elemental characterization: (a) reference electrode with highlighted black box for Ag/AgCl layer and red box for Nafion layer, (b) pH sensitive electrode with highlighted black box for Sb/Sb_2O_3 layer.

In Fig. 4.9, the locations for elemental analysis is highlighted for both reference and pH sensitive electrode. Two different sites for reference electrode were chosen as it consists of one Ag/AgCl layer and another Nafion layer. The EDX report as in Fig. 4.10 of the highlighted black region from Fig. 4.9(a) shows presence of both Ag and Cl atoms with lower weight

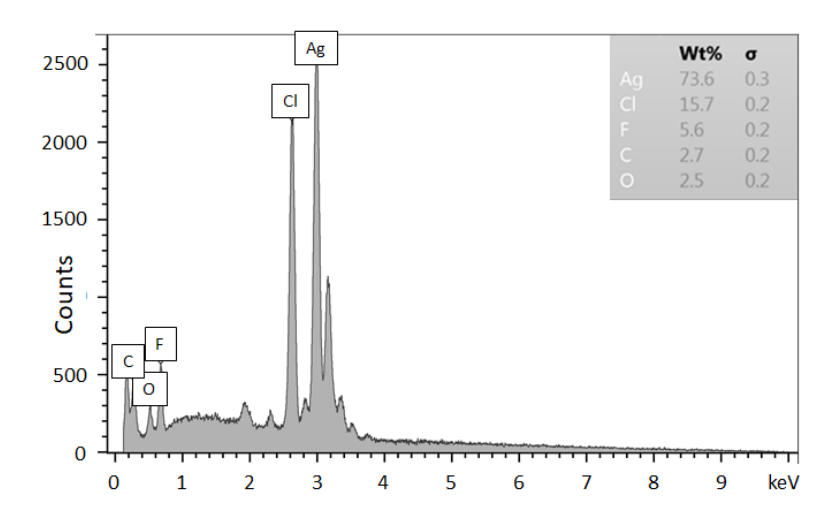


Figure 4.10: Elemental characterization for Ag/AgCl layer.

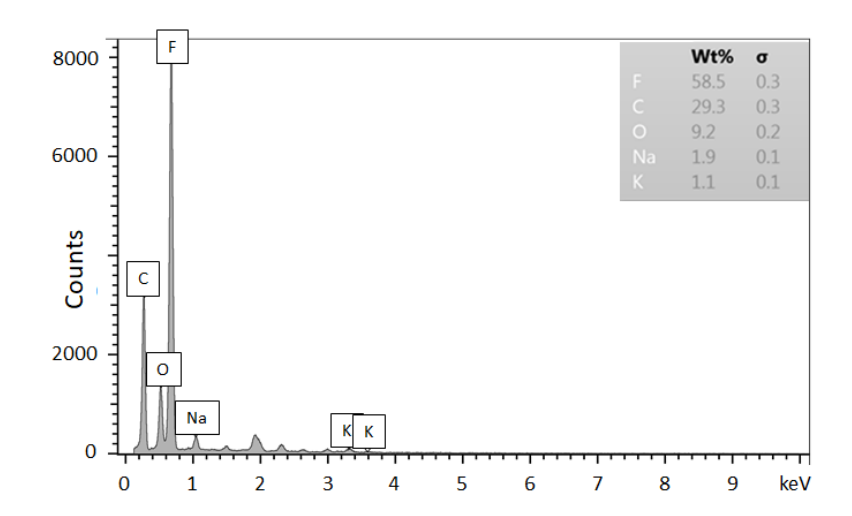


Figure 4.11: Elemental characterization for Nafion layer.

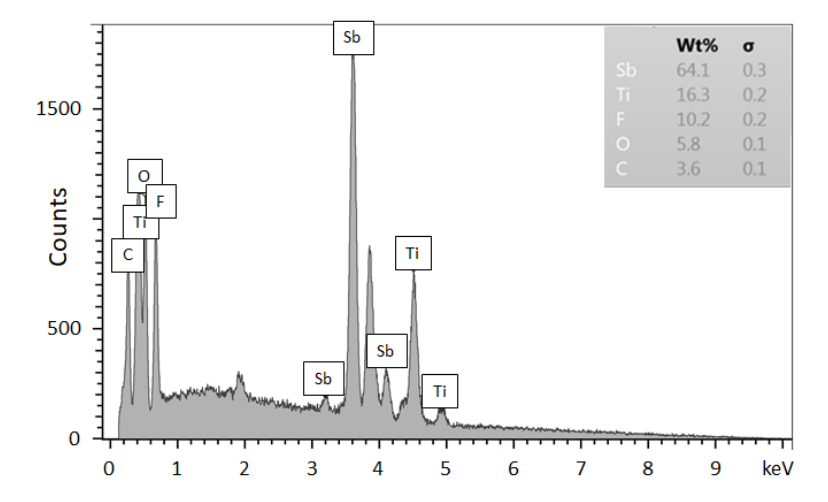


Figure 4.12: Elemental characterization for $\mathrm{Sb/Sb_2O_3}$ layer.

percentage of Cl atoms. This shows that Cl atoms are primarily accumulated at the surface. Fig. 4.11 shows the presence of C, F and O atoms, and the composition closely follows with earlier reported Nafion composition [111]. A trace amount of Na or K atoms were found, which can attach at the electrode surface during chlorination process. The presence of Sb and O atoms in Fig. 4.12 shows the oxidation of Sb layer. However, a comparatively small weight percentage of O atoms means a thin layer of oxide formation. The presence of Ti is due to the adhesion layer and C and F atoms are from the duroid substrate.

4.3.3 Multiple sensor electrode response

Due to fabrication tolerance, the voltage response of different pH sensors can be different. To study the phenomenon, voltage response of three different pH sensors was measured and is shown in Fig. 4.13. It can be noted that the sensitivity of all the sensor electrodes is close and similar. However, there is a specific offset among the different electrodes, which can arise due to fabrication process variation. Hence, one-time initial calibration is required with standard pH solutions before proceeding with measurement. In this paper, all the test results reported are based on Device 1.

4.3.4 Readout circuit

The digital signals for ID, ADC output, and union of both are shown in Fig. 4.14. The ID of the readout circuit was set to '101101001' and the DC bias point was set to 1 V at the input of ADC. The dynamic range of the input of ADC was set to 1.8 V, which means the 8 bit digital output would be '00000000' for 0 V bias and '11111111' for 1.8 V bias. For 1 V DC bias point at the ADC input, after conversion, the output of the ADC was

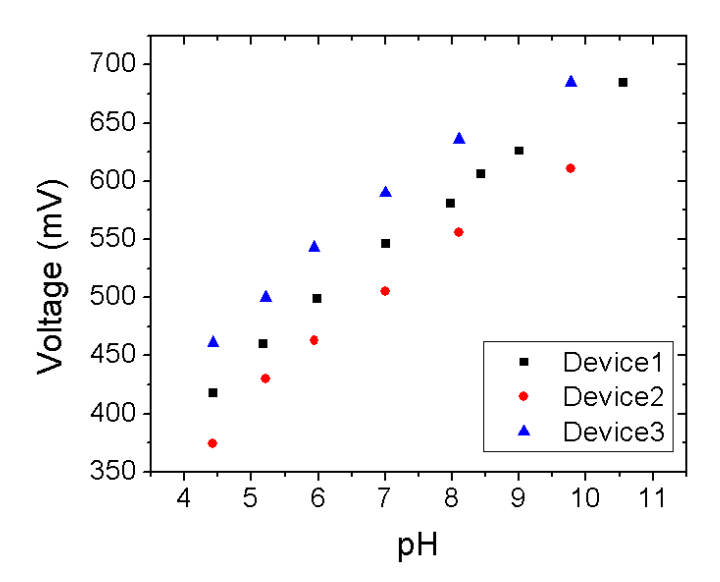


Figure 4.13: Voltage response of the three different fabricated electrode in different pH solutions.

'10010000', which corresponds to an analog 1.01 V. The microcontroller was programmed at low voltage programming (LVP) mode in MPLAB X IDE for generation of ADC clock, ADC control signal, and ID. According to the datasheet, a single bit of ADC constitutes twice the bit period of the clock generated by the microcontroller [112]. As the ID was generated internally from the microcontroller, the bit period of the ID was same as the ADC clock, which is 362 μs. Additionally, the ID bit period was half of the ADC output bit period as in Fig. 4.14. The MSB of the ID and the LSB of the ADC output are separated by 4.5 ms of idle time. The known time difference helps to resolve the sensor data accurately from the composite bit-stream of ID and ADC output together. An 'OR' gate was used to combine both the ID and ADC digital outputs. Additionally, there is another idle time of 15 ms in between two digital bit stream of combined ID and sensor data. The readout circuit harvests the required RF energy during these idle time. At this current setup, the sensor tag sends data to the interrogator at 0.595 kbps speed including the idle time. The minimum voltage for activation of the readout circuit is 2 V. When the bias voltage was set at 2.2 V,

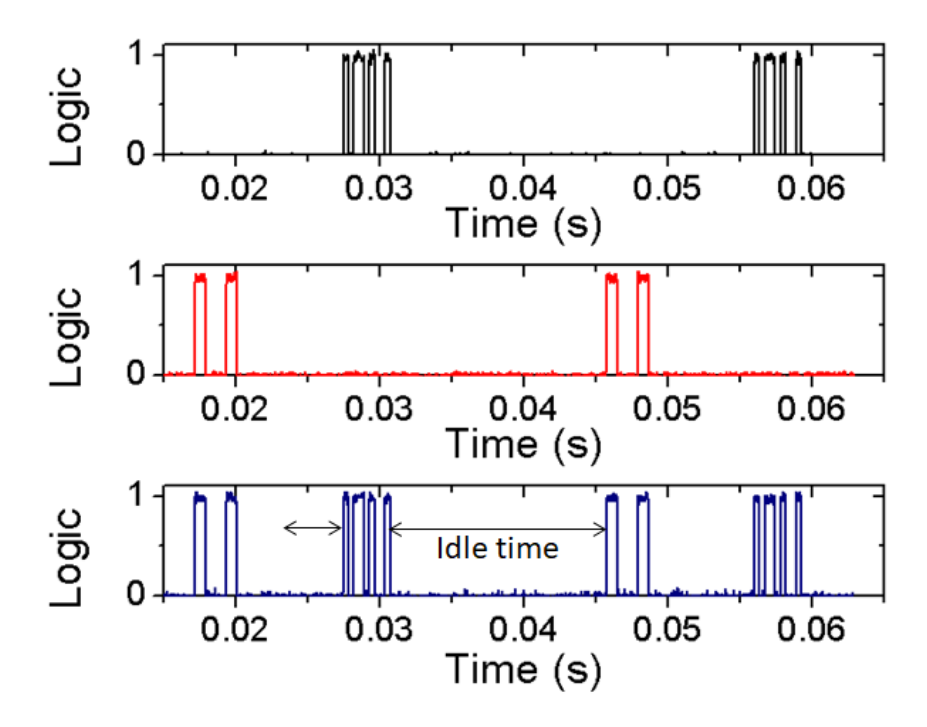


Figure 4.14: From top to bottom: a) The ID bit '101101001' b) 8 bits ADC output '10010000' of analog bias 1 V, and c) combined ID and ADC output bits. The 'idle time' in between the bit streams is also highlighted.

the readout circuit consumed a total of 33 μ W of DC power. With the current setup, the resolution of the sensor is 6.5 bits/pH according to the slope of the linear fit (46 mV/pH) as shown in Fig. 4.6.

4.3.5 Wireless measurement

An antenna resonating at 900 MHz from our earlier work was connected to the tag and interrogator for wireless measurement [41]. The sensor tag was kept at a distance of 45 cm from the interrogator, which was set at 15 dBm of transmit power at 900 MHz. The sensor tag with antenna and pH electrode pair is shown in Fig. 4.15. The complete tag was tested in different pH solutions and the digital bit sequence was recorded in the reader as shown in Fig. 4.16. The ID was kept at '101101001', which can be observed identical for all the pH

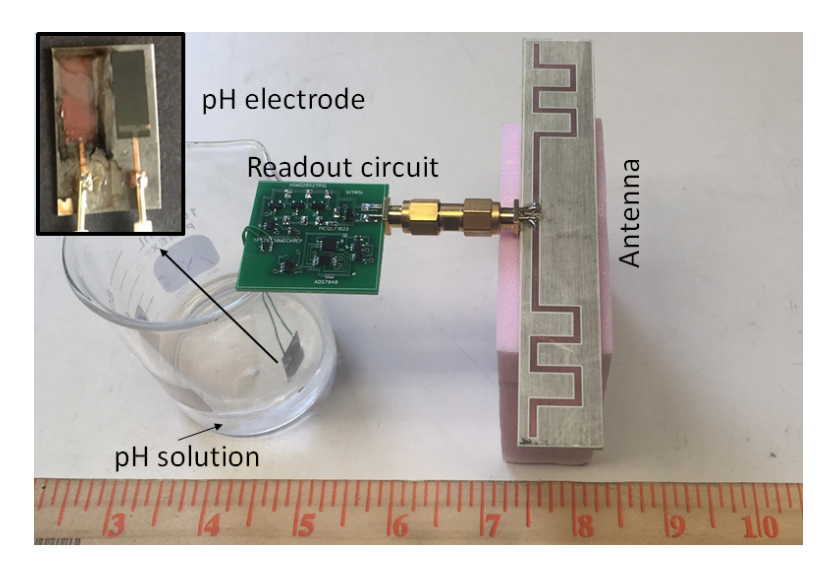


Figure 4.15: The complete sensor tag with zoomed in view of the electrode pair in the inset. The scale is shown in inches. In the inset, the left electrode is Nafion coated Ag/AgCl and the right one is Sb/Sb_2O_3 electrode.

digital bits. The digital response is '111010' for pH 4.3 solution, '1001100' for pH 7 solution, and '1010110' for pH 8.6 solution. After converting the bits into analog voltage, the voltage readings become 408 mV, 534 mV, and 605 mV for respective pH solutions of 4.3, 7 and 8.6. Using the linear fit of the data points from Fig. 4.6, the corresponding voltages are 413.6 mV, 537.8 mV, and 611.4 mV, respectively. The digitization error of 7 mV from the ADC of the readout circuit can limit the sensor tag's minimum sensitivity to 0.15 pH.

4.4 Application: Wearable Mouthguard

One biological application of pH electrode as an wireless salivary pH monitoring device is demonstrated in [113]. The importance of salivary pH monitoring in order to determine any imminent disease was already described in the introduction of this chapter. The building block components for a salivary wearable pH mouthguard are the same as a RFID based pH sensor, which is already described. In this section, the integration of different parts for

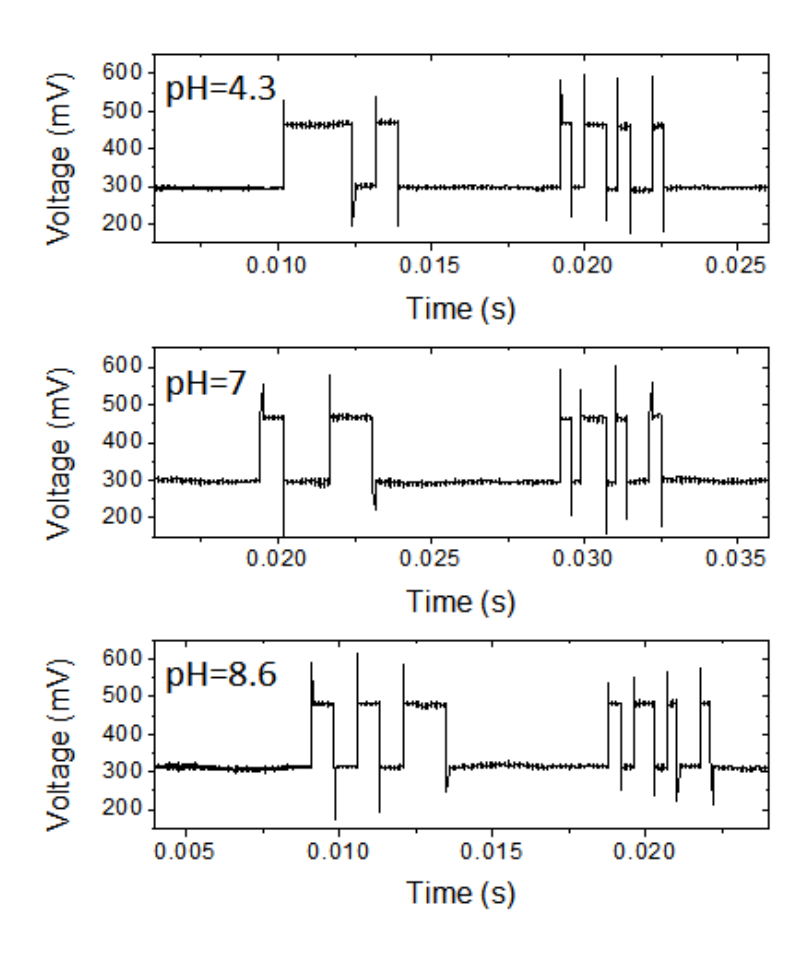


Figure 4.16: Digital bit response of the tag at different pH solutions in wireless setup. From top to bottom: a) bit response of '111010' at pH 4.3, b) bit response of '1001100' at pH 7, and c) bit response of '1010110' at pH 8.6.

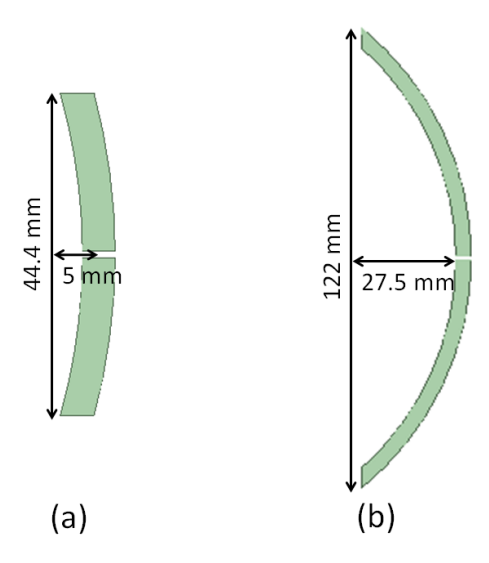


Figure 4.17: Antenna dimensions for (a) inside human mouth, and (b) in air medium.

a complete mouthguard fabrication is described. Apart from the digital circuits, and pH sensors, the transponder mouthguard includes antenna to wirelessly receive RF power and transmit back the sensor signals.

4.4.1 Antenna design

When the mouthguard is to be placed within human mouth, the antenna needs to be changed due to loading of the antenna by the human body. A human head model was considered as described in [114] to design the antenna. Due to dielectric loading, the effective length of the antenna reduces resulting in a compact and small size antenna. The antenna dimensions for inside human mouth and in air medium are given as in Fig. 4.17. The simulation result for those antennas is shown in Fig. 4.18. From the reflection co-efficient, it can be observed that the in air antenna is resonating at a fixed frequency. However, the simulation result of the in-mouth antenna shows apart from the resonance frequency, the reflection co-efficient is broad-band matched, due to loading effect by the human body.

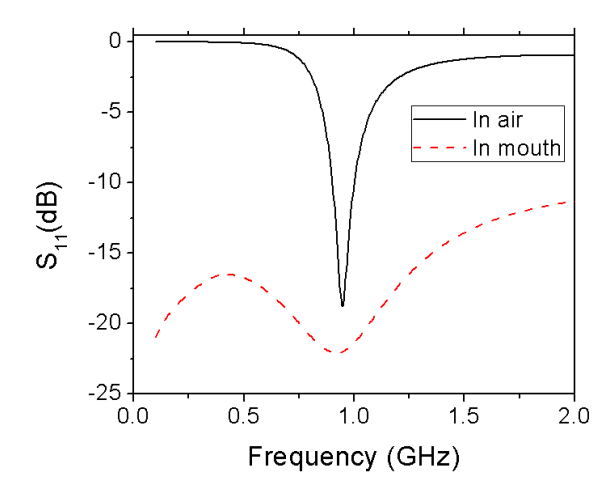


Figure 4.18: Simulated reflection co-efficient for in-air and in-mouth antenna designs.

4.4.2 Mouthguard design

The complete transponder is shown in Fig. 4.19 from different side views in Fig. 4.19(b) and Fig. 4.19(c) and the top view of the bare commercial mouthguard in Fig. 4.19(a). The transponder consists of two circuit boards a) the digital part is visible at the right side and b) the RF part is visible at the left side of mouthguard in Fig. 4.19. The dipole antenna is placed at the bottom of the mouthguard along the two arms and the electrodes are mounted at the center. HSMS 2852 Schottky diode was used to make a six stage RF to DC converter.

The complete sensor was integrated with pH sensor electrodes and transponder with connected antenna resonating at 930 MHz. Each part of the whole sensor was integrated on a mouthguard and the back-scattered response from the tag was measured using an Oscilloscope at different pH solutions. When buffer pH solution of 5.3 was used, a digital sensor sequence of '00010100' was detected. Digital sensor sequence of '00111000' was received in buffer pH solution of 9.5. The antenna was designed to use in air medium. The antenna design can be further optimized for use within human mouth as proposed earlier. During measurement, the tag was kept at 8 cm from the reader, which was transmitting 13 dBm of

power at 930 MHz.

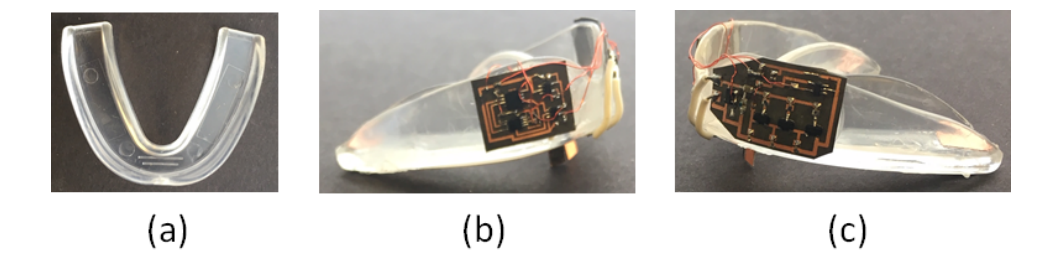


Figure 4.19: The sensor tag integrated on mouthguard (a) bare mouthguard, (b) digital part of the transponder at the right side and (c) RF circuit of the transponder at the left side of the mouthguard.

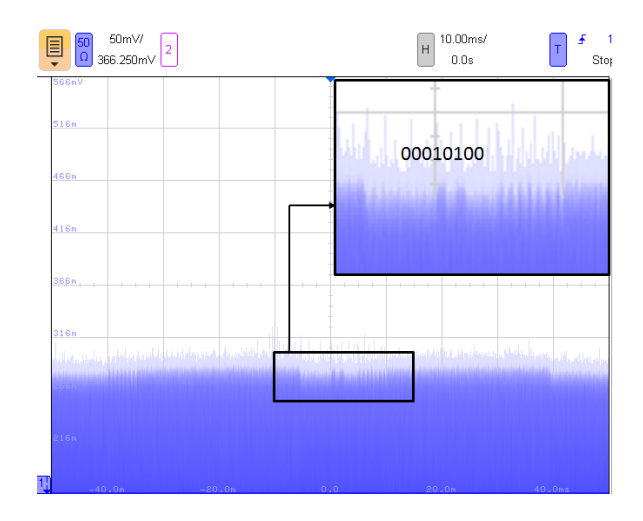


Figure 4.20: Detected signal in Oscilloscope in buffer pH solution of 5.3.

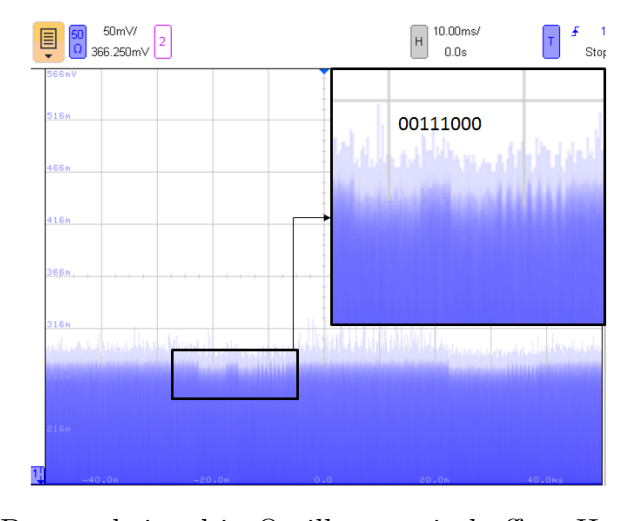


Figure 4.21: Detected signal in Oscilloscope in buffer pH solution of 9.5.

Table 4.1: Performance comparison with other works.

Ref	Application	Architecture	pH Electrode	Sensitivity	Energy Source	Read range and additional info
[102]	Numerous	Coupled coil analog	Commercial (PH105 by ExStik)	57.9 mV/pH	Not required	18 cm @5 MHz
[103]	Food supply chain	Coupled coil digital	${ m AgCl/IrO_x}$	49.7 mV/pH	RF harvested	16 cm @1.34 MHz and 100 Vpp
[96]	Biomedical	Digital	floating-electrode ISFET	48 mV/pH	On-board battery	NA
[115]	Biomedical	NFC Digital	$ m AgCl/IrO_{x}$	68.7 mV/pH	RF harvested	3.5 cm @13.56 MHz
[116]	Biomedical	Digital	ISFET	NA	On-board battery	Data rate @9.6 kbps
[3]	Numerous	Dual frequency analog	Commercial glass electrode	55 mV/pH	Not required	18 cm @2 and 4 GHz and 15 dBm
This work	Numerous	RFID digital	AgCl/Sb ₂ O ₃	46 mV/pH	RF harvested	45 cm @900 MHz and 15 dBm data rate @.595 kbps

4.5 Summary

In Table 4.1, the proposed sensor is compared with other wireless pH sensors reported earlier. In comparison to other works, the proposed sensor tag achieved a good read range with moderate sensitivity and compatible with RFID technology without any requirement of external power supply. As mentioned in Section III.C, the digital resolution of the sensor tag is limited due to the quantization error of the ADC. The resolution can be further increased by dynamically setting the low and high analog conversion voltage instead of setting them at 0 V and 1.8 V respectively. For example, changing the low and high conversion voltage from 0 V and 1.8 V to 0.4 V and 0.7 V respectively would change the resolution from 6.5 bits/pH to 39 bits/pH. However, the microcontroller has to perform additional computation for dynamic voltage allocation, which will add up the DC power consumption. Also, varying temperature is another challenge to obtain the correct reading from the sensor electrodes. The voltage response changes for the same pH solution at different temperatures. However, an additional temperature sensor can be added along with the pH sensor and the digitized temperature information can be sent in serial along with the pH and ID information. Based on the temperature information, the reader can correct the pH value.

The design and implementation of a batteryless and completely digital pH sensor is

demonstrated in this paper. The fabrication process of a thin film reference Ag/AgCl electrode and a pH sensitive Sb/Sb₂O₃ electrode pair is presented. The characterization of the electrode pair showed good linearity, good stability and fast response. As ID is integrated with the sensor tag, it makes easier to identify individual sensor tags, which is difficult for analog wireless sensors. The sensor tag harvests the required energy from the incident RF field and hence no on-board power supply is required. The passive nature of the sensor tag would extend the operating lifetime while reducing the footprint of the complete circuit. The sensor tag can be further miniaturized by custom fabricating the discrete digital circuit components into a single CMOS chip and miniaturized antenna. A read range of 45 cm was achieved using a transmitted power of 15 dBm from the RF interrogator in the wireless setup. The read range can be further increased by transmitting higher power or using higher gain antenna. As the size constraint is not so stringent on the reader antenna, with different configurations (such as Yagi-Uda) the antenna gain can be further increased by 4 to 5 dB.

Chapter 5

Energy Harvester Modeling

Energy harvester is a necessary component for passive RFID tags as it replaces the battery and supplies the necessary power for seamless operation of the tag. Batteries usually become bulky in order to achieve the required power density. Also, in structural health monitoring (SHM) applications, sensors are integrated within structures, where probing or future access is not possible for battery replacement. Hence, energy harvester is widely used in low power ultra high frequency (UHF) wireless and batteryless systems such as RFID, wireless sensors to provide required DC power for continuous operation in numerous applications, ranging from retail to hospital supply chain and real-time sensing [117–119]. One key parameter for energy harvester is RF to DC conversion efficiency, which provides a measure of how much actual power is available at the RFID tag. Apart from efficiency, another key parameter is response time. The response time can be critical for few applications with real-time constraints, such as those involved in control loops [120]. The response of a batteryless sensor tag depends on the time taken by the energy harvester to harvest enough voltage and power. Influence of different circuit components on those two parameters are examined closely in this chapter: a) efficiency, and b) response time.

5.1 Background

Among different energy harvester circuitss, charge pump (CP) configuration is widely used for RFID and wireless sensors at UHF frequency. Dickson CP was originally proposed as a DC-DC on-chip voltage multiplier. As there is no initial power available to kick-start the clock switching circuit for very low power RF energy harvesting based applications, the Dickson CP circuit was modified for RF energy harvesting while simultaneously boosting the rectified voltage and now is widely used in UHF batteryless systems [119,121,122]. The research on CP based energy harvester has been primarily focused on efficiency analysis and improvement [123,124], circuit component optimization for different harvester configurations [122,125], adaptively controlling the number of stages [126] and different material studies for harvesting element performance [127]. In [128], an equivalent model of the original Dickson CP was proposed, which can be used for transient analysis. Later, [129] extended the diode based design principle as in [128] for CMOS based CP. However, the model proposed for original Dickson CP cannot be used for modified Dickson CP due to following reasons:

- One of the primary assumptions for original Dickson CP model was that the cycle time of the clock is sufficiently large and hence the charging time constant was negligible compared to the cycle time. However, the assumption is valid when the input is DC but not applicable in modified Dickson CP, where the input is RF.
- A matching network is required in between antenna and CP for maximum power transfer in UHF energy harvester as shown in Fig. 5.1. Earlier proposed models on Dickson CP did not require to include matching network in the model.

Diode based modified Dickson CP circuit is quite popular in UHF batteryless systems due to choice of high efficiency diodes and shorter prototyping time [119,121]. In this work,

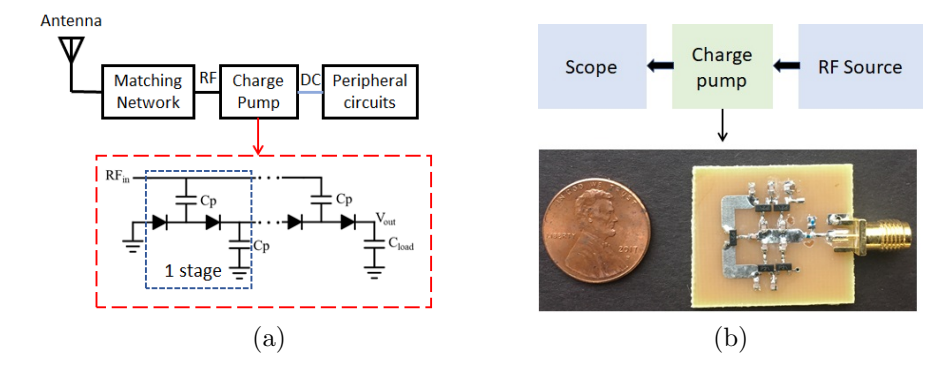


Figure 5.1: (a) The block diagram of a wireless batteryless system with a multi-stage modified Dickson charge pump; (b) Measurement setup with a fabricated 5-stage charge pump.

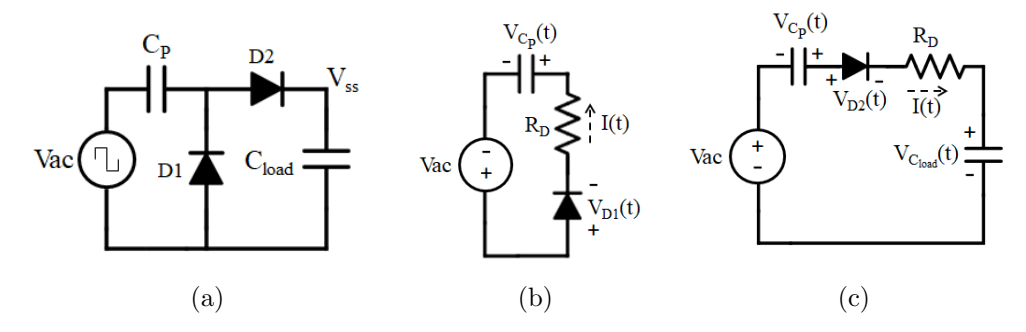


Figure 5.2: (a) A single stage CP, and it's equivalent circuit for (b) negative half cycle, and (c) positive half cycle.

an analytical model is proposed to estimate the transient response of a diode based multistage modified Dickson CP taking consideration of the matching network at any arbitrary load condition. The analysis and measurements were primarily focused on 900 MHz ISM band due to large number of earlier reported works in this band.

5.2 Modified Dickson Charge Pump

In this part, the working principle of a single stage modified Dickson CP was first analyzed and the key design parameters were identified from the analysis. The circuit components and their values were later chosen based on the analysis. A single stage CP with pump capacitance C_P , load capacitance C_{load} , and diodes D1, D2 is shown in Fig. 5.2(a). When

an ac source with amplitude V_{ac} is applied at the input, during first negative half cycle, the diode D1 is forward biased and C_P is charged through diode resistance R_D as in Fig. 5.2(b). Due to charge accumulation, a voltage $V_{C_P}(t)$ appears across C_P . In next positive half cycle, the diode D_2 will be forward biased and C_{load} gets charged. In this half cycle, the total charging voltage for C_{load} appears as $(V_{ac} + V_{C_P}(t))$ as shown in Fig. 5.2(c). By periodically charging in this fashion, the steady state DC voltage of a single stage CP will be $2 * (V_{ac} - V_D)$ as maximum voltage V_{ac} is possible for $V_{C_P}(t)$, where V_D is forward voltage drop of the diodes. In similar way, for a n stage CP, the steady state DC voltage will be $n * (V_{ac} - V_D)$.

In high frequency CP design, the choice of pump capacitor C_P and diode is important. If C_P is kept too small, it will not store enough charge to operate as a voltage source in subsequent half cycle. Simultaneously, very high value of C_P will not be practically useful as the cut-off frequency of a capacitor keeps reducing for higher capacitance value. The effect of C_P on V_{ss} is shown in Fig. 5.3 for a single stage CP. In this case, a square wave is fed with operating frequency of 1 GHz and amplitude $V_{ac} = 0.5$ V, and C_{load} was kept at 200 pF. As shown in Fig. 5.3(a), for $C_P = 1$ pF, V_{ss} saturates at much lower voltage than $(2 * V_{ac})$. With higher $C_P = 20$ pF, V_{ss} saturates close to $(2 * V_{ac})$. Hence, maximum C_P is chosen within the capacitor's practical cut-off limit. To have the maximum voltage multiplication from a CP, very low barrier Schottky diode is preferred due to very small V_D and fast response.

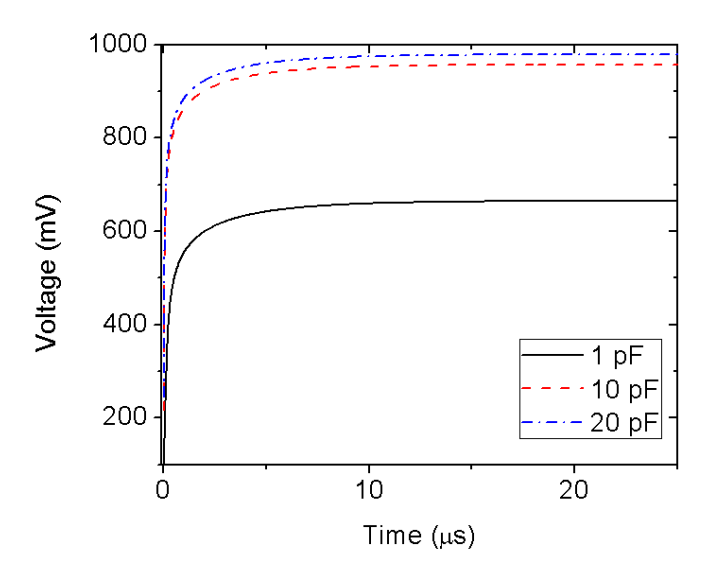


Figure 5.3: Effect of pump capacitor C_P on steady state voltage.

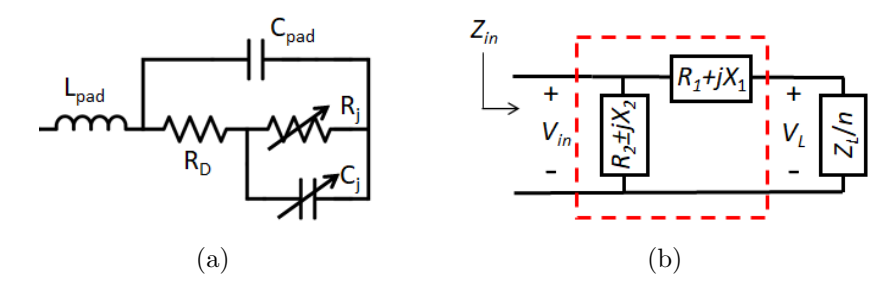


Figure 5.4: (a) A Schottky diode model with pad parasitics. (b) 'L-match' as two-element matching network for *n*-stage CP.

5.3 Effect of Matching Network

After identifying the design elements, the effect of matching network on the CP is analyzed next. Before using a standard matching configuration, it is important to determine the nature of the input impedance of a single stage CP.

The circuit model of a Schottky diode with parasitic components is shown in Fig. 5.4(a). R_j and C_j are the junction resistance and junction capacitance, L_{pad} , C_{pad} are pad inductance and capacitance, and R_D is the diode series resistance. The diode input impedance Z_D with the circuit components is expressed in (5.1), for sub-GHz frequency by assuming $(\omega C_{pad}R_D \ll 1)$. The expression for Z_D in (5.1) is further simplified in (5.2). Depending

on the operating condition of a diode, R_{eff} or C_{eff} can dominate in expression of Z_D .

$$Z_D = j\omega L_{pad} + R_D + R_j || \frac{1}{j\omega(C_j + C_{pad})}$$

$$(5.1)$$

$$Z_D = j\omega L_{pad} + R_{eff} + \frac{1}{j\omega C_{eff}}$$
 (5.2)

The diode impedance Z_D can now be used to compute the input impedance of the CP. For a single stage CP, the effective input impedance Z_L is combination of Z_{D1} , Z_{D2} , and C_P . At sub-GHz frequency, the diode and pad capacitance dominates over the pad inductance. Hence, Z_D is resistive and capacitive in nature and Z_L will be of similar nature as expressed in (5.3).

$$Z_L = \frac{1}{j\omega C_P} + Z_{D1} || \left(Z_{D2} + \frac{1}{j\omega C_{load}} \right)$$
 (5.3)

The extracted input impedance of a single stage diode pump with $C_P = 20$ pF, $C_{load} = 200$ pF, and HSMS-2852 diode was (3.8 - 105j) Ω at 900 MHz and -10 dBm input power. The capacitive nature of the CP input reactance is preserved even when multiple stages are used, as shown later.

With the knowledge of Z_L , the matching networks for single and multi-stage CP are designed. In general, two-element based impedance matching is widely used for single frequency matching. Considering the CP input impedance as $Z_L = R_L - jX_L$, two-element based 'L-match' as shown in Fig. 5.4(b) is used for $(R_L < 50)$. After matching, the input impedance Z_{in} of the combined system should be close to 50 Ω for impedance matching to a 50 Ω antenna. If V_{in} is considered as the peak amplitude of the time varying induced

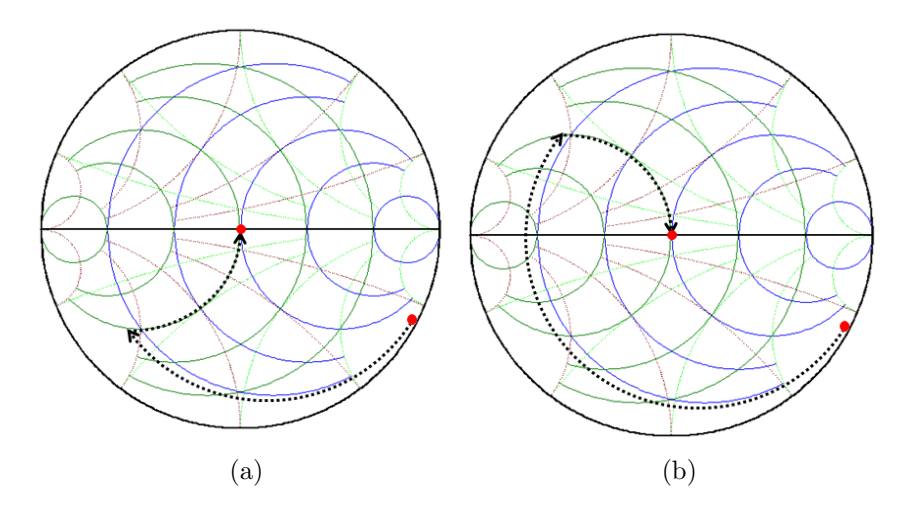


Figure 5.5: A typical matching trajectory (dotted line) of single stage CP. For case (a), the matching network uses series inductor and shunt inductor $(X_1 > 0, X_2 > 0)$. For case (b), the matching network uses series inductor and shunt capacitor $(X_1 > 0, X_2 < 0)$.

voltage across the antenna, and V_L as the peak voltage induced at the input of the CP as in Fig. 5.4(b), then V_{in} can be calculated as $\sqrt{2*(P_{in}*(1-\Gamma^2)*|Z_{in}|)}$, where Γ is reflection co-efficient and P_{in} is antenna received power. For perfect matching between antenna and the CP, Γ is 0. V_L is important to compute, as it decides the final output of the CP. The voltages V_L and V_{in} are related according to (5.4).

$$\frac{V_{inP}}{V_{LP}} = \left| \frac{R_L - jX_L}{R_L - jX_L + R_1 + jX_1} \right|$$
 (5.4)

5.3.1 Single-stage formulation

Based on the single-stage input impedance, the two possible impedance matching trajectory are shown in Fig. 5.5 by applying the proposed matching network. During matching, $(R_1 + jX_1)$ is applied in both cases to relocate Z_L on the 50 Ω admittance circle. Next, $(R_2 \pm jX_2)$ is applied to finally relocate Z_L at 50 Ω impedance point. R_1 and R_2 represent the resistive loss of the series and shunt matching elements respectively.

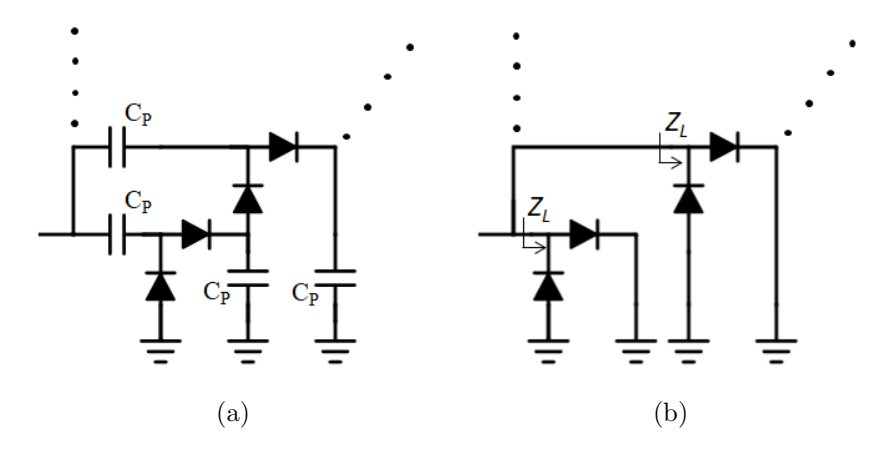


Figure 5.6: (a) n stage charge pump, and (b) it's simplified impedance model.

With application of series $(R_1 + jX_1)$, the admittance of combined Z_L and $(R_1 + jX_1)$ will be $1/((R_L + R_1) - j(X_L - X_1))$. By imposing the constant unity normalized admittance condition at the impedance tracing for both the cases as shown in Fig. 5.5(a) and Fig. 5.5(b), the following relation as (5.5) is obtained. In (5.5), R_{norm} represents the reference resistance used for normalization, which is 50 Ω . The steady state DC voltage V_{ss1} for a single-stage CP can be expressed in terms V_{in} , diode voltage drop (V_D) , CP impedance $(R_L - jX_L)$ as in (5.6) by substituting (5.5) in (5.4), which can be subsequently simplified for $(X_L >> R_L)$, and zero bias diode $(V_D \approx 0)$.

$$(R_L + R_1)/((R_L + R_1)^2 + (X_L - X_1)^2) = 1/R_{norm}$$
(5.5)

$$V_{ss1} = 2V_L - V_D$$

$$\approx \frac{2V_{in}}{\sqrt{R_{norm} \left(1 + \frac{R_1}{R_L}\right)}} \left(\frac{X_L}{\sqrt{R_L}}\right)$$
(5.6)

5.3.2 Multi-stage formulation

A simplified formulation of steady state DC voltage V_{ssn} for n-stage CP can be obtained with further approximations. By assuming pump capacitance C_P is large enough to be considered as RF short at 900 MHz, which will simplify the total input impedance as Z_L/n , as shown in Fig. 5.6. By using the equivalent impedance model, V_{ssn} can be obtained as expressed in (5.7), using approximate form of (5.6), provided the same R_{norm} was used while matching. In (5.7), R_{1n} denotes the loss resistance of the series matching element.

$$V_{ssn} \approx \frac{2n * V_{in}}{\sqrt{R_{norm} \left(1 + \frac{nR_{1n}}{R_L}\right)}} \left(\frac{X_L/n}{\sqrt{R_L/n}}\right) \approx \sqrt{n} V_{ss1}$$
(5.7)

The input impedance of the n-stage CP reduces as $(R_L/n - jX_L/n)$. As a result, the series matching element $(R_{1n} + jX_{1n})$ needs to be reduced. If series inductors of identical Q-factor are used, a further assumption can be made as $nR_{1n} \approx R_1$ to maintain the matching condition. However, this assumption is valid as long as $(X_{1n} - X_L/n)$ remains almost identical to $(X_1 - X_L)$ during matching. With the approximations, a further simplistic form of V_{ssn} for n-stage is expressed in terms of only V_{ss1} and n.

5.4 Transient Model for Arbitrary Load

The 10%-90% rise time (T_{rn}) is obtained from transient response of a n-stage CP system. The capacitive load C_{load} gets charged primarily through the diode video resistance, referred as pump resistance $R_P = n_0 kT/(q*(I_s+I_b))$, where n_0 is ideality factor, k is Boltzmann constant, I_s and I_b are reverse saturation and bias current respectively [130]. With R_P , C_{load} , and V_{ss1} , the equivalent model of a single-stage CP is shown in Fig. 5.7(a). R_P of a

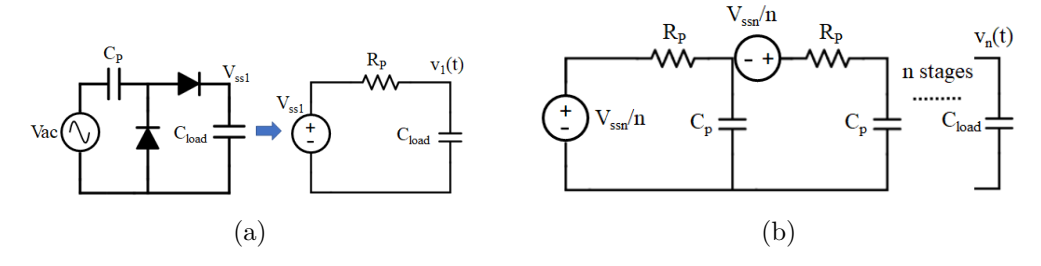


Figure 5.7: Equivalent transient model for (a) single stage CP, and (b) n stage CP.

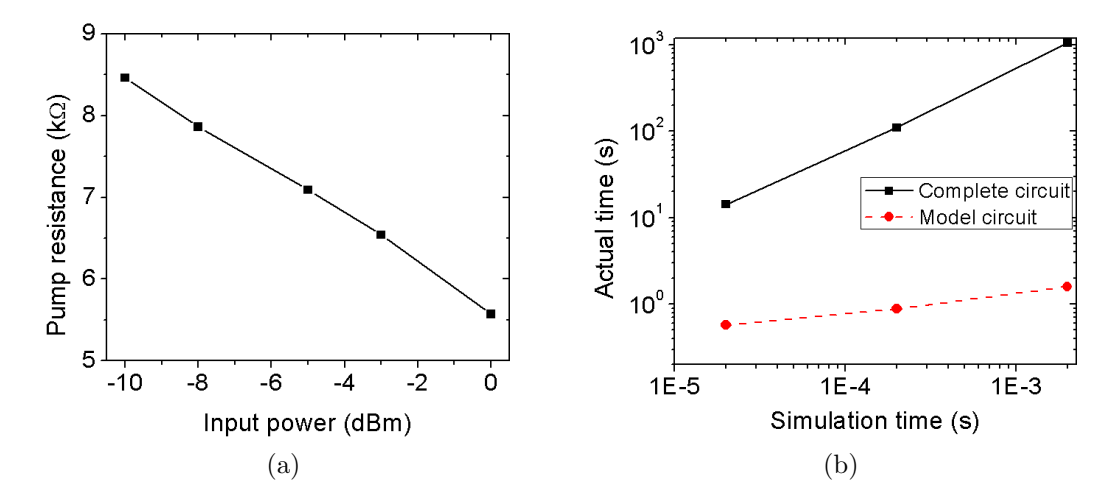


Figure 5.8: (a) Extracted pump resistance (R_P) of a single stage CP at different input power. (b) Model vs. discrete circuit based single stage CP simulation time comparison.

single-stage CP is extracted at different input power level as shown in Fig. 5.8(a). Due to self-biasing of a Schottky diode, bias current increases at higher input power and hence R_P decreases.

Using equivalent circuit from a single-stage CP, the equivalent model of a n-stage CP is extended as shown in Fig. 5.7(b). A further simplification was performed under the condition $C_{load} >> nC_P$ as C_{load} is usually in nF range or higher whereas C_P is in pF range. In addition to C_{load} , when a load resistance R_{load} is also present, R_{load} forms a voltage divider with internal nR_P . In (5.8), $v_n(t)$ of a n-stage CP is expressed in terms of V_{ssn} , R_P at any load condition. Finally, T_{rn} is calculated from time dependent $v_n(t)$ expression. It should be noted that increase in stage number will reduce the input RF

impedance whereas increase the output DC impedance.

$$v_n(t) = V_{ssn} \frac{1}{1 + \frac{n*R_P}{R_{load}}} \left(1 - e^{-\frac{t}{(n*R_P||R_{load})*C_{load}}} \right)$$

$$(5.8)$$

5.5 Measurement Results

Use of model shows a substantial reduction in actual time taken by a simulator compared to discrete component based transient circuit simulation with RF input as in Fig. 5.8(b). For example, a single stage CP with the discrete diodes, C_P , and matching network takes actual time of 1059 s for transient simulation duration of 2 ms. This happens due to a very small timestep reqirement to resolve the full bandwidth of the RF input for convergence. On the other hand, as Fig. 5.7(a) based single CP model uses a DC step input, the simulation time reduces to 1.6 s with same convergence criteria. For comparison, both the transient simulations were performed using Keysight ADS at MSU DECS server (2 Intel Xeon Gold 6150 CPU and 50 GB RAM).

One to five stage CP was assembled on a FR-4 PCB with HSMS-2852 diode and $C_P = 20$ pF to verify the developed model with setup as shown in Fig. 5.1(b). A single stage CP shows good matching ($S_{11} \le -10$ dB) around 900 MHz at diiferent input power as shown in Fig. 5.9(a). Also, CPs with different stages show good matching around 900 MHz at -10 dBm input power as in Fig. 5.9(b).

The transient model was further compared with measurements for different stages as in Fig. 5.10, and different C_{load} and R_{load} as in Fig. 5.11(a). The voltage normalization in Fig. 5.10 and 5.11(a) was performed with respect to V_{ssn} at no load resistance. Additionally, measured efficiency as shown in 5.11(b), demonstrates the maximum efficiency when R_{load}

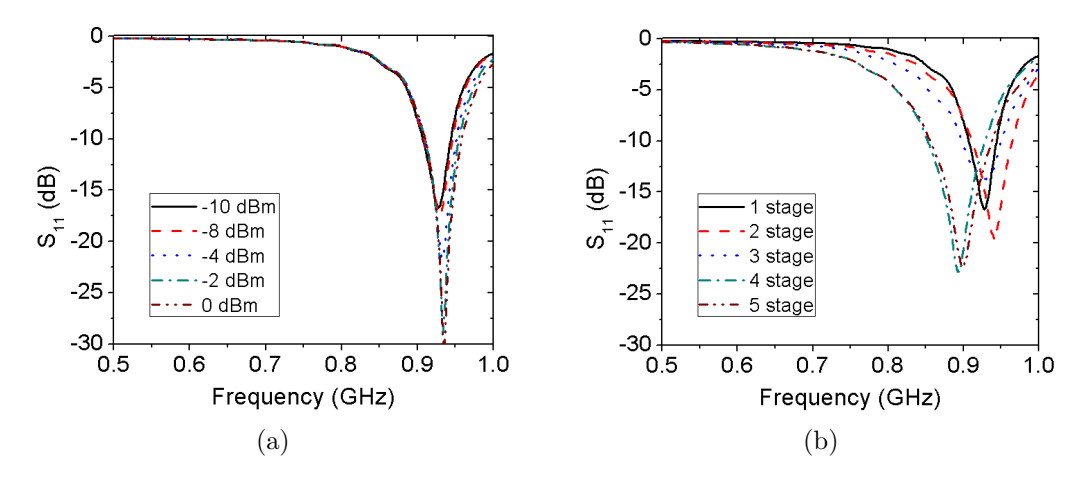


Figure 5.9: Measurement results of reflection co-efficient (S_{11}) (a) single stage CP at different input power, and (b) multiple stages CP at -10 dBm input power.

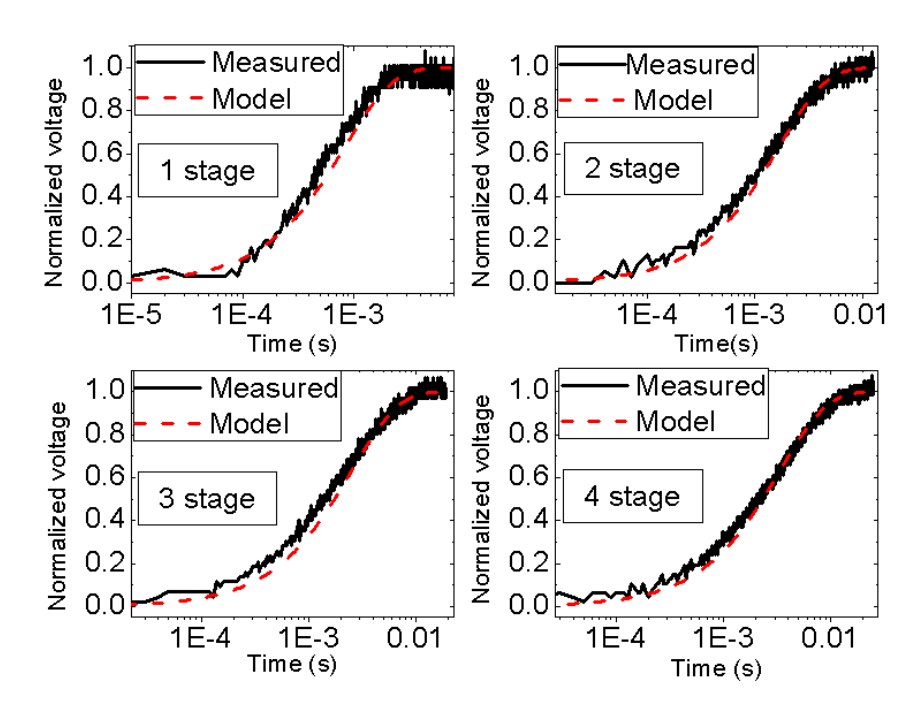


Figure 5.10: Voltage normalized transient response of CPs with different stages with $C_{load} = 100$ nF and no external R_{load} .

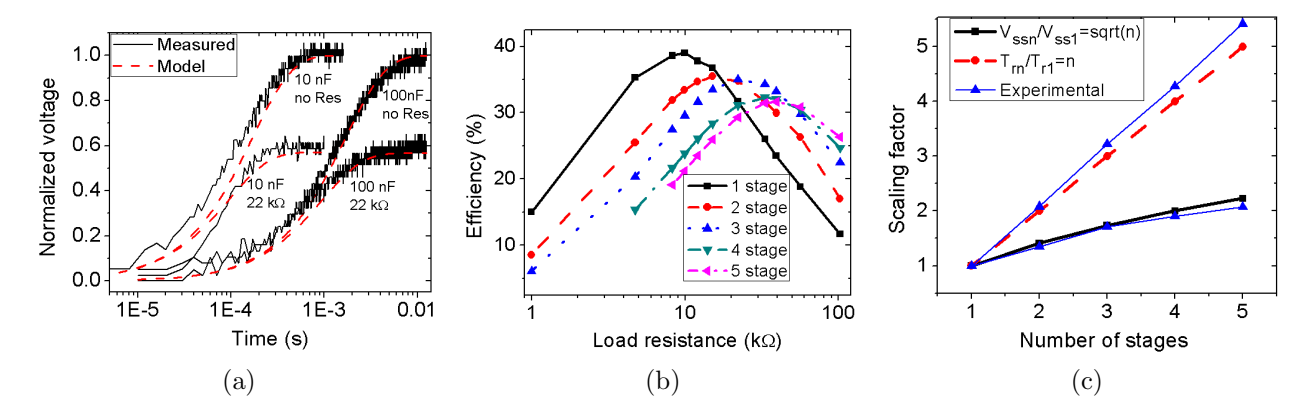


Figure 5.11: (a) Voltage normalized transient response of a 2-stage CP at different load conditions. (b) Measured efficiency of CPs with different stages. (c) Scaling factor of T_{rn} and V_{ssn} compared to a single stage CP.

Table 5.1: Comparison with relevant literature.

Ref.	Frequency	Application	Technology	No. of stages	Impedance matching in model	Transient analysis using model
[122]	950 MHz	RFID energy harvesting	180 nm CMOS	2-3 (measured)	Yes	No
[125]	915 MHz	RFID energy harvesting	90 nm CMOS	17 (measured)	No	No
[129]	DC	DC-DC voltage boost	65 nm CMOS	8-16 (simulated)	No	Yes
[128]	DC	DC-DC voltage boost	Diode based	8-16 (simulated)	No	Yes
[131]	5.8 GHz	RF-DC energy harvesting	BAT15-03W diode	Single diode	No	No *
[132]	2.45 GHz, 5.8 GHz	RF-DC energy harvesting	MA4E1317 diode	Single diode	No	No *
[This work]	900 MHz	RF-DC Energy harvesting	HSMS-2850 diode	1-5 (measured)	Yes	Yes

^{*}Modeled in steady state time domain

is close to nR_P for respective CP. As the total loss associated with diode resistance increases with n, peak efficiency drops with increase in stage number. All the measurements were performed at -10 dBm input power and within (926 MHz - 935 MHz) band depending on the CP's best S_{11} response.

Finally, the theoretical and measured scaling factor for T_{rn}/T_{r1} and V_{ssn}/V_{ss1} are compared in Fig. 5.11(c) for different number of stages at $C_{load} = 100$ nF and no external R_{load} . For a single stage CP, V_{ss1} was measured as 1.14 V and T_{r1} as 1.8 ms at 926 MHz and -10 dBm input power. As derived earlier, (T_{rn}/T_{r1}) varies proportionate to n according to (5.8), while (V_{ssn}/V_{ss1}) varies proportionate to \sqrt{n} according to (5.7). However, it should be noted that the scaling factor for different n is valid when the CPs with similar matching

configuration are measured at identical power level.

5.6 Summary

In this chapter, the modified Dickson CP circuit is analyzed for different design parameters and a model is proposed to capture the transient response. The model takes account of impedance matching network, which is necessary to match a CP to an antenna in wireless systems. Additionally, the model offers a great reduction in simulation time especially when the CP rise time starts exceeding 1 ms. The model supported by measurement result showed that the rise time increases proportionally with increasing the number of stages, which is also necessary to boost the steady state output voltage. The model will be helpful in estimating charging rise time for wireless energy harvesting applications.

Chapter 6

Effective Transmit Time Reduction of

RFID Reader

Prolonged RF radiation reduction on human body can be detrimental and there has been multiple related studies, which were mentioned in chapter 2. RFID has become a successful choice for integrated sensing due to small feature size and batteryless architecture. However, RFID tags require continuous RF illumination from the reader to transfer data from the tag. This scenario may trigger for undesired prolonged transmission from the RFID reader. To mitigate the problem, a dual mode RFID tag with active transmission is proposed in this chapter, where the RFID tag will fetch information from the sensor locally. In this chapter, a dual mode RFID system is proposed for intra-vehicle wireless sensing application, where there is a risk of prolonged RF radiation exposure to human bodies.

6.1 Background

Sleep monitoring of patients during acute illness or clinical condition is very important. The hybrid RFID based wireless and batteryless sensing system can be used to monitor a patient's movement during sleep. In this case, a pressure monitoring sensor can be integrated with the hybrid RFID system. Also, with an increase in intelligent transport system, more sensors need to be integrated within a transport system for various applications. Currently,

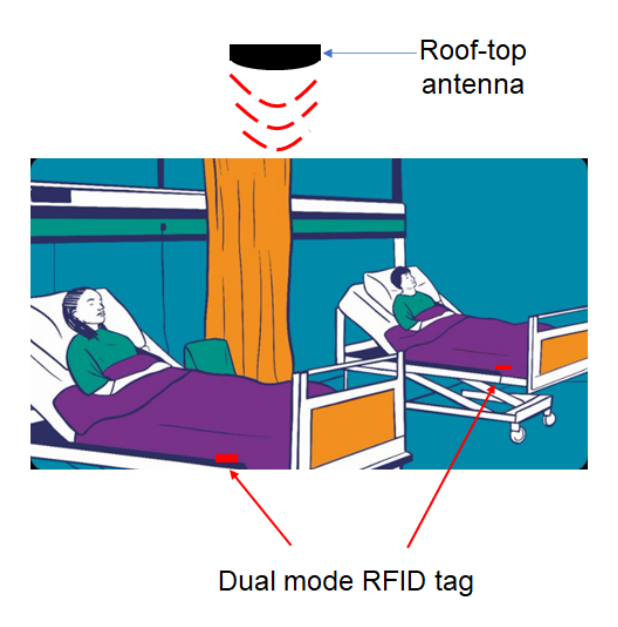


Figure 6.1: Dual mode RFID tags for patients' sleep monitoring system.

majority of the sensors are interfaced with the transport control system using wires, which results in long redundant wires routed all over a transport system's interior. This leads to added cost, weight, and wiring complexity. The size of the wire harness can be significantly reduced if the connectivity of the sensors is made wireless. Hence, there has been a drive recently to make the sensor connectivity wireless [133–135]. However, with wireless connectivity of the sensors to the transport control system, power supply becomes an issue for those sensors [136]. Usually battery is used for supplying power to the wireless sensors. However, using batteries will limit the life-time of the sensors based on power consumption. Additionally, many of those sensors are embedded within the body or parts, which may not be accessible to change batteries. Hence, a wireless and batteryless system is required for the sensors to be installed within a modern transport system to remove many redundant wire connections and will be operational over the life-time of the sensors without requiring service such as battery change.

RFID based sensors have been proposed earlier for different low power sensing applica-

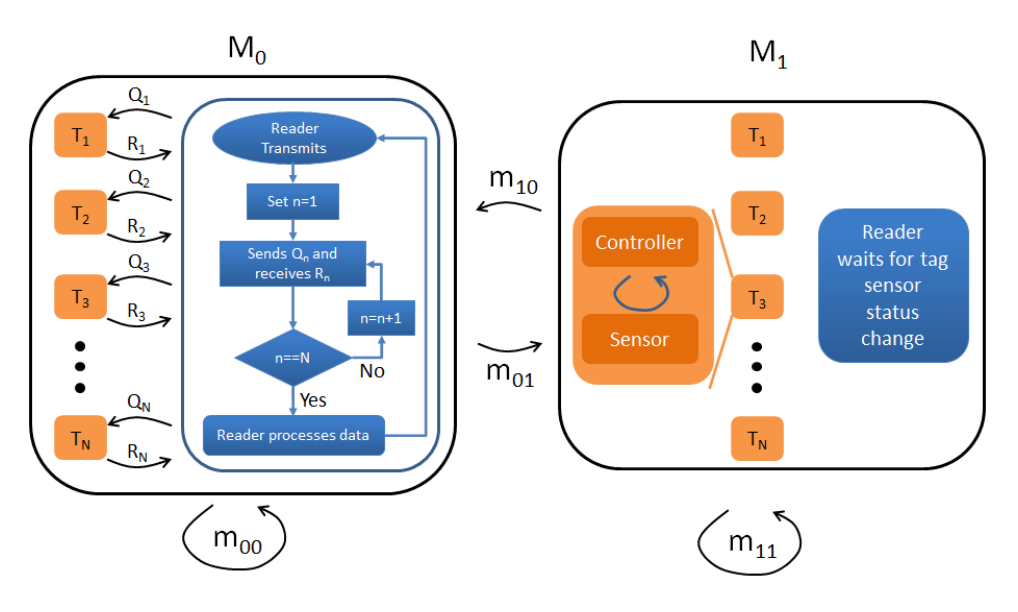


Figure 6.2: Different modes of communication in between the reader and tag.

tions [46, 118, 137]. The central controller within the tag periodically activates the sensor and transmits the data using backscatter modulation. The harvested power in the RFID is used for powering up the tag circuit and the sensor. Use of the controller with ADC enables the RFID based sensor tag to interrogate a broad range of analog and digital sensors. In [118,137], analog electrochemical sensors pH and ammonia were used. The analog output voltage was converted into digital data and sent from the tag to the interrogator. A similar technique can be used for patients' sleep monitoring in clinical conditions. In Fig. 6.1, an example scenario of the dual mode wireless sensors is shown, where rooftop reader antenna is used to monitor the embedded sensors. The sensors for sleep monitoring are usually piezoelectric or piezoresistive in nature, which generates voltage or changes impedance in case of applied pressure is changed. By detecting the pressure, the movements of a patient is quantified, which will provide the data for quality sleeping. Using the same concept, multiple sensing modalities can also be incorporated into a single tag.

6.2 Finite State Machine and Event Driven Modes

The design of the system can be conceptualized in terms of a finite state machine (FSM). FSM is a mathematical model used to develop a logical process where a finite number of operational conditions or states exist and at a time the machine can only be at a single state. Transition from one stage to another occurs based on single or multiple events. The FSM for the tag and reader communication is represented using the variables (Σ, M, M_0, δ) , where:

- Σ is the set of finite input events which initiate the state transitions.
- M is the finite set of states as $\{M_0, M_1\}$, where in M_0 the tags communicate with the reader using backscattering, and in M_1 the reader waits for the tag transmitted status change signal.
- M_0 is the initial state.
- δ is defined as the state transition function, where $\delta: \Sigma \times M \to M$.

6.2.1 M_0 state: Tag backscatter communication

In the initial state M_0 , the tags transfer the sensor status using backscatter communication. In backscatter communication, the tag modulates its antenna impedance to transfer data to the reader. In this state, the reader supplies the RF carrier and the tags use the carrier to perform the modulation as well as storing the redundant energy. As shown in Fig. 6.2, the reader sends queries sequentially as $\{Q_1, Q_2, ..., Q_N\}$ for N tags and receives the consecutive replies $\{R_1, R_2, ..., R_N\}$. The sequential and individual query of tag helps in avoiding tag reply message collision at the reader. The state M_0 stays in the same state as

long as event driven mode m_{00} prevails. When the mode m_{01} is triggered, the state changes from M_0 to M_1 .

6.2.2 M_1 state: Tag active transmit

In state M_1 , the reader does not transmit any RF carrier. Instead of the reader directly monitoring the tag sensor status as in M_0 state, the reader delegates the sensor monitoring to the tag locally in M_1 state. A tag uses the stored energy from M_0 state for sensor monitoring. In case of sensor status change of i^{th} tag T_i , the tag dispatches alarm signal. In this state, the reader waits to listen for any alarm. M_1 state is maintained as long as m_{11} mode is active until when m_{10} mode is trigerred and the state changes to M_0 .

6.2.3 Events and driven modes

The state transition takes place due to the driven modes and each of the modes is dependent of single or multiple events. The event set Σ : $\{e_1, e_2, e_3\}$ is triggered due to voltage level V_{T_i} or alarm signal status A_{T_i} of Tag T_i . The event signal e_1 is set as 0 as long as A_{T_i} status is inactive for all the tags. As soon as A_{T_i} is triggered from at least one tag, e_1 status will change to 1.

$$e_{1} = \begin{cases} 1 & [\exists T_{i} \mid (A_{T_{i}} == 1)] \\ 0 & [(A_{T_{i}} == 0) \forall T_{i}] \end{cases}$$
where, $T_{i} \in \{T_{1}, T_{2}, ..., T_{N}\}$ (6.1)

The input event e_2 is set as 0 as long as V_{T_i} of at least one tag is below the predicted voltage V_{ch}^{Peak} by the reader while the tags are charging. As soon as V_{T_i} of all the tags are higher or equal to maximum voltage V_{ch}^{Peak} , e_2 status is changed to 1. Similarly, e_3 is set at 0 as long as V_{T_i} of all tags is above the minimum voltage V_{dis}^{Peak} by the reader while the tags are discharging. When V_{T_i} of atleast one tag drops below V_{dis}^{Peak} , e_3 is set as 1. The parameters V_{ch}^{Peak} and V_{dis}^{Peak} are described later.

$$e_{2} = \begin{cases} 0 & [\exists T_{i} \mid (V_{T_{i}} < V_{ch}^{Peak})] \\ 1 & [(V_{T_{i}} \ge V_{ch}^{Peak}) \, \forall \, T_{i}] \end{cases}$$
where, $T_{i} \in \{T_{1}, T_{2}, ..., T_{N}\}$ (6.2)

$$e_{3} = \begin{cases} 1 & [\exists T_{i} \mid (V_{T_{i}} < V_{dis}^{Peak})] \\ 0 & [(V_{T_{i}} \ge V_{dis}^{Peak}) \, \forall \, T_{i}] \end{cases}$$
 where, $T_{i} \in \{T_{1}, T_{2}, ..., T_{N}\}$ (6.3)

Different modes m_{00} , m_{01} , m_{10} , m_{11} are executed based on the event combinations as expressed in (6.4). The modes are primarily triggered by e_2 and e_3 events. It should be noted that e_2 and e_3 are two mutually exclusive events, where e_2 can only occur in M_0 state and e_3 can only occur in M_1 state. Generally speaking, the machine remains in M_0 state until all the tags are fully charged. The machine then stays in M_0 state until atleast one of the tags is discharged or A_{T_i} is dispatched. In the instance of two tags dispatching A_{T_i} and A_{T_j} simultaneously where $(i \neq j)$, the reader will be unable to decipher as there will be information collision. To avoid this, the machine changes state to M_0 where the reader inquire each tag individually and sequentially.

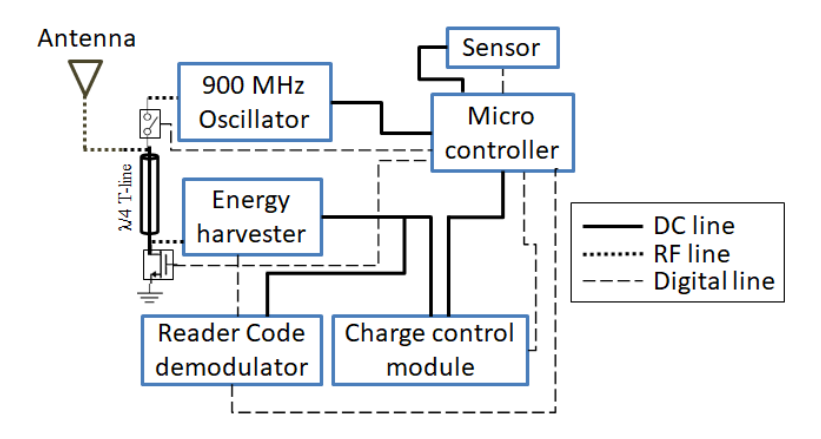


Figure 6.3: Different sub-modules of the tag circuit.

$$m_{00} = 1$$
, if $[(e_2 == 0)]$
 $m_{01} = 1$, if $[(e_2 == 1)\&\&(e_1 == 0)]$
 $m_{10} = 1$, if $[(e_3 == 1)||(e_1 == 1)]$
 $m_{11} = 1$, if $[(e_3 == 0)]$ (6.4)

6.3 System Architecture

As described earlier, the system includes multiple tags and a reader transceiver to obtain information from the tag both in backscatter and active-transmit mode. In this section, different parts of the tag circuit is described first, then the reader part is described.

6.3.1 Tag design

The complete tag circuit with the sub-modules is shown in Fig. 6.3. The tag contains:

1) Energy Harvester to harvest DC power from the RF power; 2) Reader Code Demodulator to decode specific instruction from the reader and act accordingly; 3) Oscillator to generate carrier frequency at 900 MHz; 4) Charge Control Module to store redundant charge and act

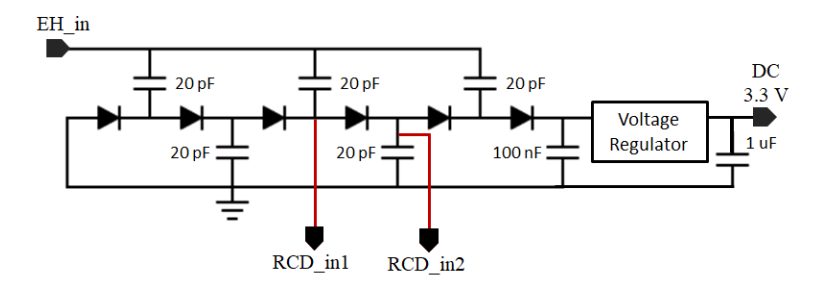


Figure 6.4: Energy harvester with 3-stage Dickson charge pump configuration.

as a power supply to the tag when the reader is not transmitting; 5) *Micro Controller* to perform the task activities; and finally 6) *Sensor* to monitor the intended parameter. Each of the sub-modules are described in detail as followed:

6.3.1.1 Energy harvester

The energy harvester converts the RF energy into DC for biasing, in order to supply DC bias to drive the peripheral circuits. Dickson charge pump configuration was used as the energy harvester as it converts DC voltage, and simultaneously boosts up the DC voltage at desired level [118]. From our previous analysis in Chapter 5, it was shown that more number of diodes help in boosting the DC voltage but simultaneously degrading the efficiency and charging rise time. Six diode based charge pump configuration was found to be optimum for the energy harvester. Very low barrier Schottky diode HSMS 2852 was used to harvest energy due to good efficiency. The generated DC voltage is regulated using a low power voltage regulator (TPS79733) at 3.3 V to drive the peripheral circuit. The schematic of the energy harvesting circuit is shown in Fig. 6.4, which takes EH_in as input RF and provides three output: 1) DC 3.3 V, and 2) RCD_in1, 3) RCD_in2 for the reader code demodulator.

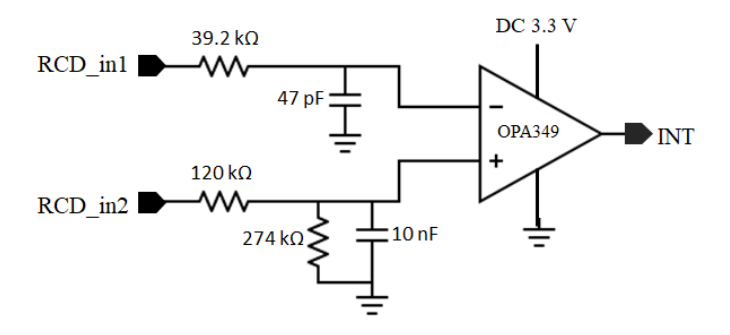


Figure 6.5: Reader code demodulator to decode reader instruction at the tag.

6.3.1.2 Reader code demodulator

The reader code demodulator decodes specific instruction from the reader and generates interrupt. To avoid tag reply collision, it is necessary that a single tag will reply at a time. In conventional RFID system, the tag reply collision is avoided by activating random counter in the tag. Randomizing the tag reply in this way minimizes the tag collision but do not fully mitigate it. By activating one tag at a time based, the system can avoid potential tag reply collision. Two low pass filters (LPF) are used in between the energy harvester and reader code demodulator to pass the low frequency reader demodulation signal and stop the high frequency RF signal as shown in Fig. 6.5. The schematic of the reader code demodulator is shown in Fig. 6.5. RCD_{in2} input provides reference level and RCD_{in1} carries the low frequency modulation. Both of the inputs are compared and interrupt INT is issued whenever RCD_{in1} is lower than RCD_{in2} . In addition to providing INT, the reader code demodulator sends the reader instruction signal through the same channel.

6.3.1.3 Oscillator

A standard oscillator in cross-couple configuration is used to generate the 900 MHz carrier as shown in Fig. 6.6. Two resistors of 10 k Ω are used to set the output voltage swing of

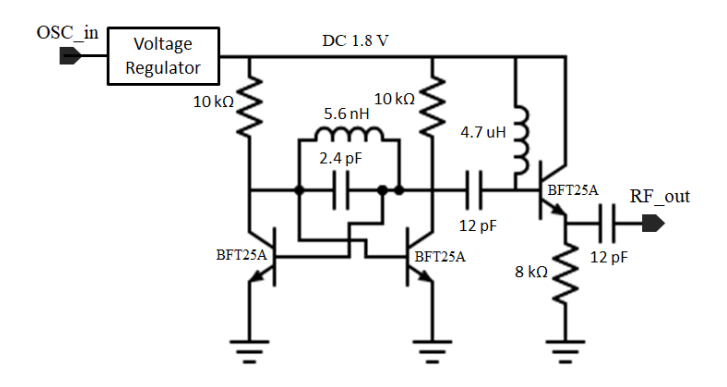


Figure 6.6: Oscillator circuit to generate 900 MHz RF carrier.

the RF output signal RF_out at low power consumption. LC tank was realized at 900 MHz using lumped 5.6 nH inductor and 2.4 pF of capacitance. BFT25A BJT with 5 GHz cut-off frequency was used to provide sufficient negative resistance for the tank to sustain oscillation. A common emitter buffer stage was used to drive the 50 Ω antenna system using the oscillator output. The base of the BJT in common emitter configuration is biased using a RF choke of 4.7 uH. Two 12 pF capacitors were used to isolate the DC biasing of cross-couple and common emitter configurations. The oscillator is triggered by micro-controller port signal, whose voltage level varies depending on the supply level of the micro-controller. The oscillator activation signal OSC_in was fed into a low power voltage regulator (TPS79718) to keep the voltage level fixed at 1.8 V and hence, the power consumption due to oscillator was fixed irrespective of the micro-controller supply voltage.

6.3.1.4 Charge control module

The charge control module uses a 2.2 mF capacitor to store energy in the tag locally and use that energy to power the tag circuit when energy is unavailable from the energy harvester as shown in Fig. 6.7(a). The charge control module uses two switches: a) current controlled switch, and b) bi-directional switch to charge the capacitor. At the initial stage of charging,

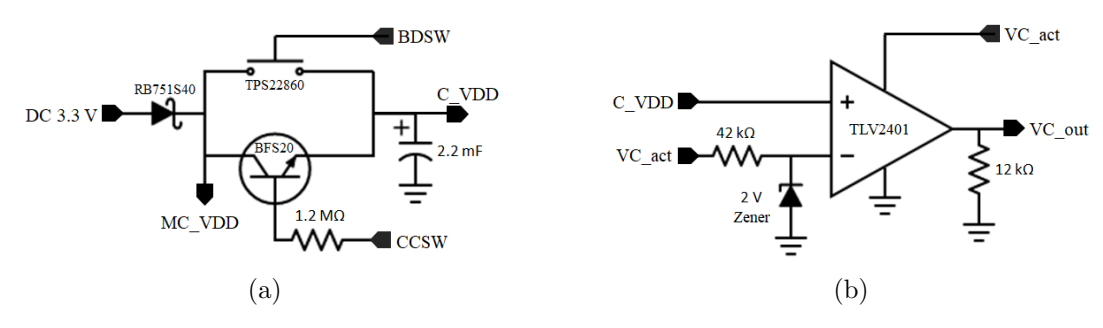


Figure 6.7: Charge control module with (a) switches and a 2.2 mF storage capacitor, and (b) voltage comparator.

the capacitor acts as a short circuit and hence charges rapidly resulting in dropping the DC voltage level of the energy harvester. When the voltage level drops from required level, the tag stops operating as desired. Hence, the charge flow in capacitor is controlled using a current controlled switch at the initial stage of charging. Once a threshold minimum voltage is reached at which the tag can perform, the charging is done through a bi-directional switch. As the charge flow is controlled in current controlled switch, it is slower, whereas charging through bi-directional switch is very fast. Control pins CCSW and BDSW are used to control the two switches. A very low barrier (0.1 V) and ultra low reverse leakage Schottky diode was used in between the energy harvester and rest of the peripheral to minimize the leakage power in reader code demodulator and energy harvester when the tag is operating on stored capacitor charge. MC_VDD is used to supply bias to the micro-controller and C_VDD denotes the voltage level of the capacitor.

A simple zener diode based reference is used for voltage comparator as shown in Fig. 6.7(b). The zener diode provides 2 V reference for activating CCSW from BDSW switch. To restrict power consumption, the voltage comparator is activated using $VC_act.\ C_VDD$ voltage level is compared with 2 V voltage level, and the comparator output is provided using VC_out as digital signal.

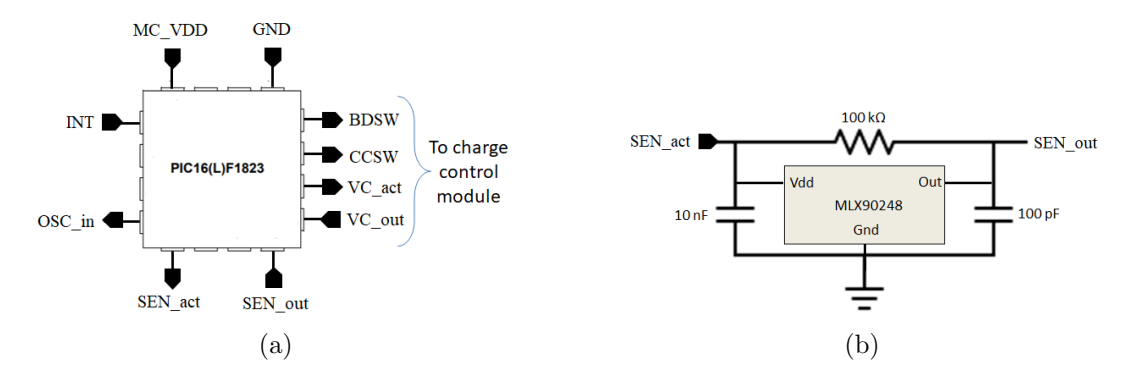


Figure 6.8: (a) Input and output ports connections of micro controller, and (b) sensor circuit configuration.

6.3.1.5 Micro controller

PIC16LF1823 with operating voltage at 1.8 V was used as the micro controller to perform the logical operations. The internal clock frequency was set at very low frequency of 31 kHz for low power consumption. The controller uses INT as external interrupt, which triggers different operational mode other than its usual operational mode. Different input and output ports of the controller are summarized in Fig. 6.8(a).

An example sensor was used as a test case. A medium power consuming sensor was used to show the efficacy of the proposed RFID system. A hall effect based sensor is used as an example sensor. The sensor with biasing components is shown in Fig. 6.8(b), where the sensor generates output depending on presence or absence of magnetic field. The sensor circuit is activated using SEN_act port and the sensor status is read from SEN_out port.

6.3.1.6 Antenna and front end

The tag requires an antenna and a RF front end consisting of RF switches to receive RF power and send oscillator trigger signals efficiently in M_0 and M_1 states respectively. A standard planar inverted-F antenna (PIFA) was designed to miniaturize the antenna structure and also to reduce human loading effect. Two different boards were used as shown in

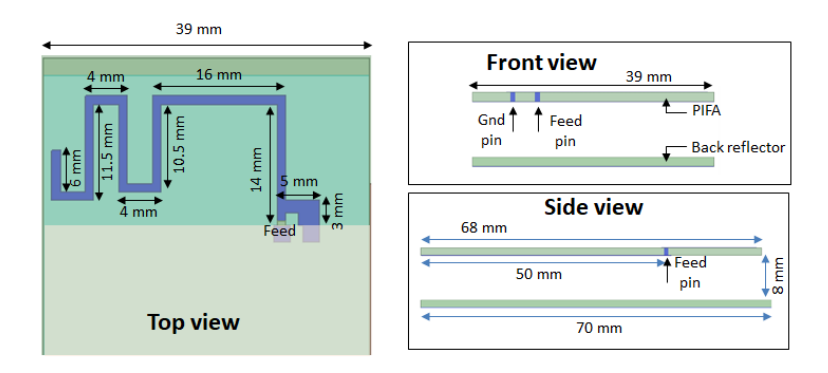


Figure 6.9: Antenna dimensions with front and side views.

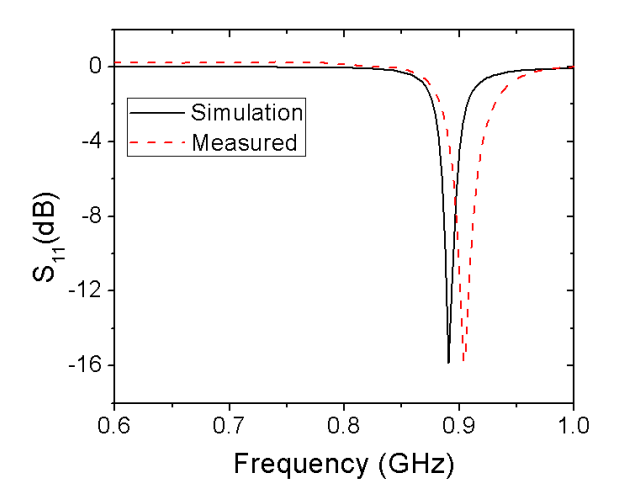


Figure 6.10: Simulated and measured PIFA antenna reflection co-efficient comparison.

front and side views in Fig. 6.9, where the PIFA is in top board and the bottom board is only back metal reflector. The back reflector was used to reduce the effect of any material from the backside of the antenna. The simulation and measurement results for reflection co-efficient (S_{11}) comparison of PIFA antenna is shown in Fig. 6.10.

6.3.2 Reader design

The reader circuit is shown in Fig. 6.11 with the RF front end, and the controller part.

The continuous frequency at 900 MHz generated by the source is modulated or controlled using a RF switch. A splitter is used to bifurcate the RF signal in two parts: a) one part

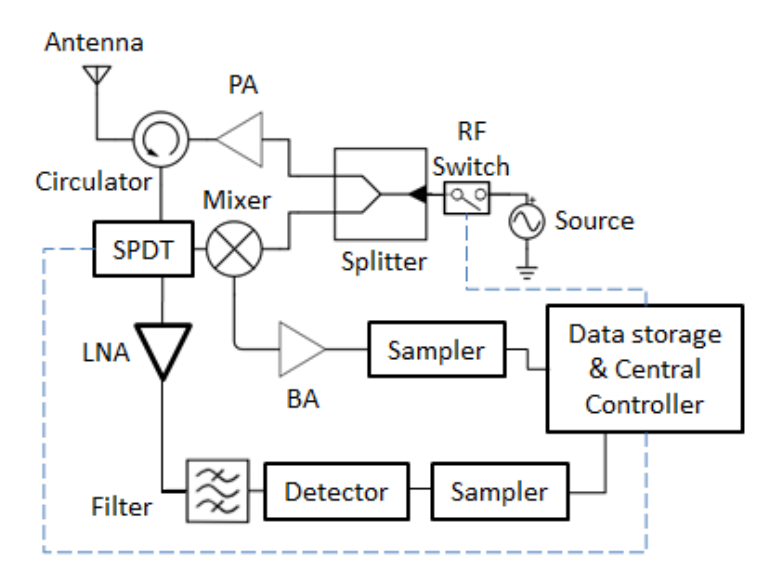


Figure 6.11: The reader to interrogate the tags in two modes.

is amplified using power amplifier (PA) and transmitted using an antenna; b) the other part is used in the mixer to downconvert the tag replied signal in M_0 state or backscatter communication mode. The circulator separates the transmit and received RF signal in the reader. After circulator, the tag return signal is fed into a SPDT switch, which directs the signal in two alternative paths. In M_0 state the signal is fed into the mixer, otherwise fed into a detector diode after passing through a bandpass filter at 900 MHz in tag active transmit mode or M_1 state. As the tag return signal is weak in both the modes, a baseband amplifier (BA) or a low noise amplifier (LNA) is used to amplify the tag signal. The two modes are controlled by interchanging the RF and SPDT switch. The RF switch is also used to send reader code targeted for specific tag reply. A high gain antenna (\sim 8 dBi) was used at the reader side to communicate with the tags.

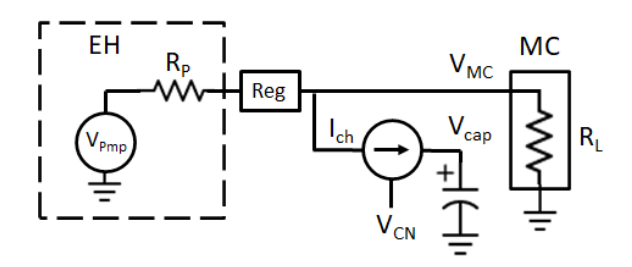


Figure 6.12: Charging of the capacitor using controlled current.

6.4 Charging and Discharging Operation

The tag has primarily two operational states: 1) backscatter communication, and 2) active transmission, as mentioned earlier. From charge holding point of view, the tag capacitor gets charged during the M_0 state and discharged during M_1 state. Now, for the reader to initiate and stop RF transmission, it is important to model the charging and discharging time at the tag.

6.4.1 Charging time

In the backscatter mode, the objective is to get the storage capacitor charged up. The charge control module uses two stages while charging the capacitor: a) controlled current charging, and b) bi-directional charging. To continue the tag microcontroller functional during charging of the storage capacitor, during the initial stage of charging, controlled current charging was used until the threshold voltage level V_{TH} is reached.

6.4.1.1 Controlled current charging

The equivalent circuit of the current controlled charging is shown as in Fig. 6.12, where the transistor emitter current is modeled as a voltage controlled current source I_{ch} . The energy harvester is modeled as equivalent source with V_{Pmp} and pump resistance R_P as

derived in Chapter 5. The impedance of micro controller is represented as an equivalent load resistance of R_L from its voltage current relationship. The micro controller and capacitor voltage level is shown as V_{MC} and V_{cap} . The transistor current I_{ch} is controlled by the voltage level of the switch signal CCSW, maintained by the micro controller and is denoted as V_{CN} , which can have maximum value of V_{MC} . In between energy harvester and the current control circuit, the voltage regulator and diode will regulate the V_{MC} level, and the maximum level of V_{MC} is defined as $V_{reg} - V_D$, where V_{reg} is the regulated output and V_D is forward diode voltage drop. By imposing KCL on the circuit as shown in Fig. 6.12, expression for V_{MC} level is obtained as in (6.5). It is important to note that the micro controller requires at least V_{lvl} supply voltage to remain operational. By using the bound $(V_{MC} \ge V_{lvl})$, the maximum bound on I_{ch} is expressed as $(I_{ch} \le V_{Pmp}/R_P - V_{lvl}/(R_P||R_L))$.

$$V_{MC} = min\left((R_P||R_L)\left(\frac{V_{Pmp}}{R_P} - I_{ch}\right), (V_{reg} - V_D)\right)$$

$$(6.5)$$

When V_{CN} is applied at the transistor base, the emitter current is obtained as in (6.6), where β is the forward current gain, R_B is base resistance, and $V_{BE,on}$ is base emitter onvoltage. V_{CN} can attain maximum value of V_{MC} , and hence $\alpha \leq 1$. Higher value of α is desired to maximize I_{ch} and hence shorter charging time for the storage capacitor. However, increasing I_{ch} will risk at dropping the V_{MC} level bellow V_{lvl} and hence, shutting down the whole system. Hence, I_{ch} should be optimally controlled by using the V_{MC} level during the initial stage. At the later stage of charging, once the capacitor starts accumulating charge, the voltage V_{cap} starts increasing and I_{ch} starts dropping. As a remedy, the value of α should be kept lower during initial charging stage and higher during later charging stage. Value of α can be controlled using micro-controller digital to analog converter (DAC). The

time dependent relation between I_{ch} and V_{cap} is expressed as in (6.7).

$$I_{ch} = \frac{\beta + 1}{R_B} (V_{CN} - V_{BE,on} - V_{cap})$$
 where,
$$V_{CN} = \alpha V_{MC}$$
 (6.6)

$$I_{ch} = C \frac{dV_{cap}}{dt} \tag{6.7}$$

Using V_{Pmp} and R_P values at different power level, at least -1 dBm input power is required to keep $V_{lvl}=2$ V for parameters at $\alpha=1$, $R_L=160$ k Ω , $V_{BE,on}=0.7$ V, $R_B=1.2$ M Ω , $\beta=80$, and C=2.2 mF. At -1 dBm input power, $V_{Pmp}=4.7$ V and $R_P=18$ k Ω are obtained for a three stage energy harvester from Chapter 5 analysis. In order to reduce the operating power of the tag while maintaining $V_{lvl}=2$ V, α should be less than 1 while keeping other parameters to be same. For example, when input power is -3 dBm, V_{Pmp} and R_P result as 3.8 V and 20 k Ω , and by solving (6.5) and (6.6) with initial condition as $V_{cap}=0$ V, $\alpha=0.86$ is required as the current controlled charging kicks in. α can only become 1 once V_{cap} reaches 0.26 V, which results in controlled current charging for at least 9.2 s with $\alpha=0.86$. The measured result of both conditions at -1 dBm and -3 dBm input power is shown in Fig. 6.13. When $\alpha=1$ starting from the begining for -3 dBm input power, the V_{MC} level falls below V_{lvl} during the initial 8 s.

6.4.1.2 Bi-directional charging

Once, V_{cap} reaches the V_{TH} level, the charging circuit switches on the bi-directional switch and turns off the current controlled switch for fast charging. The V_{cap} can be obtained by equating the power balance expression as in (6.8), where η is power conversion efficiency from RF to DC, and P_{RF} is input RF power. By imposing initial condition, time varying

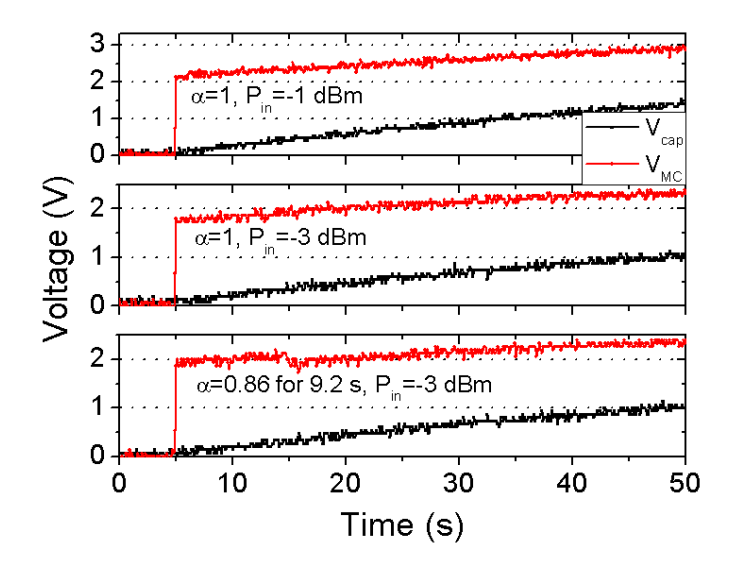


Figure 6.13: V_{MC} and V_{cap} voltage level for 3 cases: input power is -1 dBm and $\alpha = 1$, input power is -3 dBm and $\alpha = 1$, input power is -3 dBm and $\alpha = 0.86$ for initial 9.2 s and later $\alpha = 1$.

expression for V_{cap} is obtained as in (6.9).

$$\eta P_{RF} = CV_{cap} \frac{dV_{cap}}{dt} \tag{6.8}$$

$$V_{cap}(t) = V_{TH} + \sqrt{\frac{2\eta P_{RF}}{C}t}$$

$$\tag{6.9}$$

Now with understanding of the storage capacitor charging behavior, the charging voltage function $V_{ch}^{P}(\tau_{ch}, V_{TH})$ can be defined as the voltage level of the storage capacitor with peak value of $(V_{reg} - V_D)$, provided it reaches V_{TH} after a time τ_{ch} . Now, as the reader constantly monitors the voltage level of a tag, τ_{ch} will be known to the reader for a specific tag and the time required to reach from V_{TH} to $(V_{reg} - V_D)$ can be calculated based on (6.9). Then the total charging time T_{ch} for a specific tag will be as given in (6.10). Once the reader transmits RF power for T_{ch} duration, the reader sends end-of-transmit (EOT) signal to all the tags. Upon receiving EOT, all the tags enter into active transmit mode.

$$T_{ch} = \tau_{ch} + \frac{C(V_{reg} - V_D - V_{TH})^2}{2\eta P_{RF}}$$
 (6.10)

6.4.2 Discharging time

After all the tags are charged up, the reader stops transmitting and the storage capacitor starts slow discharging. To maximize the discharge time, two primary objectives are followed: a) leakage current within the tag components is as minimum as possible, and b) after knowing the sensor status, the micro controller quickly enters into sleep mode to conserve power. There are primarily four leakage current paths from the storage capacitor: 1) bi-directional switch internal leakage I_{sw} , 2) transistor emitter-base leakage I_{tran} , 3) voltage comparator positive input internal leakage I_{vc} , and 4) diode reverse leakage I_d . The micro-controller currents in sleep mode is considered as I_{sl} and in active mode as I_{ac} . Now with sensor current consumption as I_{sen} and the fractional active time as γ , the total current consumption I_{tot} can be expressed as (6.11). The discharging time τ_{dis} for a specific tag is given as in (6.12) for the voltage to drop from $(V_{reg} - V_D)$ to V_{TH} and the function is defined as $V_{dis}^P(\tau_{dis}, V_{DD})$, where $V_{DD} = V_{reg} - V_D$. The current consumption of the individual branches is provided in Table 6.1. $V_{dis}^P(\tau_{dis}, V_{DD})$ takes either τ_{dis} or V_{DD} as input and provides the other parameter as output.

$$I_{tot} = I_{sw} + I_{tran} + I_{vc} + I_{d} + \gamma * (I_{ac} + I_{sen})$$

$$+ (1 - \gamma) * I_{sl}$$
(6.11)

$$\tau_{dis} = \frac{C * (V_{reg} - V_D - V_{TH})}{I_{tot}} \tag{6.12}$$

Table 6.1: Current consumption branches.

Current branch	Value
I_{sw}	50 nA @ 3.2 V
I_{tran}	40 nA @ 3.2 V
I_{vc}	40 nA @ 3.2 V
I_d	60 nA @ 3.2 V
I_{ac}	10.2 uA @ 3.2 V
I_{sl}	1 uA @ 3.2 V
I_{sen}	10 uA @ 3.2 V
I_{osc}	400 uA @ 1.8 V

Although the current consumption in active mode is much higher compared to the sleep mode current consumption, I_{tot} can be reduced by keeping γ much lower. By employing the condition that the tag inquires the sensor once in every 250 ms, $\gamma = 0.002$ can be achieved.

When the oscillator is activated upon the sensor change event, the discharging of the storage capacitor is fast and the active mode discharging function is given as $V_{disosc}^{P}(V_f, V_{init})$, which takes V_{init} as initial voltage level of the capacitor before the oscillator starts and V_f as final voltage level after the tag stops transmitting. V_f is calculated based on the current consumption by the oscillator as I_{osc} , oscillator on time Δt , and V_{init} as in (6.13). The on time Δt is fixed at 1.5 ms, which is sufficient for the reader to detect tag transmitted RF signal.

$$V_f = V_{init} - \frac{I_{osc} * \Delta t}{C} \tag{6.13}$$

6.5 Measurement Results

Once, the working principle of the dual mode RFID is decided, both wired and wireless measurements were performed for validation. The complete fabricated wireless tag circuit and the fabricated PIFA antenna are shown in Fig. 6.14. The PIFA antenna has SMA outlet

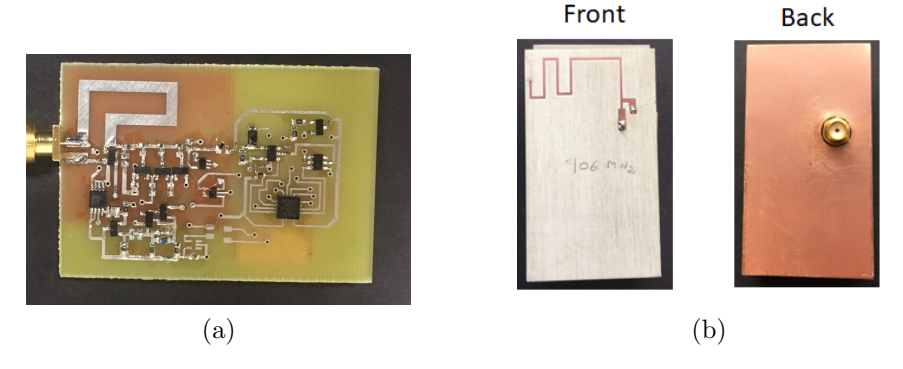


Figure 6.14: (a) Dual mode RFID tag circuit with SMA, and (b) front and back side of the PIFA antenna with SMA outlet, compatible to be embedded within seat.

from the backside, which was connected with the SMA outlet of the tag circuit using a SMA connector during wireless measurement.

The measured results for storage capacitor and micro-controller voltage level are shown in Fig. 6.15, due to charging switch control signal change. As mentioned earlier, there are two modes of charging: (a) controlled current charging, controlled by CCSW, and (b) bidirectional switch charging, controlled by BDSW. When the CCSW is active and BDSW is inactive, the storage capacitor charging is slower, which ramps up when the BDSW switch becomes active as shown in Fig. 6.15. Once the BDSW switch is active, the micro-controller and storage capacitor voltage levels get shorted and hence, the MC_VDD drops to same level as C_VDD .

To avoid tag collision, RCD module was integrated with the tag, which activates each and every tag sequentially based on the code sent from the reader. The scenario is shown pictorially in Fig. 6.16, where the tag only replies when it receives a specific code sequence. The RCD module is activated only when the MC_VDD reaches the V_{lvl} voltage, which depends upon the energy harvester time to harvest required voltage.

When the tag is measured in wireless setup, the information received at the reader from a dual mode tag is shown in Fig. 6.17. The tag returned raw signal is shown at the top, and

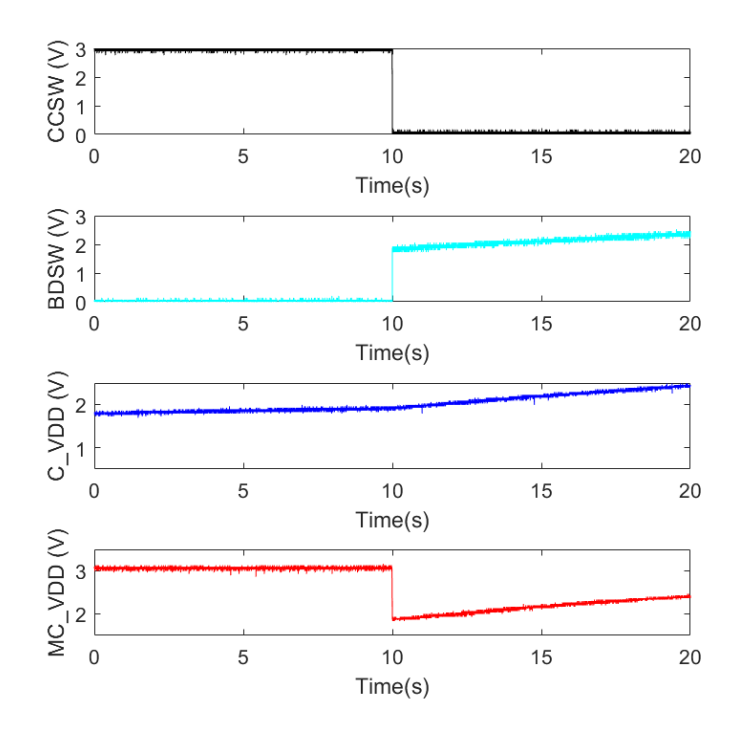


Figure 6.15: Storage capacitor and micro-controller voltage level at different switching signals.

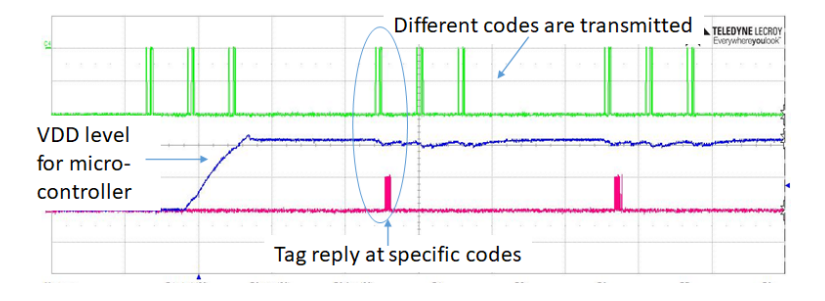


Figure 6.16: Activation of a dual mode tag due to specific code sent from the reader.

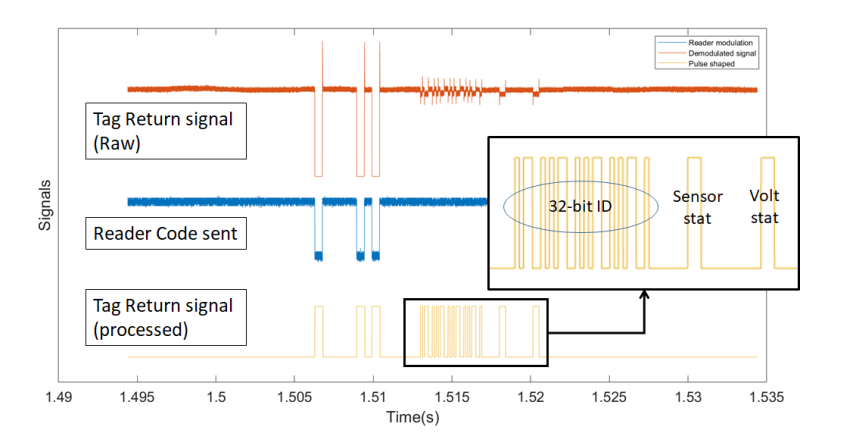


Figure 6.17: The information received at the reader sent by a dual mode RFID tag.

the processed signal is shown at the bottom. In the received bit-stream, the 32 bit ID, 1 bit sensor information, and 1 bit voltage status information are sequentially sent. The voltage status signal goes from '0' to '1' when the C_VDD level crosses the V_{TH} voltage level. The sensor status shows the presence or absence of a magnet as bit '0' and '1' respectively.

Finally, the sensor monitoring during the active transmit state was measured. The dual mode tag takes 2.5 minutes to charge up completely during initial stage and only 0.5 minutes in successive charging events. While discharging, if there is no sensor status change, the tag can monitor the sensor locally for 30 minutes. Each tag interrogates the sensor locally once in every 250 us. Hence, at worst case scenario, the reader knows of a sensor event change within 1 second.

6.6 Summary

In this work, the working principle of a dual mode RFID sensor tag is described and experimentally validated. The RFID tag monitors the sensor locally and in case of an event trigger, the tag notifies the the reader. Any analog or digital sensor can be integrated with the proposed dual mode RFID system. The sensor integrated dual mode tag showed a

significant reduction in transmit time from the reader. The transmit time reduction strongly depends upon how many times the tag sends the alert signal to the reader. This scenario is beneficial for a sensor, which doesn't change its state frequently. The proposed dual mode RFID tag has strong potential for a sensor networks such as hospital system or modern transport system, where reduced RF transmission around the patients or passengers is a desired goal.

Chapter 7

Conclusion

Four primary challenges of a conventional RFID based batteryless system are identified:

(a) clutter effect, (b) sensor integration, (c) response time, and (d) RF radiation. Many possible scenarios for how the challenges arise are discussed with various applications. Next, solutions are proposed for each of the challenges as (a) harmonic RFID for enhanced operation under cutter effect, (b) low power digital interface sensing platform for electrochemical sensor electrode integration for biochemical applications, (c) component level circuit analysis to model the harvesting efficiency and response time, and finally (d) dual mode RFID to effectively reduce the RF radiation.

A miniaturized single antenna based harmonic RFID tag was developed and demonstrated with prototype. This harmonic RFID tag only requires the harmonic generator as an extra component in addition to other components used in conventional RFID. The harmonic RFID will provide a better SNR compared to conventional RFID in presence of clutter.

A pH sensor integrated RFID tag was fabricated and demonstrated for biochemical applications. The proposed sensing system illustrates a low power digital interface for analog sensors. The architecture is scalable and multiple sensors can be integrated with a single RFID.

A dual mode RFID tag was also developed and shown to reduce the effective on time of RFID reader. The dual mode RFID tag stores the redundant harvested energy and can use the energy to monitor a sensor locally. The RFID reader will not be required to transmit RF power during this local monitoring. In dual mode tag, the tag can synthesize its own carrier and use it for communication while the reader does not provide any carrier.

Harmonic RFID, sensor integrated RFID, and dual mode RFID has inter-compatibility and one can be merged with other as per requirement. Hence, a hybrid RFID can be formed by integrating all the three RFID structures. In many applications, combination of the four primary challenges can arise and a hybrid RFID will be capable in mitigating the challenges simultaneously.

7.1 Future Work

In this thesis work, the primary work was development of different functional elements of hybrid RFID system and the reported prototypes were fabricated on a Printed Circuit Board (PCB) with discrete components. The final circuit board was quite big due to use of individually packaged components. The proposed future work primarily focuses on three aspects: (a) miniaturization, (b) security, and (c) packaging.

7.1.1 Miniaturization

The complete circuit of a hybrid RFID tag can be miniaturized greatly by using monolithic fabrication of different modules on a single substrate. There are primarily three parts for a hybrid RFID tag: (a) RF part, (b) digital part, and (c) antenna. In the current designs, the RF part consumes the primary real estate area. Using monolithic fabrication of CMOS process, a hybrid RFID tag can be miniaturized to a comparable size of conventional RFID tag circuit.

Apart from the tag circuit area, another area consuming part is antenna. While the tag circuit area can be miniaturized using monolithic fabrication without compromising the circuit performance, the antenna miniaturization is related to the tag performance. As the antenna gets smaller, the radiation efficiency reduces, impacting on the overall tag performance. There are primarily two ways for miniaturizing the tag antenna: a) use of material with high relative permittivity, or permeability, or both; and b) efficient design. Use of high dielectric constant substrate or magnetic material can reduce the effective wavelength and hence the overall antenna dimension will be smaller. However, the substrate loss increases at high frequency with increase in relative permittivity or permeability of a material. Again, a tradeoff should be maintained, as the antenna miniaturization taking advantage of material property will impact on the antenna performance. On the other hand, using optimized design with miniaturized size and considerable gain is very much desired. Use of an optimization tool such as genetic algorithm (GA) or particle swarm optimization (PSO) for antenna optimization will be helpful for optimizing with multiple objectives such as gain maximization and area minimization. Also, antennas are usually designed as a two-dimensional planar structure. Taking advantage of all the three dimensions can help in minimizing the antenna structure without sacrificing much gain. However, fabrication in bulk and installing the RFIDs with 3D antenna will be a challenge.

7.1.1.1 Electrically small antenna

In attempt to continue the above miniaturization challenges specifically for antenna, it is worthwhile to mention the requirement of small antenna design. A small antenna is defined as electrically small antenna with maximum dimension $< \lambda/3$, where λ is the effective wavelength. A significant amount of research has been done previously on small antenna and

it would be worthwhile to mention the development and integration of small antennas with RFID tags [138–140]. With antenna dimension becoming smaller, the fundamental challenges appear as reduced bandwidth, reduced gain, and reduced coupling with reader antenna, all of which can effect on the RFID system performance [140–142]. Hence, apart from making the tag antenna smaller, a broader level system analysis should also be performed keeping those three factors in mind.

7.1.2 Security

The only authentication of a RFID tag is the identification bits, which can be cloned and can be a big security breach. In next five years, there is an estimated 19.21% compound annual growth rate of RFID devices in the electronic payment market. For at least this reason, there is a need to procure data securely from RFID sensors. A tamper-proof secured RFID tag can be implemented using multiple harmonics monitoring technique [143]. An extra layer of authentication can be added to existing RFID tags by monitoring multiple harmonics. As there will always be tolerance in the components used to design the NLTL, there will always be different mismatch in the impedance of a single NLTL stage resulting in a different amplitude level and phase of the received harmonic levels. The different higher order harmonics would be a unique signature or fingerprint of the specific hybrid RFID tag under identical excitation modulation signals. The relative power level and the phase difference of the higher order harmonics is stored for a specific RFID during initial activation and always verified later against the information. A wide band antenna capable of transmitting multiple harmonics is necessary for both the RFID tag and the reader.

7.1.3 Packaging

Bulk scale packaging technology is important for hybrid RFID tags as that can effectively reduce the final cost of the hybrid RFID tag. The hybrid RFID tag will have primarily three components, which need to be integrated at the final stage of packaging: 1) antenna, 2) RFID IC, and 3) sensing elements. Single frequency resonating antenna is required for a hybrid RFID tag except harmonic operation. Hence, options for antenna can be kept at final stage of integration. Like conventional RFID, the hybrid RFID IC can be fabricated separately and then integrated with the desired antenna at the final stage of packaging. The electrochemical material requirement is different for different parameter sensing, hence the sensors need to be fabricated separately. At the final stage of packaging, the desired sensor heads can be integrated with the hybrid RFID IC along with the antenna. Different bulk printing techniques such as pad printing or inkjet printing can be used for the final stage integration. Pad printing is a fast printing technique for thin-film substrate based integration, whereas inkjet printing is more desired for fine resolution. Combination of those two printing techniques can be used for a complete hybrid RFID fabrication. The antenna can be manufactured using pad printing, whereas inkjet printing can be used for interconnect printing between antenna, IC, and sensors together.

APPENDICES

APPENDIX A

Modulation Depth Formulation of

RFID Tag Impedance

A simplified representation of coupled reader and tag antenna with different dimensions is shown in Fig. A.1. The center of the two antennas are at z = 0, and separated by r_0 . As shown in Fig. A.1, both the antennas are cylindrical center-fed dipoles. The two antenna network can be represented as a four-terminal impedance network as shown in Fig. A.2.

The impedance network with different impedance parameters is shown in Equation (A.1). For a reciprocal network, we can write $Z_{12} = Z_{21}$. In Equation (A.1), V_1 and V_2 represents the voltage across the antenna terminals and $I_1(0)$ and $I_2(0)$ represents the current flowing into the feeding terminals at location z = 0. Now, if the tag antenna is terminated with a load impedance Z_L , the terminal voltage of the tag will be according to Equation (A.2).

$$V_1 = Z_{11}I_1(0) + Z_{12}I_2(0)$$

$$V_2 = Z_{21}I_1(0) + Z_{22}I_2(0)$$
(A.1)

$$V_2 = -Z_L I_2(0) (A.2)$$

$$V_1 = \left[Z_{11} - \frac{Z_{12}^2}{Z_{22} + Z_L} \right] I_1(0) \tag{A.3}$$

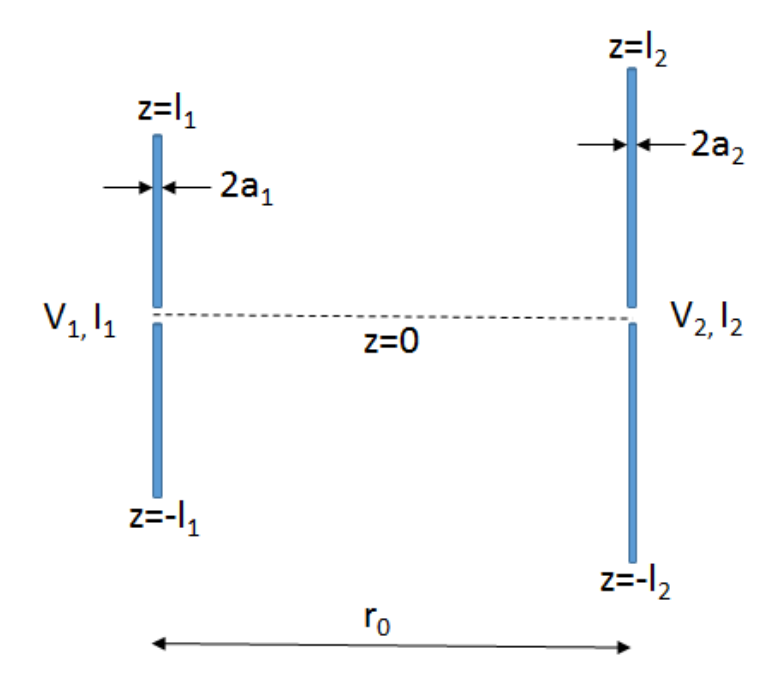


Figure A.1: Two cylindrical dipole antennas with different dimensions.

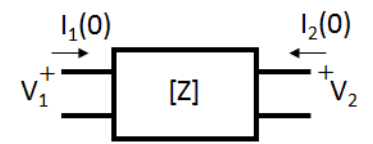


Figure A.2: Four-terminal impedance network for two antenna system.

Using reciprocity and substituting Equation (A.2) in Equation (A.1), we can obtain a relationship between V_1 and $I_1(0)$, which is given in Equation (A.3). Now in Equation (A.3), there are two parts in the impedance expression. If the input impedance of reader antenna is considered as $Z_{in,1}$ in free space, then the back-scattered voltage V_r^s induced by tag antenna at the reader antenna is given in Equation (A.4).

$$V_1 = V_r^s + Z_{in,1}I_1(0) (A.4)$$

$$V_r^s = \left[\left(Z_{11} - Z_{in,1} \right) - \frac{Z_{12}^2}{Z_{22} + Z_L} \right] I_1(0) \tag{A.5}$$

Packlington's EFIE for a single antenna

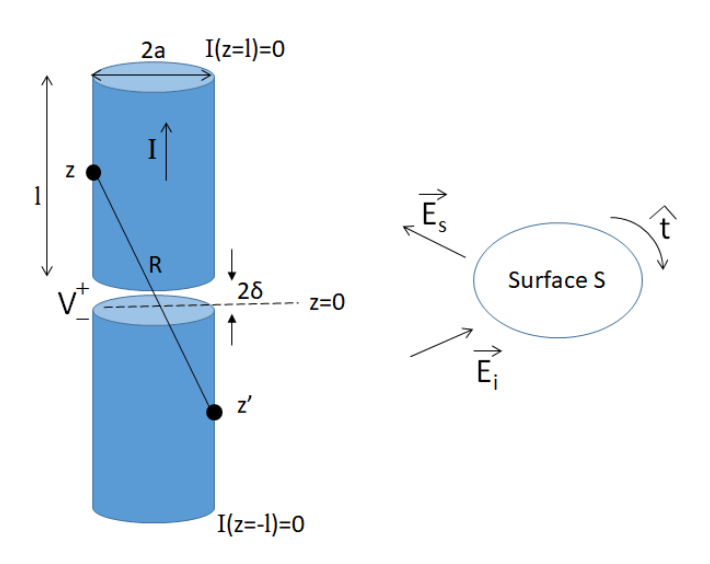


Figure A.3: A single center-fed dipole antenna.

Before deriving the system of equations for two antenna system, first the Electric Field Integral Equation (EFIE) is formed for a single antenna. To begin with, a few approximations are considered. First, the antennas are considered as center-fed cylindrical dipole. 'Thin-wire' approximation is considered for the antenna, which means dipole length is much higher

than dipole diameter. 'Slice-gap' terminal generator model is used at the feed point of the antenna. And finally, the antenna is considered made of a perfect conductor. The schematic of the antenna is provided in Fig. A.3. On a perfect conductor surface, the total tangential electric field is zero. Hence, we can write

$$\hat{t} \cdot \vec{E} = 0$$
 or,
 $\hat{t} \cdot (\vec{E_i} + \vec{E_s}) = 0$ (A.6)

The electric filed \vec{E} represents the total electric field. $\vec{E_i}$ represents the impressed electric field, which excites the system and $\vec{E_s}$ represents the scattered electric field due to induced current \vec{J} excited by $\vec{E_i}$. In the following notations, \vec{r}' denotes the source vector and \vec{r} denotes the vector at evaluation point, on the surface of conductor. We can write $\vec{E_s}(\vec{r})$ due to $\vec{J}(\vec{r}')$ as below

$$\vec{E}_s(\vec{r}) = -\frac{j\eta}{\beta} \int_S \left[\nabla' \cdot \vec{J}(\vec{r}') \nabla + \beta^2 \vec{J}(\vec{r}') \right] \frac{e^{-jkR}}{4\pi R} dS'$$
 (A.7)

 $\vec{J}(\vec{r}')$ denotes the surface current on surface S and \hat{t} is an unit vector tangential to the surface. In Equation (A.7), η is given as $\sqrt{\mu/\epsilon}$ and β is provided as $\omega\sqrt{\mu\epsilon}$, where μ is the permeability and ϵ is the permittivity of the medium through which \vec{E}_s propagates. Substituting Equation (A.7) in Equation (A.6), the following expression can be shown. With the 'slice-gap' model, the terminal voltage at the antenna input can be substituted in Equation (A.8) to form Equation (A.9). In Equation (A.9), $\delta(z)$ is dirac delta function.

$$\frac{j\eta}{4\pi\beta} \int_{S} \left[\nabla' \cdot \vec{J}(\vec{r}') \,\hat{t} \cdot \nabla + \beta^{2} \hat{t} \cdot \vec{J}(\vec{r}') \right] \frac{e^{-jkR}}{R} \, dS' = \hat{t} \cdot \vec{E}_{i}(\vec{r}) \tag{A.8}$$

$$\frac{j\eta}{4\pi\beta} \int_{S} \left[\nabla' \cdot \vec{J}(\vec{r}') \,\hat{t} \cdot \nabla + \beta^{2} \hat{t} \cdot \vec{J}(\vec{r}') \right] \frac{e^{-jkR}}{R} \, dS' = V \delta(z - 0) \tag{A.9}$$

For a thin wire antenna as shown in Fig. A.3, the current distribution is primarily a function along the \hat{z} distribution and is a weak function of radial distribution. By considering the current distribution $\vec{J}(\vec{r}') = f(\phi')I(z')\hat{z}'$ along the wire length, and few vector operations, the EFIE can be modified as shown in Equation (A.10). In Equation (A.10), $f(\phi')$ represents the circular current distribution function and Γ is the axial path along which the line integral is performed.

$$\frac{j\eta}{4\pi\beta} \int_{\Gamma} \left[\frac{\partial I(z')}{dz'} \frac{\partial}{\partial z} + \beta^2 I(z') \right] \oint_{C} f(\phi') \frac{e^{-jkR}}{R} d\phi' dz' = V\delta(z)$$
 (A.10)

After proper substitution of vector operators, and finally substituting the boundary conditions of current at the dipole ends, which is I(l) = I(l') = 0, Equation (A.10) takes form of famous Packlington's form of EFIE as shown in Equation (A.11), where $g(z|z') = \frac{e^{-jkr}}{4\pi r}$ and $r = \sqrt{((z-z')^2 + a^2)}$.

$$\frac{j\eta}{4\pi\beta} \int_{-l}^{l} \left[\frac{\partial^2}{\partial z^2} + \beta^2 \right] I(z')g(z|z') dz' = V\delta(z)$$
(A.11)

Coupling of two antennas

Once the EFIE is formulated for a single antenna, it can be extended to a system of two or more antennas. For back-scattering analysis, only two antennas are considered. The formulation for two antenna system as shown in Fig. A.1 becomes

$$V_1\delta(z) = \int_{-l_1}^{l_1} I_1(z')G_{11}(z|z') dz' + \int_{-l_2}^{l_2} I_2(z')G_{12}(z|z') dz'$$
(A.12)

$$V_2\delta(z) = \int_{-l_1}^{l_1} I_1(z')G_{12}(z|z') dz' + \int_{-l_2}^{l_2} I_2(z')G_{22}(z|z') dz'$$
(A.13)

where,
$$G_{11}(z-z') = \frac{j\beta\eta}{4\pi} \left(1 + \frac{1}{\beta^2} \frac{\partial^2}{\partial z^2}\right) \frac{e^{-jk\sqrt{((z-z')^2 + a_1^2)}}}{\sqrt{((z-z')^2 + a_1^2)}}$$

The other kernels G_{12} and G_{22} are obtained by replacing a_1 with r_0 and a_2 in Equations (A.12), (A.13), where r_0 and a_2 are distance between the two antennas and radius of the tag-side antenna as shown in Fig. A.1.

Variational formulation

Equations (A.12), (A.13) are the founding equation set for the variational formulation. In the following, steps from [33] is followed to establish the variation relation of the impedance. Once, Equation (A.1) is substituted in Equations (A.12) and (A.13), the equation pair becomes as shown in Equation (A.14) and (A.15).

$$\left[Z_{11}I_{1}(0) + Z_{12}I_{2}(0)\right]\delta(z) = \int_{-l_{1}}^{l_{1}} I_{1}(z')G_{11}(z|z')dz' + \int_{-l_{2}}^{l_{2}} I_{2}(z')G_{12}(z|z')dz' \quad (A.14)$$

$$\left[Z_{12}I_{1}(0) + Z_{22}I_{2}(0)\right]\delta(z) = \int_{-l_{1}}^{l_{1}} I_{1}(z')G_{12}(z|z') dz' + \int_{-l_{2}}^{l_{2}} I_{2}(z')G_{22}(z|z') dz' \quad (A.15)$$

Let, $I'_1(0)$ and $I'_2(0)$ be another pair of feeding current, then $I'_1(0)$ and $I'_2(0)$ pair will also satisfy the Equations (A.14) and (A.15). If Equation (A.14) is multiplied by $I'_1(z)$ and Equation (A.15) by $I'_2(z)$ followed by integration of both of them individually from $-l_1$ to

 l_1 and $-l_2$ to l_2 . After integration, followed by summing up, one obtains Equation (A.16). For Equation (A.16), at the left hand side, the integration results $\int_{l_1}^{l_1} I_1(z)\delta(z)dz = I_1(0)$ and $\int_{l_2}^{l_2} I_2(z)\delta(z)dz = I_2(0)$ are used.

$$I'_{1}(0)Z_{11}I_{1}(0) + I'_{1}(0)Z_{12}I_{2}(0) + I'_{2}(0)Z_{21}I_{1}(0) + I'_{2}(0)Z_{12}I_{2}(0)$$

$$= \int_{-l_{1}-l_{1}}^{l_{1}} \int_{-l_{1}-l_{2}}^{l_{1}} I_{1}(z')G_{11}(z|z')I'_{1}(z) dz' dz + \int_{-l_{1}-l_{2}}^{l_{1}} \int_{-l_{1}-l_{2}}^{l_{2}} I_{2}(z')G_{12}(z|z')I'_{1}(z) dz' dz$$

$$+ \int_{-l_{2}-l_{1}}^{l_{2}} \int_{-l_{2}-l_{2}}^{l_{1}} I_{1}(z')G_{12}(z|z')I'_{2}(z) dz' dz + \int_{-l_{2}-l_{2}}^{l_{2}} \int_{-l_{2}-l_{2}}^{l_{2}} I_{2}(z')G_{22}(z|z')I'_{2}(z) dz' dz$$

$$(A.16)$$

Once, we obtain Equation (A.16), one can substitute $I'_1(0) = I_1(0)$ and $I'_2(0) = I_2(0)$ as the current pair $I_1(0), I_2(0)$ and $I'_1(0), I'_2(0)$ excite same system. With same excitation current, the distribution currents become also same, reducing to $I'_1(z) = I_1(z)$ and $I'_2(z) = I_2(z)$. Also, by exchanging z' and z variables of the third integrand in Equation (A.16) and due to $(G_{12}(z|z') = G_{12}(z'|z))$, one can obtain Equation (A.17).

$$Z_{11}I_{1}^{2}(0) + 2Z_{12}I_{1}(0)I_{2}(0) + Z_{22}I_{2}^{2}(0)$$

$$= \int_{-l_{1}-l_{1}}^{l_{1}} \int_{-l_{1}}^{l_{1}} I_{1}(z')G_{11}(z|z')I_{1}(z) dz' dz + 2\int_{-l_{1}-l_{2}}^{l_{1}} \int_{-l_{2}}^{l_{2}} I_{2}(z')G_{12}(z|z')I_{1}(z) dz' dz$$

$$+ \int_{-l_{2}-l_{2}}^{l_{2}} \int_{-l_{2}}^{l_{2}} I_{2}(z')G_{22}(z|z')I_{2}(z) dz' dz$$
(A.17)

Using Equation (A.17), one can relate the variational relation in between current and

impedance. If a small variation of current at the antenna input terminal is considered about its true value, in Equation (A.17), one can replace $I_1(0)$ with $I_1(0) + \delta I_1(0)$, $I_2(0)$ with $I_2(0) + \delta I_2(0)$. Due to the excitation current change, if there is any change in impedance, which one can consider as $Z_{11} + \delta Z_{11}$, $Z_{12} + \delta Z_{12}$, and $Z_{22} + \delta Z_{22}$. A subsequent change in current distribution is also expected, which is considered as $I_1(z') + \delta I_1(z')$ and $I_2(z') + \delta I_2(z')$ in place of $I_1(z')$ and $I_2(z')$ correspondingly. In this analysis, only first order variation is considered, which means any second order variations are neglected. The second order variations such as $(\delta I_i(0))^2$, $(\delta Z_{ij})^2$, $\delta Z_{ij}\delta Z_{ji}$, $\delta I_i(0)\delta Z_{ij}$, and $\int \int \delta I_i(z')G_{ij}(z|z')\delta I_j(z)dz'dz$ are considered as 0, where i=1,2, and j=1,2. After substitution and simplification, Equation (A.17) can be expressed as in Equation (A.18).

$$\delta Z_{11}I_{1}^{2}(0) + 2\delta Z_{12}I_{1}(0)I_{2}(0) + \delta Z_{22}I_{2}^{2}(0)$$

$$+2\delta I_{1}(0) \left[Z_{11}I_{1}(0) + Z_{12}I_{2}(0)\right] + 2\delta I_{2}(0) \left[Z_{12}I_{1}(0) + Z_{22}I_{2}(0)\right]$$

$$=2\left[\int_{-l_{1}-l_{1}}^{l_{1}} \int_{-l_{1}}^{l_{1}} \delta I_{1}(z')G_{11}(z|z')I_{1}(z) dz' dz + \int_{-l_{1}-l_{2}}^{l_{1}} \int_{-l_{2}}^{l_{2}} \delta I_{2}(z')G_{12}(z|z')I_{1}(z) dz' dz \right]$$

$$+\int_{-l_{2}-l_{1}}^{l_{2}} \int_{-l_{1}}^{l_{1}} \delta I_{1}(z')G_{12}(z|z')I_{2}(z) dz' dz + \int_{-l_{2}-l_{2}}^{l_{2}} \int_{-l_{2}-l_{2}}^{l_{2}} \delta I_{2}(z')G_{22}(z|z')I_{2}(z) dz' dz \right]$$

$$(A.18)$$

By multiplying Equations (A.14) and (A.15) with $\delta I_1(z)$ and $\delta I_2(z)$ consecutively, integration can be performed on them individually from $-l_1$ to l_1 and $-l_2$ to l_2 . After addition of the two integrations, one can obtain Equation (A.19). After substitution of Equation (A.19) in Equation (A.18), one can obtain Equation (A.20).

$$\delta I_{1}(0) \left[Z_{11} I_{1}(0) + Z_{12} I_{2}(0) \right] + \delta I_{2}(0) \left[Z_{12} I_{1}(0) + Z_{22} I_{2}(0) \right]$$

$$= \int_{-l_{1} - l_{1}}^{l_{1}} \int_{-l_{1} - l_{2}}^{l_{1}} \delta I_{1}(z') G_{11}(z|z') I_{1}(z) dz' dz + \int_{-l_{1} - l_{2}}^{l_{1}} \int_{-l_{1} - l_{2}}^{l_{2}} \delta I_{2}(z') G_{12}(z|z') I_{1}(z) dz' dz$$

$$+ \int_{-l_{2} - l_{1}}^{l_{2}} \int_{-l_{2} - l_{2}}^{l_{1}} \delta I_{1}(z') G_{12}(z|z') I_{2}(z) dz' dz + \int_{-l_{2} - l_{2}}^{l_{2}} \int_{-l_{2} - l_{2}}^{l_{2}} \delta I_{2}(z') G_{22}(z|z') I_{2}(z) dz' dz$$

$$(A.19)$$

$$\delta Z_{11}I_1^2(0) + 2\delta Z_{12}I_1(0)I_2(0) + \delta Z_{22}I_2^2(0) = 0$$
(A.20)

The only solution to Equation (A.20) is $\delta Z_{11} = \delta Z_{12} = \delta Z_{22} = 0$. The solution is very important from the variational method. This shows if approximate currents differ from the true currents by first order errors, the impedance parameters differ from true values by second order error. Hence, an approximate current would provide a somewhat more accurate impedance result.

Current approximation in linear dipole

The current distribution in the dipole antennas can now be approximated to obtain the impedance parameters. Using the analytical current distribution at antenna 1 and antenna 2, the impedance parameter can be obtained. A reasonable current distribution over linear antennas can be assumed as linear combination of a constant term, a sine term, and a cosine term as shown in Equation (A.21). Using the conditions as I(z) = I(-z), I(l) = I(-l) = 0, and I(0) as the feeding terminal current, Equation (A.21) reduces to Equation (A.22).

$$I(z) = a + b\cos\beta z + c\sin\beta z \tag{A.21}$$

$$I(z) = I(0)\frac{\cos\beta z - \cos\beta l}{1 - \cos\beta l} + k\left[\sin\beta(l - |z|) + \sin\beta|z| - \sin\beta l\right]$$

$$I(z) = I^{0}(z) + kI^{1}(z)$$
(A.22)

where
$$k = \frac{c}{1 - \cos\beta l}$$

However, the above approximation fails to represent the current distribution when $l \geq \lambda$. Since both sine and cosine terms are periodic functions, their values start repeating as the argument βz changes by 2π . A better approximation can be formed by introducing another term $\cos \frac{\beta z}{2}$ and the current distribution takes form of three term King Wu current approximation. In this analysis, as dipole length upto $l = \lambda$ is considered for both the reader and tag antennas, current distribution as in Equation (A.21) is sufficient for this analysis.

Modulation depth formulation

Now in scenario of A.2, if both the antennas are fixed at their positions and the load impedance of antenna 2 or tag antenna is changed, then the back-scattered voltage V_r^s at antenna 1 terminal would be changed according to Z_L . By changing the impedance Z_L sequentially, the voltage V_r^s will be modulated and that is how information from RFID tag can be obtained at the RFID reader. For example, if $V_r^s(1)$ is induced due to Z_{L1} and $V_r^s(2)$ due to Z_{L2} , the tag would be more easily detectable with higher difference between $V_r^s(1)$ and $V_r^s(2)$. The quantity $(V_r^s(1)-V_r^s(2))$ is termed as the modulation depth. It is inquisitive to find load impedance values for set $\{Z_{L1}, Z_{L2}\}$ to maximize the modulation depth.

$$V_r^s(2) - V_r^s(1) = Z_{12}^2 \left[\frac{1}{Z_{22} + Z_{L2}} - \frac{1}{Z_{22} + Z_{L1}} \right] I_1(0)$$
 (A.23)

Now, the current distribution from Equation (A.22) can be used in Equation (A.16)

to find expressions for different impedance parameters. From Equation (A.23), only the impedance parameters Z_{22} and Z_{12} need to be found. According to [33], for Z_{22} , considering $I'_1(0) = I_1(0) = 0$ and $I'_2(0) = I_2(0)$ in Equation (A.17) provides Equation (A.24). And choosing $I_1(0) = I'_2(0) = 0$ in Equation (A.16) would provide Z_{12} as provided in Equation (A.25).

$$Z_{22}I_{2}^{2}(0) = \int_{-l_{1}-l_{1}}^{l_{1}} \int_{-l_{1}-l_{1}}^{l_{1}} I_{1}(z')G_{11}(z|z')I_{1}(z) dz' dz + 2 \int_{-l_{1}-l_{2}}^{l_{1}} \int_{-l_{1}-l_{2}}^{l_{2}} I_{2}(z')G_{12}(z|z')I_{1}(z) dz' dz + \int_{-l_{2}-l_{2}}^{l_{2}} \int_{-l_{2}-l_{2}}^{l_{2}} I_{2}(z')G_{22}(z|z')I_{2}(z) dz' dz$$
(A.24)

$$I'_{1}(0)Z_{12}I_{2}(0) = \int_{-l_{1}-l_{1}}^{l_{1}} \int_{-l_{1}-l_{1}}^{l_{1}} I_{1}(z')G_{11}(z|z')I'_{1}(z) dz' dz + \int_{-l_{1}-l_{2}}^{l_{1}} \int_{-l_{1}-l_{2}}^{l_{2}} I_{2}(z')G_{12}(z|z')I'_{1}(z) dz' dz + \int_{-l_{2}-l_{2}}^{l_{2}} \int_{-l_{2}-l_{2}}^{l_{2}} I_{2}(z')G_{22}(z|z')I'_{2}(z) dz' dz + \int_{-l_{2}-l_{2}}^{l_{2}} \int_{-l_{2}-l_{2}}^{l_{2}} I_{2}(z')G_{22}(z|z')I'_{2}(z) dz' dz$$
(A.25)

Approximation for short dipole at reader side

The set of equations becomes simplified with approximation of short dipole at the reader side. With short dipole approximation only for reader antenna, the impedance parameters in Equations (A.24) and (A.25) can be simplified for the coupled antenna system. For small dipole with $(r_0 >> l_2)$ reasonable approximations as $G_{12}(z|z') = G_{12}(z')$ for $I_1(z) = I_1(0)$ and $G_{12}(z|z') = G_{12}(z)$ for $I_1(z') = I_1(0)$ can be considered. With approximation $I_1(0) = 0$, Equation (A.24) reduces as in Equation (A.26). For Equation (A.25), with earlier

approximations as $I_1(0) = 0$ and $I'_2(0) = 0$, it reduces to Equation (A.27). As the reader antenna considered is a short dipole, the parameter Δl is the length of the dipole.

$$Z_{22}I_2^2(0) = \int_{-l_2-l_2}^{l_2} \int_{-l_2-l_2}^{l_2} I_2(z')G_{22}(z|z')I_2(z) dz' dz$$
(A.26)

$$I_1'(0)Z_{12}I_2(0) = I_1'(0)\Delta l \int_{-l_2}^{l_2} G_{12}(z')I_2(z') dz' + \int_{-l_2-l_2}^{l_2} \int_{-l_2}^{l_2} I_2(z')G_{22}(z|z')I_2'(z) dz' dz \quad (A.27)$$

Now, current distribution from Equation (A.22) can be substituted for the tag antenna in Equations (A.26) and (A.27) and the following form as in Equations (A.28) and (A.29) is obtained. To obtain Equation (A.29), $I'_2(0) = 0$ is considered as earlier.

$$Z_{22}I_2^2(0) = \int_{-l_2-l_2}^{l_2} \int_{-l_2-l_2}^{l_2} (I^0(z') + k_{22}I^1(z'))G_{22}(z|z')(I^0(z) + k_{22}I^1(z)) dz' dz$$
 (A.28)

$$I'_{1}(0)Z_{12}I_{2}(0) = I'_{1}(0)\Delta l \int_{-l_{2}}^{l_{2}} G_{12}(z')(I^{0}(z') + k_{12}I^{1}(z')) dz'$$

$$+ \int_{-l_{2}}^{l_{2}} \int_{-l_{2}}^{l_{2}} k'_{12}I^{1}(z')G_{22}(z|z')(I^{0}(z) + k_{12}I^{1}(z)) dz' dz$$
(A.29)

The constants k_{22} , k_{12} , and k'_{12} are adjustable in the trial functions and as the impedance expressions are stationary, all the constants can be determined by setting $\partial Z/\partial k = 0$. After finding the constants, the constants are substituted in Equations (A.28) and (A.29) to find expressions in terms of the trial functions and the geometry of antenna.

$$Z_{22}I_{2}^{2}(0) = \int_{-l_{2}-l_{2}}^{l_{2}} \int_{I^{0}(z')G_{22}(z|z')I^{0}(z) dz' dz - \frac{\left[\int_{-l_{2}-l_{2}}^{l_{2}} \int_{I^{0}(z')G_{22}(z|z')I^{1}(z) dz' dz\right]^{2}}{\int_{-l_{2}-l_{2}}^{l_{2}} \int_{I^{1}(z')G_{22}(z|z')I^{1}(z) dz' dz}$$

$$(A.30)$$

$$I'_{1}(0)Z_{12}I_{2}(0) = I'_{1}(0)\Delta l \int_{-l_{2}}^{l_{2}} G_{12}(z')I^{0}(z') dz'$$

$$- \frac{\left[I'_{1}(0)\Delta l \int_{-l_{2}}^{l_{2}} G_{12}(z')I^{1}(z') dz'\right] \left[\int_{-l_{2}-l_{2}}^{l_{2}} \int_{-l_{2}}^{l_{2}} I^{0}(z')G_{22}(z|z')I^{1}(z) dz' dz\right]}{\int_{-l_{2}-l_{2}}^{l_{2}} \int_{-l_{2}}^{l_{2}} I^{1}(z')G_{22}(z|z')I^{1}(z) dz' dz}$$
(A.31)

Now Equations (A.30) and (A.31) can be solved analytically to find the impedance parameters Z_{22} and Z_{12} . After further simplification, the impedance parameters are given as followed in Equation (A.32). The parameters A, B, C, D, E, F, G, and H are given in Equation (A.33)

$$Z_{22} = j30 \left[(A+jB) - \frac{(C+jD)^2}{(E+jF)} \right]$$

$$Z_{12} = j30 \left[\frac{\Delta l e^{-j\beta r_0}}{r_0} \right] \left[G - H \frac{(C+jD)}{(E+jF)} \right]$$
(A.32)

$$\begin{split} A &= \frac{1}{(1-\cos L)^2} \bigg[S(4L) + 4\cos L(L\cos L - \sin L) \big[ln \frac{4L}{\alpha} - C(2L) \big] \\ &- \frac{8}{\pi} \alpha sin^2 L - 2\cos^2 L sin 2L \bigg] \\ B &= \frac{1}{(1-\cos L)^2} \bigg[-C(4L) - (4L\cos^2 L - 2\sin 2L)S(2L) + \sin^2 2L \bigg] \\ C &= \frac{1}{(1-\cos L)} \bigg[(\sin L)S(4L) + (1-\cos L)C(4L) + 4\cos L(1-\cos L - L\sin L)C(2L) \\ &+ 4\cos L(1-\cos L)C(L) + 4\sin L(L\cos L - \sin L) ln \frac{4L}{\alpha} + 4(1-\cos L)^2 ln \frac{2L}{\alpha} \\ &- \frac{8}{\pi} \alpha sin L(1-\cos L) - (\sin 2L)^2 \bigg] \\ D &= \frac{1}{(1-\cos L)} \bigg[(1-\cos L)S(4L) + (\sin L)C(4L) + 4\cos L(1-\cos L - L\sin L)S(2L) \\ &+ 4\cos L(1-\cos L)S(L) + 2\sin^2 L sin 2L \\ E &= 2\cos L(1-\cos L)S(4L) + 2\sin L(1-\cos L)C(4L) + 4(1-\cos L)^2 S(2L) \\ &- 4L(\sin^2 L)C(2L) + 8\sin L(1-\cos L)C(L) + \big[4L\sin^2 L - 8\sin L(1-\cos L) \big] ln \frac{4L}{\alpha} \\ &- \frac{24}{\pi} \alpha (1-\cos L)^2 - 2\sin^2 L \sin 2L \\ F &= 2\sin L(1-\cos L)S(4L) - 2\cos L(1-\cos L)C(4L) - 4L(\sin^2 L)S(2L) \\ &- 4(1-\cos L)^2 C(2L) + 8\sin L(1-\cos L)S(L) + 4\sin^4 L \\ G &= \frac{2}{(1-\cos L)} (\sin L - L\cos L) \\ H &= 2\big[2(1-\cos L) - L\sin L \big] \end{split} \tag{A.33}$$

where

$$L = \beta l$$
, $\alpha = \beta a$, $C(x) = \int_0^x \frac{1 - \cos u}{u} du$, $S(x) = \int_0^x \frac{\sin u}{u} du$

APPENDIX B

Copper Etching Process

Procedure: 1. Substrate Preparation and Cleaning.

- (a) Cut the substrate to desired dimensions.
- (b) Rinse the substrate in acetone for 30 seconds.
- (c) Rinse the substrate in methanol for 30 seconds.
- (d) Rinse the substrate in DI water for 30 seconds.
- (e) Rinse the substrate in isopropanol alcohol (IPA) for 30 seconds.
- (f) Blow dry using Nitrogen.
- (g) Bake the substrate at 105⁰C for 3 minutes.

2. Spin-Coat Photoresist.

- (a) Set the rpm and time on Laurell Technologies Spinner (WS400B-6NPP LITE). Typically, for 17 μ m 30 μ m thick Copper laminates, rpm is 3000 for 30 seconds.
- (b) Spin the substrate after dropping positive photoresist S1813 over the substrate.
- (c) Soft bake the substrate at 95^0 for 45 seconds.

3. Expose and Develop

- (a) Calculate the expose time based on the power of the UV lamp in MJB 3 Mask Aligner and the spin coated thickness of the photoresist.
- (b) Typically, expose for 45 seconds (3000 rpm, 30 sec spin).
- (c) Bake the substrate at 105^0 for 30 seconds.
- (d) Develop using MF-319 for 30 seconds.
- (e) Rinse with DI water and blow dry using Nitrogen.
- (f) Hard bake at 115^{0} C for 5 minutes.

4. Copper Etching

- (a) Prepare the etchant by mixing Sodium per sulphate in DI water with 1:4 ratio (250 g in 1000 ml).
- (b) Heat the etchant at 80° C.
- (c) Immerse the exposed substrate until the desired copper pattern is etched.
- (d) Rinse with acetone, methanol for 30 seconds each.
- (e) Rinse with DI water and bake at 105⁰ for 5 minutes.

BIBLIOGRAPHY

BIBLIOGRAPHY

- [1] Y. Ma, X. Hui, and E. C. Kan, "Harmonic-WISP: A passive broadband harmonic RFID platform," in *IEEE MTT-S International Microwave Symposium (IMS)*. IEEE, 2016, pp. 1–4.
- [2] S. Mondal, S. Karuppuswami, D. Kumar, and P. Chahal, "Scope and application of harmonic RFID for implanted body area network," in *IEEE RFID Conference*. IEEE, 2020, pp. xx–xx.
- [3] S. Mondal, D. Kumar, and P. Chahal, "A wireless passive pH sensor with clutter rejection scheme," *IEEE Sensors Journal*, vol. 19, no. 9, pp. 3399–3407, 2019.
- [4] S. Karuppuswami, M. I. M. Ghazali, S. Mondal, and P. Chahal, "Wireless EAS sensor tags for volatile profiling in food packages," in 2018 IEEE 68th Electronic Components and Technology Conference (ECTC). IEEE, 2018, pp. 2174–2179.
- [5] M. Yuan, P. Chahal, E. C. Alocilja, and S. Chakrabartty, "Wireless biosensing using silver-enhancement based self-assembled antennas in passive radio frequency identification (RFID) tags," *IEEE Sensors Journal*, vol. 15, no. 8, pp. 4442–4450, 2015.
- [6] C. Occhiuzzi, S. Cippitelli, and G. Marrocco, "Modeling, design and experimentation of wearable RFID sensor tag," *IEEE Transactions on Antennas and Propagation*, vol. 58, no. 8, pp. 2490–2498, 2010.
- [7] Y. Ma and E. C. Kan, "Accurate indoor ranging by broadband harmonic generation in passive nltl backscatter tags," *IEEE transactions on microwave theory and techniques*, vol. 62, no. 5, pp. 1249–1261, 2014.
- [8] M. J. W. Rodwell, "Picosecond electrical wavefront generation and picosecond optoelectronic instrumentation," Ph.D. dissertation, Stanford University, 1987.
- [9] F. Yu, K. G. Lyon, and E. C. Kan, "A novel passive rfid transponder using harmonic generation of nonlinear transmission lines," *IEEE Transactions on Microwave Theory and Techniques*, vol. 58, no. 12, pp. 4121–4127, 2010.
- [10] S. Ahuja and P. Potti, "An introduction to RFID technology," *Communications and Network*, vol. 2, no. 3, pp. 183–186, 2010.
- [11] J. Riley, A. Smith, D. Reynolds, A. Edwards, J. Osborne, I. Williams, N. Carreck, and G. Poppy, "Tracking bees with harmonic radar," *Nature*, vol. 379, no. 6560, p. 29, 1996.

- [12] D. Zhang, L. T. Yang, M. Chen, S. Zhao, M. Guo, and Y. Zhang, "Real-time locating systems using active RFID for Internet of Things," *IEEE Systems Journal*, vol. 10, no. 3, pp. 1226–1235, 2016.
- [13] G. EPCglobal, "Epc radio-frequency identity protocols generation-2 UHF RFID; specification for RFID air interface protocol for communications at 860 MHz–960 MHz," EPCglobal Inc., November, 2013.
- [14] J. Landt, "The history of RFID," IEEE potentials, vol. 24, no. 4, pp. 8–11, 2005.
- [15] A. R. Koelle, S. W. Depp, and R. W. Freyman, "Short-range radio-telemetry for electronic identification, using modulated RF backscatter," *Proceedings of the IEEE*, vol. 63, no. 8, pp. 1260–1261, 1975.
- [16] S. Kumar, E. Swanson, and T. Tran, "RFID in the healthcare supply chain: usage and application," *International Journal of Health Care Quality Assurance*, vol. 22, no. 1, pp. 67–81, 2009.
- [17] C. Costa, F. Antonucci, F. Pallottino, J. Aguzzi, D. Sarriá, and P. Menesatti, "A review on agri-food supply chain traceability by means of RFID technology," *Food and bioprocess technology*, vol. 6, no. 2, pp. 353–366, 2013.
- [18] C. Amador, J.-P. Emond, and M. C. do Nascimento Nunes, "Application of RFID technologies in the temperature mapping of the pineapple supply chain," *Sensing and Instrumentation for Food Quality and Safety*, vol. 3, no. 1, pp. 26–33, 2009.
- [19] S. Piramuthu and W. Zhou, RFID and sensor network automation in the food industry: Ensuring quality and safety through supply chain visibility. Wiley Online Library, 2016.
- [20] D. L. Brock, "The Electronic Product Code (EPC)-A naming scheme for physical objects," White paper, 2001.
- [21] —, "Integrating the Electronic Product Code (EPC) and the Global Trade Item Number (GTIN)," White Paper available at www. autoidcenter. org/pdfs/MIT-WUTOID-WH-004. pdf, vol. 25, 2001.
- [22] A.-I. Center, "860MHz-960MHz Class I radio frequency identification tag radio frequency & logical communication interface specification proposed recommendation Version 1.0.0," *AutoID Center, MIT*, 2002.
- [23] S. Sarma, "Towards the 5 cents tag," Auto ID White Paper MIT-AUTOID-WH-006, 2001.
- [24] F. Bauchot, J.-Y. Clement, G. Marmigere, and P. Secondo, "Method and system for locating tires using RFID," Jan. 6 2009, uS Patent 7,474,214.

- [25] A. Dolgui and J.-M. Proth, "RFID technology in supply chain management: state of the art and perspectives," *IFAC Proceedings Volumes*, vol. 41, no. 2, pp. 4464–4475, 2008.
- [26] T. Zefferer, "A survey and analysis of nfc based payment solutions for smartphones," in *IADIS International Conference e-Society 2013*, 2013, pp. 275–282.
- [27] V. Coskun, B. Ozdenizci, and K. Ok, "A survey on near field communication (nfc) technology," Wireless personal communications, vol. 71, no. 3, pp. 2259–2294, 2013.
- [28] E. Haselsteiner and K. Breitfuß, "Security in near field communication (nfc)," in Workshop on RFID security. sn, 2006, pp. 12–14.
- [29] S. Roy, V. Jandhyala, J. R. Smith, D. J. Wetherall, B. P. Otis, R. Chakraborty, M. Buettner, D. J. Yeager, Y.-C. Ko, and A. P. Sample, "Rfid: From supply chains to sensor nets," *Proceedings of the IEEE*, vol. 98, no. 9, pp. 1583–1592, 2010.
- [30] A. P. Sample, D. J. Yeager, and J. R. Smith, "A capacitive touch interface for passive rfid tags," in 2009 IEEE International Conference on RFID. IEEE, 2009, pp. 103–109.
- [31] M. Buettner, R. Prasad, A. Sample, D. Yeager, B. Greenstein, J. R. Smith, and D. Wetherall, "Rfid sensor networks with the intel wisp," in *Proceedings of the 6th ACM conference on Embedded network sensor systems*. ACM, 2008, pp. 393–394.
- [32] "RFID based sensors," http://https://axzon.com/products//, [Online; accessed 14-October-2019].
- [33] Y.-Y. Hu, "Back-scattering cross section of a center-loaded cylindrical antenna," *IRE Transactions on Antennas and Propagation*, vol. 6, no. 1, pp. 140–148, 1958.
- [34] C. Levis and C. Tai, "A method of analyzing coupled antennas of unequal sizes," *IRE Transactions on Antennas and Propagation*, vol. 4, no. 2, pp. 128–132, 1956.
- [35] R. F. Harrington, "Small resonant scatterers and their use for field measurements," *IRE Transactions on Microwave Theory and Techniques*, vol. 10, no. 3, pp. 165–174, 1962.
- [36] B. S. Ciftler, A. Kadri, and I. Güvenç, "IoT localization for bistatic passive UHF RFID systems with 3-D radiation pattern," *IEEE Internet of Things Journal*, vol. 4, no. 4, pp. 905–916, 2017.
- [37] D.-Y. Kim, H.-G. Yoon, B.-J. Jang, and J.-G. Yook, "Effects of reader-to-reader interference on the UHF RFID interrogation range," *IEEE Transactions on Industrial Electronics*, vol. 56, no. 7, pp. 2337–2346, 2009.

- [38] X. Hui and E. C. Kan, "Monitoring vital signs over multiplexed radio by near-field coherent sensing," *Nature Electronics*, vol. 1, no. 1, p. 74, 2018.
- [39] M. I. M. Ghazali, S. Karuppuswami, and P. Chahal, "Embedded passive RF tags towards intrinsically locatable buried plastic materials," in *IEEE 66th Electronic Components and Technology Conference (ECTC)*. IEEE, 2016, pp. 2575–2580.
- [40] S. Mondal, D. Kumar, M. I. Ghazali, P. Chahal, L. Udpa, and Y. Deng, "Monitoring and localization of buried plastic natural gas pipes using passive RF tags," in AIP Conference Proceedings, vol. 1949, no. 1. AIP Publishing LLC, 2018, p. 020020.
- [41] S. Mondal and P. Chahal, "A passive harmonic RFID tag and interrogator development," *IEEE Journal of Radio Frequency Identification*, vol. 3, no. 2, pp. 98–107, 2019.
- [42] J. Breitbarth, "Design and characterization of low phase noise microwave circuits," Ph.D. dissertation, University of Colorado at Boulder, 2006.
- [43] H. Wu, B. Tao, Z. Gong, Z. Yin, and H. Ding, "A fast uhf rfid localization method using unwrapped phase-position model," *IEEE Transactions on Automation Science and Engineering*, vol. 16, no. 4, pp. 1698–1707, 2019.
- [44] H. Ma and K. Wang, "Fusion of RSS and phase shift using the Kalman filter for RFID tracking," *IEEE Sensors Journal*, vol. 17, no. 11, pp. 3551–3558, 2017.
- [45] L. M. Ni, D. Zhang, and M. R. Souryal, "RFID-based localization and tracking technologies," *IEEE Wireless Communications*, vol. 18, no. 2, pp. 45–51, 2011.
- [46] D. Kumar, S. Mondal, A. Kaur, Y. Deng, and P. Chahal, "An RF backscatterer system for real-time multi-sensing applications," *Sensors and Actuators A: Physical*, vol. 303, p. 111685, 2020.
- [47] P. Chahal, D. Kumar, S. Mondal, and S. Karuppuswami, "Systems and methods for a multiband sensing platform," May 28 2020, uS Patent App. 16/695,758.
- [48] S. Mondal, K. Wijewardena, S. Karrapuswami, D. Kumar, P. Chahal, M. Ghannam, and M. Cuddihy, "A Wireless Battery-less Seat Sensor for Autonomous Vehicles," in 2020 IEEE 70th Electronic Components and Technology Conference (ECTC). IEEE, 2020, pp. 2289–2294.
- [49] D. Kumar, S. Mondal, Y. Deng, and P. Chahal, "Wireless Battery-Free Harmonic Communication System for Pressure Sensing," *Micromachines*, vol. 11, no. 12, p. 1043, 2020.

- [50] S. Mondal, D. Kumar, S. Karuppuswami, and P. Chahal, "A harmonic RF phase-shifter based wireless pH sensor," in 2018 IEEE 68th Electronic Components and Technology Conference (ECTC). IEEE, 2018, pp. 796–801.
- [51] S. Karuppuswami, S. Mondal, D. Kumar, A. Kaur, and P. Chahal, "Thin-film based passive RFID sensor tag for detection of packaged food volatiles," in *International Symposium on Microelectronics*, vol. 2019, no. 1. International Microelectronics Assembly and Packaging Society, 2019, pp. 000599–000602.
- [52] S. Karuppuswami, S. Mondal, M. I. M. Ghazali, and P. Chahal, "A multiuse fully 3-D printed cavity sensor for liquid profiling," *IEEE Sensors Letters*, vol. 3, no. 2, pp. 1–4, 2018.
- [53] —, "A Reusable 3D Printed Cavity Resonator for Liquid Sample Characterization," in *International Symposium on Microelectronics*, vol. 2018, no. 1. International Microelectronics Assembly and Packaging Society, 2018, pp. 000389–000392.
- [54] S. Karuppuswami, S. Mondal, D. Kumar, and P. Chahal, "A Compact Wireless Passive Breath Analyzer for Health Monitoring," in 2020 IEEE 70th Electronic Components and Technology Conference (ECTC). IEEE, 2020, pp. 1010–1015.
- [55] M. Philipose, J. R. Smith, B. Jiang, A. Mamishev, S. Roy, and K. Sundara-Rajan, "Battery-free wireless identification and sensing," *IEEE Pervasive computing*, vol. 4, no. 1, pp. 37–45, 2005.
- [56] A. B. Miller, M. E. Sears, L. L. Morgan, D. L. Davis, L. Hardell, M. Oremus, and C. L. Soskolne, "Risks to health and well-being from radio-frequency radiation emitted by cell phones and other wireless devices," Frontiers in Public Health, vol. 7, p. 223, 2019.
- [57] A. Bortkiewicz, "Health effects of radiofrequency electromagnetic fields (RF EMF)," *Industrial health*, vol. 57, no. 4, pp. 403–405, 2019.
- [58] R. Singh, R. Nath, A. K. Mathur, and R. S. Sharma, "Effect of radiofrequency radiation on reproductive health," *The Indian journal of medical research*, vol. 148, no. Suppl 1, p. S92, 2018.
- [59] C. Mutti and A. Wittneben, "Robust signal detection in passive RFID systems," in *Proceedings of the First International EURASIP Workshop on RFID Technology*, 2007, pp. 39–42.
- [60] P. H. Cole, D. M. Hall, M. Loukine, and C. D. Werner, "Fundamental constraints on RF tagging systems," in *Third Annual Wireless Symposium and Exhibition, Santa Clara*, 1995, pp. 294–303.

- [61] P. V. Nikitin and K. Rao, "Performance limitations of passive UHF RFID systems," in *Antennas and Propagation Society International Symposium*. IEEE, 2006, pp. 1011–1014.
- [62] X. Hui and E. C. Kan, "Radio ranging with ultrahigh resolution using a harmonic radio-frequency identification system," *Nature Electronics*, vol. 2, no. 3, pp. 125–131, 2019.
- [63] L. Zhang, D. Karasiewicz, B. Cifctioglu, and H. Wu, "A 1.6-to-3.2/4.8 GHz dual-modulus injection-locked frequency multiplier in 0.18 μ m digital CMOS," in *Radio Frequency Integrated Circuits Symposium*, (*RFIC*). IEEE, 2008, pp. 427–430.
- [64] F. Benson and J. Last, "Nonlinear-transmission-line harmonic generator," in *Proceedings of the Institution of Electrical Engineers*, vol. 112, 4. IET, 1965, pp. 635–643.
- [65] F. Yu, K. G. Lyon, and E. C. Kan, "A novel passive RFID transponder using harmonic generation of nonlinear transmission lines," *IEEE Transactions on Microwave Theory and Techniques*, vol. 58, no. 12, pp. 4121–4127, 2010.
- [66] Y. Zhao, J. R. Smith, and A. Sample, "NFC-WISP: A sensing and computationally enhanced near-field RFID platform," in *IEEE International Conference on RFID*. IEEE, 2015, pp. 174–181.
- [67] S. Bhadra, D. S. Tan, D. J. Thomson, M. S. Freund, and G. E. Bridges, "A wireless passive sensor for temperature compensated remote pH monitoring," *IEEE Sensors Journal*, vol. 13, no. 6, pp. 2428–2436, 2013.
- [68] E. Recommendation, "70-03 relating to the use of short range devices (SRD)," Version of, vol. 18, 2009.
- [69] H. M. Lu, C. Goldsmith, L. Cauller, and J.-B. Lee, "MEMS-based inductively coupled RFID transponder for implantable wireless sensor applications," *IEEE Transactions on Magnetics*, vol. 43, no. 6, pp. 2412–2414, 2007.
- [70] M. Adnan and E. Afshari, "Efficient microwave and millimeter-wave frequency multipliers using nonlinear transmission lines in cmos technology," *IEEE Transactions on Microwave Theory and Techniques*, vol. 63, no. 9, pp. 2889–2896, 2015.
- [71] M. J. Rodwell, M. Kamegawa, R. Yu, M. Case, E. Carman, and K. S. Giboney, "Gaas nonlinear transmission lines for picosecond pulse generation and millimeter-wave sampling," *IEEE Transactions on Microwave Theory and Techniques*, vol. 39, no. 7, pp. 1194–1204, 1991.

- [72] S. Mondal, M. I. M. Ghazali, S. Karuppuswami, A. Kaur, and P. Chahal, "A nonlinear transmission line based harmonic rf tag," in 2017 IEEE 67th Electronic Components and Technology Conference (ECTC). IEEE, 2017, pp. 2237–2242.
- [73] K. S. Champlin and D. Singh, "Small-signal second-harmonic generation by a non-linear transmission line (short paper)," *IEEE transactions on microwave theory and techniques*, vol. 34, no. 3, pp. 351–353, 1986.
- [74] F. Callegari, J. C. Boggio, H. Fragnito, and R. Arradi, "Mixing of signals in two-pump fiber optic parametric amplifiers and wavelength converters," in *Optical Fiber Communication Conference*. Optical Society of America, 2004, p. MF18.
- [75] Y. Chen and A. W. Snyder, "Four-photon parametric mixing in optical fibers: effect of pump depletion," *Optics letters*, vol. 14, no. 1, pp. 87–89, 1989.
- [76] K. S. Rao, P. V. Nikitin, and S. F. Lam, "Antenna design for UHF RFID tags: A review and a practical application," *IEEE Transactions on antennas and propagation*, vol. 53, no. 12, pp. 3870–3876, 2005.
- [77] M. Sasaki, Q. Chen, and K. Sawaya, "Radiation efficiency of small loop antennas for pager," in *Antennas and Propagation Society International Symposium*, vol. 1. IEEE, 1999, pp. 10–13.
- [78] G. Marrocco, A. Fonte, and F. Bardati, "Evolutionary design of miniaturized meanderline antennas for RFID applications," in *Antennas and Propagation Society Interna*tional Symposium, vol. 2. IEEE, 2002, pp. 362–365.
- [79] O. O. Olaode, W. D. Palmer, and W. T. Joines, "Effects of meandering on dipole antenna resonant frequency," *IEEE Antennas and Wireless Propagation Letters*, vol. 11, pp. 122–125, 2012.
- [80] G. Marrocco, "Gain-optimized self-resonant meander line antennas for RFID applications," *IEEE Antennas and Wireless propagation letters*, vol. 2, no. 1, pp. 302–305, 2003.
- [81] K. W. Lui, O. H. Murphy, and C. Toumazou, "32- μ m wirelessly-powered sensor platform with a 2-m range," *IEEE Sensors Journal*, vol. 12, no. 6, pp. 1919–1924, 2012.
- [82] J. F. Dickson, "On-chip high-voltage generation in MNOS integrated circuits using an improved voltage multiplier technique," *IEEE Journal of solid-state circuits*, vol. 11, no. 3, pp. 374–378, 1976.
- [83] G. G. Galloway, "Addressable underground marker," May 14 2002, US Patent 6,388,575.

- [84] S. Hemour, Y. Zhao, C. H. P. Lorenz, D. Houssameddine, Y. Gui, C.-M. Hu, and K. Wu, "Towards low-power high-efficiency RF and microwave energy harvesting," *IEEE transactions on microwave theory and techniques*, vol. 62, no. 4, pp. 965–976, 2014.
- [85] A. P. Sample, D. J. Yeager, P. S. Powledge, and J. R. Smith, "Design of a passively-powered, programmable sensing platform for UHF RFID systems," in *IEEE International Conference on RFID*. IEEE, 2007, pp. 149–156.
- [86] R. Barnett, G. Balachandran, S. Lazar, B. Kramer, G. Konnail, S. Rajasekhar, and V. Drobny, "A passive UHF RFID transponder for EPC Gen 2 with-14dBm sensitivity in 0.13 μm CMOS," in *IEEE International Solid-State Circuits Conference*, (ISSCC). IEEE, 2007, pp. 582–623.
- [87] V. Palazzi, F. Alimenti, M. Virili, C. Mariotti, G. Orecchini, P. Mezzanotte, and L. Roselli, "A novel compact harmonic RFID sensor in paper substrate based on a variable attenuator and nested antennas," in *IEEE MTT-S International Microwave Symposium (IMS)*. IEEE, 2016, pp. 1–4.
- [88] J.-W. Lee and B. Lee, "A long-range UHF-band passive RFID tag IC based on high-Q design approach," *IEEE Transactions on industrial electronics*, vol. 56, no. 7, pp. 2308–2316, 2009.
- [89] "Monza 4 RFID IC," https://support.impinj.com/hc/en-us/articles/202756908-Monza-4-RFID-Tag-Chip-Datasheet, [Online; accessed 08-October-2018].
- [90] S. Gollakota, V. Talla, B. Kellogg, B. Ransford, S. Naderiparizi, and J. R. Smith, "Power transmission using wireless communication signals," Aug. 13 2019, uS Patent 10,383,126.
- [91] J. R. Smith, K. P. Fishkin, B. Jiang, A. Mamishev, M. Philipose, A. D. Rea, S. Roy, and K. Sundara-Rajan, "RFID-based techniques for human-activity detection," *Communications of the ACM*, vol. 48, no. 9, pp. 39–44, 2005.
- [92] A. P. Sample, D. J. Yeager, P. S. Powledge, and J. R. Smith, "Design of a passively-powered, programmable sensing platform for UHF RFID systems," in 2007 IEEE international Conference on RFID. IEEE, 2007, pp. 149–156.
- [93] D. J. Yeager, J. Holleman, R. Prasad, J. R. Smith, and B. P. Otis, "Neuralwisp: A wirelessly powered neural interface with 1-m range," *IEEE Transactions on Biomedical Circuits and Systems*, vol. 3, no. 6, pp. 379–387, 2009.
- [94] N. Xiao, W. Yu, and X. Han, "Wearable heart rate monitoring intelligent sports bracelet based on Internet of things," *Measurement*, vol. 164, p. 108102, 2020.

- [95] M. Chung, G. Fortunato, and N. Radacsi, "Wearable flexible sweat sensors for health-care monitoring: a review," *Journal of the Royal Society Interface*, vol. 16, no. 159, p. 20190217, 2019.
- [96] P. A. Hammond, D. Ali, and D. R. Cumming, "A system-on-chip digital pH meter for use in a wireless diagnostic capsule," *IEEE Transactions on Biomedical Engineering*, vol. 52, no. 4, pp. 687–694, 2005.
- [97] J. Kim, S. Imani, W. R. de Araujo, J. Warchall, G. Valdés-Ramírez, T. R. Paixão, P. P. Mercier, and J. Wang, "Wearable salivary uric acid mouthguard biosensor with integrated wireless electronics," *Biosensors and Bioelectronics*, vol. 74, pp. 1061–1068, 2015.
- [98] S. Baliga, S. Muglikar, and R. Kale, "Salivary pH: A diagnostic biomarker," *Journal of Indian Society of Periodontology*, vol. 17, no. 4, p. 461, 2013.
- [99] M. Fiyaz, A. Ramesh, K. Ramalingam, B. Thomas, S. Shetty, and P. Prakash, "Association of salivary calcium, phosphate, pH and flow rate on oral health: A study on 90 subjects," *Journal of Indian Society of Periodontology*, vol. 17, no. 4, p. 454, 2013.
- [100] K. Rajesh, S. H. Zareena, and M. A. Kumar, "Assessment of salivary calcium, phosphate, magnesium, pH, and flow rate in healthy subjects, periodontitis, and dental caries," *Contemporary clinical dentistry*, vol. 6, no. 4, p. 461, 2015.
- [101] H. Cao, V. Landge, U. Tata, Y.-S. Seo, S. Rao, S.-J. Tang, H. F. Tibbals, S. Spechler, and J.-C. Chiao, "An implantable, batteryless, and wireless capsule with integrated impedance and pH sensors for gastroesophageal reflux monitoring," *IEEE Transactions on Biomedical Engineering*, vol. 59, no. 11, pp. 3131–3139, 2012.
- [102] S. Bhadra, G. E. Bridges, D. J. Thomson, and M. S. Freund, "Electrode potential-based coupled coil sensor for remote pH monitoring," *IEEE Sensors Journal*, vol. 11, no. 11, pp. 2813–2819, 2011.
- [103] W.-D. Huang, S. Deb, Y.-S. Seo, S. Rao, M. Chiao, and J. Chiao, "A passive radio-frequency pH-sensing tag for wireless food-quality monitoring," *IEEE Sensors Journal*, vol. 12, no. 3, pp. 487–495, 2012.
- [104] B. E. Horton, S. Schweitzer, A. J. DeRouin, and K. G. Ong, "A varactor-based, inductively coupled wireless pH sensor," *IEEE Sensors Journal*, vol. 11, no. 4, pp. 1061–1066, 2011.
- [105] S. Bhadra, D. J. Thomson, and G. E. Bridges, "Monitoring acidic and basic volatile concentration using a pH-electrode based wireless passive sensor," *Sensors and Actuators B: Chemical*, vol. 209, pp. 803–810, 2015.

- [106] T. Litovitz, N. Whitaker, L. Clark *et al.*, "Preventing battery ingestions: an analysis of 8648 cases," *Pediatrics*, vol. 125, no. 6, p. 1178, 2010.
- [107] P. Gou, N. D. Kraut, I. M. Feigel, H. Bai, G. J. Morgan, Y. Chen, Y. Tang, K. Bocan, J. Stachel, L. Berger et al., "Carbon nanotube chemiresistor for wireless pH sensing," Scientific reports, vol. 4, p. 4468, 2014.
- [108] S. Mondal, K. Wijewardena, S. Karuppuswami, N. Kriti, D. Kumar, and P. Chahal, "Blockchain inspired RFID based information architecture for food supply chain," *IEEE Internet of Things Journal*, vol. 6, no. 3, pp. 5803–5813, 2019.
- [109] P. Hashemi, P. L. Walsh, T. S. Guillot, J. Gras-Najjar, P. Takmakov, F. T. Crews, and R. M. Wightman, "Chronically implanted, nafion-coated Ag/AgCl reference electrodes for neurochemical applications," ACS chemical neuroscience, vol. 2, no. 11, pp. 658– 666, 2011.
- [110] H. Suzuki, A. Hiratsuka, S. Sasaki, and I. Karube, "Problems associated with the thin-film Ag/AgCl reference electrode and a novel structure with improved durability," *Sensors and Actuators B: Chemical*, vol. 46, no. 2, pp. 104–113, 1998.
- [111] Y. Devrim, S. Erkan, N. Bac, and I. Eroglu, "Improvement of PEMFC performance with Nafion/inorganic nanocomposite membrane electrode assembly prepared by ultrasonic coating technique," *International Journal of Hydrogen Energy*, vol. 37, no. 21, pp. 16748–16758, 2012.
- [112] T. Instruments, 2015, ADS7040 ultra-low power, ultra-small size, 8-bit, 1-MSPS, SAR ADC. [Online]. Available: http://www.ti.com/lit/ds/sbas676c/sbas676c.pdf
- [113] S. Mondal, S. Karuppuswami, R. Steinhorst, and P. Chahal, "A wearable passive pH sensor for health monitoring," in 2019 IEEE 69th Electronic Components and Technology Conference (ECTC). IEEE, 2019, pp. 1240–1245.
- [114] F. Kong, C. Qi, H. Lee, G. D. Durgin, and M. Ghovanloo, "Antennas for intraoral Tongue Drive System at 2.4 GHz: design, characterization, and comparison," *IEEE Transactions on Microwave Theory and Techniques*, vol. 66, no. 5, pp. 2546–2555, 2018.
- [115] D. Ma, C. Mason, and S. S. Ghoreishizadeh, "A wireless system for continuous inmouth pH monitoring," in 2017 IEEE Biomedical Circuits and Systems Conference (BioCAS). IEEE, 2017, pp. 1–4.
- [116] F. Xu, G. Yan, K. Zhao, L. Lu, J. Gao, and G. Liu, "A wireless capsule system with ASIC for monitoring the physiological signals of the human gastrointestinal tract," *IEEE transactions on biomedical circuits and systems*, vol. 8, no. 6, pp. 871–880, 2014.

- [117] A. Lahtela, M. Hassinen, and V. Jylha, "RFID and NFC in healthcare: Safety of hospitals medication care," in 2008 Second International Conference on Pervasive Computing Technologies for Healthcare. IEEE, 2008, pp. 241–244.
- [118] S. Mondal, S. Karuppuswami, and P. Chahal, "ID integrated batteryless wireless digital pH sensor," *IEEE Sensors Journal*, vol. 19, no. 24, pp. 12079–12086, 2019.
- [119] A. P. Sample, D. J. Yeager, P. S. Powledge, A. V. Mamishev, and J. R. Smith, "Design of an RFID-based battery-free programmable sensing platform," *IEEE transactions on instrumentation and measurement*, vol. 57, no. 11, pp. 2608–2615, 2008.
- [120] A. C. Cabezas, R. G. Medina, N. M. Peña, and M. A. Labrador, "Low energy and low latency in wireless sensor networks," in 2009 IEEE International Conference on Communications. IEEE, 2009, pp. 1–5.
- [121] S. Hemour, Y. Zhao, C. H. P. Lorenz, D. Houssameddine, Y. Gui, C.-M. Hu, and K. Wu, "Towards low-power high-efficiency RF and microwave energy harvesting," *IEEE Transactions on Microwave Theory and Techniques*, vol. 62, no. 4, pp. 965–976, 2014.
- [122] S. Mandal and R. Sarpeshkar, "Low-power CMOS rectifier design for RFID applications," *IEEE Transactions on Circuits and Systems I: Regular Papers*, vol. 54, no. 6, pp. 1177–1188, 2007.
- [123] C. Lauterbach, W. Weber, and D. Romer, "Charge sharing concept and new clocking scheme for power efficiency and electromagnetic emission improvement of boosted charge pumps," *IEEE Journal of solid-state circuits*, vol. 35, no. 5, pp. 719–723, 2000.
- [124] X. Liu, L. Huang, K. Ravichandran, and E. Sánchez-Sinencio, "A highly efficient reconfigurable charge pump energy harvester with wide harvesting range and two-dimensional MPPT for Internet of Things," *IEEE Journal of Solid-State Circuits*, vol. 51, no. 5, pp. 1302–1312, 2016.
- [125] G. Papotto, F. Carrara, and G. Palmisano, "A 90-nm CMOS threshold-compensated RF energy harvester," *IEEE Journal of solid-state circuits*, vol. 46, no. 9, pp. 1985–1997, 2011.
- [126] Z. Luo, M.-D. Ker, W.-H. Cheng, and T.-Y. Yen, "Regulated charge pump with new clocking scheme for smoothing the charging current in low voltage CMOS process," *IEEE Transactions on Circuits and Systems I: Regular Papers*, vol. 64, no. 3, pp. 528–536, 2016.
- [127] A. Chasin, V. Volskiy, M. Libois, K. Myny, M. Nag, M. Rockelé, G. A. Vandenbosch, J. Genoe, G. Gielen, and P. Heremans, "An integrated a-IGZO UHF energy harvester

- for passive RFID tags," *IEEE Transactions on Electron Devices*, vol. 61, no. 9, pp. 3289–3295, 2014.
- [128] T. Tanzawa and T. Tanaka, "A dynamic analysis of the Dickson charge pump circuit," *IEEE Journal of solid-state circuits*, vol. 32, no. 8, pp. 1231–1240, 1997.
- [129] A. Ballo, A. D. Grasso, G. Giustolisi, and G. Palumbo, "Optimized charge pump with clock booster for reduced rise time or silicon area," *IEEE Transactions on Circuits and Systems II: Express Briefs*, vol. 66, no. 12, pp. 1977–1981, 2019.
- [130] S. A. Maas, "Microwave mixers," ah, 1986.
- [131] J.-h. Ou, S. Y. Zheng, A. S. Andrenko, Y. Li, and H.-Z. Tan, "Novel time-domain Schottky diode modeling for microwave rectifier designs," *IEEE Transactions on Circuits and Systems I: Regular Papers*, vol. 65, no. 4, pp. 1234–1244, 2017.
- [132] Q. Chen, X. Chen, H. Cai, and F. Chen, "Schottky diode large-signal equivalent-circuit parameters extraction for high-efficiency microwave rectifying circuit design," *IEEE Transactions on Circuits and Systems II: Express Briefs*, 2020.
- [133] C. A. Costa, M. Dheans, P. Baltus, and H. Gao, "Characterization of damper-to-damper wireless channel in small cars," in 2018 IEEE MTT-S International Wireless Symposium (IWS). IEEE, 2018, pp. 1–3.
- [134] T. R. Rao, D. Balachander, P. Sathish, and N. Tiwari, "Intra-vehicular RF propagation measurements at UHF for Wireless Sensor Networks," in 2012 International Conference on Recent Advances in Computing and Software Systems. IEEE, 2012, pp. 214–218.
- [135] T. ElBatt, C. Saraydar, M. Ames, and T. Talty, "Potential for intra-vehicle wireless automotive sensor networks," in 2006 IEEE Sarnoff Symposium. IEEE, 2006, pp. 1–4.
- [136] J.-R. Lin, T. Talty, and O. K. Tonguz, "On the potential of bluetooth low energy technology for vehicular applications," *IEEE Communications Magazine*, vol. 53, no. 1, pp. 267–275, 2015.
- [137] S. Karuppuswami, S. Mondal, D. Kumar, and P. Chahal, "RFID Coupled Passive Digital Ammonia Sensor for Quality Control of Packaged Food," *IEEE Sensors Journal*, vol. 20, no. 9, pp. 4679–4687, 2020.
- [138] J. S. McLean, "A re-examination of the fundamental limits on the radiation Q of electrically small antennas," *IEEE Transactions on antennas and propagation*, vol. 44, no. 5, p. 672, 1996.

- [139] W. Geyi, "Physical limitations of antenna," *IEEE Transactions on Antennas and Propagation*, vol. 51, no. 8, pp. 2116–2123, 2003.
- [140] M. Villegas, J.-L. Polleux, X. Begaud, M. Pigeon, C. Delaveaud, L. Rudant, and K. Belmkaddem, "Miniature directive antennas," *International Journal of Microwave* and Wireless Technologies, vol. 6, no. 1, p. 45, 2014.
- [141] R. M. Fano, "Theoretical limitations on the broadband matching of arbitrary impedances," *Journal of the Franklin Institute*, vol. 249, no. 1, pp. 57–83, 1950.
- [142] R. F. Harrington, "Effect of antenna size on gain, bandwidth, and efficiency," J. Res. Nat. Bur. Stand, vol. 64, no. 1, pp. 1–12, 1960.
- [143] P. J. Chahal and S. Mondal, "Harmonic RFID Tag-Reader System For Long Range Sensing Identification And Security," Nov. 28 2019, uS Patent App. 16/420,711.